New Generation Stochastic Data-Driven Calibration of the Accelerometers and Modelling of the Non-Gravitational Accelerations in GRACE Missions

Evangelia Myrto Tzamali

A DISSERTATION SUBMITTED TO THE FACULTY OF GRADUATE STUDIES IN PARTIAL FULFILLMENT OF THE REQUIREMENTS FOR THE DEGREE OF

DOCTOR OF PHILOSOPHY

GRADUATE PROGRAM IN EARTH AND SPACE SCIENCE

YORK UNIVERSITY

TORONTO, ONTARIO

September 2024

Abstract

The Gravity Recovery and Climate Experiment (GRACE) and its successor, GRACE Follow-On (GRACE-FO), have significantly advanced our understanding of Earth's gravity field and its temporal changes by measuring subtle gravity variations caused by mass redistribution on and beneath Earth's surface. A key component of these missions is the use of geodetic-quality GPS receivers for precise orbit determination and 3D accelerometers, which measure non-gravitational forces like atmospheric drag and solar radiation pressure. However, challenges in using accelerometers must be addressed to ensure data and modeling accuracy.

A primary challenge is the calibration of accelerometers, as inaccuracies can lead to significant errors in gravity field modeling and thermospheric density estimates of up to 10%, depending on the levels of solar activity. This study introduces a calibration method using matched filter techniques applied to accelerometer measurements and GPS-derived accelerations. The estimated calibration parameters show high stability with values close to 1, as expected from the ultra-sensitive electrostatic space accelerometers and proposed by other studies.

Error assessment of GRACE and future mass change missions must consider accelerometer measurements as stochastic quantities with realistic error estimates. This involves identifying and quantifying measurement errors stemming from instrument noise, thermal effects, correlations and transient effects. This study generates a stochastic (weighted) 1B accelerometer dataset to investigate systematic errors from various sources like geomagnetic storms, temperature changes, and terminator crossings. Contrastingly to the official accuracy which is $0.1\ nm/s^2$ for the along-track and radial direction and $1\ nm/s^2$ in the cross-track, the proposed dataset being clean from spikes has an accuracy of $10^{-3}\ nm/s^2$.

Accurate modeling of non-gravitational forces is essential for isolating gravitational signals and estimating drag, which is crucial for determining thermospheric densities. This study proposes a data-driven model for the dominant forces of solar and thermal radiation pressure and drag on the

GRACE-C satellite, using the new 1B dataset produced in this study. A comprehensive analysis of residuals which are up to $2\,nm/s^2$ in the along-track, $0.5\,nm/s^2$ in the cross-track and up to $5\,nm/s^2$ in the radial direction, reveals disturbances with latitudinal dependency, especially during high geomagnetic activity.

Acknowledgements

Starting my Ph.D. was a turning point in my life. It was a journey that changed me in ways I never expected, creating a clear divide between who I was before and who I became after. The process was tough, with daily struggles against my own expectations and feelings of not being enough. The long hours were exhausting, but I learned so much along the way. This decision was one of the most important I've ever made. It was a time of real self-discovery—I found strengths I didn't know I had and faced my weaknesses head-on. This experience along with the people I met, didn't just shape me as a researcher; it changed my whole outlook on life, making me stronger, more self-aware, and more balanced.

I am deeply thankful to Prof. Spiros Pagiatakis, my supervisor, who has been a guiding light and mentor, embodying the qualities of both an exceptional professor and an extraordinary human being. His guidance, support, and patience, especially during the challenging times of the pandemic, have been invaluable. He provided essential research tools and imparted lessons that will resonate with me throughout my life. Prof. Pagiatakis created a nurturing environment where I felt comfortable sharing my ideas, concerns, and excitement over discoveries. He consistently recognized and nurtured my potential, never doubting my abilities. This thesis, a symbol of his boundless enthusiasm, insightful guidance, and support, would not have been possible without him.

I would like to express my appreciation to Prof. Sunil Bisnath and Prof. Michael Daly, members of my committee, for their valuable feedback and thought-provoking discussions. Prof. Bisnath's frequent question, "Why is this important?", consistently challenged me to consider the broader impact of my work. Meanwhile, Prof. Daly's reminders about the importance of confidence have been instrumental in my personal and professional growth.

I would like to personally thank Jacob Flury and Igor Kosch from Leibniz Universität Hannover and Florian Wöske from Universität Bremen for their help. Their contributions have been invaluable in my research.

I owe a big thank you to Rosa, Athina, and Alice, my lab mates, for their unwavering support. Our discussions and brainstorming have been crucial in my journey. Special thanks to Nikeet for his support, his readiness to share ideas and discuss our work. Our friendship has been so meaningful through these challenging years.

I am grateful to Natural Sciences and Engineering Research Council of Canada (NSERC) for their financial support during my PhD studies. Their funding has been crucial in enabling my research and academic growth.

Thank you to Artemis, Angelos, Daphne, Elli, and Deme for the countless hours we shared in Toronto; your friendship has truly enriched my life. Artemis and Angelos, you were the best neighbors I could have ever asked for!

A huge shout-out to my friends and family in Greece—your love and support mean the world to me, no matter the distance.

A heartfelt thank you to my partner, Lefteris. Your encouragement inspires me to be a better person every day.

To my family – you know who you are.

Table of Contents

List of Figures

List of Tables

List of Acronyms

ACC: Accelerometer

ARF: Accelerometer Reference Frame

CHAMP: Challenging Minisatellite Payload

CRF: Celestial Reference Frame

DLR: German Aerospace Center

ECI: Earth-centered Inertial

ERP: Earth Radiation Pressure

ESA: European Space Agency

GCRF: Geocentric Celestial Reference Frame

GOCE: Gravity field and steady-state Ocean Circulation Explorer

GRACE: Gravity Recovery and Climate Experiment

ITRF: International Terrestrial Reference Frame

IRF: Inertial Reference Frame

KBR: K-band Microwave Ranging System

LEO: Low Earth Orbit

LRI: Laser Ranging Interferometer

NASA: National Aeronautics and Space Administration

POD: Precise Orbit Determination

SRF: Science Reference Frame

SRP: Solar Radiation Pressure

TRP: Thermal Radiation Pressure

1 Motivation and Problem Statement

Satellites in Low Earth Orbit (LEO) play pivotal role in understanding the Earth's dynamic processes and environmental changes. These satellites enable real-time monitoring of the Earth’s environment, weather patterns, occurrences of natural disasters and enhancement of positioning and navigation systems. Satellites like Terra and Aqua provide critical data on Earth's atmosphere, oceans, and land, contributing to research on climate change, weather patterns, and environmental health. Landsat 8 delivers high-resolution imagery, aiding in land use management, agriculture, and forest conservation. Sentinel-1 enhances our ability to monitor natural disasters and track environmental changes with its radar imagery, while CYGNSS improves our understanding of tropical storms and hurricanes, helping to refine weather forecasts. These LEO missions are invaluable in addressing global environmental challenges and informing decision-making. Consequently, they play a crucial role in efficient disaster management efforts and make significant contributions to the studies of the Earth system.

LEO missions, such as the Challenging Minisatellite Payload (CHAMP), the Gravity field and steady-state Ocean Circulation Explorer (GOCE), the Gravity Recovery and Climate Experiment (GRACE and GRACE-FO), and Swarm, have collectively advanced our understanding of Earth's gravity field dynamics, magnetic field, and various geophysical processes. These satellites, operating in lower orbits, offer numerous advantages, including reduced signal latency and faster data transfer speeds compared to satellites in higher orbits. Their frequent revisits to specific regions of Earth's surface allow for the continuous monitoring of changes in the planet's water bodies, ice sheets, solid Earth, climate, navigation, atmospheric conditions, and space weather. A crucial common instrument onboard all these satellites is the accelerometer, which measures non-gravitational forces acting on the satellites. This instrument significantly enhances our understanding of the complex environment in which satellites orbit the Earth.

1.1 Gravity Space Missions

CHAMP, a single satellite mission of the German Aerospace Centre (DLR) launched in July 2000 has played a significant role in studying the Earth's magnetic field, thermospheric dynamics, and ionospheric phenomena, providing valuable measurements for understanding atmospheric processes and space weather (Lühr *et al*., 2004; Hu *et al*., 2022). The satellite's measurements have been crucial in investigating thermospheric density enhancements (Crowley *et al*., 2010; Abadi *et al*., 2017).

GOCE, a European Space Agency (ESA) single satellite mission launched in March 2009, with its low Sun-synchronous orbit and high-quality gravitational gradient measurements, has significantly contributed to the recovery of both static and time-variable gravity fields, and provided detailed insights into the Earth's gravity field variations (Canuto, 2008; Jäggi *et al.* 2014).

GRACE and its follow-on mission (GRACE-FO), two twin-satellite missions of National Aeronautics and Space Administration (NASA) and German Aerospace Center (DLR), launched in March 2002 and May 2018, respectively, have been pivotal in monitoring global mass redistribution, measuring ocean mass changes, providing essential information for climate studies and hydrological research (Tapley *et al*., 2004; Tapley *et al*., 2019). These missions have also been instrumental in improving the precision of geoid models to global scale (Kopeikin *et al.*, 2015).

The Swarm constellation of three satellites of ESA, launched in November 2013, has been essential in studying the Earth's magnetic field dynamics, thermospheric currents, and magnetic field interactions within the Earth system (Friis-Christensen *et al*., 2006; Tozzi *et al*., 2015; Lühr *et al*., 2016). The design of the missions is illustrated in Fig. 1.1 which shows images of the four LEO satellites mentioned above.

CHAMP, GOCE, GRACE, GRACE-FO and the future Mass Change MC (NASA) and Mass Change and Geosciences International Constellation MAGIC (ESA) missions are primarily dedicated gravity space missions that have revolutionized and will continue the monitoring and studies of the Earth system via the precise determination of the Earth’s gravitational field and its changes in time that define water mass balance and solid Earth mass redistribution. When combined with high-precision and high-resolution measurements of the Earth’s magnetic field from Swarm constellation and in-situ seismological measurements of the Earth structure, a complete picture of the Earth system and contribution to climate change studies can be achieved.

The traditional method of orbit analyses on any satellite mission that has been used for decades to determine the Earth gravitational field posed two limitations: i) the orbit perturbations due to gravitational plus non-gravitational forces were determined via ground tracking which could only be available over short intervals and ii) the non-gravitational orbit disturbances could not be isolated from the total perturbations to reveal the useful gravitational signal; this could only be done only through physical models of limited accuracy. On the contrary, the modern dedicated gravity satellite missions bypass the above limitations by i) uninterrupted 3D tracking of the orbit via an on-board GPS receiver, ii) measurement or compensation of non-gravitational accelerations via an on-board 3D accelerometer, iii) low orbital altitude and iv) suppression of gravity field attenuation at altitude by measuring gravitational gradients (GOCE mission only).

An accelerometer installed precisely at the center of mass of the satellite to eliminate rotational accelerations, measures the linear and the angular non-gravitational accelerations induced by the Solar Radiation Pressure (SRP), atmospheric drag, Earth Radiation Pressure (ERP), and Thermal Radiation Pressure (TRP). Measured non-gravitational accelerations are indispensable for both determination of the gravity field and retrieval of thermospheric densities. They serve as the sole source offering valuable insights into the complex system that satellites observe the Earth. Therefore, understanding and investigating non-gravitational accelerations are crucial for accurately determining the satellites' orbits, the gravity field, the operational efficiency, the lifespan of the satellites as well as space weather effects and their impact on satellite operations. Additionally, non-gravitational accelerations are essential for predictive models for mission planning and collision avoidance (Ziebart *et al*., 2005; McMahon & Scheeres, 2010) .

The utilization of spaceborne accelerometers in LEO satellites has significantly enhanced our understanding of non-gravitational accelerations acting on satellites. This improved knowledge is essential for accurate orbit determination, gravity field recovery and retrieval of the thermospheric densities (Wei *et al.,* 2023). However, challenges exist in ensuring the accuracy and reliability of the on-board accelerometer measurements, which are susceptible to systematic errors, necessitating precise calibration to mitigate these errors prior to the gravity recovery or thermospheric neutral density estimations (Koop *et al*., 2002; Vielberg *et al*., 2018).

Since the calibration of the accelerometers is not feasible on the ground due to the strong gravitational signal, the on-orbit calibration process for high-precision accelerometers used in LEO missions must consider factors such as scale, bias, operating temperatures, and potential accelerometer deformation during launch (Astrua *et al.,* 2023). Additionally, it is important to consider temperature-induced bias drifts due to the high temperature sensitivity of the accelerometers and the coupling errors between the accelerometer and the spacecraft (Massotti *et al*., 2022). In LEO missions, integrating accelerometer and other sensor measurements, such as measurements from GPS receivers, is vital for precise orbit determination (Kang *et al*., 2006; Van Helleputte & Visser, 2008). Enhancing the prediction of LEO orbits using accelerometer measurements can be achieved through advanced propagation algorithms that integrate refined models of non-gravitational accelerations. This approach enables more precise predictions of future satellite positions (Yang *et al*., 2023). Moreover, employing accelerometer measurements in orbit determination necessitates the concurrent estimation of the accelerometer's calibration parameters, such as scale and bias, along with the initial position and velocity of the LEO spacecraft (Ge *et al*., 2020). Additionally, the real-time processing of the accelerometer measurements facilitates immediate orbit corrections, which are crucial for accurately predicting re-entry timelines in LEO environments (Montenbruck & Gill, 2000; Vallado, 2007). Despite the challenges associated with accelerometer measurement processing, efforts have been made to streamline the processing from raw accelerations to thermospheric neutral densities, demonstrating continuous advancements in handling accelerometer measurements in LEO missions (Sutton *et al*., 2012; Siemes *et al.,* 2016). However, due to significant challenges, such as temperature sensitivity, the significant spikes in the cross-track and radial direction, spurious jumps and data gaps in accelerometer measurements, some studies opt to use GPS-derived densities (Bruinsma & Boniface, 2021).

While accelerometers are invaluable instruments in LEO missions, addressing calibration, integration with other sensors and data processing challenges is crucial to ensure the accuracy and effectiveness of accelerometer measurements in various applications within the LEO environment. In this research, we introduce an innovative approach to the accelerometer calibration challenge, utilizing solely the measurements from the accelerometer and the POD data. Furthermore, we propose a more sophisticated method to address the systematic errors in the accelerometer measurements, which can arise during the transition of the satellite through the Earth's shadow, across the terminator, or from the activation of magnetotorquers[1] during passages over the equator or the poles. Our findings and contributions, although applied to the GRACE missions, can be directly adapted for use in any future missions that carry an accelerometer and POD capabilities.

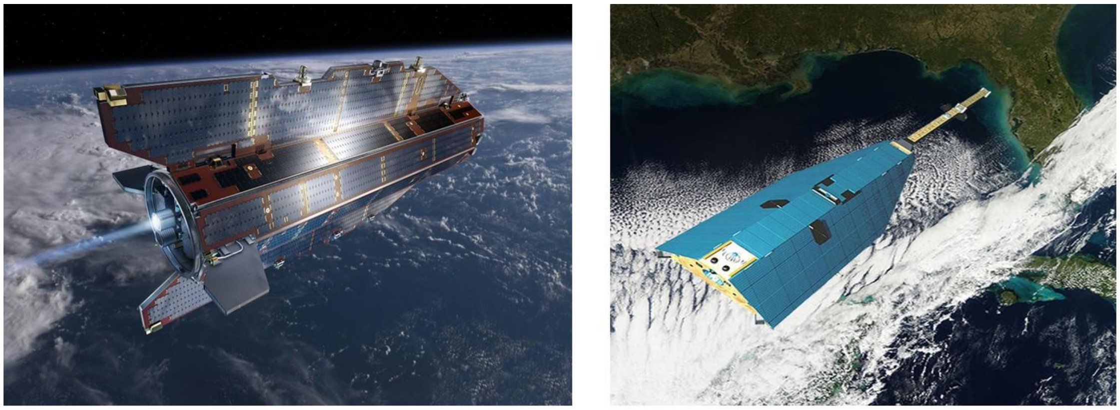

a) GOCE mission

b) CHAMP mission

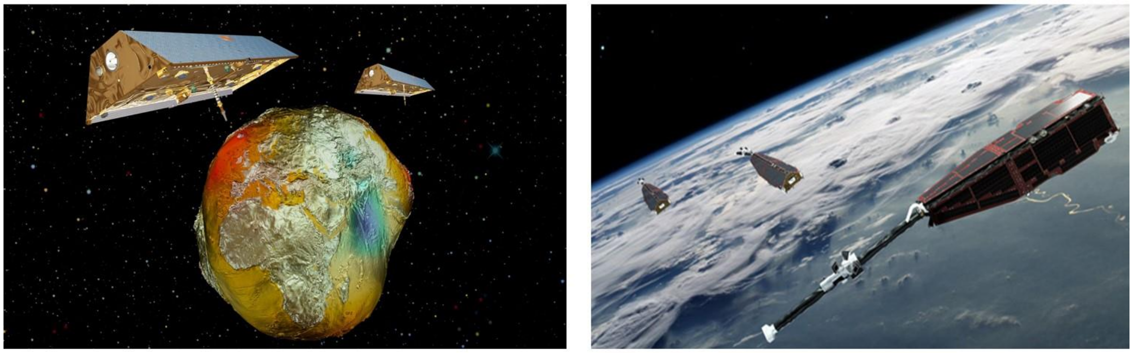

c) GRACE mission

d) SWARM mission

Figure 1.1 Images of LEO satellites: (a) GOCE Satellite[2], (b) CHAMP Satellite[3], (c) GRACE Satellite[4], (d) Swarm Satellite[5].

---

[1] Magnetotorquers are used in satellites for attitude control by generating a magnetic moment which interacts with the Earth's magnetic field to create a torque. This torque allows the satellite to adjust its orientation and stabilize its attitude without using propellant (Wood *et al.*, 2006).

[2] ESA : https://www.esa.int/Applications/Observing_the_Earth/FutureEO/GOCE/Introducing_GOCE

[3] NASA : https://eospso.nasa.gov/missions/challenging-mini-satellite-payload

[4] DLR: https://www.dlr.de/en/latest/news/2017/20171027_grace-mission-comes-to-an-end-after-15-years-of-successful-operation_24627

[5] ESA: https://earth.esa.int/eogateway/missions/swarm/description

1.2 The Challenges of GRACE Missions and Our Contributions

The GRACE and GRACE-FO missions play a vital role in observing temporal changes in Earth's gravitational field, global water movement, and mass redistribution. To achieve precise gravity field determination, accelerometer measurements are required during gravity field recovery to ensure that changes in satellite accelerations are solely due to gravity field variations (Touboul *et al.*, 1999). Accelerometer measurements are also used to estimate thermospheric density from drag forces acting on the satellite which is currently the only method capable of providing thermospheric densities. Typically, the accelerometer measurements when used for the extraction of the thermospheric densities, achieve an accuracy of about 4% during periods of high solar activity and 5%-20% during periods of low solar activity, as errors in radiation pressure modeling become more significant when aerodynamic acceleration decreases (Emmert, 2015; Siemes *et al.*, 2024).

However, there are many challenges associated with accelerometers, such as the determination of their calibration parameters and their high thermal sensitivity, which can lead to numerous spikes in the measurements. Additionally, modelling the non-gravitational forces acting on the satellite is demanding and can result in inaccurate determination of drag, a crucial parameter throughout the satellite's lifetime. In this research we focus on the following three challenges:

a. Develop an all-new method for the on-board accelerometer calibration of GRACE and GRACE-FO accelerometers based only on the accelerometer measurements and on the precise orbit determination (POD) data emphasizing that our contributions will be valid for any future missions with continuous 3D precise position capability (GNSS) and a 3D accelerometer on-board.
b. Develop a new statistical evaluation method to determine the covariance matrix of the accelerometer measurements. Currently the accelerometer measurements are considered deterministic quantities in the recovery of the gravity field models and other studies.
c. Develop data-driven models of radiation pressure (RP) and atmospheric drag for GRACE and GRACE-FO based solely on the spectral characteristics of the accelerometer measurements.

In the next three subsections, we present conceptually each of the above three challenges and delineate the innovation and originality of the models developed.

1.2.1 On-Orbit Accelerometer Calibration

The on-orbit accelerometer calibration is one of the most crucial challenges in LEO missions that carry an accelerometer (Wu & Bar-Sever, 2001; Tapley *et al.*, 2004; Zhang *et al.*, 2023). Accelerometers cannot be calibrated on the ground for several reasons: i) they operate in the microgravity environment in space, which is significantly different from Earth's gravity; ii) the non-gravitational forces, such as solar radiation pressure (SRP), drag, and thermal radiation pressure (TRP) are significantly different in space from those on the ground, making laboratory calibration inadequate; iii) the thermal environment in space differs significantly from that on Earth; and iv) the instrument calibration needs to be monitored and repeated while the accelerometers are in the actual operational environment, as the calibration parameters could change over long periods due to radiation exposure in space.

In contrast to existing calibration methods presented in the literature (Bezděk *et al.*, 2010; Zheng *et al.*, 2011; Calabia & Jin, 2015; Wöske *et al.*, 2019), where calibration parameters (bias and scale factor) are typically calculated during gravity field recovery alongside hundreds of other unknown parameters or by using advanced physical models, we introduce an original, all new calibration method. This new approach relies solely on the on-board non-gravitational accelerometer measurements and on the total accelerations of the spacecraft determined from its precise orbit determination (POD) using the on-board GPS receiver. This original idea considers that the non-gravitational accelerations are also a minute part of the total accelerations of the satellite, taking advantage of the fact that the total POD kinematic accelerations are the “absolute standard” for the calibration based only on geometric observations and not taking any forces into account leading to a satellite position accuracy of a few centimeters. The term "absolute standard" refers specifically to kinematic orbits, as they are derived solely from raw observations without the application of force models typically used in the calculation of dynamic or reduced-dynamic orbits. In this study, we use kinematic orbits provided by Graz University, which were obtained through an iterative least-squares adjustment process, where systematic effects are either corrected or incorporated as additional parameters.

This method however has two critical challenges: first, we must find unique characteristic signals that are present in both non-gravitational and total accelerations to be able to compare or “correlate” them with the same signatures in the accelerometer measurements and second, the non-gravitational accelerations are about -120dB of the total accelerations. The former challenge can be bypassed by recognizing that the transitions of the satellite from the Sun-lit region to the Earth’s shadow and vice versa, known as penumbra transitions, jolt the satellite with an acceleration of about $20-50\ nm/s^2$ and thus they can be used as the desired calibration pulses. The latter challenge is that the equivalent jolt in the total accelerations is very small compared to the total accelerations.

The comparison or “matching” of the penumbra transitions in both signals that will allow the retrieval of the scale factor is inspired by the wave focusing methodology using time reversals, commonly employed in radar applications for the detection of a transmitted (known) waveform (template) in the unknown reflected (scattered) signal from a target, contaminated by stochastic noise. The time reversal approach in this study is implemented via the matched filter method with the understanding that the penumbra transitions in both acceleration signals occur at precisely the same time. We focus solely on the penumbra transitions, using a normalization factor which is the ratio of the powers between the total accelerations and the non-gravitational accelerations, without the need to separate the penumbra transition pulses from the total accelerations as it has been done routinely over the past 25 years since the launch of the first gravity space mission. The problem with the current state-of-the-art methods is that the separation of the non-gravitational accelerations from the total ones is achieved via physical (theoretical) models that have errors and thus the scale factors are biased. In our approach, in addition to the retrieval of the scale factor, the bias of the accelerometers is estimated independently of the scale factor by applying a daily second-order polynomial fit to the accelerometer measurements.

1.2.2 Uncertainties of Accelerometer Measurements

The presence of random and systematic errors in the accelerometer measurements can significantly impact their accuracy and reliability. (Vielberg *et al*., 2018). Due to the accelerometer high thermal sensitivity, which is a major contributor to systematic error analysis, temperature effects on measurements that depend on the solar activity, could significantly affect all three axes of the accelerometer (Rodrigues *et al*., 2022). Systematic errors, such as heater spikes, twangs[6], fluctuations due to the magnetotorquers, thruster firings, and spurious accelerations, are present along the three axes of the accelerometers (Chen *et al*., 2021; Zhang *et al*., 2023). Currently, the state-of the-art-approach of producing and using an accelerometer dataset (Level 1B) from the original accelerometer measurements (Level 1A dataset) considers both 1A and 1B as deterministic datasets with no covariance matrices associated with them. The second challenge that our research focuses on is the conception and production of a new 1B dataset for the accelerometer of GRACE C satellite (GRACE-FO mission), namely the ACW1B (Level 1B – sampling rate 1Hz), which is estimated from the original accelerometer measurements provided in the ACC1A dataset (Level 1A – sampling rate 10 Hz). The original ACC1A measurements are treated, for the first time, as a stochastic process, possessing a covariance matrix derived from experimental autocovariance functions of short duration ACC1A segments. Subsequently, the ACC1A is filtered, and its covariance matrix is propagated through the convolution algorithm to the filtered values, thus forming the new ACW1B as an uncorrelated random process.

The variances of the new ACW1B that can be seen as a proxy to the power of the ACW1B at any instant of time, highlight all the disturbances to which the accelerometer is subjected, such as geomagnetic storms, penumbra transitions, and solar terminator crossings, among many others. The variances of the ACW1B also reveal disturbances that can be associated with the creation of acoustic gravity waves[7] in the thermosphere created at the terminator crossings. Addressing the systematic disturbances on the accelerometer and creating a weighted dataset that eliminates spikes due to thruster activations or to other unknown reasons is imperative. It introduces a new approach

---

[6] Twangs are disturbances present in GRACE measurements which can exceed the instrument resolution by three or more orders of magnitude. These disturbances are termed 'twangs' because of the prolonged oscillation that follows the high-amplitude spikes (Frommknecht *et al*., 2006; Schlicht, 2022).

[7] Acoustic Gravity Waves (AGW) are created in the thermosphere and in the vicinity of the solar terminator due to the supersonic speed of the terminator (Afraimovich *et al*., 2009; Cheremnykh *et al*., 2023).

to how the measurements should be treated and provides us with information on the accuracy of the measurements and the different factors that affect the satellite during its lifetime. This is crucial for deriving thermospheric mass densities, which rely on the accelerometer measurements.

1.2.3 Modelling of Radiation Pressure (RP) and Atmospheric Drag

Modelling non-gravitational accelerations is fundamental in satellite missions since they significantly affect the satellite orbit. Such accelerations are ‘noise’ in some applications, for example in the estimation of the gravitational field, while they are ‘signals’ in others, such as in precise orbit determination and prediction, mission planning and operations, thermospheric density estimation, space weather, and others. While the total non-gravitational accelerations are measured by the accelerometers on board gravity satellite missions, it is important to separate the atmospheric drag from the other non-gravitational accelerations induced primarily by the SRP and to a lesser extent by ERP and TRP.

The final and critical challenge that this dissertation focuses on is the development of *data-driven models* of the three dominant non-gravitational forces acting on the satellites: The SRP, the TRP and the atmospheric drag. Our study contrasts with the force (physical) modelling of the non-gravitational accelerations developed by others. To the best of our knowledge, our data-driven SRP, TRP and drag models along with their error estimates are the first of their kind because they are developed from our ACW1B dataset of GRACE-FO, developed in this research (Section 1.2.2). The method of developing these models is in the frequency domain and is based on the Least Squares spectral and wavelet analyses.

By modelling the two dominant forces (SRP and drag in the along-track direction, SRP and TRP in the cross-track and radial directions) acting on the satellite, we analyze the weighted residuals that reveal disturbances during even minor geomagnetic storms, during penumbra transitions—most probably due to temperature fluctuations since the accelerometers are subjected to temperature changes—and during pole crossings—disturbances connected to magnetic field disturbances. The extensive analysis of the accelerometer residuals can shed light on the various factors that affect the satellite while orbiting the complex upper atmosphere. It can provide us with insights into the changes in the atmosphere during geomagnetic storms and terminator crossings, which might hold promising potential for future forecasting efforts. We would like to emphasize that, to the best of our knowledge, this is the first extensive analysis of the residual series of the accelerometers.

1.3 Thesis Outline

The outline of the thesis is as follows: In Chapter 1, we introduce the significance of LEO missions and underscore the importance of a new analysis of accelerometer measurements as a crucial source of information on the complex dynamics of the upper atmosphere. Chapter 2 comprises an extensive literature review, which will encompass the evolution of research in accelerometer measurements pertaining to gravity field determination and thermospheric densities. This chapter also offers an in-depth examination of the challenges associated with accelerometer measurements and the various methodologies that have been developed to address these issues. In Chapter 3, we provide an extensive discussion of the theory behind the matched filter and time reversal methods, which are commonly used in radar applications but not widely applied in geodetic studies. Given that our calibration method is based on the matched filter approach, it was deemed necessary to offer a thorough background on these techniques. This is particularly important as this thesis represents the first application of the matched filter method for retrieving the scale factors of accelerometers in a geodetic context. Chapter 4 presents the results of the calibration parameters derived for the GRACE and GRACE-FO missions using the matched filter method. In Chapter 5, we introduce the new weighted dataset ACW1B and analyze the calculated variances of the accelerometer measurements, addressing all systematic errors presented in the measurements. Chapter 6 presents the data-driven models of SRP, TRP and atmospheric drag for the GRACE-FO mission, along with an analysis of the weighted residuals. This analysis reveals disturbances during geomagnetic storms, field-aligned currents, and penumbra crossings. Finally, in Chapter 7, the conclusion of the thesis contribution is presented, along with an outline of future work.

2 Comprehensive Review of the State-of-the-Art Developments in Gravity Space Missions

---

This chapter reviews the essential literature on the importance of LEO missions in geodetic applications and the significance of the accelerometer, along with its associated challenges. Additionally, it emphasizes the importance of measurement accuracy, the modelling of non-gravitational forces, the difficulties in accelerometer calibration, and the various factors influencing the satellite orbit. The scope of this chapter is to provide readers with a comprehensive overview of the state-of-the-art models and their shortcomings, highlighting the motivation and contributions of this dissertation. A more focused literature review on each of three objectives of this research is included in the relevant chapters.

2.1 Non-gravitational Accelerations

The accelerometer plays a pivotal role in Low Earth Orbit (LEO) missions, offering critical insights into spacecraft dynamics and environmental interactions due to its high sensitivity and accuracy. This instrument measures non-gravitational forces acting on the spacecraft, such as atmospheric drag, Solar Radiation Pressure (SRP), and thruster firings, which can significantly affect its trajectory and orientation. By precisely quantifying these forces, accelerometers enable accurate orbit determination, aiding in the optimization of spacecraft maneuvers, collision avoidance, and orbit maintenance (Helleputte & Visser, 2008; Visser & IJssel, 2016). Additionally, accelerometers contribute to scientific investigations on Earth's gravity field variations, atmospheric density profiles, and space weather phenomena.

The accelerometer measures the total non-gravitational accelerations of the satellite, however due to the instrument sensitivity, other factors also affect the measurements. These additional sources include thermo-dynamical effects, thermal motion of molecules, radiation pressure due to differential temperatures, thruster firing events during the control of the spacecraft attitude and magnetic static forces on the proof mass (Peterseim *et al.*, 2012). The impact of these systematic errors on the accuracy of the measurements is discussed in Section 2.5.

The accelerometer is currently the only instrument capable of measuring with high precision the total non-gravitational forces acting on a satellite. This capability is important for modelling various mission parameters, such as satellite lifetime, atmospheric drag, recovery of the gravity field, and understanding the dynamics of the upper atmosphere. For such applications, the accelerometer expected resolution must be better than the 1 pg (Touboul *et al.*, 1999). In the science reference frame (SRF[8]) the most dominant forces along the flight path (X_{SRF}) are the SRP and the atmospheric drag. The latter can fluctuate significantly based on the intensity of solar activity, either increasing or decreasing accordingly. In the transverse (cross-track or lateral) direction (Y_{SRF}) the most dominant forces are the SRP and TRP, whereas in the radial direction (Z_{SRF}) both SRP and ERP are dominant.

2.1.1 Solar Radiation Pressure – SRP

The SRP accelerations arise from the non-conservative force exerted on the satellite by the sunlight photons impacting on its surface. Modelling the SRP is crucial since it constitutes one of the two dominant non-gravitational forces acting on a satellite. Its magnitude depends on various factors including the satellite surface reflectivity, the illuminated surface area, the direction from the Sun to the satellite, and the satellite mass.

The investigation of SRP effects on actual satellites was pioneered by Musen (1960) and Sehnal (1970) proving its impact on satellite orbits and on orbital velocity over time. An important element in the SRP studies is the effect of the Earth's shadow. Sehnal (1970) addressed the challenges in

---

[8] Science Reference Frame (SRF) will be discussed in Table 2.2.

modelling the radiation pressure and introduced a specialized shadow function to account for effects when the satellite moves in and out of Earth's shadow, namely during the transitions through the penumbra. Mello (1972) conducted a study on the Earth's shadowing effects on satellite orbits. The author introduced the concept of the shadow function, denoted as ψ, which acts as an on-off switch namely, it equals to one when the satellite is illuminated and zero when in shadow. Updated shadow models consider factors, such as light diffusion, atmospheric absorption, ozone effects, relative positions of the Sun, Earth, and the satellite, and the shape of the conical shadow surface (Montenbruck *et al*., 2015; Ikari *et al*., 2016).

2.1.2 Atmospheric Drag

The atmospheric drag force acts in a direction opposite to the satellite motion and is co-linear with it. It is the resistive force exerted by the Earth's atmosphere on the satellite as it moves through it, producing both short-periodic and slow perturbations. It originates from collisions between the satellite and neutral and charged particles in the atmosphere, leading to deceleration of the satellites and reducing their lifetime. The magnitude of the atmospheric drag depends on various factors, including the speed of the satellite, altitude, cross-sectional area, shape and the density of the atmosphere, which even if it decreases with altitude, can vary significantly due to solar activity or other atmospheric conditions (Kirkpatrick *et al*., 1999; Vallado & McClain, 2001). Jastrow & Pearse (1957) were among the first scientists to discuss how collisions with neutral and charged particles influence satellite orbits.The magnitude of the atmospheric drag is often represented by the formula (Cook, 1965):

$$a_{drag} = -\frac{c_D}{2}\frac{A}{m}\rho|V_{rel}|V_{rel} \tag{2.1}$$

where ρ is the atmospheric density, A is the cross-sectional area, c_D is the aerodynamic coefficient, m is the satellite mass and V_{rel} is the satellite velocity with respect to the atmosphere[9]. In this equation

---

[9] In a rotating atmosphere the velocity of rotation of the atmosphere is small compared to the orbital velocity of the satellite (Jacchia, 1963).

$$\boldsymbol{V}_{rel} = \boldsymbol{V}_R - \boldsymbol{\Omega} \times \boldsymbol{R} \tag{2.2}$$

where $\boldsymbol{V}_R$ is the velocity of the satellite relative to Earth, $\boldsymbol{\Omega}$ is Earth rotation and $\boldsymbol{R}$ is satellite radius-vector. This equation is applicable when the atmosphere is at rest relative to the solid Earth, otherwise the atmospheric wind speed should be considered.

Modeling the atmospheric density accurately is challenging due to uncertainties arising from varying solar activity and its disturbances in the upper atmosphere. Additionally, the drag coefficient approximation holds true only when the density and velocity along the satellite orbit remains relatively constant (Qian & Solomon, 2012; Emmert, 2015). The aerodynamic coefficient can be categorized as fixed (it uses a constant value that remains unchanged throughout the analysis), fitted (it is derived through a fitting or filtering process and is typically updated over time, such as every few hours or orbits), or physical (it is calculated by modeling the interaction between the satellite and the flow-field particles, factoring in the momentum and energy exchange). In the models of aerodynamic coefficients, which are dimensionless quantities characterizing the aerodynamic force and moment acting on the satellite, various factors are considered. These include the velocity, temperature, and chemical and physical conditions of the satellite surface. For satellites with complex shapes, the aerodynamic coefficient is calculated by dividing the body of the satellite into finite elements and aggregating (integrating) their contributions (Yamazaki *et al*., 2015). Aerodynamic coefficients have been calculated for GRACE, CHAMP and GOCE missions, to extract thermospheric densities from accelerometer measurements, showing significant fluctuations depending on the satellite's shape, solar activity levels, and altitude, with values ranging from 2.5 to 4.9 (Mehta *et al.*, 2023). Moreover, a critical variable in drag determination is the relative velocity to the rotating atmosphere which is assumed to be accurate only under the assumption that the lower part of the atmosphere rotates with the Earth (Capon *et al*., 2019). However, this assumption is not entirely valid at LEO altitudes due to the presence of neutral winds, which can exhibit high velocities and significantly impact drag estimation (Sutton *et al*., 2007).

2.1.3 Earth Radiation Pressure – ERP

ERP comprises the Earth's reflected and emitted radiation, with the reflected sunlight acting on the satellites and causing ERP accelerations. Knocke *et al*. (1988) investigated the effects of ERP on LAGEOS satellites, demonstrating that it can induce significant accelerations along the track their track with highly eccentric orbits. Models for the ERP are based on three main assumptions: the Earth behaves like a Lambertian sphere[10], radiation is reflected or emitted, and there is global conservation of energy. The Earth's irradiance (radiation power per unit area) primarily impacts the satellite in the radial direction. Local changes in atmospheric and surface properties influence the amount of reflected energy affecting the satellite. It is important to distinguish ERP from the albedo term, which refers to the radiative flux including shortwave variations, measured in the visible and near-infrared spectrum (Iziomon & Mayer, 2002). In the physical models derived for GRACE missions, the ERP is divided into two components: albedo and irradiance (IR).

Studies have shown both the Northern and Southern Hemispheres receive similar amounts of irradiance. Additionally, there is a seasonal cycle of surface albedo, reaching a maximum in boreal spring due to increased reflectivity of snow-covered land surfaces between 30°N and 60°N. The maximum annual values of irradiance occur in March and October, with a minimum between June and July (Corripio, 2002). A detailed study on modeling SRP and ERP for Low Earth Orbit satellites, with an application to GRACE A data, was published by Vielberg & Kusche (2020).

2.1.4 Thermal re-radiation pressure - TRP

The electromagnetic radiation from the Sun as well as the reflected and emitted radiation from the Earth, not only causes radiation pressure acceleration on the satellite but also heat the illuminated surface (Hesar *et al*., 2017). This absorbed radiation leads to temperature variations throughout the spacecraft due to heat transfer mechanisms. According to the Stefan-Boltzmann law[11], the thermal

---

[10] Lambertian sphere is an idealized sphere that describes a perfectly diffuse reflector. It reflects incident light uniformly, regardless of the angle of incidence (Robertson *et al*., 2015).

[11] The Stefan-Boltzmann law describes *the intensity of the thermal radiation emitted by matter in terms of that matter's temperature:* $\mathrm{E} = \sigma \mathrm{T}^4$, where $\sigma = 5.670374419 \times 10^{-8}$ is the Stefan-Boltzmann constant (Karam, 1998).

energy emitted by the satellite contributes to its acceleration. This acceleration depends on the absorbed radiation, the internal and external geometry of the satellite, and the thermo-optical properties of its materials (Ziebart *et al*., 2005). Despite previous studies often overlooking the impact of thermal radiation, TRP can significantly contribute up to 10% to the total RP, depending on solar activity (Wöske *et al*., 2019).

2.1.5 Challenges of Accelerometer Measurements

The accelerometer on board LEO missions measures the total non-gravitational accelerations due to all forces described above plus thruster forces, magnetic disturbances, magnetic storms and thermospheric winds. The GPS on-board these missions measure the total accelerations of the spacecraft that is, it measures the gravitational plus the non-gravitational accelerations through precise orbit determination (POD) solutions. For gravity field modelling, it is in general adequate to subtract the non-gravitational accelerations measured by the accelerometer without necessarily knowing the individual contributions for the various sources. However, there are mainly two important requirements:

i) the accelerometer must be precisely and frequently calibrated (scale and bias) throughout the mission operations. These calibration parameters can vary a lot depending on the calibration method and the context of data usage,

ii) the use of the accelerometer measurements for the studies of the thermosphere must have a continuous and precise knowledge of the atmospheric drag and the SRP, not just the total non-gravitational accelerations.

To resolve the above two challenges, the state-of-the-art approach is to develop theoretical models for the Earth’s gravity field and individually model every non-gravitational acceleration component (Bezděk, 2010; Chen *et al*., 2016).

For the calibration of the accelerometer on CHAMP, GRACE and GRACE-FO missions, there are two similar approaches: Conceptually, a gravity field model is subtracted from the total accelerations determined by the GPS POD to provide the total non-gravitational accelerations to be compared (correlated) directly with the accelerometer measurements to deduce the accelerometer scale factor (Calabia & Jin, 2015; Klinger & Mayer-Gürr, 2016). Alternatively, all non-gravitational accelerations are modelled and compared with the accelerometer measurements to provide the scale of the accelerometer (Siemes *et al*., 2023). Another approach for the calibration of the accelerometer is to parameterize the scale and bias into the dynamic orbit and obtain the calibration parameters along with the gravity field solution (Flury *et al*., 2008; Behzadpour *et al*., 2021). For the GOCE mission, the calibration of the accelerometers was typically carried out using POD accelerations, while the modeled gravity gradients were used to validate the observed gravity gradients from the individual accelerometers (Siemes *et al*., 2012; Visser &Ijssel, 2016). To extract thermospheric densities, atmospheric drag must be isolated from other non-gravitational accelerations. This is achieved by subtracting theoretical non-drag models from the total accelerations observed by the accelerometer (Bruinsma & Biancale, 2003; Volkov *et al*., 2008; Calabia & Jin, 2016).

The physical (theoretical) models are in general incomplete and not sufficiently accurate, rendering the calibration parameters and atmospheric drag poorly estimated. In this research we take an all-new approach of *data driven models*, using only the POD and the accelerometer measurements to calibrate the accelerometer (Chapter 4) and isolate the atmospheric drag from the total non-gravitational accelerometer measurements without the use of any physical model (Chapter 6).

2.2 Accelerometer Principles and Historical Overview

An accelerometer operates based on the principle that a proof mass is suspended within a cage formed by six pairs of electrodes. This concept of the full electrostatic suspension of the proof mass is very suitable for space applications but requires very high resolution of accelerometer measurements or drag free control of the satellite (Touboul *et al*., 1996). When non-gravitational accelerations occur, the cage shifts relative to the proof mass within a limited range. The electrodes, functioning as sensors, detect this movement of the proof mass by measuring the instantaneous change in capacitance within the cage. To maintain the reference capacitance the same i.e., to maintain the proof mass in its original zero position, with respect to the cage or equivalently w.r.t.

the Accelerometer Reference Frame (ARF)[12], a control voltage, through a feedback loop, applied to the electrodes generates electrostatic forces to the proof mass to recenter it to its nominal position. The amount of voltage required to maintain this position is directly proportional to the acceleration (Frommknecht *et al.*, 2003; Kornfeld *et al.*, 2019). In Fig. 2.1 the STAR model and the inner cage of the accelerometer of CHAMP satellite is shown, while in Fig 2.2 the GOCE gradiometer[13] and its assembly are shown[14].

Before delving into the importance of the accelerometers in GRACE missions, it is essential to provide a brief overview of the history of accelerometers in the field of space geodesy. Accelerometers were first included in each of the Atmosphere Explorer (AE) satellites to measure density variations in the atmosphere. In those satellites, measurements were taken four times per second (Champion & Marcos, 1973). The CACTUS accelerometer of the CASTOR D5B[15], developed by Office National d'Études et de Recherches Aérospatiales (ONERA), achieved better sensitivity than anticipated before its launch, enabling the first multiyear measurements of atmospheric density (Boudon *et al.*, 1979). Two additional missions, SETA 2 (May-November 1982) and SETA 3[16] (July 1983-March 1984), operated in near-circular, sun-synchronous orbits with altitudes ranging between 170 and 240 km, provided accelerometer measurements for the retrieval of atmospheric density (Marcos, 1982; Rhoden *et al.*, 2000).

Since 2000, several satellites equipped with GPS receivers and electrostatic accelerometers have been launched. However, their primary goals were not to observe thermospheric density but to extract the Earth's gravity field. Notable missions include GOCE, CHAMP, GRACE, Swarm and GRACE-FO. These missions have provided invaluable measurements, advancing our understanding of the gravity field of the Earth while also offering insights into thermospheric densities as a secondary benefit.

---

[12] The Accelerometer reference frame (ARF) is a satellite body-fixed reference frame described in Table 2.2.

[13] ONERA uses the term 'GRADIO accelerometer' to refer to the individual accelerometers of the gradiometer unit.

[14] For a more detailed description of the accelerometers employed in different satellites, please refer to Krasnov *et al*. (2022).

[15] CASTOR D5B, also known as EOLE, was a satellite launched by CNES in 1971 with a primary mission to collect meteorological data and improve weather forecasting (Beaussier *et al*., 1977).

[16] SETA 2 and SETA 3 missions were critical in advancing our understanding of atmospheric density. The measurements from these missions contributed to models such as the Drag Temperature Model (DTM) and the Mass Spectrometer Incoherent Scatter (MSIS) series (Bruinsma & Forbes, 2010).

Launched on July 15, 2000, the CHAMP mission operated in a circular orbit with a 100° inclination and eccentricity less than 0.01 and utilized the STAR accelerometer, developed on ONERA's high voltage levitation scheme (Reigber *et al*., 2002). This accelerometer played a pivotal role in estimating and understanding mass redistribution processes and mapping of the Earth's gravitational field dynamics (Moore *et al*., 2003; Reigber *et al*., 2005). The mission aimed to measure both the gravity and magnetic fields of Earth, carrying out simultaneous measurements of numerous thermospheric and ionospheric parameters.

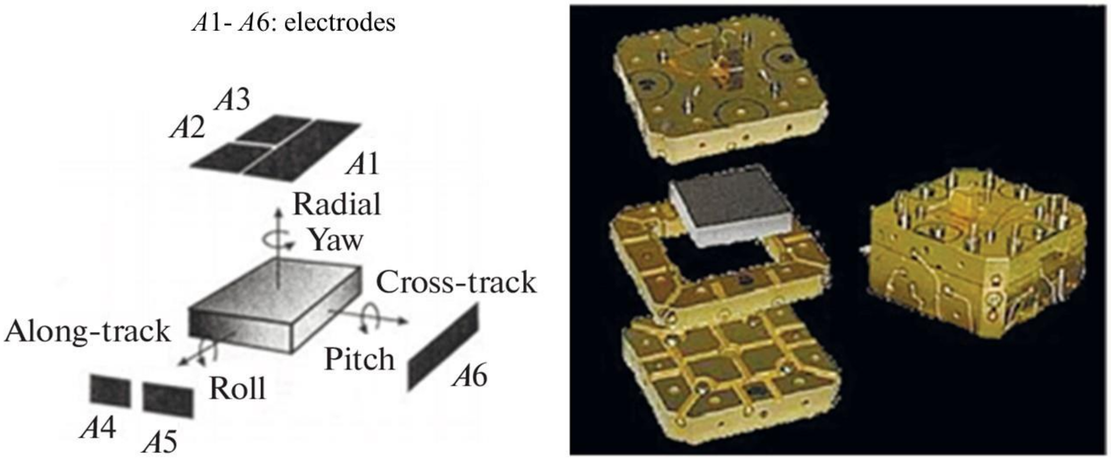

Figure 2.1 STAR accelerometer of CHAMP satellite: The STAR model (left) and the inner cage of the accelerometer (right). Electrodes A1 through A6 detect the movements of the proof mass, and the internal cage of the device is composed of three electrode plates made of silica glass (Adapted from Krasnov *et al*. 2022).

These parameters encompassed the thermospheric total mass density, electron density and temperature as well as ionospheric field-aligned and horizontal currents. Using the accelerometer measurements aboard CHAMP, investigations were conducted into thermospheric density estimations during geomagnetic storms, alongside the exploration of thermospheric wind patterns over the polar regions (Liu *et al*., 2005; Schlegel *et al*., 2005; Sutton *et al*., 2005). After 10 years of orbiting the Earth, the satellite concluded its mission on September 19, 2020, marking one of the most successful satellite missions for Earth observation.

The GOCE mission, launched on March 17, 2009, in a sun-synchronous orbit with an inclination of 96.7°, at an altitude of 260 km, utilized for the first time gravity gradiometer developed on a high voltage levitation scheme proposed by ONERA (Visser, 2011). For the first time, a three-axis gradiometer comprising six electrostatic accelerometers in a diamond configuration (two accelerometers aligned along each axis), delivered precise measurements, facilitating the development of global gravity field models and deepening our comprehension of Earth's gravitational field (Touboul *et al*., 1999; Drinkwater *et al*., 2003; van der Meijde *et al*., 2015). The gradiometer was 100 times more sensitive than any other sensor of its kind ever used in a space mission before. These measurements helped estimate the thickness of polar ice sheets, mapped short-wavelength features of the dynamic ocean topography, and advanced our understanding of the physics of Earth’s interior (Muzi & Allasio, 2004; Pail *et al*., 2011; Rummel *et al*., 2011). Due to the low altitude of its orbit, the successful mission concluded on October 21st, 2013.

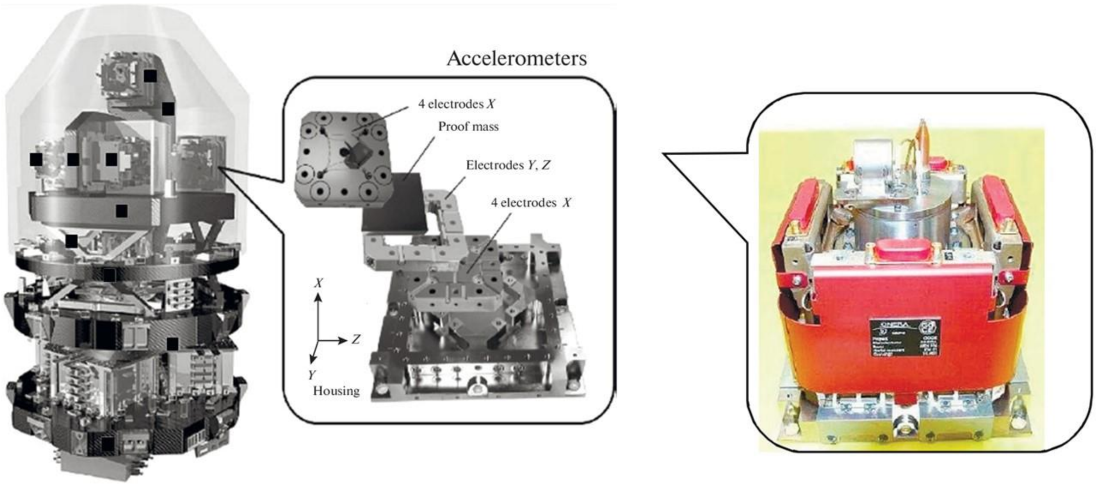

Figure 2.2 GOCE gradiometer (left), GRADIO accelerometer assembly (middle) and the three pairs of GRADIO accelerometers (right). The difference of the accelerations measured by each pair of accelerometers will provide the gravitational gradients (Adapted from Krasnov *et al*. 2022).

Accelerometer measurements play a crucial role in the Swarm mission, which was launched in November 2013 to study the Earth's magnetic field (Macmillan & Olsen, 2013; van den Ijssel *et al*., 2015). The Swarm mission, which, at the time of writing, is still in operation, comprises three satellites (Swarm A, Swarm B, and Swarm C) positioned in different orbits. Swarm A and Swarm C fly in tandem at an altitude of 450 km, while Swarm B orbits at an altitude of 530 km (Friis-Christensen *et al*., 2006). Even if the main goal of this mission was to monitor precisely the magnetic field of the Earth, these satellites are equipped with an accelerometer to monitor non-gravitational accelerations to derive information about the thermospheric density and wind, offering essential measurements for scientific investigations (Olsen *et al*., 2013).

The accelerometer employed on each of the three Swarm satellites was designed and developed at the Aeronautical Research Institute of Prague. Challenges have arisen in processing the accelerometer data, since the raw accelerations are affected by various disturbances. Some of these disturbances are unexpected or have a much larger amplitude that impact data processing more than anticipated (Siemes *et al*., 2016). Swarm C is the only one of the three satellites with the highest signal-to-noise ratio. As a result, acceleration measurements from Swarm C are available throughout the entire operational period of the mission, while data from the other two satellites are only available for certain months (Iorfida *et al*., 2023). The secondary goal of Swarm mission was to bridge the gap in gravity field recovery between GRACE and GRACE-FO (van den IJssel *et al*., 2015; Texeira *et al*., 2020). The third goal of the mission is the estimation of the thermospheric densities (van den IJssel *et al*., 2020). Due to the low signal-to-noise ratio, temperature sensitivity and gaps in accelerometer measurements, the accelerometer measurements are usually replaced or corrected by the non-gravitational measurements derived from POD.

Overall, the accelerometers on GOCE, CHAMP, GRACE, and Swarm differ significantly in design, sensitivity, and operational focus, tailored to each mission's unique objectives. GOCE's accelerometer, one of the most sensitive ever flown, was designed to detect very small accelerations to map Earth's gravity field with unprecedented detail, particularly in low-altitude orbits where atmospheric drag is more pronounced. CHAMP, an earlier mission, featured a less sensitive accelerometer primarily focused on capturing larger-scale gravity field variations and atmospheric density, which laid the groundwork for future missions. GRACE and GRACE-FO employed highly sensitive electrostatic accelerometers, crucial for detecting the non-gravitational forces affecting twin satellites and operating with exceptional stability over long periods, given the mission's focus on temporal changes in the gravity field. In contrast, Swarm's accelerometers are designed with a focus on measuring the non-gravitational forces that could impact the accuracy of its magnetic field observations. While not as sensitive to gravity variations as those on GOCE or GRACE, Swarm's accelerometers are optimized for identifying and compensating for the disturbances that could interfere with its primary mission of mapping Earth's magnetic field.

Figure 2.3 presents a visual comparison of the electrostatic accelerometers and the gradiometer used in the missions mentioned above, showing the different designs and configurations employed by each mission.

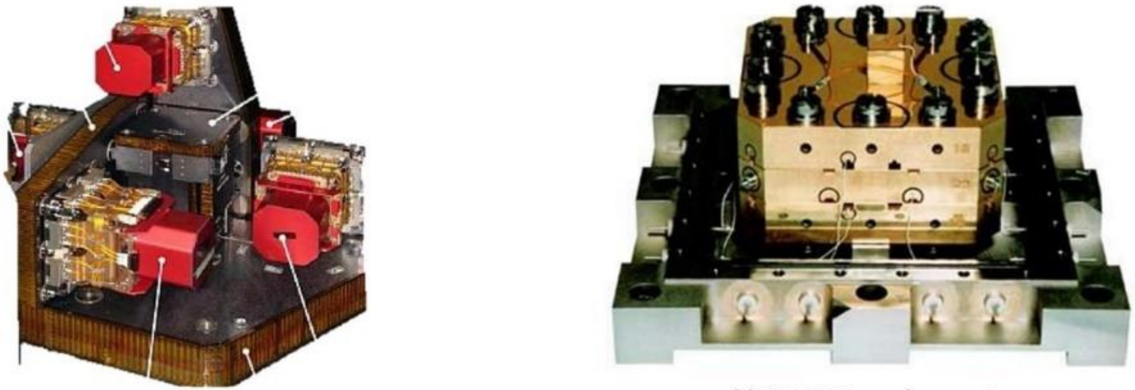

a) GOCE accelerometer

b) CHAMP accelerometer

c) GRACE accelerometer

d) SWARM accelerometer

Figure 2.3 Comparison of electrostatic accelerometers used in various space missions. (a) GOCE accelerometer used for high-precision gravity gradient field measurements. (b) CHAMP accelerometer designed for studying the Earth's gravity field as well as the thermospheric density. (c) GRACE accelerometer: crucial for isolating time variations of the Earth's gravity field from other forces. (d) SWARM accelerometer utilized for the extraction of the thermospheric densities. *Image courtesy of ONERA (GOCE, CHAMP and GRACE) and Aeronautical Research and Test Institute, Prague (SWARM).*

2.3 GRACE and GRACE-FO Missions

The Gravity Recovery and Climate Experiment (GRACE) and its successor, GRACE Follow-On (GRACE-FO), are pioneering satellite missions designed to revolutionize our understanding of Earth's gravitational field and its dynamic changes (Tapley *et al*., 2004; Loomis *et al*., 2020). The primary objective of the GRACE missions was to extend the record of the climate change observations initiated by CHAMP and GOCE missions by continuing the provision of high-resolution monthly global models of the Earth's gravity field (Balmino *et al*., 1999; Flechtner *et al*., 2016; Tapley *et al*., 2019). The GRACE and GRACE-FO missions, launched in 2002 and 2018 respectively, are collaborative efforts between NASA and the German Aerospace Center (DLR). These missions have significantly advanced our ability to monitor the Earth's water distribution, ice mass changes, and the movement of water across the planet with a spatial resolution of approximately 300 km (Flechtner *et al.,* 2014; Croteau *et al*., 2021; Barnoud *et al*., 2023).

Both GRACE missions consist of twin-satellites orbiting the Earth in tandem at approximately 220 km apart (2 degrees), precisely measuring variations in the gravitational pull on the satellites caused by shifts in mass distribution (Kornfeld *et al*., 2019). This separation was deemed suitable to capture spherical harmonics within the desired range. By measuring the changes in the distance between the two satellites, we can track variations in the distribution of water, including underground aquifers, ice sheets, and even changes in the amount of water stored in the soil (König *et al*., 2003).

The altitude of 450-500 km chosen for both missions was optimal for monitoring the time-variable gravity field over an extended period, essential for climate science research. With a near-polar inclination of 89°, it provided global coverage while accommodating the necessary launch mass, covering all local times in ≈ 161 days. Maintaining a low orbital eccentricity of 0.005 ensured that both satellites shared similar eccentricities, reducing sensitivity to altitude changes during orbits and minimizing spacecraft attitude adjustments to maintain alignment (Loomis *et al*., 2012; Frappart & Ramillien, 2018).

2.3.1 Instrumentation

GRACE and GRACE-FO missions comprise twin satellites, A–B and C-D, respectively, equipped with highly sensitive instruments designed to precisely measure variations of the Earth's gravitational field. Each satellite in the GRACE mission carries a K-band Microwave Ranging System (KBR), a precise tri-axial accelerometer and is equipped with star cameras and GPS receivers (Goswami *et al.*, 2018). Building upon this technological foundation, GRACE-FO incorporates a similar instrumentation setup to enhance measurement capabilities. GRACE-FO includes a next-generation accelerometer, the SuperSTAR accelerometer, which offers improved sensitivity and stability compared to its predecessor. Additionally, GRACE-FO features a Laser Ranging Interferometer (LRI) system, which further enhances the precision of the measurements by accurately tracking the distance between the satellites (Abich *et al.*, 2019; Ghobadi-Far *et al.*, 2022).

2.3.2 Products and Reference Frames

In GRACE and GRACE-FO missions there are three different levels of products, and they are presented in Table 2.1. In this thesis only Level 1A and Level 1B have been used[17]. Depending on the product level, each measurement might be given in different reference Frames.

In both GRACE missions, the SuperSTAR accelerometers created by ONERA are placed at the center of mass of the satellite. These accelerometers measure linear accelerations along three perpendicular axes as well as angular accelerations around these axes. The three accelerometer axes define the *Accelerometer Reference Frame* (ARF) which is a satellite-fixed reference frame. The origin of ARF is at the center of the accelerometer proof mass, which is within 0.1 mm of the center of mass of the satellite. *The* Z_{ARF} is pointing towards the K-Band antenna of the other satellite in the pair, the Y_{ARF} is nadir pointing and the X_{ARF} (cross-track) forms a right-handed system triad (Case *et al.*, 2010). Level 1A accelerometer data (raw observed accelerometer data)

---

[17] All the data from both missions can be accessed from FTP ftp://isdcftp.gfz-potsdam.de.

are sampled every 0.09997s, meaning that they have a sampling frequency of $10.034Hz$ and they are given in the ARF. In Fig. 2.4 the ARF is shown with respect to the two satellites.

Another commonly used reference frame is the *Science reference Frame* (SRF). Like the ARF, SRF is a satellite-fixed reference frame with origin at the center of mass of the satellite. The X_{SRF} is pointing along the satellite track ($X_{SRF} = +Z_{ARF}$), Z_{SRF} is in the radial (nadir) direction ($Z_{SRF} = +Y_{ARF}$) and Y_{SRF} ($Y_{SRF} = +X_{ARF}$) is in the cross-track direction forming a right-hand triad. The $Y_{SRF} =$ is the least sensitive axis. In this study, all results and figures refer to SRF, unless stated otherwise.

The *International Terrestrial Reference Frame* (ITRF) is an Earth-fixed frame with its origin at the Earth's center of mass. The xy-plane of the ITRF aligns with the mean equatorial plane of the Bureau International de l'Heure (BIH) reference frame orientation of 1984 (BTS84), within 0.005 arcseconds, and the z-axis is perpendicular to xy-plane defining the IERS Reference Pole (IRP), This is a right-handed reference frame.

Finally, a reference frame that links ARF (and SRF) to the ITRF is the *Terrestrial Intermediate Reference Frame* $-$TIRF (Luzum & Petit, v. 1.3.0., 2019). The frame is formally known as the *Geocentric Celestial Reference Frame* – intermediate (GCRF) in the latest IERS Conventions 2010 (Petit & Luzum, 2010). Other currently used names are the Celestial Reference Frame (CRF) and Earth-centered Inertial (ECI) frame. In general, for both GOCE and GRACE missions, the '*Inertial Frame*' is the TIRF. We choose to adopt the *Celestial Reference Frame* (CRF) nomenclature in this research to be in harmony with the terminology used by the GRACE and GOCE science teams and relevant literature. The xy-*plane* of the CRF is kinematically very close to the mean equator of J2000. The x-*axis* is kinematically fixed to the mean equator and points very close/towards the vernal equinox, i.e., the intersection of celestial equator with the ecliptic, in a direction known as the Celestial Intermediate Origin (CIO). The z-*axis* is normal to the xy-plane and is fixed to the Conventional Reference Pole – CRP. The CRP is nearly aligned to the Earth spin-axis. The y-*axis* forms the right-handed triad.

From the available measurements of the GRACE and GRACE-FO missions, we use the following data sets throughout this thesis, as presented in Table 2.2. The accelerometer products are extensively discussed in Section 2.4. For more details on the reference frames and the products of

GRACE missions, readers are referred to GRACE Level 1b User Handbook (Case *et al.*, 2010). Most of the products in Level 1B are given in the Science Reference Frame (SRF).

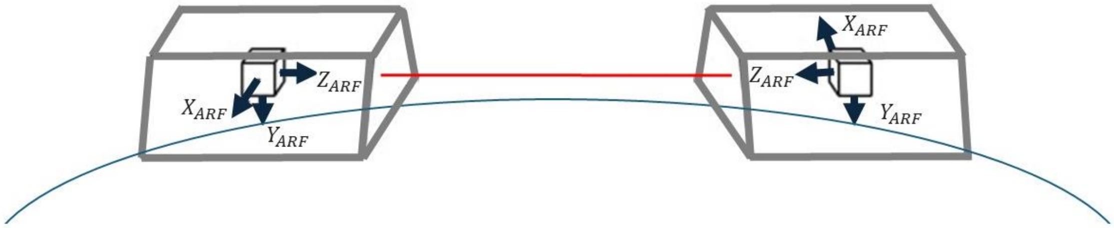

Figure 2.4 The Accelerometer Reference Frame (ARF) of GRACE missions.

Table 2.1 GRACE and GRACE-FO processing levels.

Level of Products	Description
Level 0	The result of receiving, collecting and decommissioning telemetry data. Each satellite provides two of these files.
Level 1A	The result from non-destructive processing applied to Level 0 measurements. It comprises sensor calibration, time tagging, quality control, and reformatting. Ancillary data needed for further processing are also included.
Level 1B	The result from processing Level 1A and Level 0 data. It involves time-tagging and reduction of the data sampling rate. This processing collectively constitutes **Level 1**.
Level 2	Includes precise **satellite orbits** and estimates of the **spherical harmonic coefficients** for the Earth's gravitational potential.
Level 3	Includes monthly ocean and land mass anomaly datasets.

Table 2.2 Description of measurements on GRACE missions

Measurements and Reference Frames	Satellite	Description
ACC1A (ARF)	GRACE C	3D linear and Angular accelerations. The sampling frequency of linear accelerations is $f_s = 10Hz$. The ACC1A is provided to users only for GRACE-FO mission.
ACC1B (SRF)	GRACE A GRACE B	3D linear and angular accelerations. The sampling frequency is $f_s = 1Hz$. The ACC1B is provided only for GRACE mission
ACT1B (SRF)	GRACE C	3D linear and angular accelerations. ACT1B is derived from the ACT1A. The sampling frequency is $f_s = 1Hz$.
SCA1B (IRF to SRF)	GRACE A GRACE B GRACE C	Rotation quaternions from Inertial Reference Frame (IRF) to SRF. The sampling frequency is $f_s = 0.2\ Hz$.
GNV1B (ITRF)	GRACE A GRACE B	3D position coordinates in Earth - Fixed Frame. The sampling frequency is $f_s = 1\ Hz$.
GNVI1B (IRF)	GRACE C	3D position coordinates in Inertial Frame. The sampling frequency is $f_s = 1\ Hz$. The GNI1B dataset is provided only for GRACE-FO mission.

2.4 Accelerometers Onboard GRACE Missions

In both GRACE and GRACE-FO missions the accelerometer is placed in the center of the mass of the satellite in a thermally controlled environment, measuring the linear acceleration with a precision of $10^{-10}\ m/s^2/\sqrt{Hz}$ for the X_{SRF} and Z_{SRF} and $10^{-9}\ m/s^2/\sqrt{Hz}$ for the least sensitive axis Y_{SRF} (Bandikova *et al.*, 2019).

In Figure 2.5 we present the ACC1A measurements $(10Hz)$ along the three axes of the ARF, and their Power Spectral Densities (PSDs), while in Fig. 2.6 the ACT1B measurements $(1Hz)$ along the three axes of the *SRF* and their PSDs are shown. Both figures correspond to GRACE-C satellite of GRACE-FO mission. The GRACE-B accelerometer was turned off in 2016 due to a battery issue (Bandikova *et al.*, 2019). Meanwhile, the GRACE-D accelerometer experienced a significant increase in noise levels in June 2018 and has not recovered since (Harvey *et al.*, 2022).

Level 1B accelerometer data (sampling frequency $1Hz$) are derived from Level 1A data by applying a 35mHz low-pass Butterworth filter and a time correction from on board time to GPS time (Case *et al.*, 2010). This process is slightly different in the GRACE-FO mission compared to the GRACE mission due to the presence of spurious spikes in the accelerometer measurements. Consequently, the dataset provided to users for GRACE-FO is referred to as ACT1B instead of ACC1B. The distinct methodology employed to eliminate these spikes is detailed in Wen *et al.*, (2019).

As highlighted in Chapter 1, the primary challenges addressed in this thesis regarding accelerometer studies include the on-orbit calibration of the instrument, the numerous data spikes caused by thruster activations, and the spurious accelerations resulting from temperature variations in the satellite orbital environment. Additionally, accurately modelling non-gravitational accelerations is crucial for calibrating the accelerometer, retrieving thermospheric densities, and validating the non-gravitational accelerations derived from GPS—a widely used method when accelerometer performance falls short of expectations, as seen in the Swarm mission. These challenges are presented in detail in the following subsections.

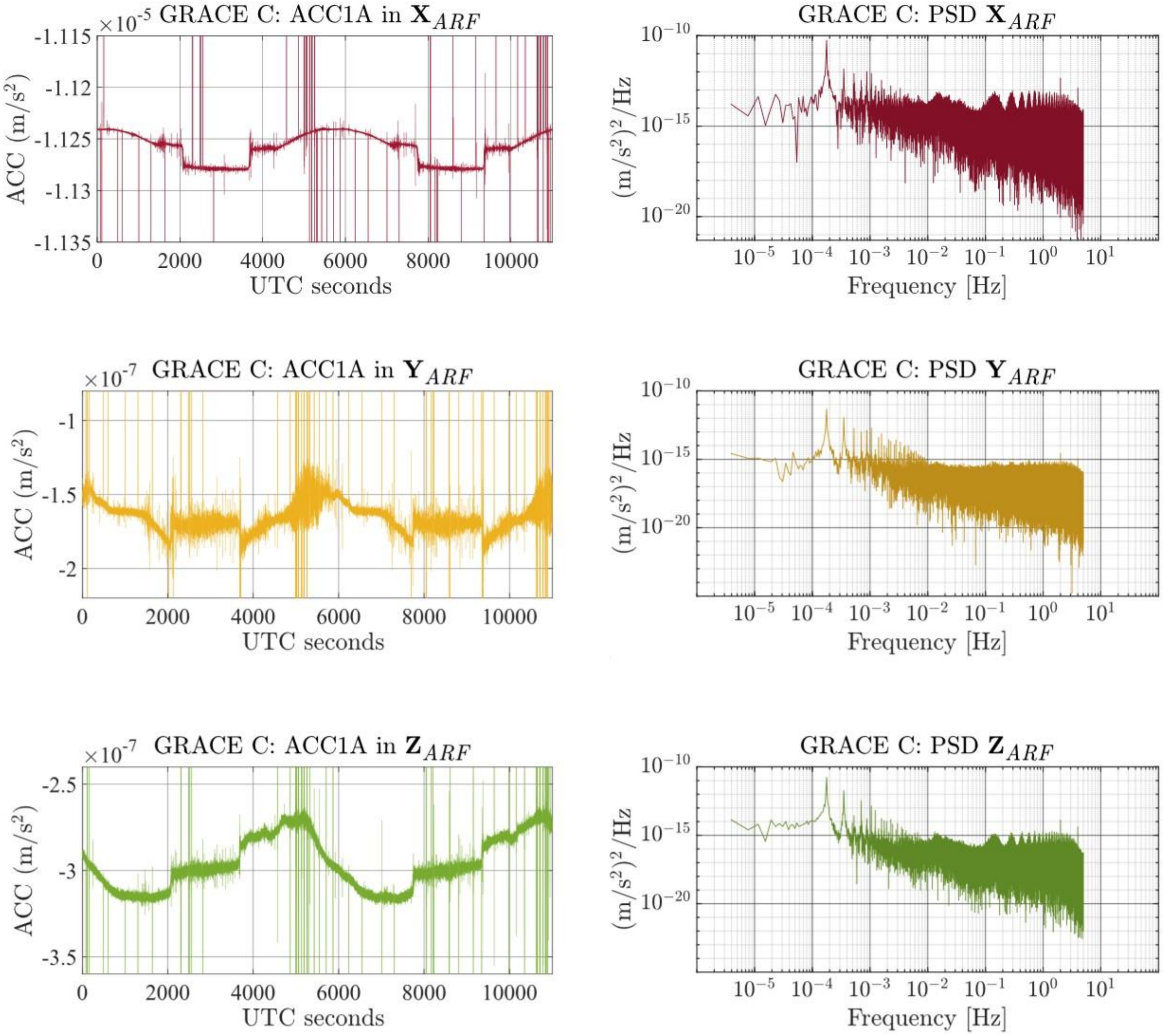

Figure 2.5 GRACE C, January 1st, 2020: Two orbital evolutions of the accelerometer measurements along the three axes of the ARF and their PSDs. X_{ARF} measurements are displayed in red, Y_{ARF} are displayed in yellow and Z_{ARF} are displayed in green. The accelerometer measurements are given in m/s^2 and the PSDs in $(m/s^2)^2/Hz$.

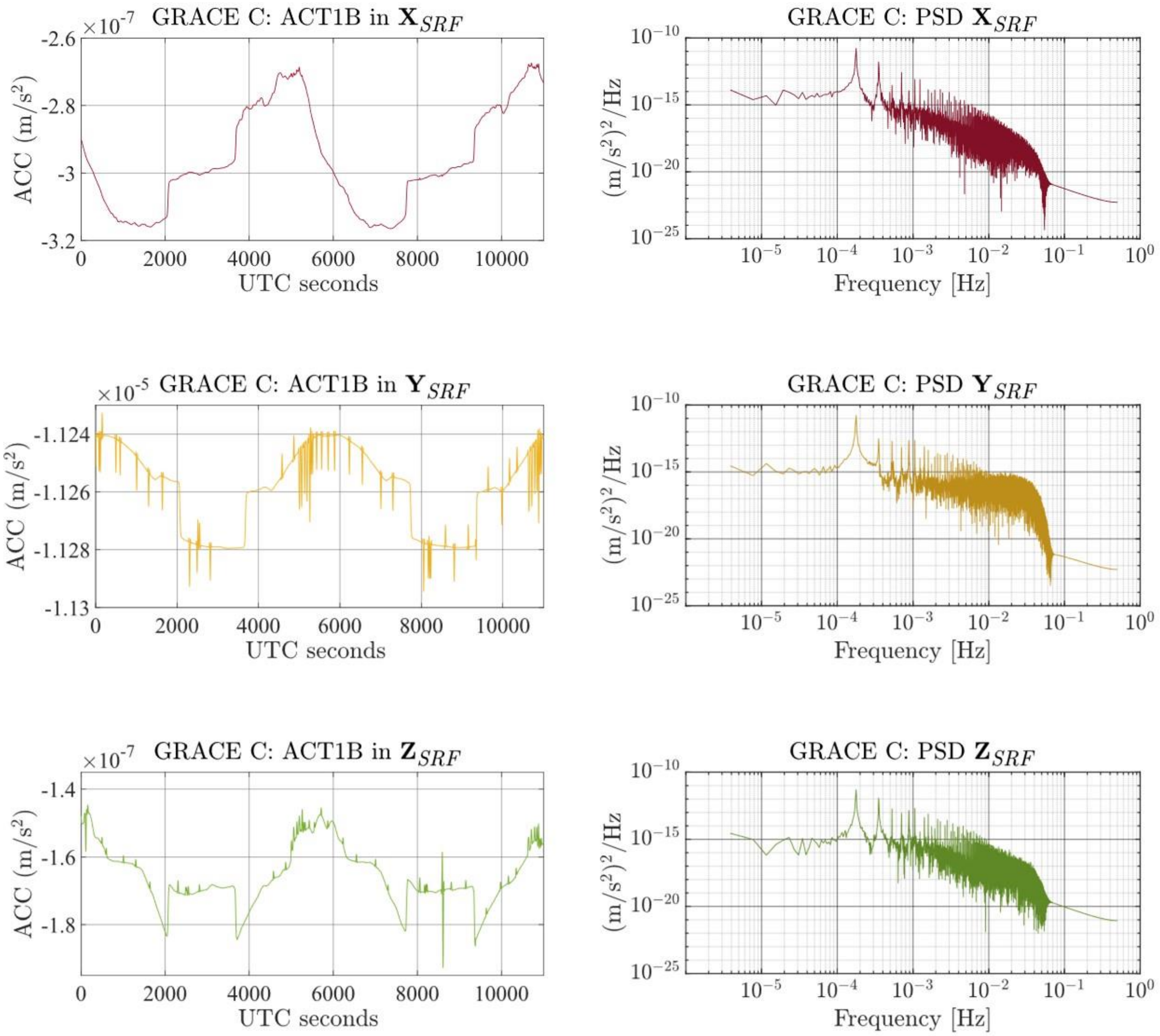

Figure 2.6 GRACE C, January 1st, 2020: ACT1B measurements (Level 1B) along the three axes of the SRF and their corresponding PSDs. X_{SRF} measurements are displayed in red, Y_{SRF} are displayed in yellow and Z_{SRF} are displayed in green. The accelerometer measurements are given in m/s^2 and the PSDs in $(m/s^2)^2/Hz$.

2.4.1 Calibration Parameters

Due to the reliance of the accelerometers on the electrostatic principle, the most challenging aspect is the continuous calibration of the accelerometers because the calibration before the satellite launch is impossible due to the strong gravitational signal on the ground.

The calibration equation is

$$\boldsymbol{a_{cal}} = \boldsymbol{S a_m} + \boldsymbol{b} \, , \tag{2.1}$$

where $\boldsymbol{a_{cal}}$ represents the calibrated non-gravitational accelerations along the three axes of the SRF, $\boldsymbol{a_m}$ represents the measured non-gravitational accelerations, $\boldsymbol{S}$ is a $3x3$ matrix (usually diagonal) representing the scale factor and $\boldsymbol{b}$ is a $3x1$ matrix of the accelerometer bias along the 3 axes. The fully populated S matrix contains diagonal elements that are not equal to one and off-diagonal elements that are non-zero, due to minor instrument imperfections and a misalignment between the ARF and the SRF that result in mutual interference between the accelerometer axes. The initial misalignment arises from inaccuracies in the installation of the accelerometer on the spacecraft. Usually, in the literature the off-diagonal elements are neglected in the literature.

Numerous studies underscore the importance of accelerometer calibration in enhancing the accuracy of gravity field measurements (Behzadpour *et al*., 2021) and estimates of thermospheric densities (Siemes *et al*., 2023). Zheng *et al*. (2011) emphasized the efficacy of calibrating non-conservative force measurements from GRACE accelerometers, demonstrating advancements in calibration techniques for satellite missions. Chen *et al*. (2018) elaborated on strategies for deriving high-precision gravity field models using refined accelerometer calibration models, underscoring the pivotal role of precise calibration in achieving accurate results. Vielberg & Kusche (2020) validated SRP extensions using calibrated GRACE accelerometer measurements, illustrating the significant impact of calibration on enhancing model fits.

2.4.2 Errors in Accelerometer Measurements

The accelerometer sensitivity allows for the observation and analysis of various effects induced by satellite instruments and onboard electronic devices. However, challenges related to the performance and reliability of the accelerometers have impacted the quality of measurements collected for gravity field recovery and scientific research (Kvas *et al.*, 2019). Signals that degrade the quality of the measurements are typically present in Level 1A (10 Hz) data, as many of them undergo attenuation through filtering during the conversion from Level 1A to Level 1B. Thruster firings may be triggered during center of mass calibration maneuvers and other satellite-induced effects occur during the activation and deactivation of onboard heaters. Temperature-induced drift in the accelerometers must be considered, because it can lead to misalignment of satellite orbits and introduce errors in the estimation of mass changes (McGirr *et al.,* 2022). Another dominant effect, particularly in the radial direction, is referred to as "twangs," named for the prolonged oscillation that accompanies high-amplitude spikes (Schlicht, 2022). Lastly, spikes can be created during changes within the magnetic torquers, which are responsible for maintaining the nominal attitude of the satellites (Peterseim *et al*., 2014).

As mentioned in the previous section, one of the most significant issues observed with the accelerometers of GRACE is battery problems leading to accelerometer shutdowns, as documented by the accelerometer aboard GRACE-B toward the end of the mission. Additionally, degradation in accelerometer measurements on one of the GRACE-D satellites has been noted, resulting in higher noise levels and bias jumps, particularly during thruster firings (Koch *et al*., 2021). To address decreased performance in both GRACE-B (towards the end of its operational years) and GRACE-D (from the beginning of the mission), new accelerometer data have been generated using the so-called transplant method (Bandikova *et al*., 2019; Behzadpour *et al*., 2021; Nie *et al*., 2024). In Chapter 5, a comprehensive review of the literature will be presented, focusing on the impact of accelerometer errors.

2.4.3 Modelling Non-Gravitational Accelerations

Numerous physical models have been proposed for modeling the non-gravitational accelerations in the GRACE mission, serving valuable roles in upper atmosphere studies and instrument calibration. These models often incorporate detailed surface representations of satellite bodies to improve the accuracy of gravity field determination up to 5% in higher harmonics (Knabe *et al*., 2022). Solar radiation pressure (SRP) models developed for GRACE missions demonstrate high precision and low correlation with solar activity levels. Unlike drag models, which are sensitive to atmospheric density fluctuations associated with changing solar activity, SRP remains largely unaffected (Vielberg & Kusche, 2020).

A common method for modeling non-gravitational accelerations is the satellite acceleration approach (Klokočník *et al*., 2008). This approach involves deriving the total accelerations acting on the satellite through double numerical differentiation of positions estimated from GPS measurements. Despite potential noise introduced by double differentiation, this method maintains high accuracy, as satellite positions can be determined with centimeter-level precision. Modeled gravitational accelerations are subsequently subtracted from the total accelerations to estimate non-gravitational accelerations. Another high-precision model has been introduced for the GRACE mission, serving as a valuable tool for instrument calibration. This model employs a finite element approach to calculate the TRP acting on the satellite (Woske *et al*., 2019). These high-precision models have proven to be invaluable for estimating thermospheric neutral mass densities, as accurate knowledge of the precise drag affecting the satellite is essential for their calculation (Forootan *et al*., 2022). Inaccurate modelling of the non-gravitational forces could significantly affect the extraction of the thermospheric densities from accelerometer measurements, which are crucial for orbit prediction, reducing uncertainties in satellite positioning and collision avoidance maneuvers (Sutton *et al*., 2007; Bruinsma *et al*., 2023). Chapter 6 will feature an extensive literature review on the modeling of non-gravitational accelerations.

2.5 Summary

This chapter highlighted the pivotal role of accelerometers in LEO missions, with particular emphasis on their crucial contribution to GRACE missions. It covered:

a) Introduction to the accelerometer sensor.

b) Explanation of non-gravitational accelerations impacting satellites.

c) Onboard instrumentation and the resultant products from GRACE missions.

d) The significance of the calibration of the instrument which is addressed in Chapter 4 of this thesis.

e) Errors inherent in accelerometer measurements and contemporary strategies to mitigate them, highlighting the importance of a weighted dataset presented in Chapter 5.

f) Modeling non-gravitational accelerations to accurately retrieve gravity field solutions (models) and extract thermospheric mass densities., which is addressed in Chapter 6 of this thesis.

This chapter highlighted the critical role of accelerometers in geodetic missions, particularly emphasizing the GRACE missions, which are central to this thesis. In the following chapters, a detailed literature review will address each challenge discussed in this thesis, equipping the reader with the essential background needed to thoroughly comprehend the advancements and findings in each specific area.

3 A Novel Calibration Approach: Matched Filter

As highlighted in the previous two chapters, calibrating the accelerometers on board LEO missions presents a significant challenge. Accurate and continuous calibration of these instruments is essential for precise gravity field recovery and for deriving thermospheric densities from non-gravitational acceleration measurements. Over the years, a range of calibration methods that leverage on-board GPS data and physical models of non-gravitational accelerations have been developed. In Chapters 3 and 4, we introduce an all-new accelerometer calibration method, drawing inspiration from the wave focusing methodology of time reversals (matched filter). This method, widely used in radar technology, involves detecting known emitted waveforms (templates) within unknown, noise-contaminated reflected signals. Matched filters are applied in radar and sonar systems for target detection, digital communication systems for signal demodulation, and image processing for template matching. Additionally, they are used in seismology to identify specific seismic events, optical systems for waveform detection, and biomedical signal processing to analyze ECG or EEG waveforms. This innovative technique represents a substantial advancement in the calibration of accelerometers for space applications. Our approach uses as calibration templates the transition offsets in the accelerometer measurements as the spacecraft transitions to and from the Earth’s shadow known as penumbral phases or transitions. These characteristic transition signals are matched with the total accelerations of the spacecraft estimated from GPS-based precise kinematic orbit determination (POD).

A unique aspect of our method is that it solely relies on measurements on board spacecraft namely, the total accelerations of the spacecraft, derived from kinematic positions calculated by Graz University that serve as the absolute standard for the calibration, and the accelerometer measurements from the Level 1B dataset provided by JPL. This new method allows the estimation of the accelerometer scale factors independently of its biases. We present scale factors for both GRACE missions along with mean biases, assessing different operational periods for GRACE and GRACE-FO. Chapter 3 delves into the theoretical background of time reversal methods used in radar, while Chapter 4 details the results and effectiveness of the calibration parameters for the GRACE and GRACE-FO missions.

3.1 Calibration Parameters of Accelerometer

The accelerometers measure the non-gravitational accelerations of the spacecraft caused by the Solar Radiation Pressure (SRP), atmospheric drag, Earth Radiation Pressure (ERP) and Thermal Radiation Pressure (TRP) of the satellite itself. For the determination of the Earth's gravity field, it is crucial to distinguish the effects caused by both gravitational and non-gravitational forces (Kang *et al.*, 2020). During this operation, the accelerometers must be calibrated on orbit, a quite challenging task, since they cannot be calibrated on the ground due to the presence of the strong gravitational signal (cf., Chapter 2). The accelerometer measurements are provided in the ACC1B and ACT1B datasets for GRACE and GRACE-FO, respectively. Both ACC1B and ACT1B datasets refer to $1Hz$ preprocessed accelerometer measurements in the satellite-fixed Science Reference Frame (SRF). The accelerometer measurements are provided in the along-track direction (X_{SRF}), cross-track direction (Y_{SRF}) and radial direction (Z_{SRF}) (cf., Chapter 2). The accelerometer measurements are subject to unknown scale factors, biases, and stochastic noise, which introduce uncertainties and inaccuracies in the measurements (Kim, 2000). Therefore, many studies have followed various approaches to estimate the calibration parameters of bias and scale, which can be used in the Earth's gravity field recovery process or for the retrieval of the thermospheric density and neutral winds. The calibration equation is given by

$$\boldsymbol{a}_{cal} = \mathbf{S} \cdot \boldsymbol{a}_{obs} + \mathbf{b}, \tag{3.1}$$

where $\boldsymbol{a}_{cal}$ denotes the calibrated non gravitational accelerations, $\boldsymbol{a}_{obs}$ are the accelerometer measurements provided by the ACC1B and ACT1B datasets, $\mathbf{S}$ is the 3×3 diagonal matrix comprising the scale factors along each axis by which the original measurements need to be multiplied, and $\mathbf{b}$ is the three-dimensional bias vector added to the measurements. The off-diagonal elements in the scale matrix represent the misalignment of the SRF and the Accelerometer Frame (AF).

Klinger & Mayer-Gurr (2016) proposed utilizing the fully populated scale matrix to mitigate the impact of misalignment and instrument imperfections on gravity field recovery since the estimate of the C20 coefficient was significantly improved. Teixeira da Encarnação *et al.,* (2020) also employed different calibration parameterization schemes, with the most complex one involving the full matrix representation. However, in most calibration studies presented below, the off-diagonal elements have been ignored.

3.2 Calibration Challenges and Methodologies

Two approaches are usually followed for the calibration of the accelerometers, both based on analytical force models (physical models). In the first approach, the non-gravitational accelerations are estimated from force models and compared directly with the acceleration measurements, whereas in the second approach, the non-gravitational accelerations are derived from the total accelerations (using POD double numerical differentiation) by subtracting modelled gravitational accelerations. The studies listed herein represent diverse scientific research from which the calibration parameters for GRACE and GRACE-FO have been estimated.

A study based on CHAMP and GRACE missions proposed the use of the GPS high precision reduced dynamic orbits with the non-gravitational force models replaced by the accelerometer measurements (Helleputte *et al*., 2009). After an extensive investigation, the authors estimated daily calibration parameters with the use of the GPS High precision Orbit determination Software Tools (GHOST; Wermuth *et al*., 2010) simultaneously with the orbital parameters from the GPS measurements (Montenbruck *et al*., 2005). That study showed a time-variable scale factor which became more precise when the accelerometer signal was stronger, during increased solar activity. The study showed that by applying a constant scale factor, the biases showed visible trends due to their strong correlation with the scale factor, even after applying constraints in the bias calculation in Y_{SRF} and Z_{SRF}.

In another study, Bezděk (2010) calculated the total satellite accelerations by double numerical differentiation of the kinematic positions of the satellite. The purpose behind this approach was to derive precise calibration parameters for the accelerometers that could be used in aeronomy studies. The modelled non-gravitational accelerations were derived using the surface properties of the satellite, the neutral thermospheric density model DTM-2000 (Bruinsma *et al.*, 2003) and the seasonal models of the Earth's albedo and emissivity (Stephens *et al.*, 2015). Then, the gravitational accelerations were subtracted from the filtered total accelerations, which were derived by applying the Savitzky-Golay polynomial filter of degree 6 and window length 9 during the double numerical differentiation of the GPS positions. Then the uncalibrated non-gravitational accelerations derived from this subtraction, were calibrated with respect to the non-gravitational accelerations derived from force models through generalized least squares. The calibration parameters were estimated for all three axes of the accelerometer for both GRACE A and B satellites. However, due to the strong correlation between biases and scales in all three axes, the stability of the solution decreased, and realistic uncertainties were obtained only in X_{SRF} (the most important axis in aeronomy studies due to the dominant drag).

A similar approach was followed by Calabia *et al.*, (2015) revealing a strong sinusoidal signal in the scale factor along Y_{SRF}. The total accelerations (POD accelerations) were calculated after interpolation and differentiation of the velocity vectors and then the time varying gravitational model was subtracted from the POD accelerations thus isolating the non-gravitational accelerations. They demonstrated (ibid., 2015) that non-gravitational accelerations can be computed accurately from the velocities. The accelerations in the cross-track direction revealed an unknown periodic signal which was removed since Y_{SRF} was the only axis showing this behaviour. Then, the remaining non-gravitational accelerations were used as reference accelerations for the calibration of the accelerometer. Their results agree with the calibration parameters proposed for GRACE in X_{SRF}, while there is a constant difference in Z_{SRF}. The correlation between Y_{SRF} biases and β' angle[18] is clearly recognized, similarly to other studies.

A study that used simulated non-gravitational accelerations as reference accelerations was presented by Klinger & Mayer-Gurr (2016) for GRACE gravity field recovery purposes. In that

---

[18] β' angle: It is defined as the angle between the Sun-Earth line and the vector perpendicular to the orbital plane of the satellite.

study, force models of the non-gravitational accelerations played the role of the reference accelerations for an initial calibration of the accelerometers and then the calibration parameters were estimated again during the gravity field recovery. The retrieved calibration parameters showed thermal dependency, especially after April 2011, when the thermal control of GRACE was switched off. The highest dependency was presented in Y_{SRF} since the cross-track component is the least sensitive. The off-diagonal elements of the scale factor matrix were different from zero presumably due to a small misalignment between the two coordinate systems namely, the SRF and AF. The presence of non-zero off-diagonal elements improved the C_{20} coefficients, suggesting that the use of a fully populated scale factor matrix will be a great addition in the gravity field recovery process. As noted in Chapter 2, it is a common approach that only the diagonal elements of the scale factor matrix are calculated. The temporal evolution of the scale factors in X_{SRF} showed a strong correlation with temperature variations due to the variability of β' angle, the angle that signifies the duration of illumination of the satellite by the Sun.

Wöske *et al.*, (2019) followed a similar calibration approach by introducing high precision force models for the estimation of the non-gravitational accelerations without using any empirically or estimated stochastic parameters. The accelerometer measurements were used to validate the force (physical) models, which were based on finite element modeling of the satellite using its surface properties (Bettadpur, 2012). An innovative approach for the modelling of the TRP of the satellite itself was presented and the residuals of the TRP model showed a strong correlation with β', especially in Y_{SRF} and Z_{SRF} due to the cooling and heating of the satellite when it enters or exits the Earth's shadow. Due to unrealistic extreme values of the calculated scale factors, especially when the magnitude of the accelerations was quite small, they used constant scale factors for the calibration, similarly to the previous studies presented herein. In X_{SRF}, the calibration parameters strongly agreed with the other POD methods. For the other two axes, their high precision models, combined with the application of strong constraints similar to those presented in Helleputte *et al.,* (2009), led to more reliable calibration parameters.

Zhang *et al.*, (2023) derived calibrated accelerometer parameters that exhibit excellent agreement with the non-gravitational force models for GRACE-FO from July 1, 2018, to December 31, 2021. In that study, modeled non-gravitational forces were used as a reference to initially calibrate the raw accelerometer measurements. Then, the scale and bias parameters were estimated along with other dynamic and geometric parameters within a POD strategy. It was shown that weak signals amplify the coupling between scale and bias in specific periods. To address this, the authors fixed the scales to their mean values and re-estimated the bias to extract the long-term trend. The calibrated accelerations showed disparities of less than 5 nm/s^2 in the along track direction and 6 nm/s^2 in the other two directions when compared with independent non-gravitational force models.

In a study conducted by Koch *et al.,* (2019), calibration parameters for GRACE were estimated for both low and high solar activity periods. Their research investigated the two calibration methods outlined earlier for the GRACE accelerometer. The first method used surface forces affecting the satellite to compute the reference accelerations. In the second approach, the total accelerations, which encompass both gravitational and non-gravitational components, were initially calculated based on reduced-dynamic orbits. The results showed that the calibration parameters obtained from the two approaches differed notably during periods of low solar activity, primarily due to the relatively small magnitude of non-gravitational accelerations. Interestingly, the calibration parameters from the first approach were not significantly influenced by solar activity variations. However, in the second approach, realistic calibration parameters for X_{SRF} and Y_{SRF} could only be obtained during high solar activity periods and revealed a disturbing periodic signal in Y_{SRF} similar to what was previously noted by Calabia *et al.,* (2015).

The importance of the calibration of the accelerometer does not end at the gravity field modeling. Accelerometers measure the atmospheric drag, among others, which is crucial for the determination of the thermospheric density. Many researchers have derived calibration parameters and state-of-the-art radiation pressure models to effectively extract the aerodynamic acceleration, facilitating the derivation of neutral mass densities. Mehta *et al.,* (2017) introduced novel thermospheric density datasets derived from accelerometer measurements aboard CHAMP and GRACE satellites utilizing advanced models for gas-surface interactions and accurate physical modelling. Vielberg *et al.,* (2018) improved and compared three calibration procedures to estimate accurate thermospheric neutral densities via a multi-step numerical estimation approach based on the numerical differentiation of kinematic orbits, the calibration of accelerometer within the dynamic POD procedure and a comparison of observed to modeled forces acting on the satellite. The three approaches aligned better during medium and high solar activity.

Li *et al.*, (2022) explored the calibration of the GRACE accelerometer during 2004 and 2007 using dynamic calibration. Two methods were implemented and compared: the first estimated calibration parameters during a GPS-based POD procedure and the second during fitting using kinematic orbits. These two calibration schemes were then used to derive thermospheric densities which exhibited a remarkably high correlation coefficient of 0.9976. However, a small bias of 2.2% was observed between the orbit-fitting and POD densities.

Siemes *et al.*, (2023) estimated accelerometer-derived neutral mass density and crosswind observations for CHAMP, GRACE and GRACE-FO missions using state-of-the-art modelling of radiation pressure modelling by taking into consideration the temperature-induced bias variations for GRACE mission. The formal standard deviations of the scale factors are all below 10^{-3}, suggesting high precision. Given their minor impact compared to the uncertainty of at least a few percent in the aerodynamic coefficient vector, they can be considered negligible.

From the above studies, it is evident that calibrating the accelerometer presents a particularly challenging task, especially given the dynamic environment in which the satellites orbit the Earth, coupled with varying solar activity levels. This complexity arises from various factors and constraints that must be considered. The accelerometer measurements are highly influenced by temperature variations, and a strong correlation between the two calibration parameters, namely the bias and scale, is a crucial aspect that was addressed in all the studies discussed herein. Especially in our proposed method, discussed in the sequel, the constraints can be dismissed since the calibration is based only on a convolution between the accelerometer measurements and the POD total accelerations therefore, the scale factor and the bias can be calculated independently.

Our study introduces an original, unique, and robust method for calibrating accelerometers on board any satellite in a non-sun-synchronous orbit. This is due to the reliance of the method on penumbra transitions that occur as the satellite enters and exits the Earth's shadow. Our new calibration approach is inspired by the ´wave focusing´ technique that is widely used in radar applications (Sack *et al.,* 1985; Scheer & Holm, 2010) for detecting emitted (known) waveforms in scattered or reflected signals transmitted through linear or nonlinear environments (Helstrom, 1960; Kelly & Wishner, 1965). We utilize the time-reversal method (matched filter) to apply the wave focusing principle. This is specifically aimed at orbital arcs of short duration ($30s - 50s$), specifically when the spacecraft transitions through the Earth's penumbra (penumbra transitions), which we refer to as *focal regions*. Through this method we aim to estimate the magnitude of the penumbra transitions of the accelerometer measurements, which are detected within the total accelerations of the satellite during the penumbra crossings.

In our method, the total acceleration of the satellite is determined by double numerical differentiation of the orbit from three distinct datasets. The first dataset employs the positions derived from TU Graz kinematic orbits, serving as the *absolute calibration* standard solely based on measurements thus avoiding any physical models and their shortcomings. The second dataset utilizes the POD positions derived from JPL's reduced dynamic method (GNV1B dataset), while the third employs the positions derived from TU Graz reduced dynamic method.

Our calibration method primarily focuses on the total accelerations obtained through numerical double differentiation of positions derived from the kinematic approach. This is because positions derived from kinematic orbits rely solely on raw GPS measurements. The last two position datasets, derived from the reduced dynamic approach, are employed for comparison purposes and validation of our calibration method. The diagonal scale factor matrix is obtained from GRACE A and B datasets for the year 2006, and from GRACE C datasets for years 2019 and 2020. The accelerometer biases are produced using a daily polynomial fit of second order on the accelerometer measurements, independently of the diagonal scale matrix. It is shown that the matched filter when used for the accelerometer calibration can detect changes in the scales even when the differences between the POD datasets are below $-50dB$.

3.3 Methodology Concepts

In this contribution, we use the concept of *wave focusing* methodology that is customarily applied in radar electromagnetic wave propagation and wireless communications (Jin *et al*., 2011; Punnoose *et al*., 2011). The fundamental idea behind wave focusing is the identification of transmitted waveforms that have traversed a medium, such as the atmosphere, and subsequently received by an antenna at the source after undergoing reflection and scattering by one or more targets (Bazargani & Snieder, 2016). The detection or determination of the scattered waveforms is usually achieved by an amplification of the scattered wave amplitude or equivalently, amplification of the wave power at a particular time and location in a heterogeneous medium in a region of interest thereafter called *focal region*. Methods of wave focusing include *phase conjugation* (Parvulescu, 1961), *time-reversal* (Fink *et al.*, 2000; Fink & Prada, 2001) and *inverse scattering* (Haddadin & Ebbini, 1998).

In this study we choose the *time-reversal* (TR) method that is robust and optimal (Tanter *et al.*, 2002; Ulrich *et al.*, 2012). The TR is a wave focusing technique that makes use of the *reciprocity* of wireless propagation of waves, a property that was used in previous studies (e.g., Pagiatakis & Peidou, 2021). The main idea of this method is that a known short pulse transmitted by a source through a dissipative medium, returns as an echo from a 'point' target with shifted frequency. Detection of the short pulse echo is accomplished by taking its TR, normalizing its energy (mathematically or physically), and cross-correlating it (focusing, or matching) with the transmitted pulse; this maximizes the signal-to-noise ratio (SNR) between the echo and its source pulse (Bell & Reynolds, 1991; Jin & Moura, 2009).

In radar applications, the reciprocity of waves works particularly well in a cluttered environment with associated multipath reflection (Punnoose *et al.,* 2011). The TR method relies on the *time-reversal invariance* of the wave operator and on the *spatial reciprocity* between emitted and scattered waves. In signal processing, the simplest form of the TR method is merely the convolution of the emitted wave with the time-reversed received signal or vice versa (reciprocity), also known as *matched filter.* The matched filter has been widely recognized as the optimal correlation method for estimating the unknown amplitude and delay of a known waveform (template) that is embedded in additive Gaussian noise (Giannakis *et al.*, 1990; Román *et al.*, 2000). This method effectively detects a known waveform buried in an unknown signal by maximizing the signal-to-noise ratio (SNR) at the sampling instant, or *focal region*, where the known signal is expected to be present. By applying matched filtering, we can enhance the detection and extraction of the desired signal, even in the presence of noise.

In general, to detect the presence of any band-limited signal $s(t)$ in a measured signal $x(t) + n(t)$, where $n(t)$ is noise, we use an appropriate linear, time invariant (LTI) filter of impulse response $h(\tau)$ expecting that the filter output $y(t)$ after convolution will be of larger magnitude (power) where $s(t)$ is present and lower magnitude where it is absent. The detection of $s(t)$ is easier when the instantaneous power in the filtered series is much larger than the average power of the noise i.e., when the signal-to-noise-ratio (SNR) is maximum.

When $s(t)$ has a known form, its detection in the measured signal is simpler when $n(t)$ is Gaussian white noise, since $s(t)$ is used to formulate the impulse response of the filter to maximize the SNR. In addition, when $s(t)$ is of finite length T, the impulse response of this filter is (Turin, 1960)

$$h(\tau) = \begin{cases} ks(T-\tau), & 0 \le \tau \le T \\ 0, & \text{otherwise} \end{cases} \tag{3.2}$$

where k is an arbitrary scale (gain factor) to be determined later and T is the sampling time.

The maximization of SNR is possible in the frequency domain by taking the Fourier transform of $s(t)$ and $y(t)$, forming the SNR and maximizing it by taking into consideration the Cauchy-Schwarz inequality. This leads to a special type of optimal LTI filter namely, the matched filter that is used for the detection of the presence of a known delayed waveform $s(T-\tau)$ hidden in a measured signal $x(t)+n(t)$, where $n(t)$ is Gaussian white noise. As it turns out, the global SNR maximum is achieved by cross correlating the time reversed version $s(T-\tau)$ with $x(t)$, meaning that the SNR at the output of the matched filter will be maximized when the filter lines up with the point of reception of the signal.

$$y(t) = \int_0^T s(T-\tau)x(t-\tau)d\tau + \int_0^T s(T-\tau)n(t-\tau)d\tau \tag{3.3}$$

The filter output $y(t)$ will attain a maximum value at time $t = T$,where the known waveform $s(t)$ is present in the input (measured) signal $x(t)$. The impulse response of a matched filter satisfies the following equation:

$$\mathbb{E} = \int_{-\infty}^{\infty} |h(\tau)|^2 d\tau = k^2 \int_{-\infty}^{\infty} |s(t)|^2 dt, \tag{3.4}$$

where $\mathbb{E}$ is the signal energy (Turin, 1960). The impulse response produces the maximum response when $y(T) = \mathbb{E}$, meaning that $s(t)$ is identified in $x(t)$ at time T**.** From the Cauchy-Schwarz inequality it turns out that the output of the matched filter has a unique global maximum $\mathbb{E}$ at time $t = T$ and for any other t, $y(t) < y(T) = \mathbb{E}$. Theory shows that no filter other than the matched filter can produce an output as large as $\mathbb{E}$ at time $t = T$ therefore it maximizes the SNR only at the sampling instant T**.** Due to the convolution between the impulse response $h(\tau)$ and the input signal $x(t)$ the shape of the output is constrained by the shape of the autocorrelation function (Turin, 1960). The matched filter, as convolution between the received signal and the time reversed copy of the original signal is equivalent to cross-correlation of the two signals. In general, convolution and cross correlation only differ by a time reversal.

A typical example demonstrating the matched filter is readily available in the literature, where a unit square pulse $s(t)$ is injected into Gaussian white noise $n(t)$ forming the measured signal $x(t)$ i.e.,

$$x(t) = s(t) + n(t). \tag{3.5}$$

Figure 3.1 illustrates a typical example of a rectangular pulse as well as a sigmoid pulse. In our calibration method, detailed in Chapter 4, the shape of the signal we want to detect (penumbra transitions) closely resembles a sigmoid.

In this figure, a) is the transmitted pulse, which is a rectangular pulse $s(t)$ of unit amplitude and duration $T_1 = 1s$. This pulse serves as the reference signal for the matched filter process; b) represents a signal containing white noise of duration $T_2 = 5s$. In this signal the original rectangular pulse is injected at t_1=3s (we denote the position of the rectangular pulse in the received signal by a black line, because it is not visible due to the presence of high-level noise). The SNR of the received signal is -20dB; c) the time-reversed pulse is shown, also known as the matched filter impulse response $h(t)$ delayed by τ, which is obtained by flipping the transmitted pulse in the time domain i.e., $h(t) = s(-t + \tau)$. Since the selected pulse for this example is rectangular, the time-reversed pulse is identical to the original; d) matched filter output that matches (‘correlates’) the time reversed rectangular pulse $s(t)$ with $x(t)$, resulting in a distinct peak that indicates the presence of the original transmitted pulse in the received signal $x(t)$. This peak is highlighted in the plot with a red marker, demonstrating the matched filter ability to detect the signal despite the presence of significant noise. The position of the peak at $t_{peak} = 3.5s$.

Another example is presented in Fig. 3.1 (right column; panel (e)), where the pulse to be injected exhibits characteristics similar to the pulse used in the calibration of the accelerometer, specifically to the penumbra transitions. In this example, the transmitted pulse $s(t)$ is generated using the sigmoid function, which provides a smooth, continuous transition from 0 to 1. The sigmoid function used is defined as

$$s(t) = \frac{1}{1+e^{-10(t-\frac{T}{2})}} \;, \tag{3.6}$$

where t is the time, and $T = 1s$ is the duration of the sigmoid pulse. This function creates an S-shaped curve centered at $T/2$, with a steep transition controlled by factor 10 in the exponent. The sigmoid pulse is advantageous in signal processing applications due to its smoothness, which can reduce the high-frequency components and make the signal more resilient to noise; Panel (*f*) shows the received signal containing white noise of duration $T = 5s$. In this signal the original sigmoid pulse is embedded at t=3s (we denote the position of the sigmoid pulse in the received signal by a black line, as it is not visible due to the presence of high-level noise). The SNR of the received signal is also -20dB; c) the time-reversed sigmoid pulse is shown (panel (*g*)), also known as the matched filter impulse response $h(t)$ delayed by τ, which is obtained by flipping the transmitted pulse in the time domain i.e., $h(t) = s(-t + \tau)$; Panel (h) shows the matched filter output that matches ('correlates') the time reversed sigmoid pulse $s(t)$ with $x(t)$ during convolution, resulting in a distinct peak that indicates the presence of the original transmitted pulse in the received signal $x(t)$. This peak is highlighted in the plot with a red marker. The position of the peak at $t_{peak} = 3.5s$.

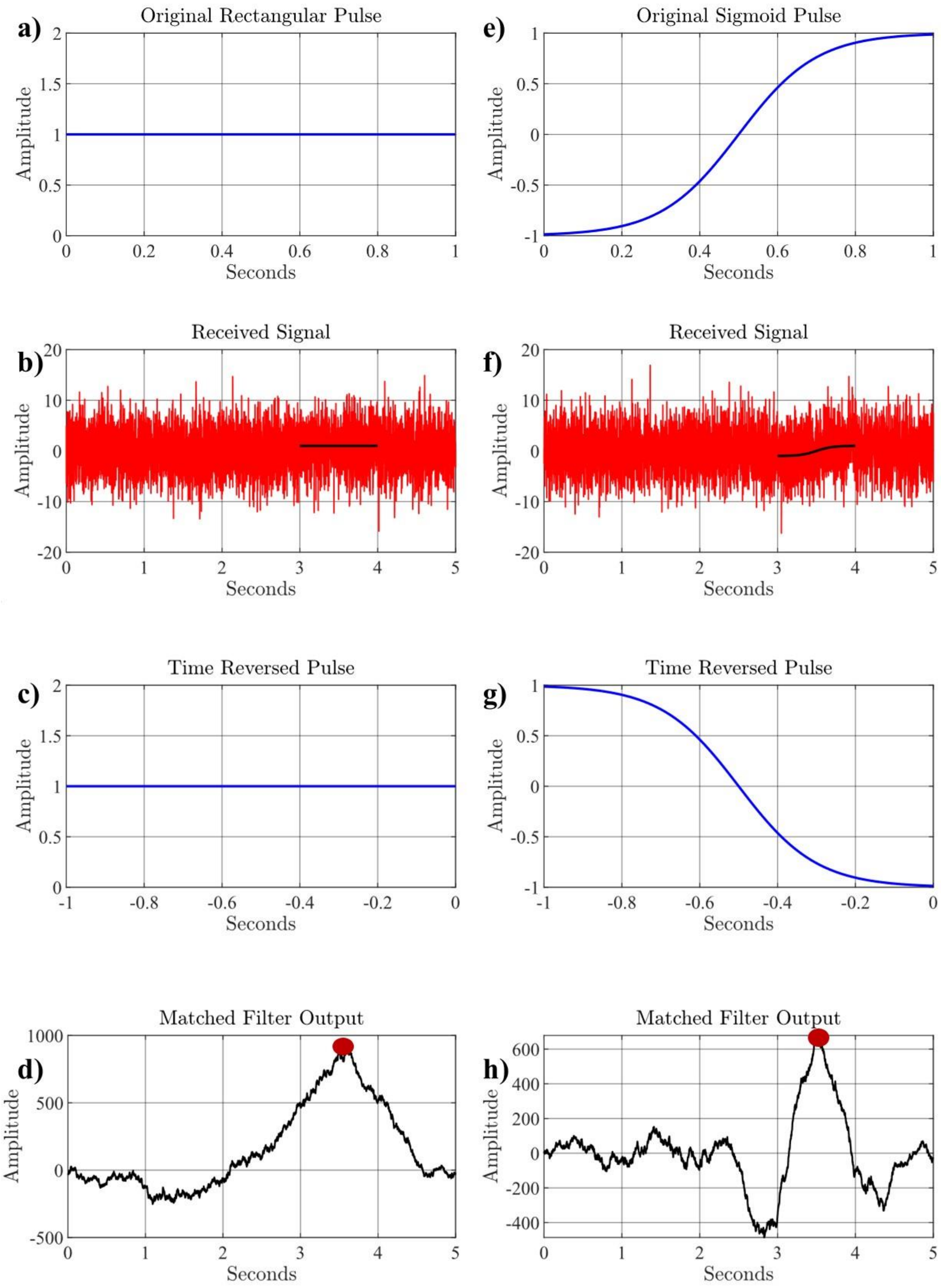

Figure 3.1 Matched Filter: Unit Square Pulse example (left column) and Sigmoid example (right column). a) Transmitted rectangular pulse with unit amplitude and duration of 1s. b) Received signal comprising the transmitted pulse plus noise; c) Time Reversed pulse (Matched Filter); d) Matched Filter Output. e) Transmitted sigmoid pulse; f) Received signal comprising the sigmoid plus Gaussian noise; g) Time reversed pulse (Matched Filter); h) Matched Filter output displaying a distinct peak indicating the presence of the original transmitted pulse (red marker).

The above two examples illustrate the robustness of the matched filter to detect a known pulse embedded in a noisy signal. To retrieve the scale factor of the matched filter output, meaning the degree to which the amplitude of the additive known pulse is distorted in the received signal, we introduce a normalization factor. This adjustment ensures that the peak value of the matched filter output accurately represents the distortion (scale factor) of additive known pulse. According to Zhang *et al.* (2021), the energy normalization factor k is calculated from the ratio of the energy of the known (added) signal $s(t)$ to the total measured signal $x(t)$. In digital form, scale factor k is given by

$$k = \sqrt{\frac{\sum_{i=1}^{N} s_i^2}{\sum_{i=1}^{N} x_i^2}}, \tag{3.7}$$

where N is the number of samples of the finite signal $s(t)$. This scale factor is crucial when working with signals of different power levels, as it allows us to normalize one signal to match the energy level of the other signal.

In Figure 3.2 we present an example illustrating the necessity of the energy normalization factor to detect the amplitude of the known sigmoid pulse embedded within a received signal. The steps are as follows (the letters correspond to the numbered panels in Fig. 3.2):

a) Generate a sigmoid pulse with an amplitude $A_{original} = 1$. Calculate its energy $E_{original}$.

b) Embed the sigmoid pulse into the received signal similarly to the previous two examples, but this time, the embedded pulse has been multiplied by a factor of 40, resulting in $A_{embedded} = 40$. Calculate the energy of the received signal $E_{received}$. Apply energy normalization to the received signal that contains the embedded pulse by multiplying it with the energy normalization factor. The normalized received signal, $received_{norm}$, is computed as:

$$received_{norm} = received \times \sqrt{\frac{E_{original}}{E_{received}}}. \tag{3.8}$$

In this example, the $E_{received}$ is 5 orders of magnitude larger than the $E_{original}$.

c) Time- reverse the original pulse with $A_{original} = 1$.

d) Convolve the time-reversed pulse and the $received_{norm}$. The peak of the matched filter output occurs at $t_{peak} = 3.5s$ and its amplitude is $A_{matchedpeak} = 41.1$. This value indicates that the original sigmoid pulse of $A_{original} = 1$ should be multiplied by approximately 41.1 to match the amplitude of the embedded pulse of $A_{embedded} = 40$.

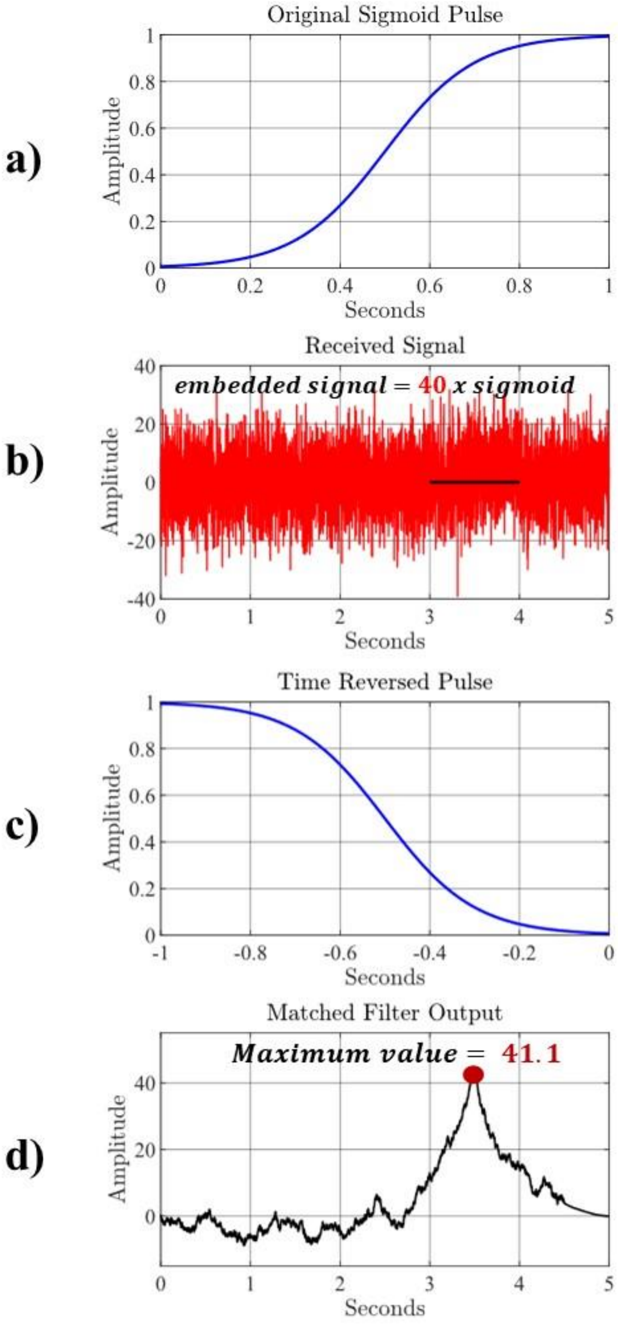

Figure 3.2 Matched Filter example for the amplitude retrieval using the energy normalization factor: a) The original sigmoid pulse of with $A_{original} = 1$. b) The received signal that contains the sigmoid pulse of $A_{embedded} = 40$. c) Time-reversal of the original sigmoid pulse. d) The output of the matched filter (product of the convolution) between the time-reversed pulse and the $received_{norm}$.

In the case of the accelerometer calibration, however, the measured signal $x(t)$ is the penumbra transition signal that is not calibrated, whereas $s(t)$ is the calibrated penumbra transition hidden in the total POD-derived accelerations and needs to be matched with the accelerometer. Thus, the total POD-derived accelerations must be multiplied by the reciprocal of this energy normalization factor k to match the energy level of the penumbra transitions. Since the two signals used to retrieve the scale factor have the same length, the energy normalization factor in this specific method is identical to the power normalization factor.

Contrastingly to Zhang *et al.* (2021), in this study the situation is far simpler than the two-way propagation of electromagnetic waves in a complex environment. Conceptually, and based on the reciprocity of the two signals for calibration purposes, we consider as '*emitted signal*' the non-gravitational accelerations measured by the on-board accelerometer while the '*scattered signal*' comprises the gravitational plus the non-gravitational accelerations derived from the GPS POD kinematic positions. The accelerometer signal ('emitted signal') being uncalibrated, includes the calibration pulses we need to use, namely the SRP offsets during the penumbra transitions (*focal regions*), hereafter called *calibration waveforms* or simply *waveforms*. Based on the reciprocity property of the signals, the calibration factor of the accelerometer is the reciprocal of the ratio of the scattered-to-emitted signal ratio in the focal regions. Therefore, when applying the TR method, the non-gravitational SRP waveform is time-reversed and '*propagated*' back to focus on the POD-derived acceleration signal. This TR is *time-invariant* because both waveforms do not 'occur' in a dissipative medium, and thus is robust and efficient (Fink, 2006).

To calibrate the accelerometers on board GRACE, we need a reference or more specifically an *absolute standard*, for example an injected waveform or pulse of known magnitude as we do metrologically in a laboratory. For this, we examine the possible use of the total accelerations estimated from the GPS POD positions derived from the kinematic orbit determination at TU Graz since they are inherently '*absolute*' by virtue of using the speed of light in their estimation. We therefore develop a new calibration methodology based solely on two signals: a) the estimated total accelerations derived from the GPS POD kinematic positions and b) on the accelerometer measurements (Level 1B). These two fundamental measurements are explained in Chapter 4, along with the results of this new calibration approach.

3.4 Summary

In this chapter, we provided a comprehensive literature review of the various calibration approaches followed for the calibration of the accelerometer and a thorough of time reversal methods. To the best of our knowledge, this is the first time the matched filter method has been employed to derive the scale factor of accelerometer measurements. Consequently, we deemed it necessary to provide the concepts of our methods and a detailed explanation of the application of this method. In the next chapter, the results of the scale factor retrieval for GRACE A, B and C satellites will be presented.

4 On-Orbit Calibration of Accelerometers in GRACE Missions

In Chapter 3 we introduced the theory of the matched filter, as used in radar applications for the detection of a known signal hidden in a received signal with added Gaussian noise. We also introduced the energy normalization factor k which will be key in the scale factor retrieval. In Chapter 4, we apply the theory of the matched filter in the calibration of the accelerometers on GRACE missions. We show that the calibration parameters can robustly be determined by rigorous signal processing without the need to subtract model gravitational accelerations from the POD total accelerations nor model the non-gravitational accelerations.

4.1 Description of Datasets

The diagonal accelerometer scale matrix $\mathbf{S}$ (cf., Eq. (3.1)) is derived from three different POD datasets from which we calculate the total accelerations by double numerical differentiation of the precise GPS-determined orbits. The first dataset comprises the POD positions of the satellites, kinematically calculated by TU Graz (Zehentner & Mayer-Gürr, 2015; Suesser-Rechberger *et al.*, 2022). The kinematic orbit determination from TU Graz employs raw GPS observations, achieving a satellite position accuracy of up to a few centimeters. This method considers a comprehensive set of parameters, including the satellite orbits, station positions, clock errors, and signal biases. To accommodate the varying accuracy of the measurements, a weighted scheme was employed.

The second dataset provides the reduced-dynamic POD positions provided by GRACE and GRACE-FO Level 1 products (GNV1B dataset). These reduced-dynamic POD positions were obtained through orbit integration utilizing two types of force models (Kuang *et al.*, 2019; Bertiger *et al.*, 2020). These models encompass gravitational forces (static gravity field, ocean, direct and anelastic solid Earth tides) and non-gravitational forces (atmospheric drag and SRP). The atmospheric drag model was calculated as recommended in Montenbruck & Gill, (2000, p.84), while the SRP model incorporated a shadow model with umbra and penumbra cones, disregarding the atmosphere and Earth's flattening (Montenbruck & Gill, 2000).

In the third dataset, comprises the reduced-dynamic POD positions of the satellites provided by TU Graz. For the reduced-dynamic orbit, a two-step process was employed, involving force modeling of Earth's gravity field (Kvas *et al.*, 2020), tides (Desai, 2002; Dobslaw *et al.*, 2017), SRP (Lemoine *et al.*, 2013) and atmospheric drag (Bowman *et al.*, 2008) among others and least squares fit of the dynamic orbits to the observed kinematic ones[19]. It is important to note that the abbreviations corresponding to the datasets from TU Graz are not official; they have been selected for the sake of readability and comprehension. All three position datasets used have RMS values of approximately 2 cm in the along-track, 4 cm in the cross-track, and 6 cm in the radial components.

Given that the quaternions in Level 1 products of both GRACE and GRACE-FO missions (SCA1B datasets) are presented as rotation quaternions from the ICRF-intermediate (quasi-Inertial Frame or Celestial Reference Frame - CRF) to the Science Reference Frame (SRF), we opt for the SCA1B dataset for the matrix transformations (Wu *et al.*, 2006; Bettadpur, 2018; Wen *et al.*, 2019). This choice is made because the quaternions provided by TU Graz have a lower sampling rate than the quaternions provided by SCA1B. To ensure that the total accelerations derived from the three different datasets maintain a sampling rate of 1Hz, spline interpolation is employed whenever necessary. In Fig. 4.1 all the datasets used in this study are shown, with their description. The rotation matrix used to transform the POD total accelerations from the Inertial Frame (see Section 2.3.2) to the SRF is as follows (Wu *et al.*, 2006):

---

[19] For more information about the process and the force models, we refer the readers to Suesser-Rechberger *et al.*, (2022).

$$R_{CRF\rightarrow SRF} = \begin{bmatrix} q_0^2 + q_1^2 - q_2^2 - q_3^2 & 2(q_1q_2 + q_0q_3) & 2(q_1q_3 - q_0q_2) \\ 2(q_1q_2 - q_0q_3) & q_0^2 - q_1^2 + q_2^2 - q_3^2 & 2(q_2q_3 + q_0q_1) \\ 2(q_1q_3 + q_0q_2) & 2(q_2q_3 - q_0q_1) & q_0^2 - q_1^2 - q_2^2 + q_3^2 \end{bmatrix} \quad (4.1)$$

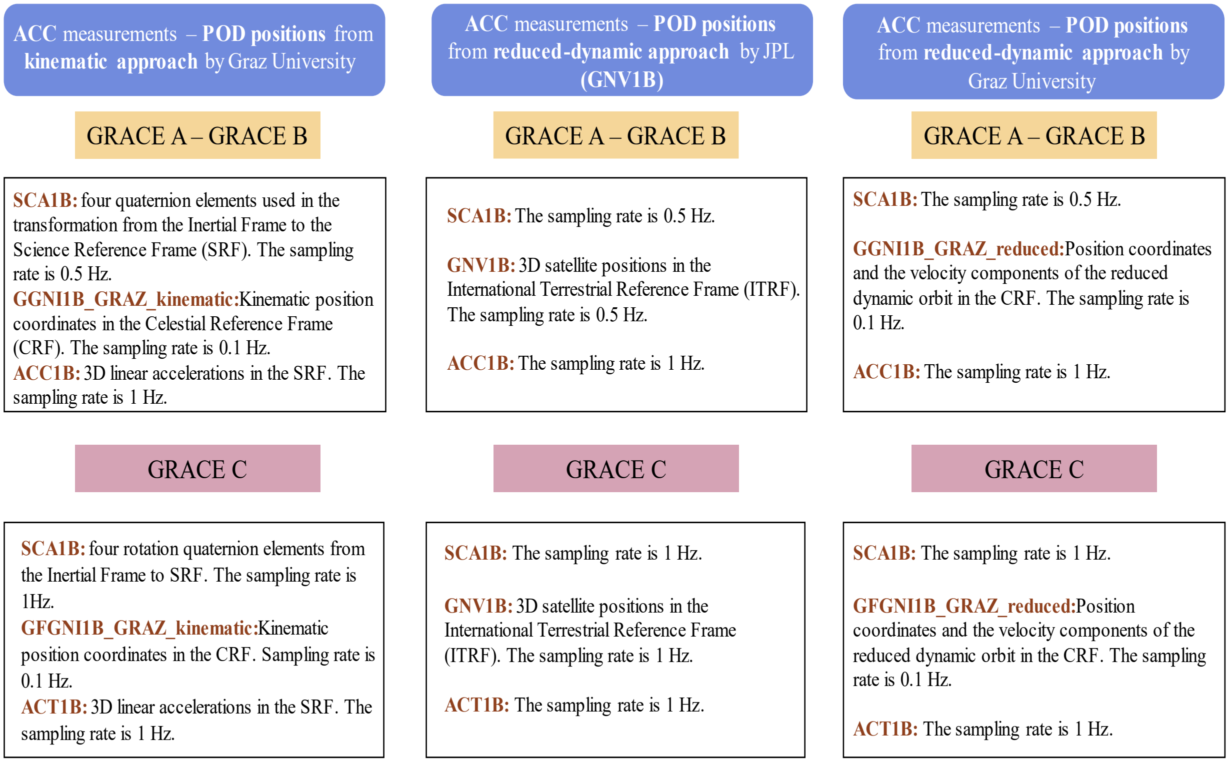

ACC measurements – **POD positions** from **kinematic approach** by Graz University	ACC measurements – **POD positions** from **reduced-dynamic approach** by JPL **(GNV1B)**	ACC measurements – **POD positions** from **reduced-dynamic approach** by Graz University
GRACE A – GRACE B	GRACE A – GRACE B	GRACE A – GRACE B
SCA1B: four quaternion elements used in the transformation from the Inertial Frame to the Science Reference Frame (SRF). The sampling rate is 0.5 Hz. **GGNI1B_GRAZ_kinematic:** Kinematic position coordinates in the Celestial Reference Frame (CRF). The sampling rate is 0.1 Hz. **ACC1B:** 3D linear accelerations in the SRF. The sampling rate is 1 Hz.	**SCA1B:** The sampling rate is 0.5 Hz. **GNV1B:** 3D satellite positions in the International Terrestrial Reference Frame (ITRF). The sampling rate is 0.5 Hz. **ACC1B:** The sampling rate is 1 Hz.	**SCA1B:** The sampling rate is 0.5 Hz. **GGNI1B_GRAZ_reduced:** Position coordinates and the velocity components of the reduced dynamic orbit in the CRF. The sampling rate is 0.1 Hz. **ACC1B:** The sampling rate is 1 Hz.
GRACE C	GRACE C	GRACE C
SCA1B: four rotation quaternion elements from the Inertial Frame to SRF. The sampling rate is 1Hz. **GFGNI1B_GRAZ_kinematic:** Kinematic position coordinates in the CRF. Sampling rate is 0.1 Hz. **ACT1B:** 3D linear accelerations in the SRF. The sampling rate is 1 Hz.	**SCA1B:** The sampling rate is 1 Hz. **GNV1B:** 3D satellite positions in the International Terrestrial Reference Frame (ITRF). The sampling rate is 1 Hz. **ACT1B:** The sampling rate is 1 Hz.	**SCA1B:** The sampling rate is 1 Hz. **GFGNI1B_GRAZ_reduced:** Position coordinates and the velocity components of the reduced dynamic orbit in the CRF. The sampling rate is 0.1 Hz. **ACT1B:** The sampling rate is 1 Hz.

Figure 4.1 Description of the datasets used in this study.

We note that for GRACE-FO, the ACC1B dataset is not provided. Instead, the ACT1B is provided to the users in which the accelerometer measurements are corrected from known errors, spurious accelerations, and high frequency signals. For more information about this process we refer the readers to McCullough *et al.*, 2019. A detailed description of the Level-1B datasets[20] of GRACE

---

[20] GRACE and GRACE-FO Level-1 data are available at: NASA's PO.DAAC (https://podaac.jpl.nasa.gov), and GFZ's ISDC: (https://isdc.gfz-potsdam.de/grace-fo-isdc/).
All handbooks are available at: https://podaac-tools.jpl.nasa.gov/drive/files/allData/gracefo/docs/.

and GRACE-FO missions is given in Case *et al*., (2010) and Wen *et al*., 2019. For a detailed description of the TU Graz[21] datasets, we refer the readers to Suesser-Rechberger *et al*., (2022).

4.1.1 Penumbra Transitions

The key principle of our calibration method is that characteristic non-gravitational signals in the form of identifiable and suitable waveforms (pulses) are present in both POD-determined accelerations and in the accelerometer measurements in certain *focal regions* namely, the penumbra transitions. In our quest for such waveforms (pulses) and after lengthy experimentation, we identified that the short-duration acceleration offsets (jumps) which are known as penumbra or eclipse transitions, are ideal for our purpose because they appear ~ 30 times per day when the satellite enters and exits the Earth's shadow. The challenge is to optimally amplify the penumbra transitions in the POD-derived accelerations, without subtracting the strong gravitational signals estimated from models.

When $\beta' < 70°$[22], the satellite orbit is divided into three distinct arcs: the *illuminated or Sun arc*, where the satellite is exposed to the Sun, the *umbra arc* where the satellite is in total occultation in the inner most region of the Earth's shadow (umbra), and the *penumbra arc* where the satellite is in the partial shadow between the umbra and full illumination. The penumbra transition modeling is of significant importance in satellite orbit determination and the SRP modeling (Fixler, 1964; Robertson *et al*., 2015). Various penumbra transition modeling methods have been proposed but to the best of our knowledge, none of the proposed models can determine the transitions in a fast, accurate, and non-complex way. The appearance of the penumbra transitions is dependent on β', a highly valuable parameter for visualizing the orbital environment which determines the proportion of time during which the satellite remains directly exposed to sunlight. Specifically, it is defined as the smaller angle between the geocentric position vector of the Sun and the orbital plane of the spacecraft. It can vary between +90° and -90°, and the sign is determined by the

---

[21] All available datasets of the TU Graz can be found in https://www.tugraz.at/institute/ifg/downloads/satellite-orbit-products.

[22] β' is the angle between the plane of the obit of the satellite and the vector from the Sun to the Earth, describing the orientation of the satellite orbit relative to the Sun (RM, 2019).

direction in which the satellite orbits its primary body. When $\beta' = 0^\circ$, the satellite spends the maximum possible amount of time in Earth's shadow (Duan *et al.*, 2016).

Both GRACE and GRACE-FO exhibit analogous characteristics regarding the penumbra transitions, wherein these transitions follow a similar pattern and disappear when the satellite is constantly illuminated by the Sun, which occurs every ~161 days for both missions. An extensive investigation of the relationship between β' and the accelerometer drift was conducted by McGirr *et al.* (2022). The magnitudes of the penumbra transitions vary over time, especially as the satellite approaches its full Sun orbit, during which it neither enters nor exits the Earth's shadow. To address this, we have considered the gradual decrease in these magnitudes as the satellite approaches its full Sun orbit since the retrieval of the penumbra transitions has been performed manually on a day-by-day basis from accelerometer measurements, accounting for these changing conditions.

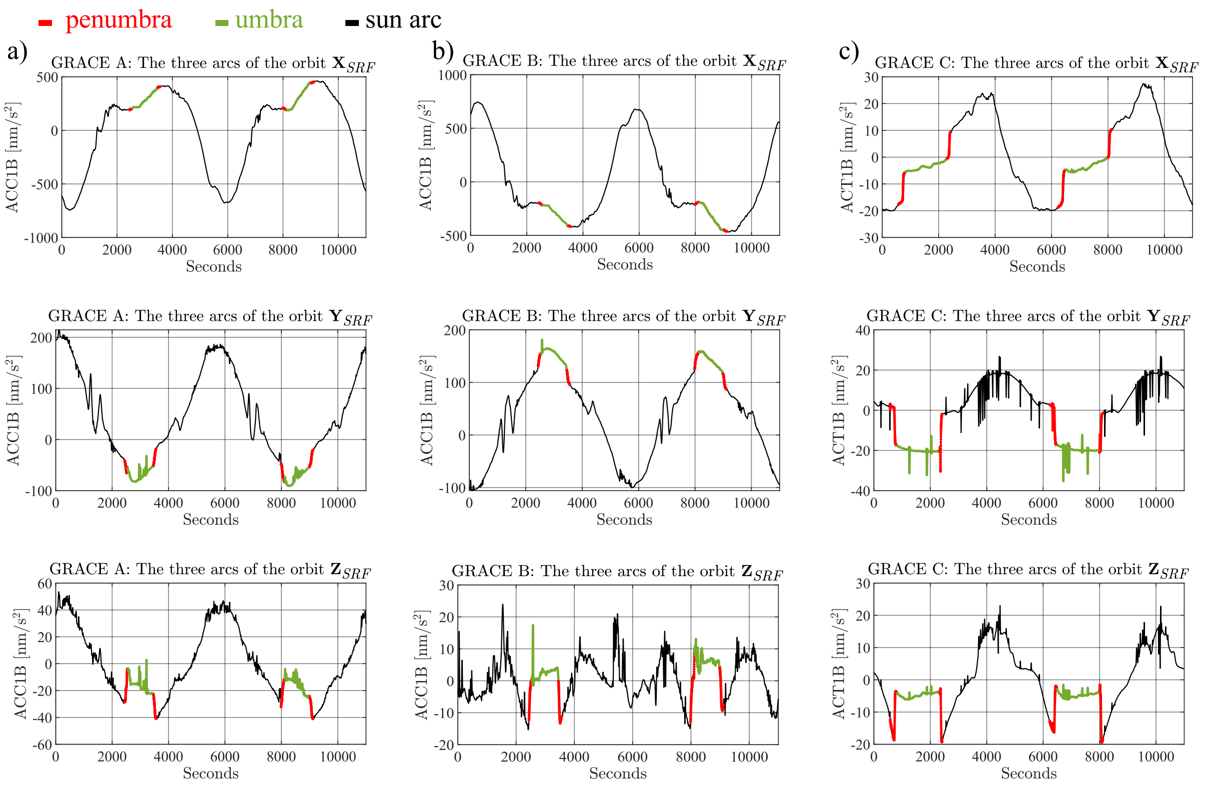

Figure 4.2 Two orbital revolutions of a) GRACE A (left column), b) GRACE B (middle column) and c) GRACE C (right column). GRACE A and B correspond to April 1st, 2015, while GRACE C correspond to January 1st, 2020. The penumbra transitions (red) are depicted as sudden jumps occurring before and after the entrance of the satellite to the umbra arc (green) of the orbit. The accelerometer measurements are represented w.r.t. to zero mean.

In Figure 4.2, we show the three distinct accelerometer time series segments corresponding to the three different orbital arcs for two orbital revolutions of GRACE A and B of GRACE mission and GRACE C satellite of GRACE-FO mission. The focal point of our accelerometer calibration methodology lies in utilizing the measured penumbra transitions as calibration waveforms that serve as the reference signals allowing for precise calibration of the accelerometer measurements.

4.1.2 Total 3D Accelerations Derived from Precise Orbit Determination (POD)

For the double numerical differentiation of POD positions there are different numerical tools, such as the Newton-Gregory interpolation, the interpolation by fitting polynomials, and the interpolation using cubic splines (Földváry, 2007). In our methodology, we use polynomial fitting of degree 7 with a window length of 9 points (7/9) for the calculation of the total accelerations using the three different position datasets presented above. Since the GNV1B datasets are given in the International Terrestrial Reference Frame (ITRF), a rotation to the ICRF-intermediate (quasi-Inertial Frame or Celestial Reference Frame - CRF) is applied as function of time as specified in the 2010 IERS Conventions (Petit & Luzum, 2010). This process is complemented by additional measurements used to determine the Earth's variable rotation (UT1) and polar motion. The results through this rotation have been compared with the GNIB dataset available for GRACE-FO for validation purposes. The rotation between the ICRF-intermediate and ITRF used in Level 1B algorithms is described in detail in Bettadpur, (2018) and Yuan, (2018). Interpolation is carried out on the positions of the satellites in the non-rotating, ICRF-intermediate reference frame due to its stability. Interpolation in the SRF is not feasible because it introduces additional gravitational accelerations.

Subsequently, using the SCA1B dataset, the accelerations are transformed from the ICRF-intermediate to the SRF where the non-gravitational accelerations are given using the rotation matrix given by Eq. 4.1. Different polynomials have been used such as 9/11 or 11/14 that produced comparable results. However, increasing the degree of the polynomial above 11 can introduce differences up to 5 $\mathrm{m/s}$ in the velocity vectors. Consequently, to maintain better accuracy, we opt for the lower degree polynomial. In Fig. 4.3, we present the calculated total accelerations in the SRF from the three distinct datasets, alongside their corresponding power spectral densities (PSD) and their differences for GRACE C. The results are similar for GRACE A and B. Across all three axes the differences $acc_{kinGraz} - acc_{redGraz}$ are less than $10^{-5} m/s^2$ (left column) which is comparable to the difference $acc_{kinGraz} - acc_{redGNV1B}$. The difference $acc_{redGraz} - acc_{redGNV1B}$ is nearly zero, with its PSD indicating a difference below $-50dB$. From the PSDs, high frequency artifacts are observed above 0.1 Hz that appear to be overtones of the orbital period of the satellite. These artifacts are beyond the scope of our research since the penumbra transitions are of lower frequency phenomena.

The solar radiation pressure (SRP) is embedded in the changes of the position of the spacecraft (POD), whereas it is directly measured by the on-board accelerometer. However, in both types of measurements, the SRP is blended with other accelerations that are mostly larger or significantly larger in magnitude than the SRP, particularly the gravitational accelerations present in the POD signal or the atmospheric drag in the accelerometer measurements during high solar activity. Considering that the SRP is scaled correctly in the POD kinematically derived accelerations, while it has an inherent scale defect in the accelerometer measurements, we strive to 'focus' the SRP waveform onto its reciprocal in the POD signal using the time reversal method. Thus, in principle, POD accelerations and non-gravitational accelerations will be the waves to be focused but with one provision: The focusing must be 'local' when the SRP has unique characteristics namely during the penumbra transitions. These transitions are also present in the POD accelerations, even though they are invisible due to their significantly smaller magnitude compared to gravitational accelerations.

Now that the total accelerations derived from POD and the non-gravitational accelerations measured by the accelerometer are both in the same reference frame, specifically the SRF, in the following sections we will proceed as follows: We will apply the matched filter method to the accelerometer (self-calibration method), we will demonstrate that the detection of the penumbra transition in the POD is successful and apply the proposed calibration method using the three different POD datasets and the three accelerometer datasets from GRACE A and B (GRACE) and GRACE C (GRACE-FO). The accelerometer on GRACE D is not functioning properly, so it is excluded from this calibration process. The two approaches which utilize the reduced-dynamic orbits are exclusively employed for the purposes of comparison and validation with respect to the kinematic approach in which the measurements are free from any force model. Daily bias and scale factors are calculated for different periods of solar activity of both missions and the dependency of the accelerometer measurements to β' angle is investigated.

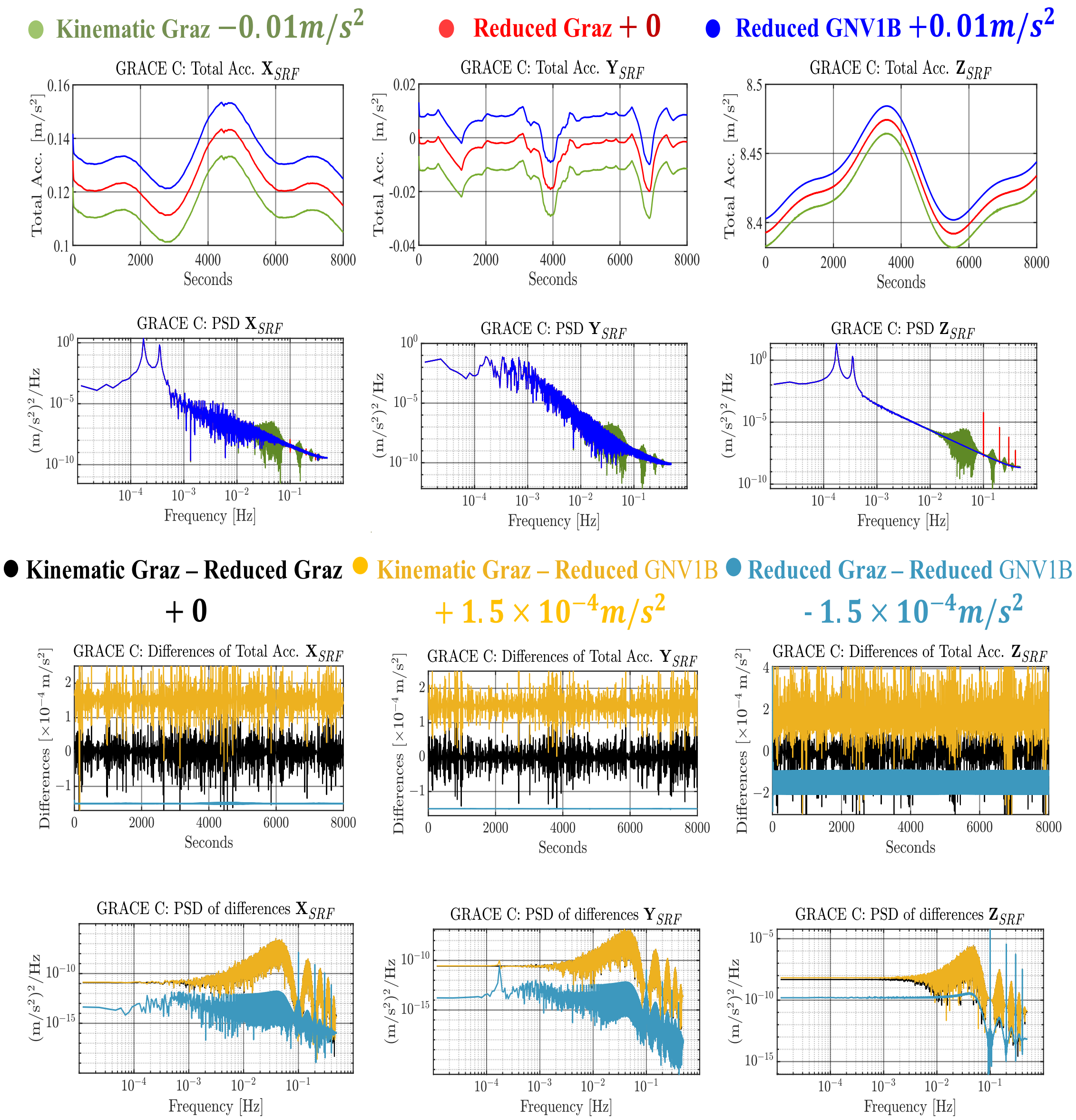

Figure 4.3 GRACE C (January 1st, 2020): Top two rows: The total accelerations in SRF computed for the three datasets along with their respective PSDs along the three axes of the accelerometer. The $acc_{kinGraz}$ and the $acc_{redGNV1B}$ are presented with an offset of $\pm 0.01m/s^2$ for visualization purposes. Bottom two rows: The differences between the datasets and their PSDs. The differences $acc_{kinGraz} - acc_{redGraz}$ (black) have zero offset while the $acc_{kinGraz} - acc_{redGNV1B}$ (yellow) and $acc_{redGraz} - acc_{redGNV1B}$ (light blue) are presented with an offset of $\pm 1.5 \times 10^{-4} m/s^2$, for visualization purposes.

4.2 Detection of Calibration Waveforms and Self-Calibration

In the context of matched filters, a significant challenge known as the false detection problem can arise, where the filter incorrectly identifies a non-matching signal as a match. False detection can arise from various factors, including the presence of noise, interference in the signal, differences in amplitude, frequency, or phase. To address false positive or false negative detections, preprocessing techniques like noise filtering, fine-tuning filter parameters, adjusting detection thresholds and statistical methods for validations have been widely applied (Hamilton & Tompkins, 1988; Cheng *et al.*, 2020; Develter *et al.*, 2022). Since in our case the times of the penumbra transitions are known, we can proactively prevent false detections without taking any preprocessing steps. However, to ensure that the matched filter accurately identifies the penumbra transitions within the total accelerations obtained from POD positions we incorporate two tests outlined in Sections 4.2.1 and 4.2.2.

4.2.1 Detection and Self-Calibration in the ACC of GRACE-FO Using One Calibration Waveform

In matched filter applications, specific detection pulses are commonly used due to their advantageous properties. Examples include rectangular pulses, gaussian pulses or sinc function pulses. Due to their structure, the series length and noise characteristics of the signals, these pulses, when detected successfully, result in a triangular shape in the matched filter output. In our study, the penumbra transitions do not share similar characteristics with the usual standard pulses described in the literature. Our pulses (calibration waveforms) are sigmoid-like functions monotonously increasing or decreasing in time within their domain and can be compared to monopulses, an effective technique used in radar system for direction finding and tracking of a target particularly in scenarios requiring accurate angle determination (Develter *et al.*, 2021). As noted in Chapter 3, the matched filter, as convolution, is equivalent to cross-correlation operation by a time reversal of one of the signals (Proakis & Salehi, 2008; Chapter 5) thus we expect to see negative correlations when the calibration waveform encounters opposite trending pulses.

To evaluate the accuracy of detecting a known waveform using the matched filter, we conduct a test by utilizing a full day of ACC measurements, denoted as $x(t)$, as the emitted (input) signal. In the accelerometer signal (black line in Fig. 4.4), 30-31 penumbra transitions are observed during the day. For testing purposes, we isolate one specific penumbra transition from the emitted signal, denoted as the *entry transition*, which corresponds to the transition of the satellite into the umbra. Similarly, we select another transition marking the satellite's transition from the umbra to the sun arc of the orbit, referred to as *exit transition*. (Both entry and exit transitions are represented by the red lines in Fig. 4.4). It is very important to differentiate the entry from the exit transitions, since in the Y_{SRF} and Z_{SRF}, the entry transitions consistently increase monotonously, whereas the exit transitions decrease monotonously. This distinction has an effect in the local minima and maxima observed in the following tests on the Y_{SRF} and Z_{SRF}. When the entry transition is chosen as the calibration waveform, the matched filter output during entry transitions will exhibit a local maximum, whereas during exit transitions, it will display a local minimum.

Before introducing the energy normalization factor k that will be used in the retrieval of the scale factor, the objective of this test, namely convolving the accelerometer signal with its own time reversed and normalized signal (thus the name self-calibration) is to determine whether the selected waveform (entry or exit transition) could be detected in the ACC measurements. The chosen entry or exit transition, having a zero mean, undergoes normalization by its energy followed by time reversal and subsequently convolved with the one day ACC measurements. As depicted in Fig. 4.4, the matched filter output (blue line) is exactly 1 when the calibration waveform is correctly aligned with itself. It is also evident that while all the other transitions are also detected, they do not yield a value of exactly 1 in the matched filter output due to the differences in their amplitudes compared to the selected penumbra transition. It is worth highlighting that at the focal points, the scale factor (sharp peak) exhibits a remarkable $SNR \approx 15\ dB$, where the 'noise' is the variance (power) of the high frequency output of the filter. The presence of spikes in the Y_{SRF} results in numerous false detections in the matched filter output. However, knowing the precise timing of the penumbra transitions, these false peaks have no consequences on the calibration and can be disregarded.

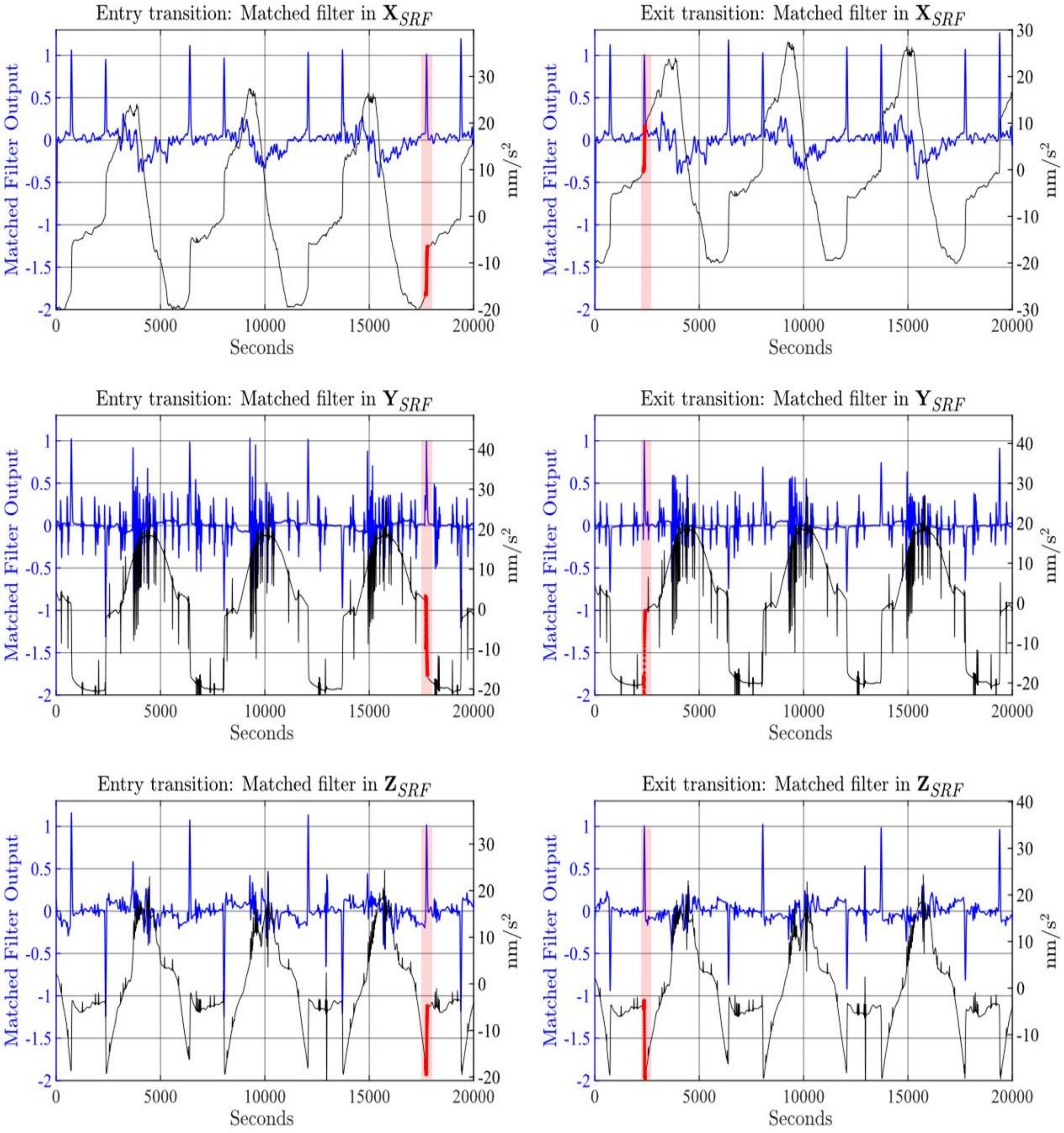
Entry transition: Matched filter in $\mathbf{X}_{SRF}$

Exit transition: Matched filter in $\mathbf{X}_{SRF}$

Entry transition: Matched filter in $\mathbf{Y}_{SRF}$

Exit transition: Matched filter in $\mathbf{Y}_{SRF}$

Entry transition: Matched filter in $\mathbf{Z}_{SRF}$

Exit transition: Matched filter in $\mathbf{Z}_{SRF}$

Figure 4.4 GRACE C (January 1, 2020) Left: Scale Factors of the penumbra transitions in the three axes of the accelerometer obtained from one entry transition waveform (red). Right: The same analysis when an exit transition is selected as the calibration waveform. The ACC measurements along the three axes are shown in black and the normalized filtered measurements (matched filter output) in blue.

Through a series of comprehensive tests, we verify that our methodology consistently yields scale factor estimates of unity for both types of transitions, when they are aligned with their corresponding transitions in the ACC signal. Notably, our approach also excels in effectively distinguishing the disparate magnitudes of the entry and exit transitions, a task that presents significant challenges in SRP modeling (Robertson, 2015).

In Fig. 4.5, we show the relative scales as retrieved from the method explained above, in the X_{SRF}. The X_{SRF} has been selected for this example because both the entry and exit transitions increase monotonously, therefore we expect the output of the matched filter to be positive (similarly to the top two figures on Fig. 4.4). We select the first entry transition of January 1, 2020, that occurs at $t = 723s$. After the removal of the mean, energy normalization, and time reversal, we convolve it with one year of accelerometer measurements. As expected, in the selected transition, the output of the matched filter was exactly one, while in the following penumbra transitions, the output of the matched filter changed significantly with respect to the β' angle variation. When the satellite reached $\beta' = 0°$, the amplitude of the penumbra was two times larger than the amplitude for $|\beta'| = 70°$. This figure aims to demonstrate the advantage of the matched filter in determining the relative differences and amplitude changes during penumbra transitions. These insights can be utilized in the modeling of Solar Radiation Pressure (SRP) to minimize the mismodeling of penumbra transitions.

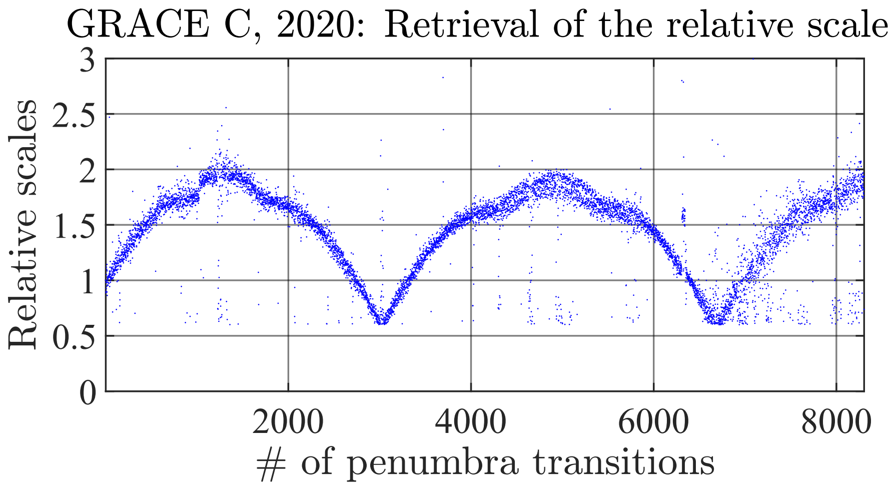

Figure 4.5 GRACE C: Scale factors that show the changing relative amplitude of the penumbra transitions with respect to the entry transition of January 1, 2020, chosen for this self-calibration (self-test). The relative scale starts from 1 (self-calibration).

4.2.2 Detection of Calibration Waveform in POD Total Accelerations

Before we introduce the energy normalization factor k and the accelerometer scale factor retrieval, given the substantial variance (power) in the PSDs between the two datasets, our priority is to verify the detection of penumbra transitions within the POD accelerations, even when their magnitude is significantly smaller compared to the total acceleration levels present in the POD. In this approach, due to the substantial difference in power between the two signals (as is shown in Fig. 4.6 and Fig. 4.7), the output of the matched filter serves solely for detection purposes rather than for the retrieval of the scale factor.

In Figures 4.6 and 4.7, we present one and one-half orbital revolution of GRACE A and GRACE C respectively, illustrating the total accelerations obtained from the kinematic orbits of TU Graz (green line), alongside the non-gravitational accelerations from the ACC1B of GRACE A or ACT1B dataset (black line) of GRACE C. From their power spectral densities (PSDs), it becomes evident that the accelerometer measurements are approximately $-120dB$ in comparison to the total accelerations of the satellite.

So, the question is: Can the penumbra transition be detected in a signal that is six orders of magnitude larger? The answer is yes. The key to this detection scheme, in contrast to the other matched filter methods utilized in radar systems, is that we know the exact shape and the precise time of occurrence of the penumbra transition pulse that is hidden within the POD accelerations. The detection analysis can be carried out either via convolution in time domain or via spectral multiplication in the frequency domain. In this contribution we choose the frequency domain filtering due to the easier and more efficient calculations, using the discrete direct and inverse Fourier transforms. It is important to note that to implement the matched filter in either domain, due to the significant difference in the powers of the two signals and to avoid edge effects, ensuring proper alignment, the calibration waveform should be zero-padded to match the length of the POD accelerations. The following tests are implemented on all three satellites, GRACE A, B, and C.

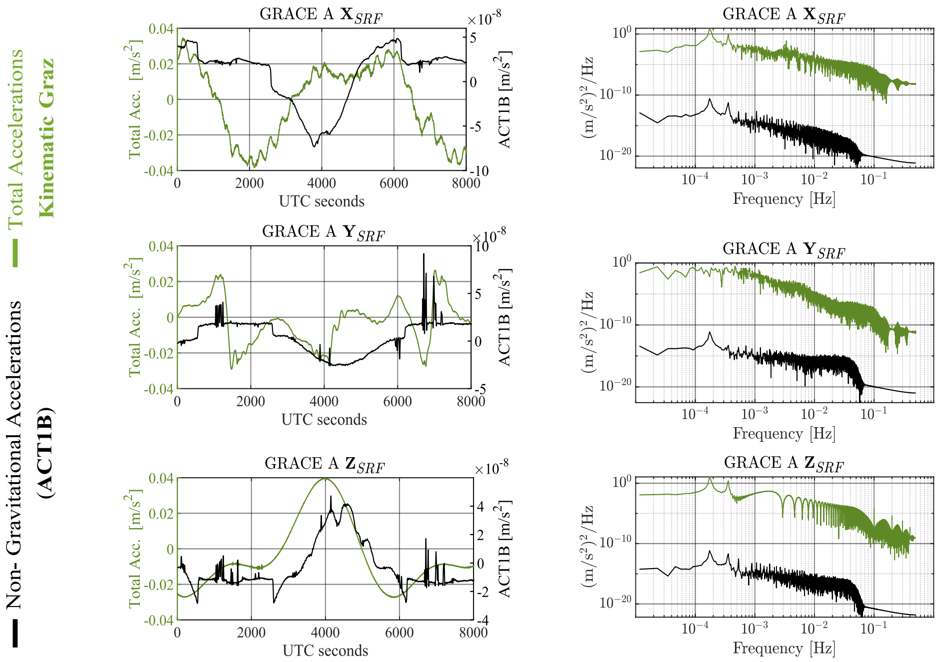

Figure 4.6 GRACE A, February 1st, 2006**.** Left: The total accelerations derived by the double numerical differentiation of TU Graz positions (green) and the non-gravitational accelerations from ACC1B dataset (black). Both time series refer to SRF. Both time series are w.r.t. zero mean. Right: The PSDs of the two time series along the three axes of the SRF.

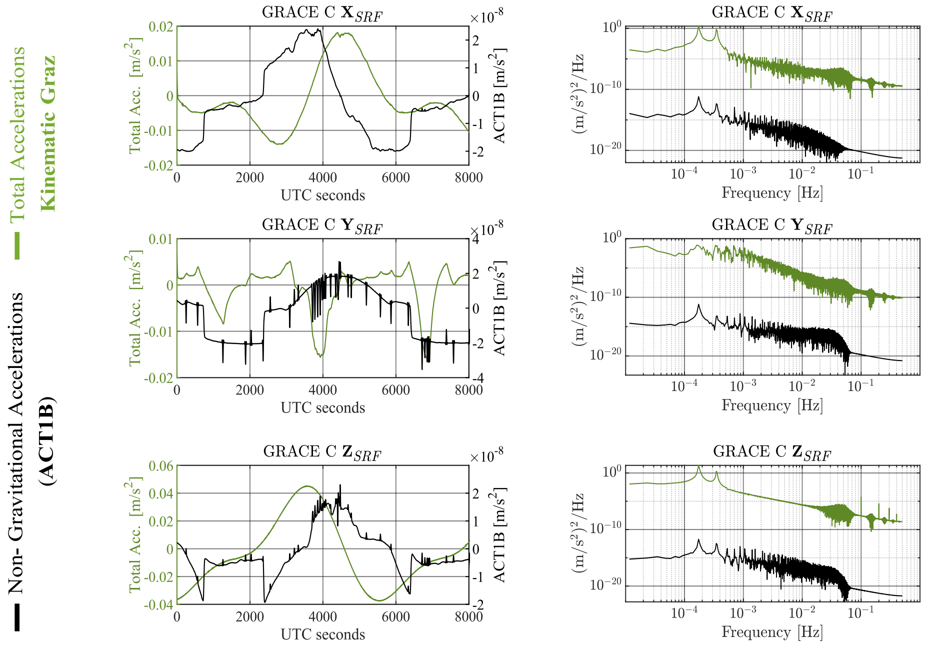

Figure 4.7 GRACE C, January 1st, 2020**.** Left: The total accelerations derived by the double numerical differentiation of TU Graz positions (green) and the non-gravitational accelerations from ACC1B dataset (black). Both time series refer to SRF. Both time series are w.r.t. zero mean. Right: The PSDs of the two time series along the three axes of the SRF.

However, since the results from all three satellites are similar, only the results for GRACE C are presented here.

- 1^{st} Detection test

In the first test, we select the second penumbra transition of January 1st, 2020, starting at $t = 2323$ UTC seconds. The selected POD-derived total accelerations from the kinematic positions provided by TU Graz spans the interval December 31st, 2019, to January 3rd, 2020. The steps followed are:

a) Removal of the mean from both time series (penumbra transition and the POD series).

b) Zero-padding of the penumbra transition (calibration waveform) so that the two time series have the same length.

c) Time-reversal of the calibration waveform.

d) Fast Fourier Transform (FFT) of both time series.

e) Multiplication of the conjugate part of the FFT of the calibration waveform with the FFT of the selected POD time series. This step ensures that the multiplication operation performed in the frequency domain effectively corresponds to ‘cross-correlation’ in the time domain. Here ‘cross-correlation’ means the cross power spectral density between the two series and not cross-correlation function or coherency of the two series that is expected to be bounded in the interval $[-1,1]$.

f) Inverse Fourier Transform (IFFT) to derive the matched filter output in the time domain.

In Fig. 4.8, we show the zero-padded calibration waveform, the POD series over three days, and the matched filter output. The matched filter output displays a peak when the detection is achieved, as well as two additional false peaks, which are associated with spikes present in the POD series.

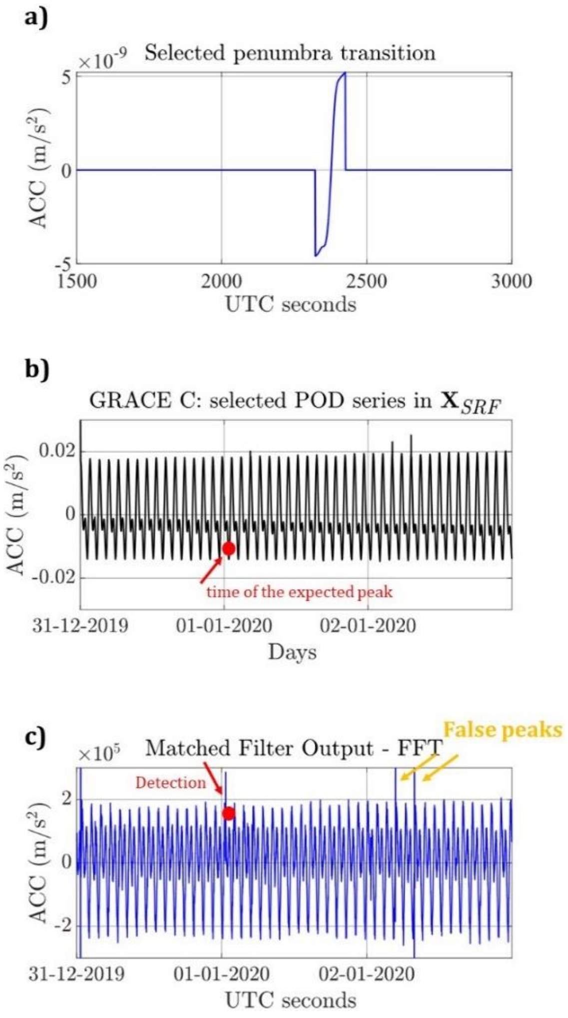

Figure 4.8 GRACE C: a) The zero-padded calibration waveform after the removal of the mean. b) The total accelerations derived from POD from December 31st, 2019, to January 3rd, 2020. The red arrow indicates the expected time of the penumbra transition, which is at t = 2323 seconds from 00:00 on January 1st, 2020. c) The output of the matched filter. The red arrow indicates the peak where the detection is achieved, and the yellow arrows indicate false peaks that coincide with two spikes existing in the POD time series.

- 2nd Detection test

In the second detection test, we use the same penumbra transition as in the first test but alter artificially the POD time series. Specifically, we randomly insert different days of the POD and segments of the POD series that contain the selected penumbra transition from January 1st, 2020. This random padding shifts the position of the penumbra transition relative to the beginning of the series, ensuring that detection using FFT can be performed accurately. We follow the same steps (a) through (f) as outlined in the previous test.

Figure 4.9 shows the same zero-padded calibration waveform, the randomly stacked POD time series (indicating with red arrows the times where the POD segments should contain the calibration waveform we are trying to detect), and the matched filter output. Again, in the matched filter output, we see peaks at the times where the calibration waveform was detected in our POD. The false peaks correspond to spikes existing in the POD due to random stacking of different days.

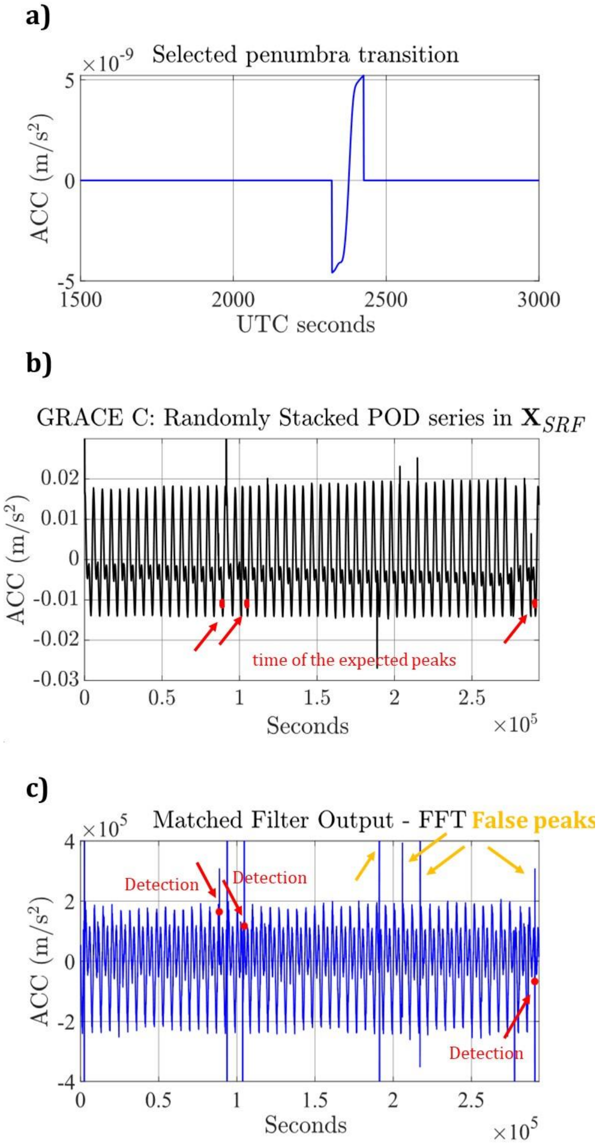

Figure 4.9 GRACE C: a) The zero-padded calibration waveform after the removal of the mean. b) Randomly stacked POD segments. The red arrows indicate the segments that theoretically contain the selected calibration waveform. c) Matched filter output. The red arrows indicate the successful detection of the selected waveform within the POD. The yellow arrows show the false peaks that were created due to the random stacking of the POD measurements.

- 3rd Detection test – All three axes of the accelerometer

Figure 4.10 shows the results of the matched filter output for all the three axes of the accelerometer using one calibration waveform (left column) and all the entry transitions (right column). The matched filter output (blue line) has a maximum or minimum value at the exact time of the selected calibration waveform, and it is confirmed both in time and frequency domains for the three axes of the accelerometer. In contrast to the self-calibration method, when we utilize one penumbra transition as the calibration waveform, the detection in the POD is limited to detecting only itself due to much higher power level of the POD-derived accelerations, noise and systematic signals. Therefore, we can infer that achieving detection in the POD is possible primarily because we know the timing and the characteristics of the signal we intend to detect. False peaks have been detected during the illuminated arc of the orbit in the X_{SRF} and the Y_{SRF}. These false peaks (local maxima or minima) suggest the presence of a signal in the total accelerations that closely resembles the calibration waveform of the penumbra transitions. Since we know the precise start time of the penumbra transitions, we disregard these false peaks.

To further validate the detection in the POD accelerations, an additional test was conducted involving data preprocessing, specifically incorporating the pre-whitening method (Gagne & Wagner, 1998; Tucco, 2001). Pre-whitening is widely used in signal detection since it reduces the impact of noise on the matched filter output by decorrelating the noise, improving the SNR and enhancing certain characteristics of the signal that are important for the detection. Since the results obtained from the pre-whitening succeed in the detection but differ in the amplitude of the matched filter output from the previously described approach, we opt to exclude them. We would like to emphasize that the pre-whitening method is exclusively used to enhance the detection of the calibration waveforms in the POD accelerations and is not applied during the calibration process in order to prevent any potential distortion of the signals during calibration.

Due to the substantial difference between the power of the POD accelerations and the accelerometer measurements, scale factor estimates can be obtained when the power levels of the calibration waveform and the 'scattered signal' are the same. This is done here by using the normalization factor k (Chapter 3; Eq. (3.7)) that removes the influence of varying power levels (Kammoun *et al.*, 2015; Sibbett *et al.*, 2018) of the two signals. This is particularly crucial since the SRP-induced penumbra transitions undergo variations from one orbit to the next. Consequently, the calibration must be performed only during the occurrence of the penumbra transitions by selecting all measured penumbra transitions as calibration waveforms, ensuring that each waveform aligns with its corresponding segment in the POD-derived accelerations. A comprehensive explanation of this process can be found in Section 4.3.

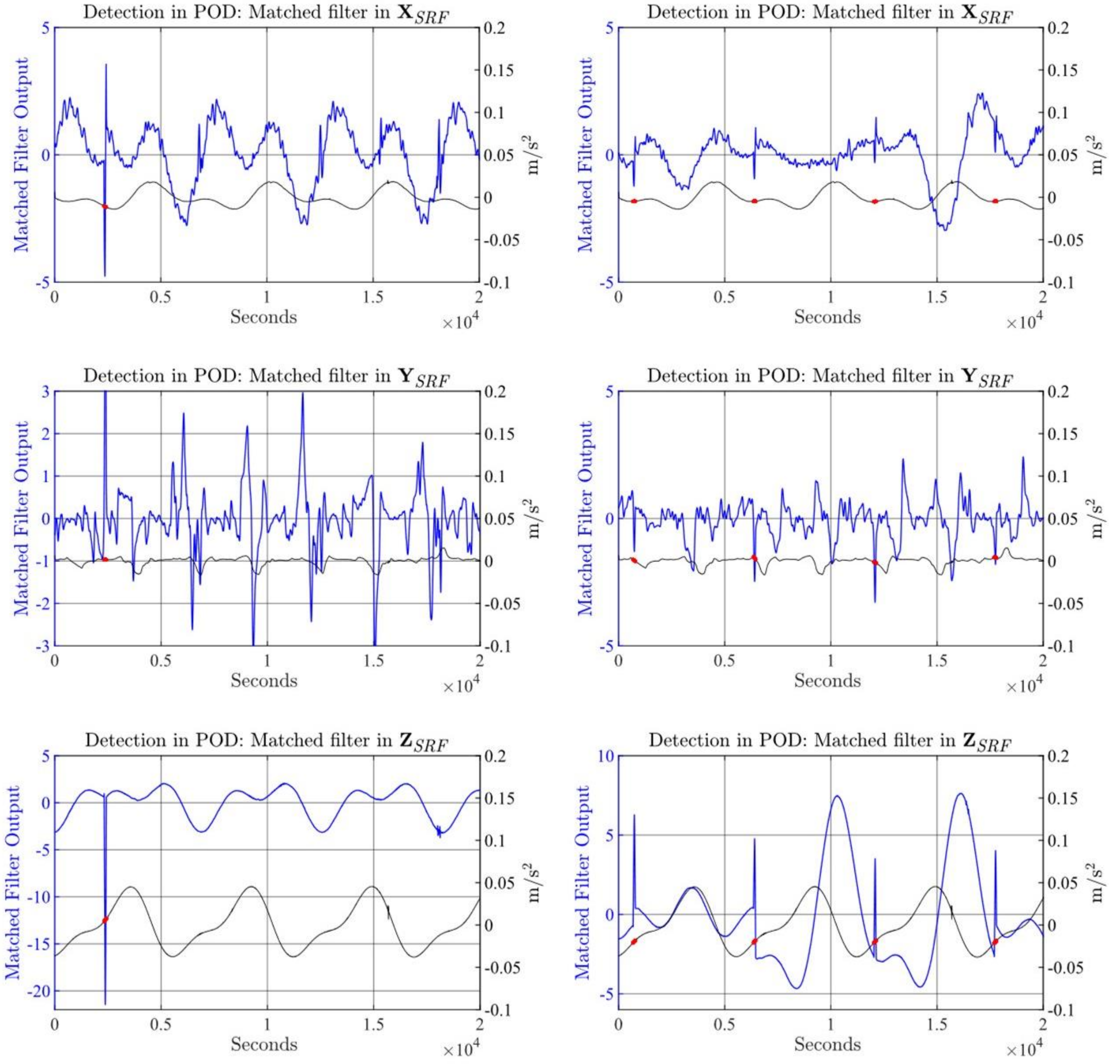

Figure 4.10 GRACE C (January 1, 2020): Left column: Detection of the penumbra transitions in the three axes of the POD total accelerations derived from the kinematic orbits when one exit transition is selected. Right column: Detection of the penumbra transitions in the three axes of the POD total accelerations derived from the kinematic orbits when all the entry transitions are selected as the calibration waveform. The POD accelerations are shown in black and their filtered values (output of the matched filter) in blue. The red lines indicate the times of the penumbra transitions, which match exactly the local maxima or minima of the matched filter output.

4.3 Full 3D Calibration

Since we showed that the penumbra transition detection can be achieved reliably, the proposed calibration approach is applied across the three different datasets detailed in Section 4.1. Therefore, to enhance readability and avoid redundancy, whenever we mention "POD-derived total accelerations", we imply that this method is being applied to the accelerations derived from both the kinematic positions (TU Graz) and the two reduced dynamic position datasets (GNV1B, TU Graz).

To ensure numerical stability in the calculation of the energy normalization factor k (Eq. (3.7)) and knowing that the maximum SNR occurs exclusively at the penumbra transitions, the matched filter is applied only within the time span where these transitions are present in the accelerometer measurements. This indicates that the calibration waveform and the POD-derived total accelerations have the same length with their initial and final points aligned with the starting and ending time of the penumbra transitions. The advantage of choosing strictly the penumbra transitions is that they contain primarily the SRP signal, with small variability of drag, and spurious accelerations which are present in other orbital arcs. The steps we follow for the retrieval of the scale factor, which is applied to GRACE A, B and C, as showing in the following sections, are the following (time domain convolution):

a) Since this method will work exclusively on the time of the penumbra transitions, both the penumbra transition signal and POD-derived total accelerations have the same length. So, we select one penumbra transition and the corresponding POD time series.
b) Removal of the mean in both series
c) Time reversal of the penumbra transition
d) Calculation the energy of both time series
e) Calculation of the energy normalization factor k
f) Multiplication of the POD time series by the reciprocal of the factor k, to ensure that the energy of the POD time series matched the energy of the penumbra transition signal
g) Convolution of the two signals
h) Division of the output of the matched filter with the energy of the selected penumbra transition and determination of the scale factor of the accelerometer.

When spurious accelerations or thruster activations are detected in the penumbra transitions from the accelerometer measurements (a common occurrence in the Y_{SRF} and Z_{SRF}), these solutions are rejected from our analysis. This is because the presence of such distortions would prevent the calibration waveform from exhibiting its characteristic pulse shape. To enforce this exclusion, we impose a constraint that the matched filter output should demonstrate a triangular shape. This principle is rooted in the theory of time reversal methods, wherein, when the two convolved signals are of equal length, the matched filter output assumes a triangular configuration with the highest output value occurring at the midpoint of the calibration pulse indicating successful detection.

The deviation of the output from a triangular shape is used as condition or constraint in our analysis in detecting weak solutions that introduce outlier scale factors. From visual analyses, it turns out that distorted triangular shapes provide scale factors $\mathrm{SF} < 0.85$[23] that are outliers compared to the neighboring values. Figure 4.11 shows a typical example of an accepted normalized matched filter output (blue triangle). The time duration of the penumbra transition selected for this example is $65s$. Figure 4.12 shows typical examples of rejected triangles, which usually arise from spikes in accelerometer measurements during the penumbra transitions or from the less defined shape of the selected penumbra transition.

---

[23] The accelerometer measurements provided in the ACT1B dataset are roughly scaled, so we expect the output of our calibration to be close to unity. Thus, the $\mathrm{SF} < 0.85$ is a reasonable lower limit of the scale factors we seek to determine.

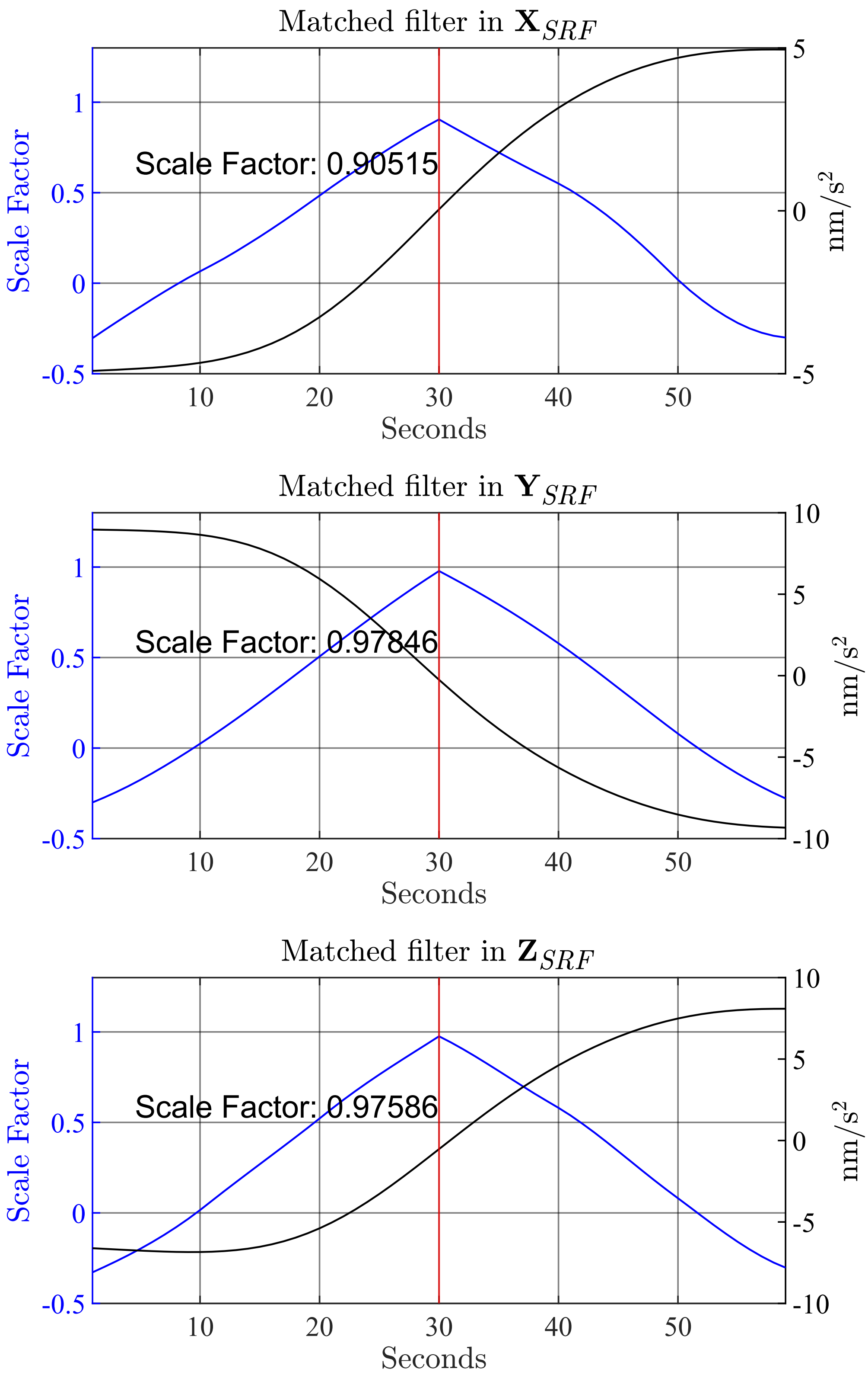

ACCEPTED TRIANGLES

Matched filter in $\mathbf{X}_{SRF}$

Matched filter in $\mathbf{Y}_{SRF}$

Matched filter in $\mathbf{Z}_{SRF}$

Figure 4.11 Example of a reliable scale factor (blue line) from random penumbra transitions along the three axes of the accelerometer. The accelerometer measurements (black line) show w.r.t. zero mean.

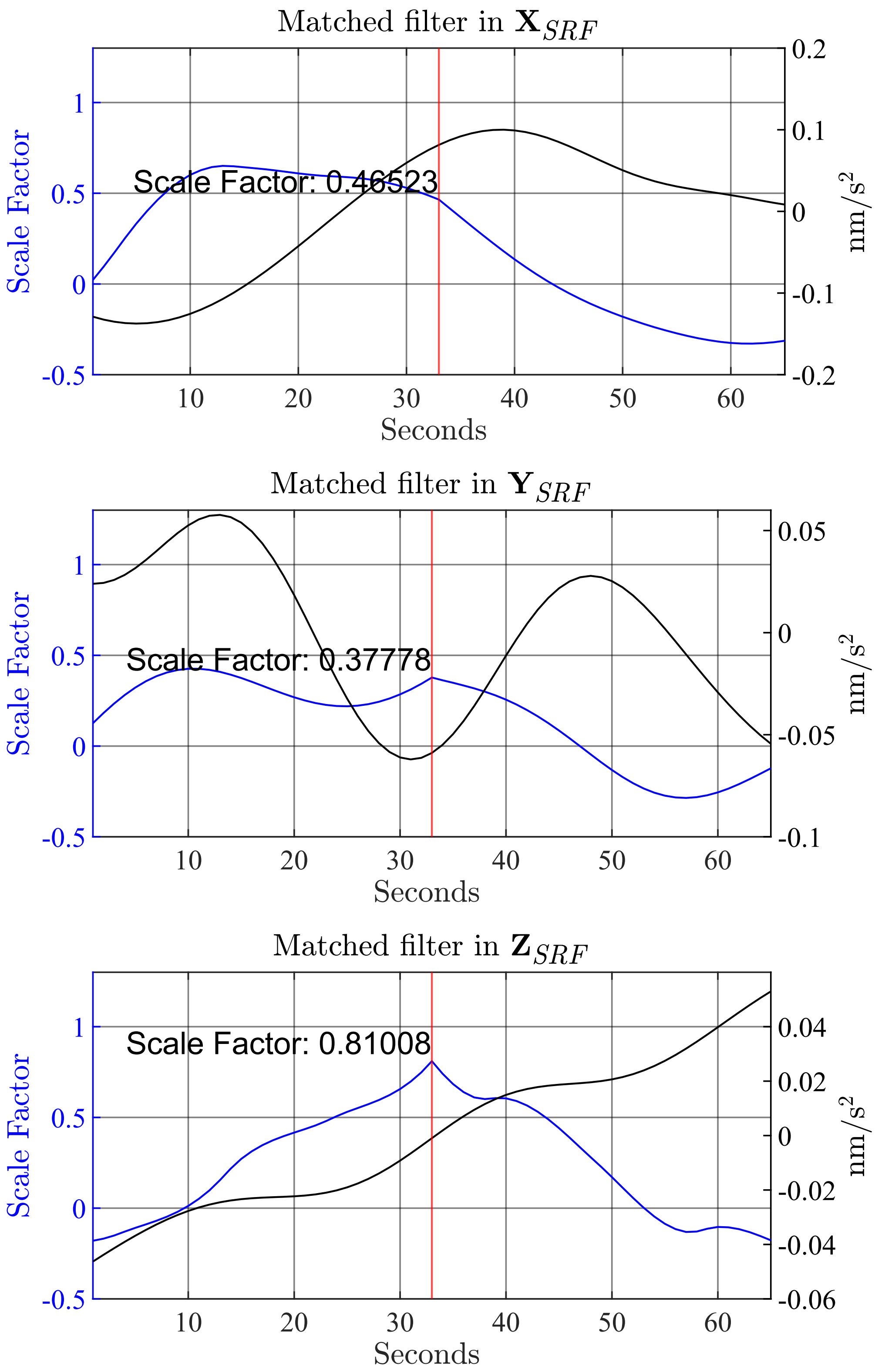

REJECTED TRIANGLES

Figure 4.12 Example of rejected scale factors (blue line) from random penumbra transitions along the three axes of the accelerometer. The accelerometer measurements (black line) show w.r.t. zero mean.

4.3.1 Calibration Parameters for GRACE Satellites

Following the same approach, we apply our methodology to retrieve 30 or 31 scale factors per day for all three axes of the accelerometer on GRACE A and B for the year 2006. After excluding the solutions that do not pass the triangular-shape criterion, we calculate daily means and their standard error. In Fig. 4.13, the number of the daily accepted triangles for each dataset is shown for GRACE A and GRACE B for the year 2006. Like in the previous and following figures, the results derived from kinematic positions are represented in green, those from reduced-dynamic GNV1B positions are shown in blue, and the ones from reduced-dynamic positions provided by TU Graz are depicted in red.

The results demonstrate consistent behavior for both GRACE A and GRACE B. Interestingly, in the X_{SRF} direction, the number of accepted daily triangles passing the test is similar across all three datasets. The highest count is observed when $0^\circ < \beta' < 67^\circ$ and the lowest count of accepted triangles occurs when $-67^\circ < \beta' < 0^\circ$. In the Y_{SRF} direction, the results from all three datasets exhibit similar trends, with the number of accepted triangles remaining relatively constant, typically ranging from 20 to 25 throughout the examined period.

When $\beta' = 0$, the cross-track direction remains unaffected by the satellite crossings into the Earth's shadow. Consequently, there are no penumbra transitions, and the calibration method cannot be applied in the Y_{SRF}. As β' transitions from negative to positive, the accelerometer measurements in the Y_{SRF} shift from positive to nearly zero, and then to negative, as depicted in Fig. 4.14. Regarding the Z_{SRF} direction, the two reduced dynamic datasets display notably robust results, with more than 26 accepted triangles per day. The kinematic dataset yields the fewest accepted triangles as $|\beta'|$ approaches 65°. This is attributed to the significant reduction in the magnitude of the penumbra transitions, ultimately reaching zero. Nevertheless, it is important to mention that, overall, the number of accepted triangles tends to exceed 20 per day despite the increased levels of noise in the total accelerations derived from the kinematic dataset.

1

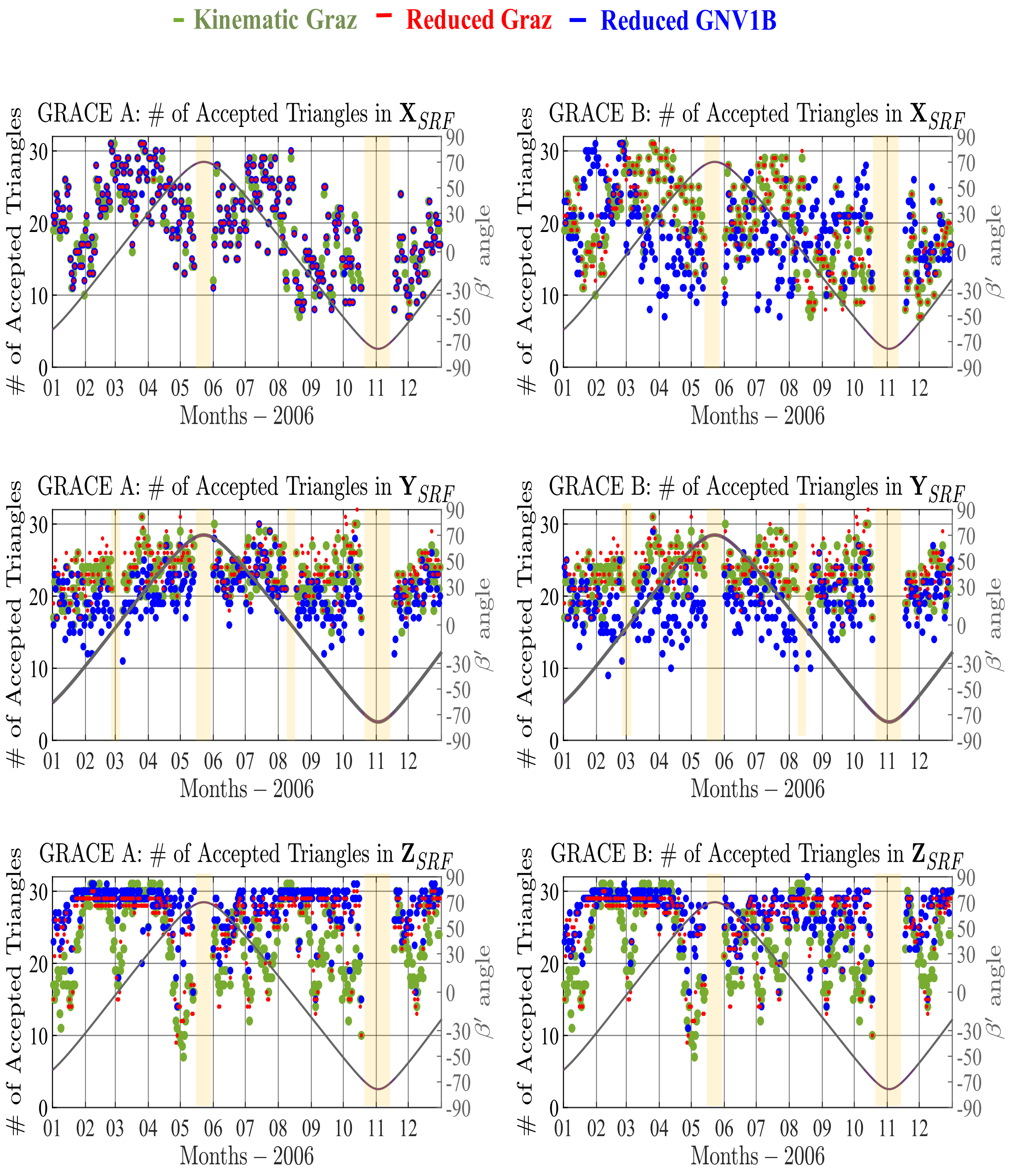

Figure 4.13 GRACE A and GRACE B (2006): The daily count of accepted triangles during the matched filter process for the three different datasets, alongside the variations of β' (black line). The light-yellow bands denote periods, where penumbra transitions are absent, and the proposed calibration method is not applicable.

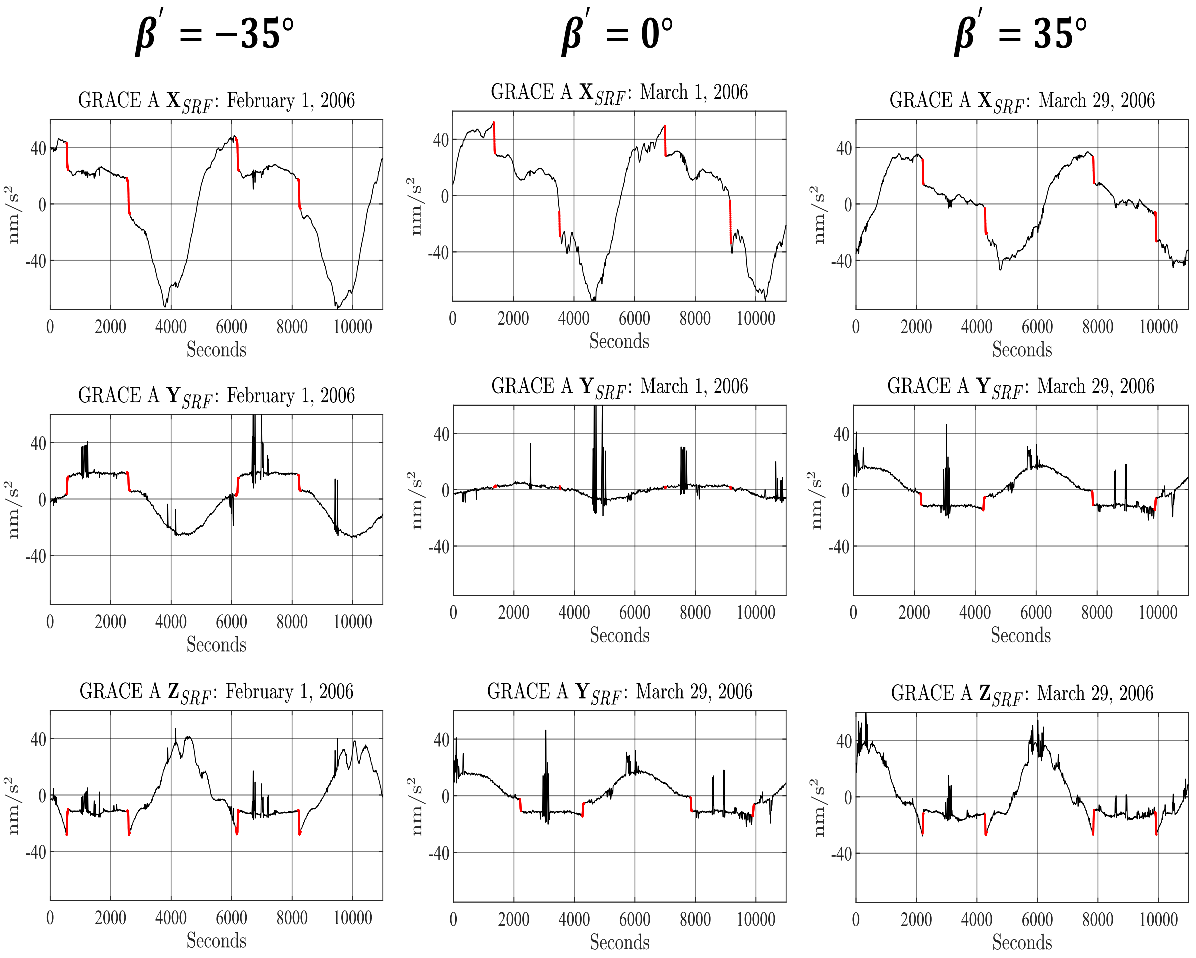

Figure 4.14 GRACE A: 2 orbital revolutions of the accelerometer measurements w.r.t zero mean along the three axes for various values of β'. The penumbra transitions are shown in red. In the Y_{SRF}, when β' is close to zero, the penumbra transitions are not observed (center figure). The accelerometer measurements are shown in nm/s^2, w.r.t. zero mean.

For the daily scale factors, we calculate the daily mean and their corresponding standard error. We reckon that the standard error of the mean provides a reliable representation of the accuracy of the calibration method, since it provides similar results to the error propagation during the convolution process. To calculate the errors of the retrieved scales, we assign initial variances to each value of the non-gravitational accelerations a_{ng} and total accelerations a_{POD} by computing the variance of the values within a moving window of 11 points (equivalent to 11 seconds in the time domain and approximately 77 km in the spatial domain). Since $\sigma_{\alpha_{ACC}}^2 \ll \sigma_{\alpha_{POD}}^2$, we focus only on the error of a_{POD}, which yields similar errors to the standard error of the mean through our specific scheme of double numerical differentiation. We suggest that the error analysis be revisited if different interpolation methods are applied in the estimation of the POD-derived accelerations, as this may impact the results.

We calculate daily scale factors for GRACE A and GRACE B for 2006 which was in the declining phase of Solar Cycle 23 that ended in December 2008. We select this period because during high solar activity the penumbra transitions do not appear as distinct jumps in the ACC measurements due to the increased drag which can reach a magnitude of $\sim 100\ nm/s^2$. Figure 4.15 shows the daily scale factors of GRACE A and GRACE B over the specified period. These scale factors are estimated for each of the three different datasets, along with the standard error. The standard error is calculated only for the scale factors derived from the kinematic orbits, as these scales are the only ones derived solely from actual measurements.

From a least-squares spectral analysis, the scale factors in X_{SRF} and Z_{SRF}, show insignificant dependency on the β' variations (percentage variance from the Least Squares spectrum is 10%), while in Y_{SRF} there is a periodicity of 322 days which could be attributed to β' variations of ~ 161 days (percentage variance from the Least Squares spectrum is 20%). The amplitude of this periodicity is 0.03 but from the PSD this periodicity appears not to be statistically significant. Since our method is based on the penumbra transitions, we cannot claim that this periodicity shows a direct relationship between the scale factor and β'variations. As the satellite approaches a full Sun orbit, which lasts for ~ 28 days, the penumbra transitions (calibration waveforms) progressively decrease in magnitude until they vanish. Consequently, the reduced magnitude of the calibration waveform of the matched filter intensifies the challenge of detection, leading to a decrease in detection accuracy. The scale factors derived from the three different POD datasets are almost identical in the X_{SRF}. In the Y_{SRF} and Z_{SRF} the scale factors derived from the reduced dynamic orbits of JPL (GNV1B dataset) differ from the scales derived from the reduced dynamic orbits of TU Graz although the difference in the total accelerations is less than$10^{-6}\ m/s^2$ (cf., Fig. 4.3).

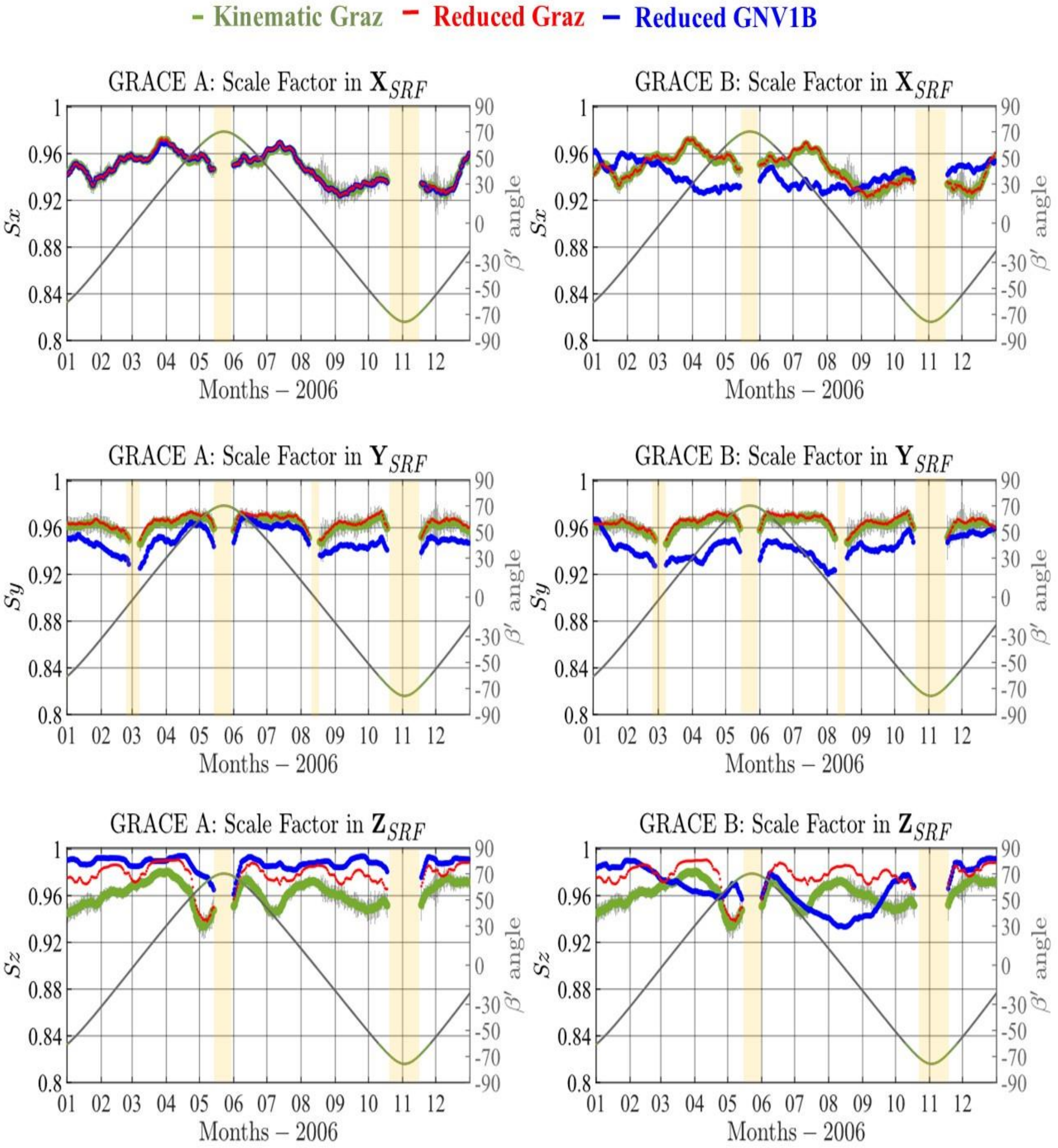

Figure 4.15 GRACE A and B (2006): The daily scale factors of the three axes of accelerometer, alongside β' variations (black line). Light-yellow bands emphasize the periods during which the scale factors cannot be obtained.

Since the penumbra transitions are selected manually for each day, there may be a slight deviation of $3-4$ seconds in the starting or ending points. After extracting the penumbra transitions from the measurements, to ensure the robustness of our results, we perform a sensitivity analysis by modifying their lengths by $\pm 20\ s$. Remarkably, our results demonstrate that the scale factors remain stable even when the selected penumbra transition duration exceeds the chosen value by up to 10 seconds. However, when it exceeds this threshold, our findings are impacted as the distinct shape of the pulse is distorted. Reducing the duration of the penumbra transition significantly also affects our results. This is because the matched filter cannot capture the entire penumbra transition pulse, leading to a reduction in signal clarity in the calibrated waveform.

For the matched filter to succeed, the calibration waveform must maintain a distinct pulse shape. To refine our analysis, we use a weighted least-squares regression, as described by Ghaderpour & Pagiatakis (2019; 2021), to parameterize the scale factor. This approach allows us to characterize the scale factor using the following formulation:

$$\boldsymbol{S_i}(t) = c_s + b_s t + a_s t^2, \qquad \text{where } i = x, y, z \tag{4.8}$$

Tables 4.1 to 4.3 display the calibration parameters of Eq. (4.8) as we vary the length, making it either shorter or longer for the three axes of the accelerometer of GRACE A. In this parameterization process, variable t is expressed in days, beginning from January 1, 2006. The standard deviations of the c_s reach up to 10^{-3} while b_s and a_s reach 10^{-6} and 10^{-9}, respectively. Hence, we can disregard them as they are negligible.

Table 4.1 GRACE A: Scale Factors for different lengths of penumbra transitions in the X_{SRF}.

Scale Factor parameter	Duration deviation from manual extraction (seconds)					
	-6	-4	-2	0	2	4
$\boldsymbol{c_s}$	0.9492	0.9500	0.9502	0.9501	0.9507	0.9510
$\boldsymbol{b_s}$	-7×10^{-5}	-6.8×10^{-5}	-6.1×10^{-5}	-5.8×10^{-5}	-5.2×10^{-5}	-4.7×10^{-5}
$\boldsymbol{a_s}$	4.3×10^{-7}	3.8×10^{-7}	3.5×10^{-7}	3.5×10^{-7}	3.4×10^{-7}	3.3×10^{-7}

Table 4.2 GRACE A: Scale Factors for different lengths of penumbra transitions in the Y_{SRF}.

Scale Factor parameter	Duration deviation from manual extraction (seconds)					
	-6	-4	-2	0	2	4
$\boldsymbol{c_s}$	0.9610	0.9594	0.9592	0.9587	0.9573	0.9564
$\boldsymbol{b_s}$	3.7×10^{-5}	3.5×10^{-5}	3.1×10^{-5}	2.7×10^{-5}	3.9×10^{-5}	4.1×10^{-5}
$\boldsymbol{a_s}$	1.3×10^{-7}	1.3×10^{-7}	1.3×10^{-7}	1.1×10^{-7}	1.4×10^{-7}	1.5×10^{-7}

Table 4.3 GRACE A: Scale Factors for different lengths of penumbra transitions in the Z_{SRF}.

Scale Factor parameter	**Duration deviation from manual extraction (seconds)**					
	-6	-4	-2	0	2	4
$\boldsymbol{c_s}$	0.9626	0.9632	0.9638	0.9640	0.9638	0.9644
$\boldsymbol{b_s}$	-4.6×10^{-5}	-4.8×10^{-5}	-5.1×10^{-5}	-5.7×10^{-5}	-5.5×10^{-5}	-6.3×10^{-5}
$\boldsymbol{a_s}$	1.0×10^{-7}	1.0×10^{-7}	1.0×10^{-7}	1.1×10^{-7}	1.1×10^{-7}	1.2×10^{-7}

Given the high consistency of the scale results, in Table 4.4, we present the scales derived from kinematic positions in the format of Eq. (4.8) for the year 2006, for GRACE A and GRACE B.

Table 4.4 GRACE A and B: Parameterized equations of the scale factors derived by kinematic approach. t is in days, starting from January 1st, 2006.

Satellite	**Scales**	**Parameterized Equation**
GRACE A	$\boldsymbol{S_X}$	$\boldsymbol{S_X}(t) = \mathbf{0.9528} + 6.6 \times 10^{-5} t - 3.3 \times 10^{-7} t^2$
	$\boldsymbol{S_Y}$	$\boldsymbol{S_Y}(t) = \mathbf{0.9559} + 9.1 \times 10^{-5} t - 2.7 \times 10^{-7} t^2$
	$\boldsymbol{S_Z}$	$\boldsymbol{S_Z}(t) = \mathbf{0.9689} - 6.1 \times 10^{-5} t + 8.9 \times 10^{-7} t^2$
GRACE B	$\boldsymbol{S_X}$	$\boldsymbol{S_X}(t) = \mathbf{0.9578} - 2.7 \times 10^{-4} t + 7.3 \times 10^{-7} t^2$
	$\boldsymbol{S_Y}$	$\boldsymbol{S_Y}(t) = \mathbf{0.9606} - 1.4 \times 10^{-4} t + 4.3 \times 10^{-7} t^2$
	$\boldsymbol{S_Z}$	$\boldsymbol{S_Z}(t) = \mathbf{0.9617} - 3.6 \times 10^{-4} t + 7 \times 10^{-7} t^2$

In Table 4.5, we present the constant values c_s which serve as scale factors. These values are derived from three distinct datasets, facilitating comparisons. This information is provided for both GRACE A and B, in addition to the values proposed by Bettadpur (2009).

Table 4.5 Scale factors for GRACE A and B, derived for 2006 based on the three different datasets. These values are presented alongside those suggested by Bettadpur (2009).

Satellite	**Scales**	Kinematic orbits (**TU Graz**)	Reduced-dynamic orbits **JPL** (GNV1B)	Reduced-dynamic orbits (**TU Graz**)	Bettadpur (2009)
GRACE A	$\boldsymbol{s_X}$	0.9528	0.9513	0.9516	0.9595
	$\boldsymbol{s_Y}$	0.9559	0.9426	0.9603	0.9797
	$\boldsymbol{s_Z}$	0.9689	0.9894	0.9807	0.9485
GRACE B	$\boldsymbol{s_X}$	0.9578	0.9574	0.9582	0.9465
	$\boldsymbol{s_Y}$	0.9606	0.9479	0.9614	0.9842
	$\boldsymbol{s_Z}$	0.9617	0.9967	0.9887	0.9303

As mentioned in Section 4.1, the calibration parameters using state-of-the-art methods are determined concurrently with the observations and other dynamic parameters. These calibration parameters are estimated alongside the spherical harmonic coefficients to attain the optimal gravity field solution. The suggested initial values for ACC bias parameters in the case of GRACE are computed within the POD process (Bettadpur, 2009). In our method, since we do not compute the calibration parameters during the gravity field determination process, it is not possible to obtain a bias estimation using the conventional approach found in the existing literature. Hence, we calculate the daily bias parameters independently from the scale factors. This is achieved through a daily quadratic fitting applied to the accelerometer data (ACC1B and ACT1B for GRACE and GRACE-FO, respectively). The bias is based only on the accelerometer measurements representing the variations of the measurements through the examined operational period for each mission. The accelerometer biases determined in this manner can serve as initial values or as weighted parameters in the gravity field determination process, when employing scale factors derived from kinematic positions. The bias terms are given as:

$$\boldsymbol{b}(t) = \boldsymbol{c}_0 + \boldsymbol{c}_1(t - t_0) + \boldsymbol{c}_2(t - t_0)^2, \tag{4.9}$$

where t in days, and t_0 is the reference epoch of January 1, 2006.

In Table 4.6, we show the mean values of the $\boldsymbol{c}_0$, $\boldsymbol{c}_1$ and $\boldsymbol{c}_2$ for GRACE A and B.

Spectral analysis of daily variations of the bias parameters shows notable strong periodicity of 161 days for GRACE A and GRACE B, in the Y_{SRF} and Z_{SRF}. However, we do not detect this same periodicity in the spectrum of X_{SRF}, probably due to the presence of larger drag-induced variations.

Table 4.6 Mean values of the daily estimates of $\boldsymbol{c}_0$, $\boldsymbol{c}_1$ and $\boldsymbol{c}_2$ bias parameters for GRACE A and B for 2006.

Satellite	**Bias**	c_0 $(\mu m/s^2)$	c_1 $(\mu m/s^2)$ /day	c_2 $(\mu m/s^2)$ / day^2
GRACE A	b_X	-1.1790	-4.95×10^{-4}	8.9×10^{-9}
	b_Y	29.447	4.47×10^{-4}	-6.5×10^{-10}
	b_Z	-0.5560	-1.56×10^{-3}	1.99×10^{-8}
GRACE B	b_X	-0.6479	-1.91×10^{-3}	2.37×10^{-8}
	b_Y	10.844	2.3×10^{-3}	-1.74×10^{-7}
	b_z	-0.7883	9.96×10^{-4}	-1.39×10^{-8}

4.3.2 Calibration Parameters of GRACE C

We follow the same approach for the scale factors of GRACE C, for the period 2019 to 2020. The values of the scale factors of GRACE C are closer to unity than GRACE A and B, which can be attributed to the improved insulation and higher sensitivity of the accelerometer compared to GRACE mission (Kornfeld *et al.*, 2019; Landerer *et al.*, 2020). In Table 4.7, we provide the parameterized equations for the scale factors obtained from the three different datasets.

In Fig. 4.16, we depict the number of accepted triangles utilized to calculate the scales along the three axes of the accelerometer using the three different datasets. Due to the better performance of the accelerometer measurements of GRACE C, the number of accepted triangles along the three axes is higher than that of GRACE A and B, especially in the X_{SRF}. In the Z_{SRF} the number of the accepted triangles in the kinematic approach consistently surpasses 15 throughout the examined period. However, it exhibits less consistency compared to the number of accepted triangles derived from the reduced-dynamic datasets, which remains generally higher than 27 throughout the same period. This discrepancy is expected, given that the total kinematic accelerations are derived from real measurements free from any force model.

Table 4.7 GRACE C: The parameterized equations of the scales with an initial $t_0 = 0$ corresponding to January 1, 2019, and t measured in days.

Scales	Dataset	Parameterized Equation
$\boldsymbol{S_X}$	Kinematic	$\boldsymbol{S_X}(t) = \mathbf{0.9856} - 6.5 \times 10^{-5}(t - t_0) + 6.1 \times 10^{-8}(t - t_0)^2$
	Reduced-dynamic (GNV1B)	$\boldsymbol{S_X}(t) = \mathbf{0.9862} - 1.3 \times 10^{-5}(t - t_0) + 3.7 \times 10^{-9}(t - t_0)^2$
	Reduced-dynamic (TU Graz)	$\boldsymbol{S_X}(t) = \mathbf{0.9861} - 1.3 \times 10^{-5}(t - t_0) + 3.6 \times 10^{-9}(t - t_0)^2$
$\boldsymbol{S_y}$	Kinematic	$\boldsymbol{S_Y}(t) = \mathbf{0.9596} - 1.5 \times 10^{-5}(t - t_0) + 1.1 \times 10^{-8}(t - t_0)^2$
	Reduced-dynamic (GNV1B)	$\boldsymbol{S_Y}(t) = \mathbf{0.9651} + 1.4 \times 10^{-5}(t - t_0) - 3.8 \times 10^{-8}(t - t_0)^2$
	Reduced-dynamic (TU Graz)	$\boldsymbol{S_Y}(t) = \mathbf{0.9655} + 1.5 \times 10^{-5}(t - t_0) - 3.8 \times 10^{-8}(t - t_0)^2$
$\boldsymbol{S_z}$	Kinematic	$\boldsymbol{S_Z}(t) = \mathbf{0.9555} + 2.7 \times 10^{-5}(t - t_0) - 4.3 \times 10^{-8}(t - t_0)^2$
	Reduced-dynamic (GNV1B)	$\boldsymbol{S_Z}(t) = \mathbf{0.9865} + 2.1 \times 10^{-5}(t - t_0) - 3.2 \times 10^{-8}(t - t_0)^2$
	Reduced-dynamic (TU Graz)	$\boldsymbol{S_Z}(t) = \mathbf{0.9691} + 1.3 \times 10^{-5}(t - t_0) - 2.4 \times 10^{-8}(t - t_0)^2$

In all three axes, a semi-annual period of 182.4 days is observed. The scale factors in the X_{SRF} and Y_{SRF} exhibit a periodicity similar to β' periodicity with an amplitude of 0.015. However, in the Z_{SRF} the amplitude is 0.025. This periodicity, akin to GRACE results, does not imply a dependence of the scale factors on β'. Rather, it is attributed to the decrease in the magnitude of the penumbra transitions as the satellite approaches its full Sun orbit. The difference in the scales derived from the two reduced-dynamic datasets can be attributed to their difference in the total accelerations, which follow a modulated signal pattern (as described in Section 4.1.2). This observation further supports our statement that the matched filter, as a calibration method, can detect change even when the difference between datasets falls below -50dB. The standard error of the mean in the Z_{SRF} is the highest of all three axes and can reach ± 0.02, while the standard error in the other two axes can reach ± 0.006. Similar to the analysis conducted for GRACE A and B, we use weighted least-squares regression to present the scale factors in the form of Eq. (4.8) with an initial $t_0 = 0$

corresponding to January 1, 2019, and t measured in days. Here, it is important to highlight that the parameterized equations were derived after removing the semi-annual periodicity.

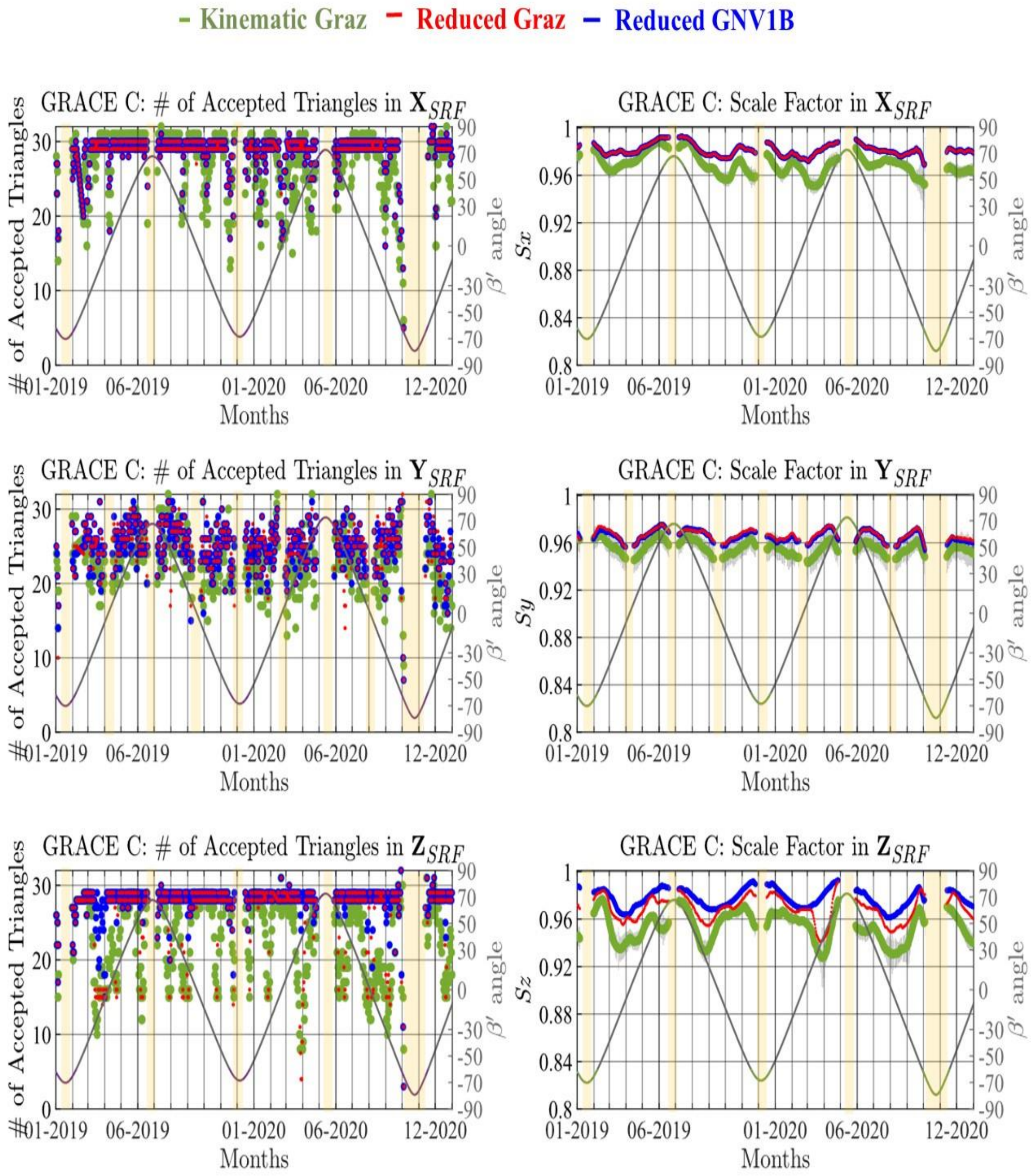

Figure 4.16 Left: Number of accepted triangles used for scale calculations from three different datasets, along with β' variations from January 1, 2019, to January 1, 2021, for GRACE C. Right: Scales derived along the three axes of the accelerometer using the three different datasets. Light yellow bands highlight periods during which the penumbra transitions are absent. Scales cannot be calculated in the colored bands. Different dot sizes and linewidths are used for the purpose of visualization.

The biases of GRACE C for the year 2019-2020 are calculated using the same approach as applied to GRACE A and B: through a daily quadratic fitting to accelerometer measurements. The mean bias terms, namely $\boldsymbol{c}_0$, $\boldsymbol{c}_1$ and $\boldsymbol{c}_2$, are presented in Table 4.8. Once again, these biases can serve as initial or weighted parameters when integrated with the scales during the gravity field determination process.

Table 4.8 Mean values of the daily estimates of $\boldsymbol{c}_0$, $\boldsymbol{c}_1$ and $\boldsymbol{c}_2$ for GRACE C from January 1st, 2019, to December 31st, 2020.

Bias	$\boldsymbol{c_0}$ $\boldsymbol{(nm/s^2)}$	$\boldsymbol{c_1}$ $\boldsymbol{(nm/s^2)}$ **/day**	$\boldsymbol{c_2}$ $\boldsymbol{(nm/s^2)}$ **/** $\boldsymbol{day^2}$
$\boldsymbol{b_X}$	297.156	0.0704	-3.1×10^{-6}
$\boldsymbol{b_Y}$	-11397.8	-0.0815	6.2×10^{-6}
$\boldsymbol{b_Z}$	162.369	0.5320	6.3×10^{-6}

4.4 Comparison with Other Studies

We compare our monthly solutions, obtained by averaging daily values, for GRACE A with the monthly scale factors supplied by Leibniz Universität Hannover (Flury, 2023) and the Center of Applied Space Technology and Microgravity (ZARM), Universität Bremen for the calendar year 2006. These monthly scale factors are generated as part of the gravity field determination process. For more detailed information regarding the estimation of these scale factors from Leibniz Universität Hannover and Universität Bremen, we recommend consulting the works of Koch *et al.* (2019, 2021), Wöske (2021) and Rievers & Wöske (2022). Figure 4.17 shows our monthly scale factors derived from the three distinct datasets, alongside those from the University of Hannover and the University of Bremen. Our monthly averages obtained from the kinematic dataset exhibit a standard error ranging between ±0.001 and ±0.005 for GRACE A. None of the monthly scales display any dependence on β' during this period. It is important to note that all solutions refer to the year 2006, prior to the thermal control switch-off on GRACE A in 2011.

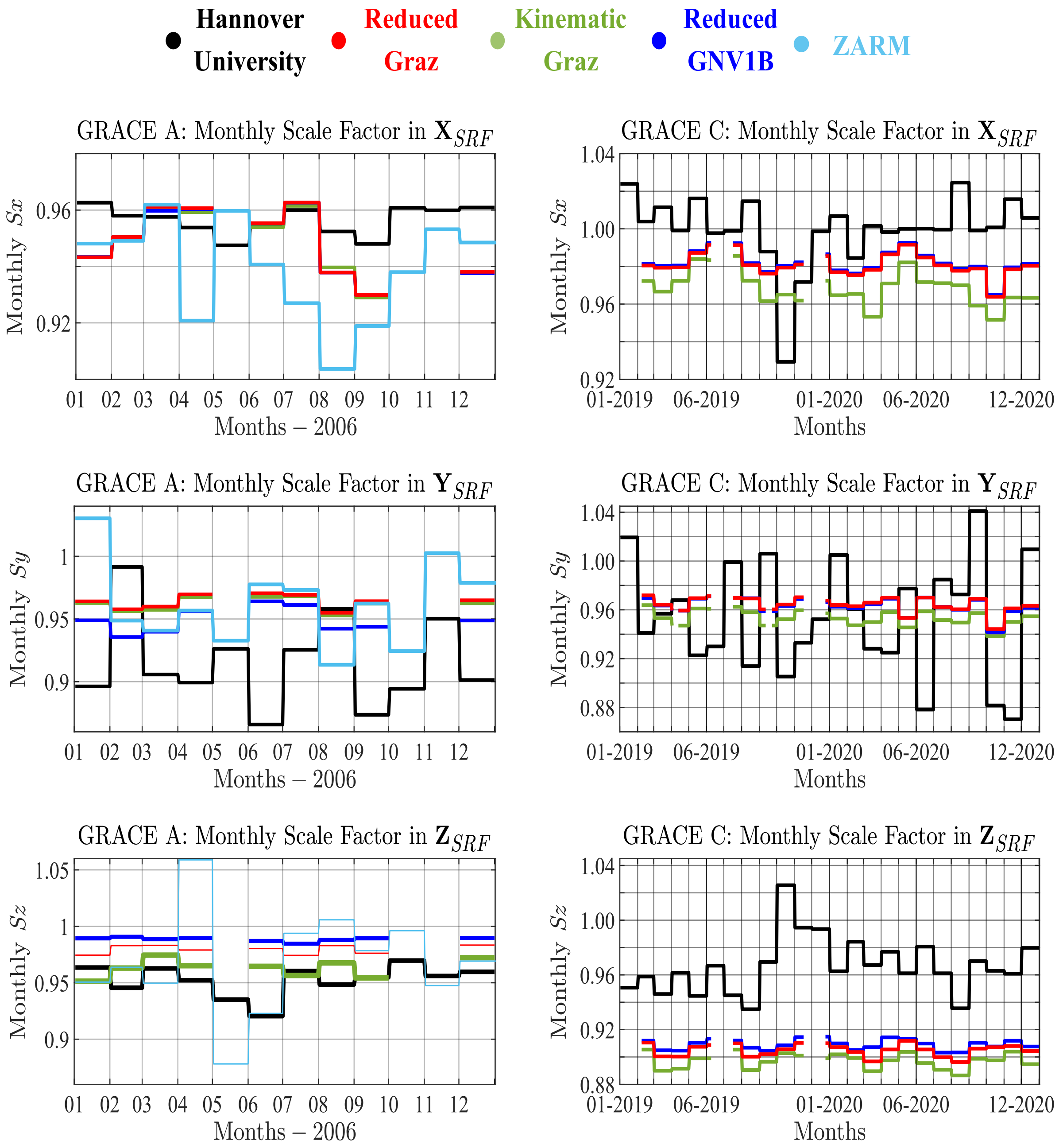

Figure 4.17 Monthly scales estimated by the matched filter method for the three datasets (green, red, blue), Leibniz Universität Hannover (black) and by Universität Bremen (light blue) for the three axes of accelerometer for GRACE A (left panels) and GRACE C (right panels).

Upon comparison, all datasets demonstrate remarkable similarity in X_{SRF} with ZARM's scale factors showing the highest deviation of 0.04. In the Y_{SRF}, our results closely align with ZARM's monthly scales with scale factors provided by the Leibniz Universität Hannover showing the highest deviation of 0.09. Meanwhile, in the Z_{SRF} the scales obtained from the kinematic orbits show the closest agreement with those from Hannover University.

For GRACE C, our monthly scale factors derived from the kinematic orbits, with standard error between ± 0.001 and ± 0.003 are compared with the scale factors derived by Leibniz Universität Hannover between 2019 and 2020. Similar to our previous findings, there is no dependency on β' in the monthly solutions, with the X_{SRF} scales showing better agreement. An interesting observation is that in Z_{SRF}, our solutions remain nearly stable throughout the two-year period, while the Leibniz Universität Hannover scales deviate by up to 0.14.

4.5 Discussion

In this chapter, we presented an innovative time-reversal filtering approach for calibrating the accelerometer measurements of GRACE A, GRACE B, and GRACE C. This method relies solely on accelerometer measurements and kinematic POD-derived total accelerations. We used the kinematic orbits from TU Graz as our 'absolute' standard for calibration and compared them with two reduced-dynamic orbits from JPL (GNV1B) and TU Graz. The use of a kinematic orbit ensures that our calibration method is independent of force models, providing scale factors based on actual measurements. In contrast, scales derived from reduced-dynamic positions were used for validation and comparison. Biases along the three axes of the accelerometer were computed independently using weighted least squares quadratic regression. The $\boldsymbol{c_0}$ term demonstrates good agreement with the values proposed by Bettadpur (2009). However, differences in the $\boldsymbol{c_1}$ and $\boldsymbol{c_2}$ terms reach one to two orders of magnitude. These biases could serve as initial values or weighted parameters in the gravity field determination process.

We have demonstrated that the signal focusing method, widely used in radar applications for signal detection, is a reliable and robust method for the calibration of the accelerometers and in concert with standard instrument calibration methods. The calibration parameters derived in this study must be used as weighted parameters in the gravity field solution processes. The key advantage of this method lies in its independence of physical models enabling its easy application to any of the available accelerometer datasets.

5 Exploring Thermospheric Patterns Through Measurement Errors: A weighted Accelerometer Dataset of GRACE C

Satellite data serve as the foundation for understanding the Earth's complex structure and physical properties. However, achieving high measurement accuracy requires careful attention. This chapter introduces a new methodology designed to improve the reliability of satellite measurements and parameter estimation by assigning observational covariance matrices and propagating their effects to the estimated parameters. The method, which can be applied to any satellite measurements, is applied to the accelerometer measurements of GRACE C satellite and provides a new weighted accelerometer 1B dataset. The method begins by establishing initial variances through autocorrelation analysis. Subsequently, employing a low-pass Gaussian filter, which incorporates the covariance matrix of the measurements and its propagation through the Gaussian window to the values of 1B dataset. The analysis of the variances highlights disturbances associated with geomagnetic storms, satellite passages through Earth's shadow and crossings with the terminator (twilight zone)[24], showcasing monthly intensity fluctuations that peak during equinoxes.

This chapter is a modified version of an article submitted for publication to *Geophysical Research Letters* under the title "Exploring Thermospheric Disturbance Patterns Through Space-borne Accelerometer Measurement Errors: A Weighted Accelerometer 1B Dataset of GRACE C".

---

[24] Terminator or twilight zone divides the daylit side and the dark (night) side of a planetary body. The Earth terminator moves with an approximate speed of $463\ m/s$ at the equator (supersonic speed due to the spin of the Earth).

5.1 The Necessity of Weighted Accelerometer Measurements

Analyzing satellite measurements faces challenges such as errors, correlations, and uncertainties. As it is standard practice in estimation theory, a covariance matrix associated with any measurements is unequivocally needed for the characterization of the stochastic properties of the measurements. Defining a reliable a-priori covariance matrix for the measurements is challenging and in the case of the GRACE mission data, for example the 1A and1B datasets that are key in the determination of the gravity field parameters, have no covariance information. To bypass this deficiency, we introduce a straightforward method to create such covariance matrices directly from the measurements using their statistical characteristics. This method is adaptable to any satellite measurements that are in form of a time (or space) series. The method excels in outlier detection and in the reliable determination of low-frequency signals without undesirable modifications of the measurements, such as the removal of "bad" observations, spikes, various other flaws, and interpolations. We demonstrate its effectiveness using GRACE C accelerometer measurements, showcasing its potential for the treatment of any satellite time series through covariance matrix assignment and propagation to the model parameters. We select the accelerometer measurements from GRACE C satellite for its high sampling rate ($10Hz$) and its ability to measure the non-gravitational forces acting on the satellite.

In GRACE-FO, the accelerometers show substantial errors during the initiation and conclusion of roll thruster firings, which could be caused by aliasing during the digital conversion (Harvey *et al.*, 2022). Another challenge is the presence of large spikes – denoted as phantom outliers/spikes accelerations, which mostly occur when the satellite enters the Earth's shadow. Both types of "unrealistic" accelerations are removed during the conversion from Level 1A to level 1B and the gaps are filled using linear interpolation as required to obtain the gravity field solutions (Bandikova *et al.,* 2019). Peterseim *et al.* (2012) conducted a comprehensive examination of the systematic errors resulting from magnetic torquers and heaters in the ACC1A dataset of the GRACE mission. Murböck *et al.* (2023) advanced the separation of signal and noise in estimated gravity field parameters by integrating accelerometer data with the inter-satellite Microwave ranging Instrument (MWI). The authors suggested that in the future, a more sophisticated preprocessing approach for ACC1A and the modeling of the spikes should be followed. Eliminating spikes from the ACT1B dataset is impactful due to its role in the transplant method, in which accelerometer measurements from GRACE C are utilized to generate corresponding measurements for GRACE D. Consequently, various methodologies have been suggested to address the treatment of accelerometer measurements from GRACE C for the creation of alternative GRACE D datasets (Behzadpour *et al.*, 2021).

Assigning variances to the non-gravitational acceleration measurements is significant in thermospheric density modeling. To address the problem of excessive prediction discrepancies observed in the NRLMSISE-00 model when compared to density observations obtained from GNSS data (Callejón *et al.*, 2023), a weighted least squares estimation (WLSE) was introduced. The authors have disassembled the NRLMSISE-00 model into its primary constituents using principal component analysis and subsequently they fine-tuned each constituent through the WLSE calibration process.

Uncertainties associated with accelerometer measurements contribute to variations in thermospheric mass densities, contingent upon the methods employed for density extraction (Mehta *et al*., 2017). Kodikara *et al*. (2023) underscored the significance of comprehending these uncertainties because they are essential for investigating errors in neutral mass density estimation. Siemes *et al*. (2024) propagate measurement noise and errors from satellite sensor specifications, thermospheric models, and radiation flux data to quantify thermospheric neutral density uncertainty from accelerometer and GNSS tracking data. While accelerometer-derived thermospheric density uncertainties decrease with enhanced satellite geometry modeling, they also increase at higher altitudes due to radiation pressure errors. The authors acknowledge that the method accounts for known models and error sources, but caution that uncertainty may be underestimated due to unknown factors.

The need to determine a reliable a-priori covariance matrix for the accelerometer measurements becomes even more imperative when considering the estimation of the neutral wind vector component along the cross-track axis of the accelerometer. This importance arises because calculations of the cross-track wind component using the accelerometer measurements in the along-track axis, cannot effectively distinguish between the effects of neutral density and wind speed. Additionally, in the radial direction, the accuracy of the accelerometer measurements is insufficient for the calculation of neutral densities (Sutton *et al*., 2007). On GRACE satellites the cross-track acceleration measurements are subject to spurious spikes, which can significantly disrupt the accurate determination of the crosswind components, which are much more sensitive to errors in the models and measurements (Lu *et al*., 2014).

In early 1970s, Chimonas & Hines (1970) and Davis & da Rosa (1970) theorized that traveling ionospheric disturbances (TID) could be generated during a solar eclipse. Later, Beer (1973) predicted that the supersonic motion of the solar terminator may generate wave-like atmospheric disturbances throughout the Earth's upper atmosphere in form of acoustic gravity waves (AGWs). Crombie (1964) had already shown that the propagation of radio waves was substantially affected around the solar terminator. Somsikov & Troitskii, (1975) proved theoretically Beer's hypothesis and new vigorous research has been carried out on this subject ever since; more information can be found in Somsikov (2011). Closely related to this contribution, the LEO satellites transition abruptly through the solar terminator before and after their transition to the Earth's umbra and are expected to be disturbed by the AGWs. The observation of large-scale gravity waves in the thermosphere has been investigated using CHAMP and GRACE missions (Forbes *et al.,* 2008; Guo *et al*., 2015; Park *et al*., 2020)

Our motivation for this contribution goes beyond the mere determination of the Earth's variable gravity field that requires both the measurement of the total accelerations of the spacecraft via onboard GNSS tracking and the independent measurement of its non-gravitational accelerations by means of onboard 3D accelerometer. The uncertainties of the non-gravitational accelerations and the products thereof, albeit crucial, have not been estimated or accounted for previously. We look at this challenge from the perspective of these measurements forming a stochastic and non-stationary time series, focusing on their *second-order stationarity* expressed by the variance, which also defines the variable energy (quadratic norm of the measurements) or power (average quadratic norm) of the series short segments. Whereas the stochastic consideration of these measurements, expressed through their covariance matrix will enhance the accuracy of the gravity field models in the future, we show that the variances of the non-gravitational accelerations represent the level of energy or power of the complex phenomena occurring in the ionosphere/thermosphere and magnetosphere systems.

5.2 Accelerometer Measurements as Stochastic Series – Methodology

For GRACE-FO mission the ACC1A raw measurements, up to a scale factor defect, are provided along with the ACT1A and ACT1B datasets which represent the raw measurements corrected from phantom outliers or implausible accelerations occurring during thruster firings in 10Hz and 1Hz, respectively (Wu *et al.*, 2006). The ACT1B dataset provides the non-gravitational accelerations in the Science Reference Frame (SRF). In the SRF, X_{SRF} points toward the other satellite, Z_{SRF} is nadir-pointing, and Y_{SRF} completes a right-handed triad. The definition of the reference frames used in GRACE missions can be found in Chapter 2.

A new 1B dataset, namely the ACW1B for GRACE C is derived and proposed in this study that is estimated from ACC1A raw measurements that are treated as a stochastic process, possessing a covariance matrix derived from experimental autocovariance functions of short ACC1A segments. The ACC1A is filtered, and the covariance matrix is propagated through the convolution algorithm to the filtered values, thus forming the ACW1B as an uncorrelated random process. The down sampling from 10 Hz to 1 Hz is executed concurrently with the filtering process while all time corrections pertaining to Level 1A are applied to Level 1B.

All the results and relevant graphs presented in this study, refer to the SRF. A comprehensive analysis on the reference frames of GRACE-FO and the time corrections, can be found in Wen *et al.* (2019). The procedure followed in this study consists of the following sequential steps:

a. Data Availability: The ACC1A dataset ($1Hz$ sampling rate) is used as the primary data source because it provides the "raw" measurements in the Accelerometer Frame (AF).

b. Autocorrelation Analysis of the ACC1A measurements: The autocorrelation analysis is performed after eliminating the dominant periodicities (orbital period plus its three dominant harmonics) from the ACC1A. This analysis shows a substantial decrease in correlation (less than $|0.3|$) for time lag $\tau > 10$ $(1s)$. Thus, we set the variance of each point in the ACC1A dataset, equal to the calculated variance of a moving window of $n = 11$ points (1.1s), centered at the point under consideration. The removal of the dominant periodicities (frequencies $< 1\ mHz$) is applied only in this step to calculate the window length n and the initial variances of the ACC1A measurements, ensuring that the series can be treated as a random process by eliminating most systematic signals. In addition, the calculated variance of the 11 points is reliable because it corresponds to a short orbital segment of ~7.5 km (1.1s duration), which is 30-40 times shorter than the typical spatial resolution of GRACE (200-300km), thus all 11 points practically correspond to the same location.

c. Low-Pass Filtering (smoothing): A symmetrical Gaussian kernel is selected but any other filter (smoother) can be used as required. The bandwidth of the Gaussian impulse response (kernel) is calculated by $\sigma = f_s/2\pi f_c$, where f_s is the sampling frequency in Hz, and f_c is the selected cut-off frequency of 0.035 Hz (as in the estimation of the official ACT1B). The $6\sigma = 271$ points define the size of the symmetric Gaussian kernel, which is adjusted to $N = 301$ points to align the power spectral density (PSD) of the resulting ACW1B with the attenuation characteristics of the official ACT1B which is derived from a Butterworth filter of 0.14 delay (Wu *et al.*, 2006). For alternative accelerometer measurement analyses, such as those focusing on higher frequency signals, the kernel size can be adjusted accordingly. Let $\overline{\mathbf{G}}$ be the *N*-dimensional deterministic vector of the normalized Gaussian kernel and let $\boldsymbol{x}$ be the *N*-dimensional vector of the ACC1A accelerometer measurements within the Gaussian window. Matrix $\mathbf{P}_{\boldsymbol{x}} = \boldsymbol{\Sigma}_{\boldsymbol{x}}^{-\mathbf{1}}$ is the *N*-dimensional weight matrix of $\boldsymbol{x}$, equal to the inverse of its covariance matrix $\boldsymbol{\Sigma}$ (to be derived below). The filtered values are the weighted least-squares estimates given by (Vaníček and Krakiwsky, 1986)

$$\hat{x}_f = (\overline{\mathbf{G}}^{\mathrm{T}}\mathbf{P}_{\boldsymbol{x}}\overline{\mathbf{G}})^{-1}\overline{\mathbf{G}}^{\mathrm{T}}\mathbf{P}_{\boldsymbol{x}}\boldsymbol{x} \tag{5.1}$$

where superscript ‘T’ indicates matrix transposition. For different filters and different cutoff frequencies, the coefficient vector **G** must be modified accordingly.

d. Construction of correlation matrices of short ACC1A segments: As shown from step (b), the correlation matrix is set to $n \times n,\ n = 11$, to consider the correlation between the measurements for $\tau \leq 10\ (1s)$. The diagonal elements of the correlation matrix are $\rho_{ii} =$

$1, i = 1, \dots n$, while the non-diagonal elements $\rho_{ij}, i = 1, \dots n,\ j = 1, \dots n$ and $i \neq j$, comprise the correlations derived from the experimental ACF for $0 < \tau \leq 10$.

e. Construction of the $n \times n$ sub-covariance matrix of each segment of ACC1A: The diagonal elements include the initial variances $\sigma_i^2, i = 1, \dots n$ calculated from step (b) and the non-diagonal elements σ_{ij}, include the covariances calculated from the variances σ_i^2, and the correlations ρ_{ij} according to

$$\rho_{ij} = \frac{\sigma_{ij}}{\sigma_i \sigma_j}. \tag{5.2}$$

f. Generation of the full covariance matrix $\mathbf{\Sigma}$: The covariance information (from step (e)) is embedded into the diagonal covariance matrix $N \times N$ ($N = 301$), corresponding to the entire Gaussian kernel. The matrix is populated with the variances calculated in step (b) along the main diagonal and the fully populated $n \times n$ covariance matrix from step (e) is implanted at the center (shaded submatrix in Eq. (3)), incorporating the correlation information into the analysis. Centering the $n \times n$ covariance matrix means that the element $\sigma_{(n-1)/2+1} = \sigma_{(N-1)/2+1}$ (red shaded element in Eq. (3)), ensuring proper alignment. All other off-diagonal elements (non-shaded elements in Eq. (3)) are set to zero. It is noted that the shaded main diagonal elements comprise single variances and not sub-matrices. The resulting block-diagonal covariance matrix $\mathbf{\Sigma}_x$ is given by

$$\boldsymbol{\Sigma}_{\boldsymbol{x}} = \begin{bmatrix} \sigma_1^2 & 0 & \cdots & \cdots & \cdots & \cdots & \cdots & \cdots & 0 & 0 & 0 \\ 0 & \ddots & 0 & \cdots & \cdots & \cdots & \cdots & \cdots & \vdots & \vdots & \vdots \\ \vdots & 0 & \ddots & 0 & \cdots & \cdots & \cdots & \cdots & \vdots & \vdots & \vdots \\ \vdots & \vdots & 0 & \sigma_{146}^2 & \cdots & \sigma_{146,151} & \cdots & \sigma_{146,156} & \vdots & \vdots & \vdots \\ \vdots & \vdots & \vdots & \vdots & \ddots & \vdots & \vdots & \vdots & \vdots & \vdots & \vdots \\ \vdots & \vdots & \vdots & \sigma_{151,146} & \cdots & \sigma_{151}^2 & \cdots & \sigma_{151,156} & \vdots & \vdots & \vdots \\ \vdots & \vdots & \vdots & \vdots & \vdots & \vdots & \ddots & \vdots & \vdots & \vdots & \vdots \\ \vdots & \vdots & \vdots & \sigma_{156,146} & \cdots & \sigma_{156,151} & \cdots & \sigma_{156}^2 & 0 & \vdots & \vdots \\ \vdots & \vdots & \vdots & 0 & \cdots & \cdots & \cdots & 0 & \ddots & 0 & \vdots \\ \vdots & \vdots & \vdots & 0 & \cdots & \cdots & \cdots & \cdots & 0 & \ddots & 0 \\ 0 & 0 & 0 & \cdots & \cdots & \cdots & \cdots & \cdots & \cdots & 0 & \sigma_{301}^2 \end{bmatrix} \tag{5.3}$$

g. Calculation of the variances of the ACW1B (1Hz): The variance of a single filtered value is calculated by propagating the error covariance matrix of $\boldsymbol{x}$ through Eq. (2) thus,

$$\sigma_f^2 = \overline{\mathbf{G}}\boldsymbol{\Sigma}_x\overline{\mathbf{G}}^{\mathrm{T}} \tag{5.4}$$

The steps followed for the calculation of the variance at each point are shown in Fig. 5.1 for a clearer representation.

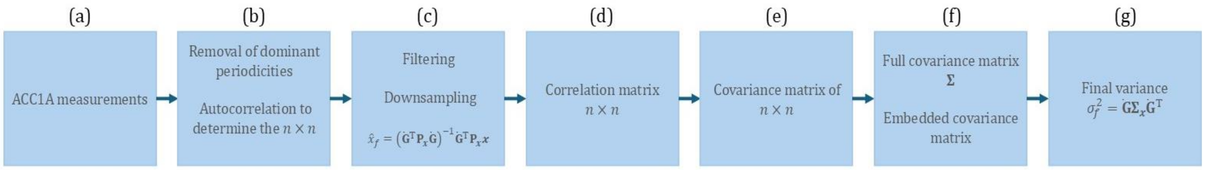

Figure 5.1 A flowchart outlining the steps to derive the ACW1B dataset, and the variances calculated at each point, with each step labelled by a corresponding letter that is explained above.

Figure 5.2 illustrates the ACT1B and the ACW1B with its corresponding standard deviations of 1σ and Fig. 5.3 displays their power spectral densities (PSDs). Figure 5.4 shows the differences between the two datasets and the PSDs of these differences along the three axes of the accelerometer. Considering that during the filtering process the initial variances have been taken into consideration, ACW1B dataset does not contain spurious spikes which are notably dominant in the Y_{SRF} and Z_{SRF} of the ACT1B dataset (Fig. 5.2; right panels; blue line). Many of these spikes present in the ACT1B dataset are due to thruster activations which are dominant in the Y_{SRF} and Z_{SRF} as one of the magnetic torquer rods aligns parallel to Earth's magnetic field lines, resulting in inadequate generated control torque (Bandikova *et al*., 2019).

In segments where the ACT1B dataset does not have spikes, the differences between the two datasets are consistently less than $3 \times 10^{-2}\ nm/s^2$ across all three axes. From the three PSDs of the differences (Fig. 5.4; right panels), it is also evident that the smallest difference between the two datasets is in the X_{SRF} ($\sigma^2 = 0.11\ nm^2/s^4$), followed by the Z_{SRF} ($\sigma^2 = 3.61\ nm^2/s^4$) and the Y_{SRF} ($\sigma^2 = 46.24\ nm^2/s^4$). In Figure 5.2 (right panels) the average variances of the ACW1B dataset along the three axes are: $\sigma_X^2 = 0.008\ (nm/s^2)^2$, $\sigma_y^2 = 0.001\ (nm/s^2)^2$ and $\sigma_z^2 = 0.01\ (nm/s^2)^2$. Since the Y_{SRF} is the least sensitive axis, its variance is the smallest, as expected. Interestingly, the variances of the Z_{SRF} are the highest and show orbital periodicity. Due to the elimination of the spikes during the filtering process, the standard deviation of the new ACW1B dataset is significantly smaller than the standard deviation of the ACT1B which is $\sigma_{ACT1B,x} = \sigma_{ACT1B,y} = \sigma_{ACT1B,z} = 1 nm/s^2$.

The proposed ACW1B dataset excludes thruster activations by accounting for the variances during filtering. This ensures that non-gravitational accelerations from drag, SRP, ERP, or TRP are included, while accelerations from thruster activations for attitude control, or other reasons, such as those caused by electric current changes, are eliminated. Consequently, this dataset is suitable for thermospheric density determination without the need to remove accelerations around thruster activation times, thereby minimizing unwanted residuals (Doornbos *et al*., 2010; Calabia & Jin, 2017; March *et al*. 2021). Figure 5.2 displays both the ACT1B and ACW1B datasets for GRACE C over the examined period (August 2018 to August 2020) along with the variations in $\beta^{'}$. While there is no notable difference between the two datasets in the X_{SRF}, it is evident from Figs. 5.6 and 5.7 that in the other two axes, the ACW1B dataset enhances the non gravitational acceleration signal by eliminating the spikes. The differences between the two datasets in the X_{SRF} do not exceed 4 nm/s^2, with the largest differences observed when $\beta^{'} = 0°$. The differences in both the Y_{SRF} and Z_{SRF} reach up to 20 nm/s^2 across the examined period, with the largest differences again occurring in the Z_{SRF} when $\beta^{'} = 0°$. In the Y_{SRF}, the disturbances are high and consistent throughout the examined period, due to dominant spurious spikes present in the ACT1B dataset. In the Y_{SRF} and Z_{SRF} (Figs. 5.6 and 5.7, respectively) significant disturbances of unknown origin are observed in the ACT1B dataset between November 2018 and February 2019. These disturbances are not present in the X_{SRF} but importantly, they are not present in our proposed ACW1B dataset.

Similar to the differences between the two datasets, the magnitude of the accelerations, changes w.r.t. $\beta^{'}$angle variability. As $|\beta^{'}| \rightarrow 70°$, the satellite enters in a full-sun orbit. Positive $\beta^{'}$ signifies that the satellite travels counterclockwise when observed from the Sun. As $\beta^{'} \rightarrow 0°$, the satellite orbital plane aligns with the Earth-Sun direction, and nearly half of its orbit is into the Earth's shadow. When this occurs, the accelerations in the X_{SRF} and Z_{SRF} reach their maximum amplitude, while the accelerations in the Y_{SRF} are nearly negligible.

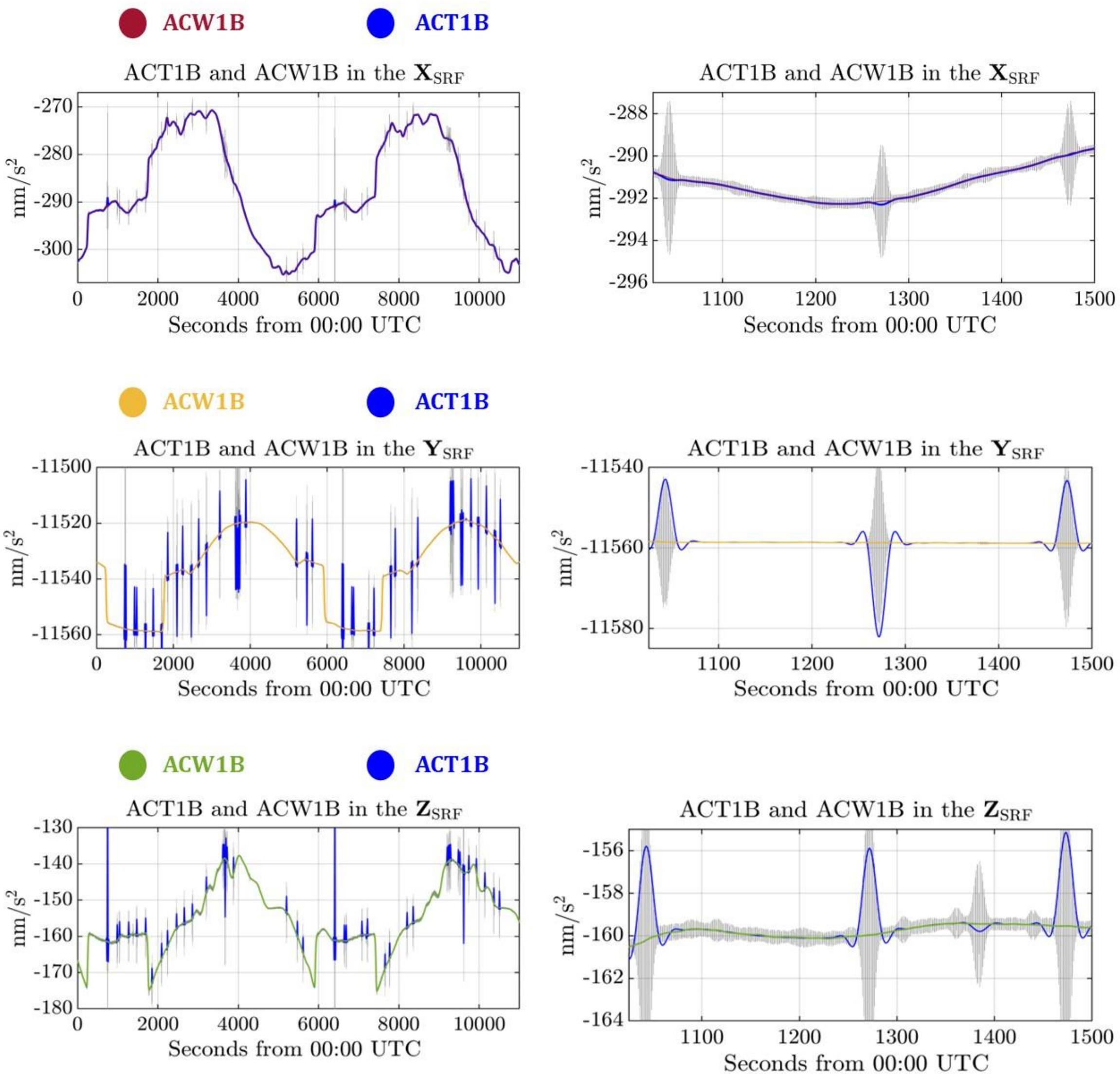

Figure 5.2 GRACE C, February 11, 2019. Each row of panels corresponds to each axis of the accelerometer. Left panels: Two orbital revolutions of ACT1B (in blue) and ACW1B (in red, yellow, and green) along the three axes of the accelerometer in the SRF. Right panels: A Closer Examination of the standard deviations in the ACW1B Dataset (grey areas represent 1σ).

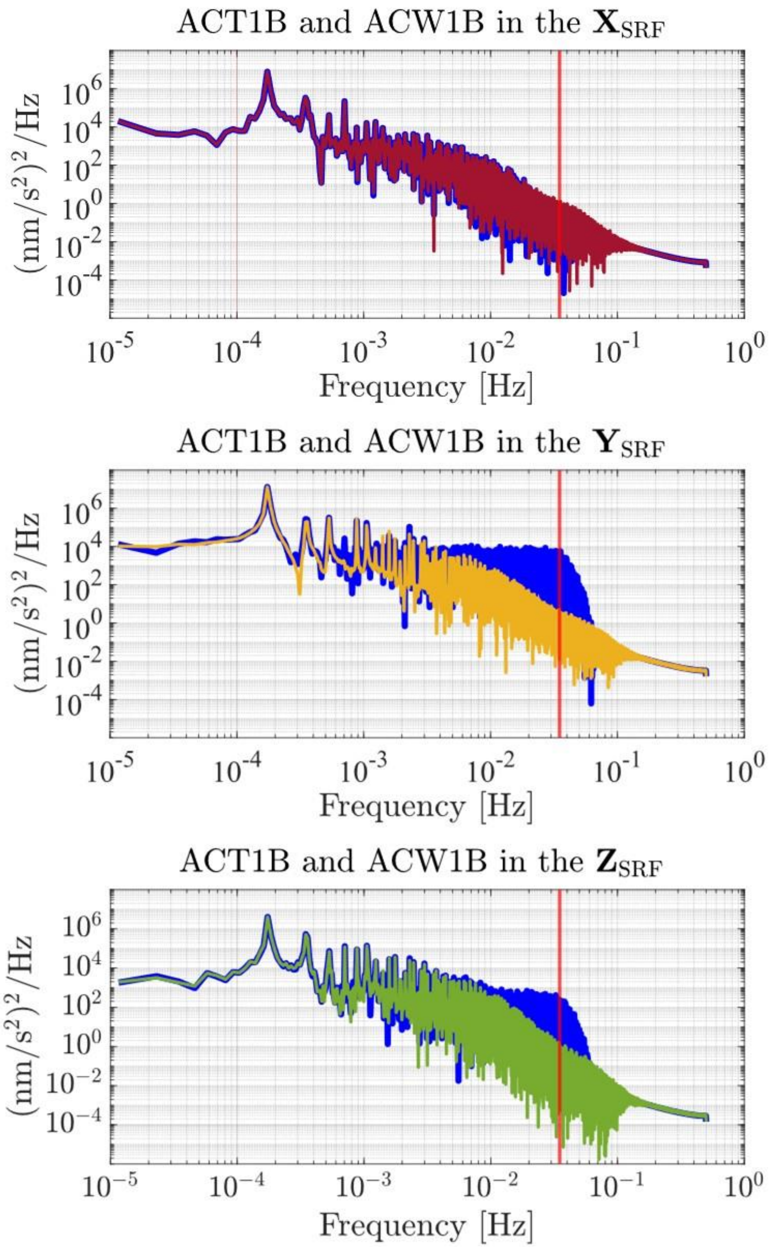

Figure 5.3 Power Spectral Densities (PSDs) of ACT1B alongside the weighted PSD of ACW1B dataset.

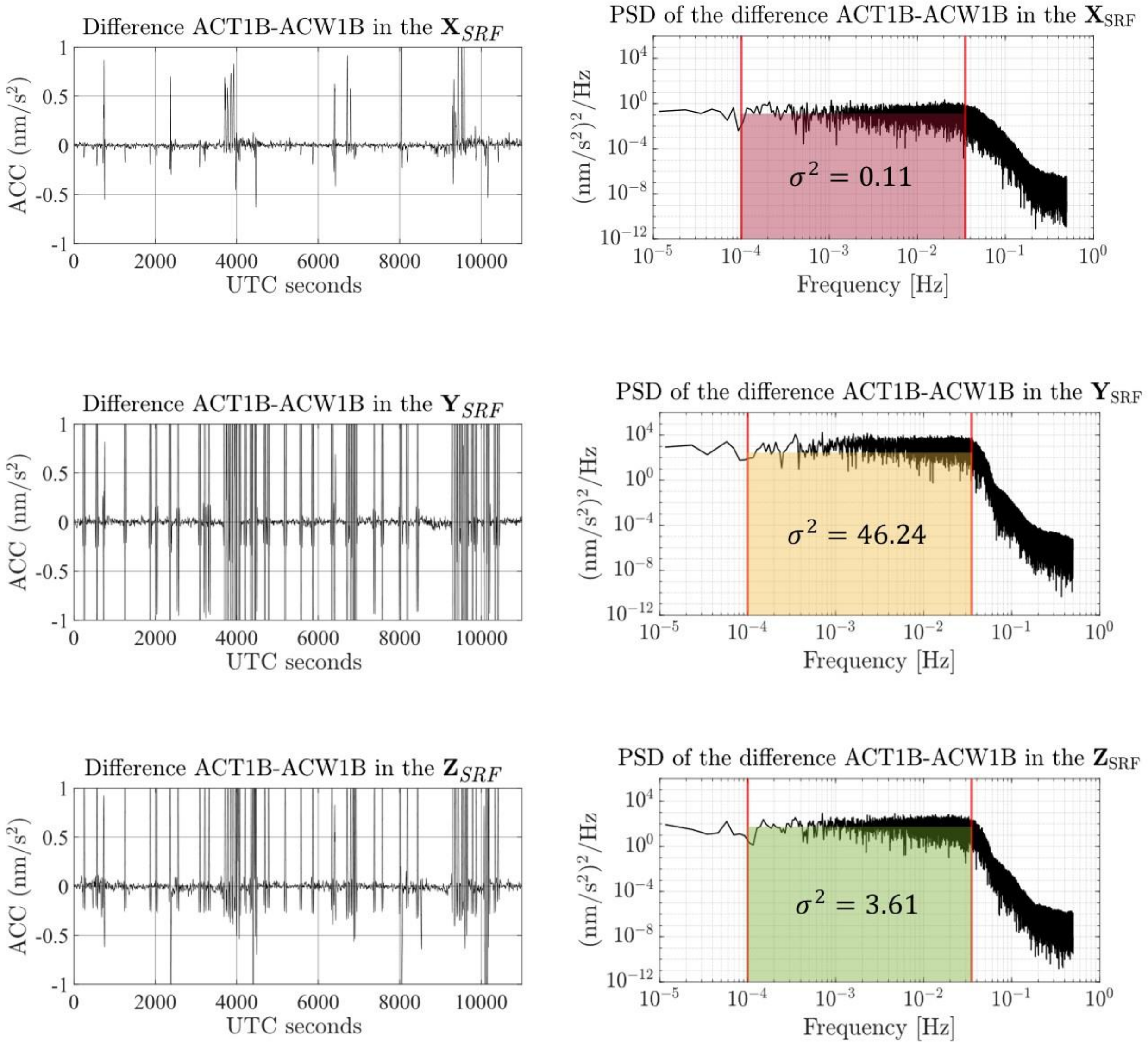

Figure 5.4 Left panels: The differences $(ACT1B - ACW1B)$. Right Panels: The PSD of the difference $(ACT1B - ACW1B)$ for all three axes. The variance calculated by the area of the three PSDs is shown in the colored boxes for each axis.

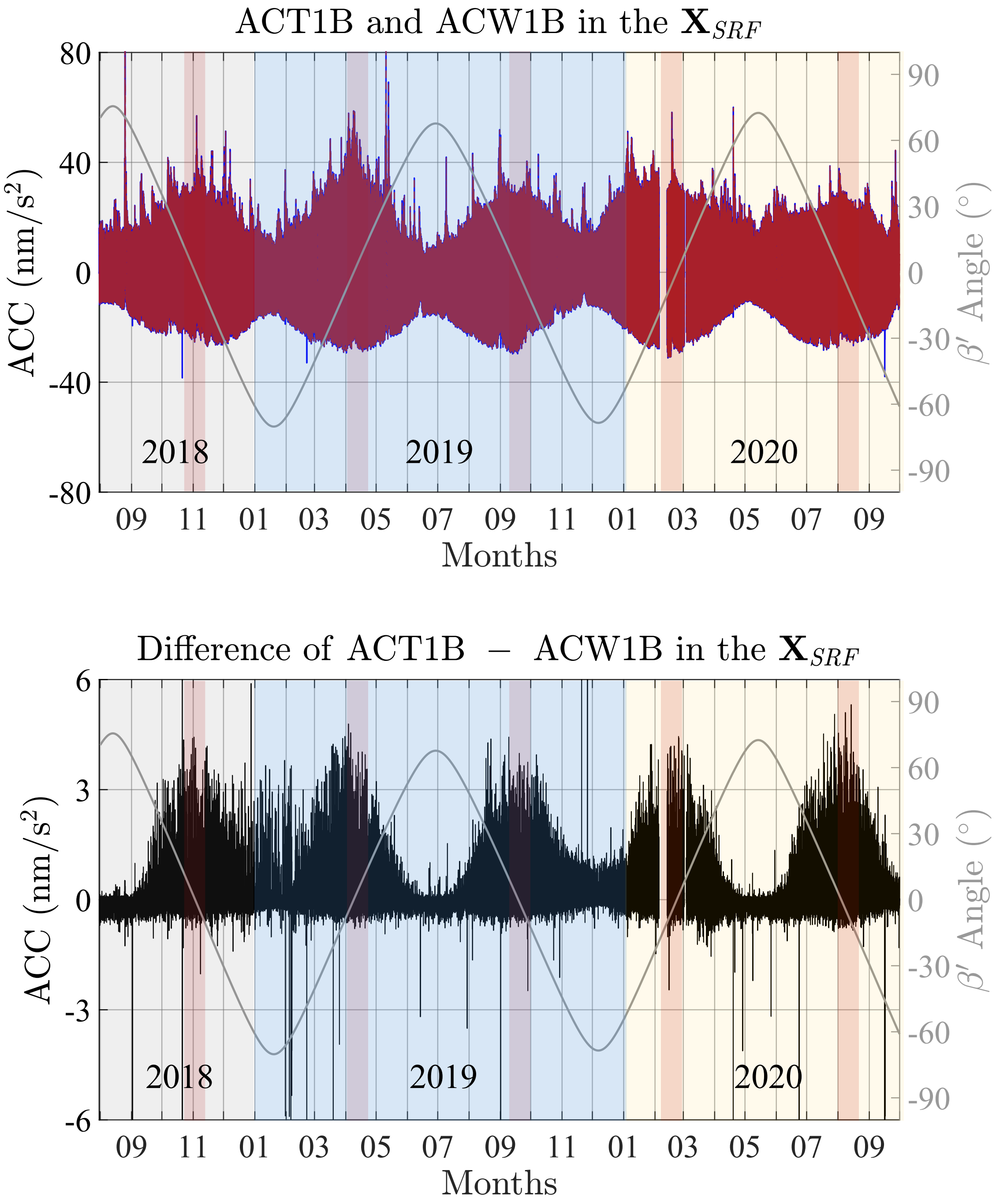

Figure 5.5 GRACE C: ACT1B (blue) and ACW1B in X_{SRF} datasets from August 2018 to August 2020. Both datasets are represented w.r.t. zero mean and after the removal of the linear trend, for visualization clarity. The β' variability is overlayed on the graph (gray line) to show the changes in the differences between the two datasets over time. The colored regions denote the different years over the examined period and the red colored bands indicate the periods of $\beta' = 0$.

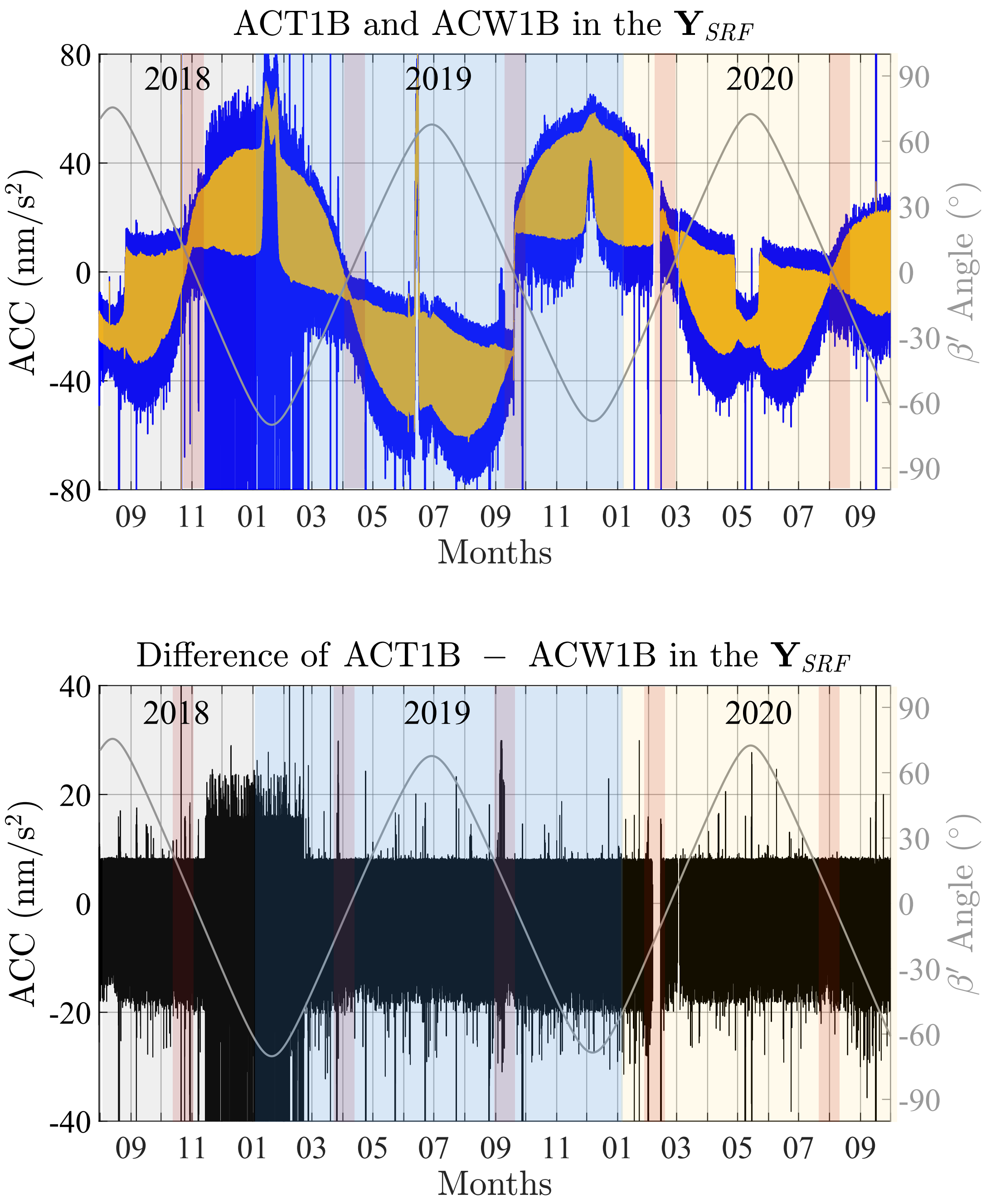

Figure 5.6 GRACE C: ACT1B (blue) and ACW1B (yellow) in the Y_{SRF} from August 2018 to August 2020. Both datasets are represented w.r.t. zero mean and after the removal of the linear trend, for visualization clarity. The β' variability is overlayed on the graph (gray line) to show the changes in the differences between the two datasets over time. The colored regions denote the different years over the examined period and the red colored bands indicate the periods of $\beta' = 0$.

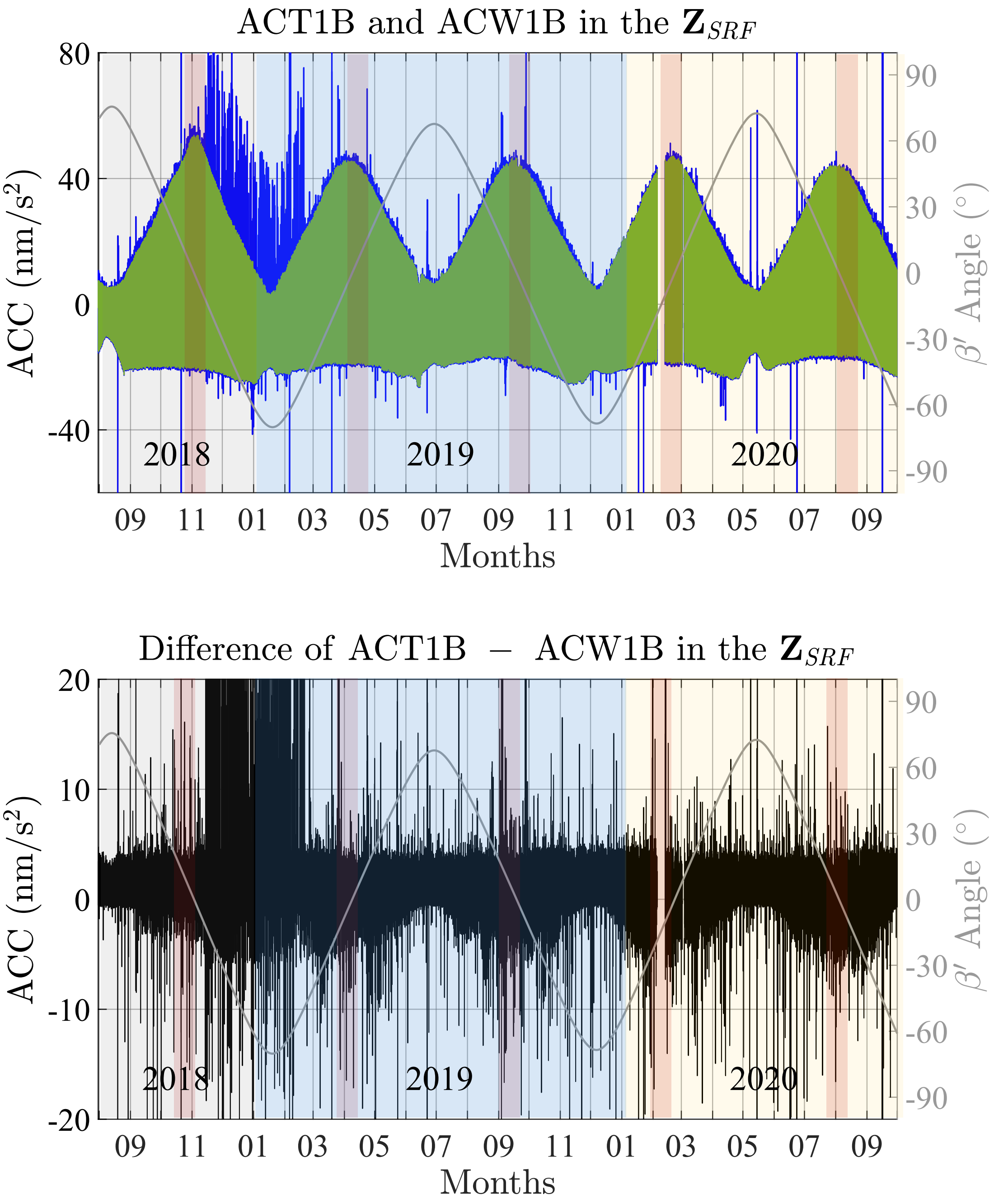

Figure 5.7 GRACE C: ACT1B (blue) and ACW1B (green) in the Z_{SRF} datasets from August 2018 to August 2020. Both datasets are represented w.r.t. zero mean and after the removal of the linear trend, for visualization clarity. The β' variability is overlayed on the graph (gray line) to show the changes in the differences between the two datasets over time. The colored regions denote the different years over the examined period and the red colored bands indicate the periods of $\beta' = 0$.

5.3 Validation of the Method

The newly derived ACW1B dataset for GRACE C cannot be tested directly as a stochastic dataset in the gravity field solutions since this would require the production of an associated transplant dataset for GRACE D plus a significant modification of the existing models/software to accept and propagate an input covariance matrix of the accelerations to the final solutions. Additionally, since the total satellite acceleration includes thruster accelerations, using only the ACW1B dataset without applying the same methodology to other datasets implicated in the gravity field determination would result in failure to remove thruster activation accelerations, leading to a substantially noisier solution beyond the SH_{20}(Koch, 2023).

Testing the validity of the derived variances of the ACW1B for GRACE C can be performed by comparing their long-term systematic trends and patterns with known disturbances in the thermosphere as elaborated on in the introduction. As noted, the accelerometers exhibit sensitivity to the thermospheric composition and its changes, including magnetic storms, various radiation types, fluctuations in temperature, the transition to and from the Earth's shadow, and the interactions with the acoustic gravity waves (AGW) generated forward to the motion of the terminator at subsonic speeds[25]. We find that the most revealing graphs are the ones that display long-term calculated variances versus the argument of latitude. For the discussion that follows, we plot the variances spanning a period of 2 years (August 2018 to August 2020) along the three axes of the accelerometer (Fig. 5.8 for the X_{SRF}, Fig. 5.9 for the Y_{SRF} and Fig 5.10 for the Z_{SRF}). In these figures, the data have been down sampled to every 10 seconds for computational efficiency.

---

[25] These are like the shock waves generated by an aircraft when it exceeds the speed of sound (supersonic boom).

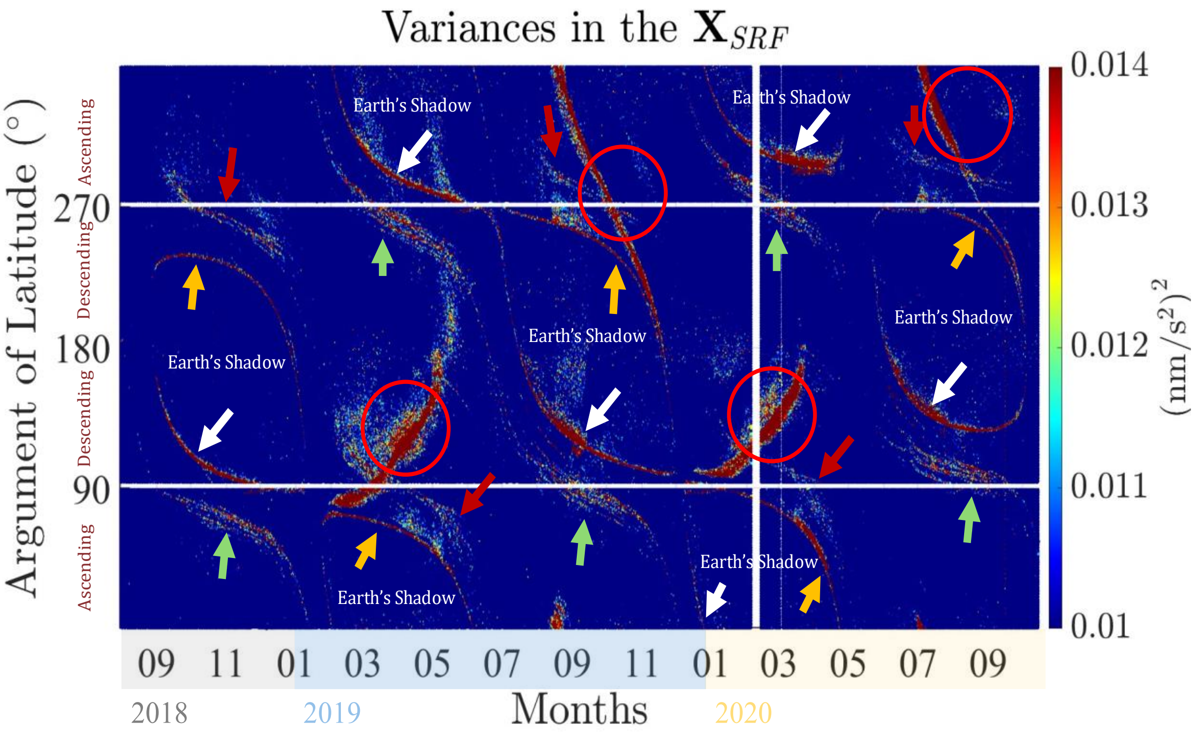

Figure 5.8 Variances of the accelerometer measurements (1Hz) from August 2018 to August 2020 in the X_{SRF}. The argument of latitude, ranging from 0 to 360 degrees, describes a satellite's position in its orbit relative to Earth's equatorial plane. It signifies 0° at the equator, 90° at the North Pole, 180° back at the equator, 270° at the South Pole, and 360° again at the equator. The white bands visible in the data for February and March 2020 indicate missing data during that time. The arrows, the circles and the ellipses are explained in the text.

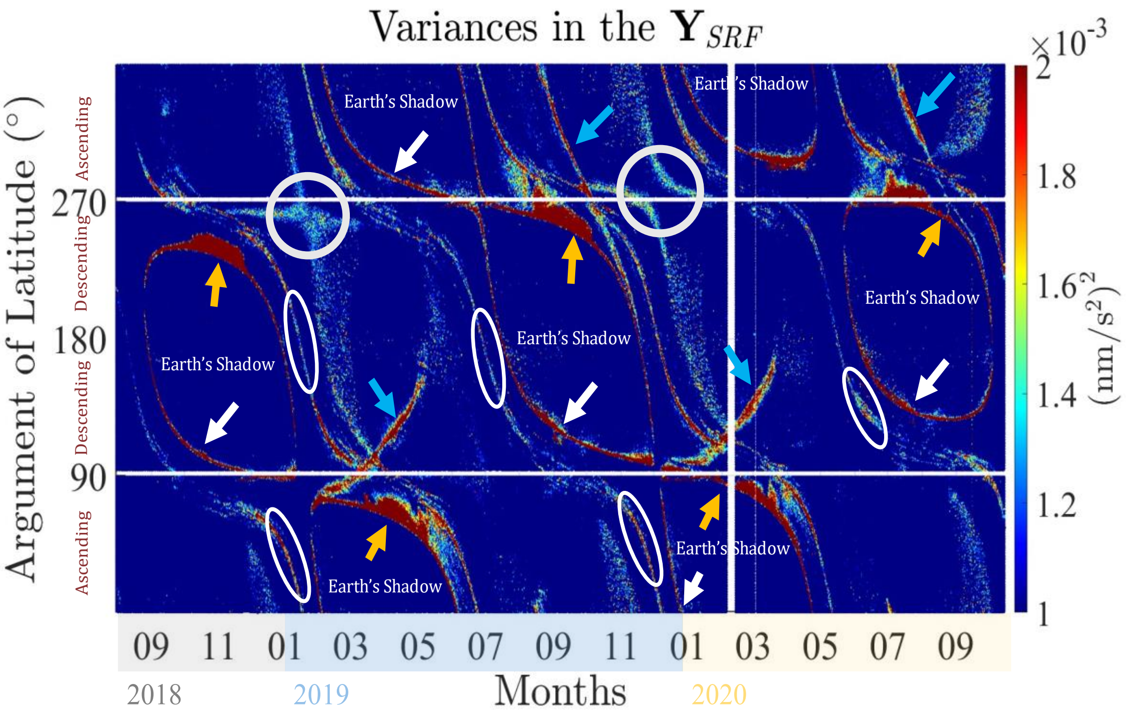

Figure 5.9 Variances of the accelerometer measurements (1Hz) from August 2018 to August 2020 in the Y_{SRF}.

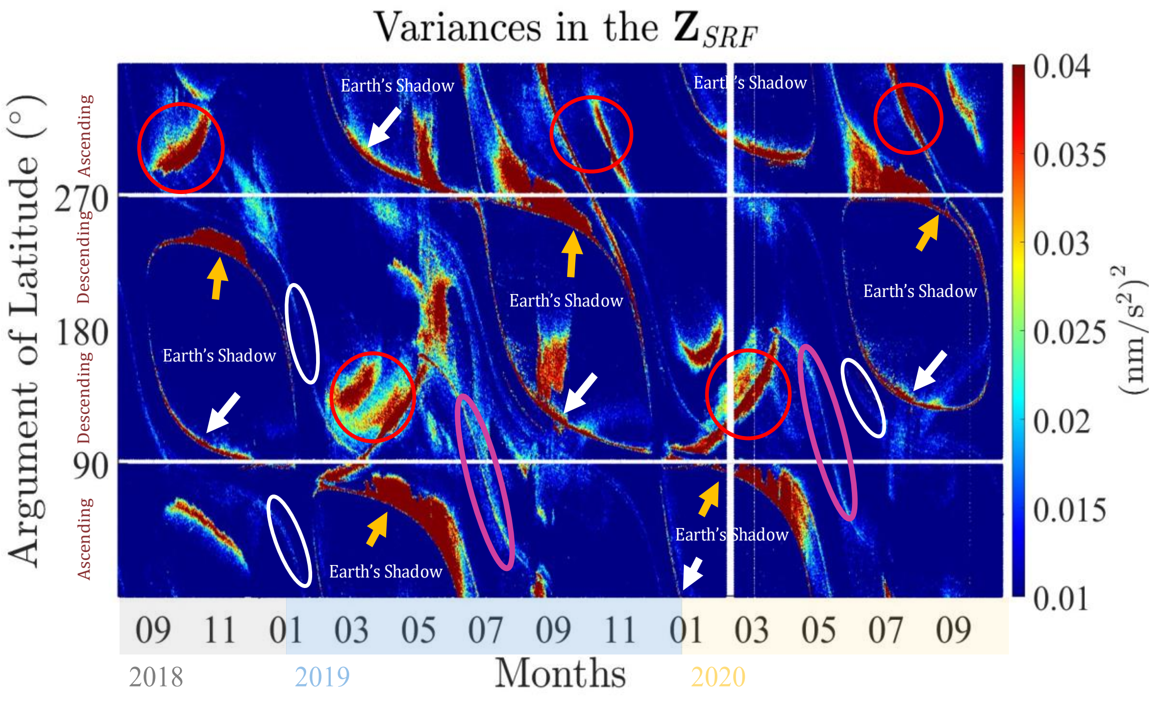

Figure 5.10 Variances of the accelerometer measurements (1Hz) from August 2018 to August 2020 in the Z_{SRF}.

Throughout the examined period of two years, the satellite traversed the terminator and the Earth's shadow, covered all local times, and encountered diverse geomagnetic storm activities. The terminator represents the shifting border between illuminated and shadowed areas at orbit altitude, marking the boundary between day and night. This division affects temperature, solar flux and density variations throughout the atmosphere therefore the accelerometer variances reflect those readings. The accelerometer is also affected by temperature variations during the penumbra transitions, where the light from the Sun is partially blocked as the satellite moves further unto the shadow. As shown in the figures above, there are distinct regions with higher variances along the three axes of the accelerometer. We explain many of these variances here, while others remain unexplained and will be highlighted for future research.

White/Orange arrows: GRACE-FO takes about 161 days to cover the 24 local time hours. As expected, the variances during the entrance/exit or dusk/dawn (white/orange arrows) time to and from the Earth's shadow (penumbra transitions) are higher in all three axes of the accelerometer as highlighted by Harvey *et al.* (2022), who emphasized the significance of accurately addressing the spikes induced by thruster firing or during the satellite passage through the Earth's shadow. The Y_{SRF} and the Z_{SRF} are notably disturbed during the exit transition from the Earth's shadow, which is consistent with the numerous spikes in the ACT1B dataset during the penumbra transitions. There is currently no explanation why the disturbances, as depicted in the variances and in the ACT1B data, are most prominent during the exit transition. However, it is likely that there is a local time dependence that requires further investigation.

Green/Red arrows: Interesting signatures in the accelerometer variances occur during the terminator crossings, particularly along the X_{SRF} when the satellite crosses the terminator at nearly right angle (green and red arrows) near the north and south poles (at 90° and 270° argument of latitude). While the terminator crossings are not clearly visible in the X_{SRF} in the equatorial region (for argument of latitude of 0° and 180°), they are more visible in the Y_{SRF} and Z_{SRF} (white ellipses in Figs. 5.9 and 5.10).

Somsikov (1995) discusses a notable inconsistency in atmospheric disturbances occurring during the transition between sunset (green arrows) and sunrise (red arrows) regions (Fig. 5.8). In these regions and thermospheric altitudes the ACWs are often generated by the inconsistency of the atmosphere and their subsonic speed. These wavelike oscillations in electron temperature have typical horizontal wavelengths that peak near 1000 km (Raitt & Clark, 1973), although CHAMP mission showed scales by a factor of 3 less than the typical ones (Forbes et al., 2008).

Green arrows show that in the sunset regions, significant disturbances are present in the X_{SRF} during October to December 2018, September to November 2019 and June to August 2020, affecting the northern hemisphere. Additionally, disturbances in the sunset regions were observed in March to May 2019 and December 2019 to February 2020, impacting the southern hemisphere. The red arrows indicate the same structured disturbances in the sunrise regions for the same periods. We can claim that these disturbances are connected to the AGWs, and are dependent on local time, the terminator and the season rather than latitude. The solar terminator and the generated AGWs have been studied in the thermospheric densities derived from CHAMP satellite (Forbes *et al*., 2008; Liu *et al*., 2009) as well as from GRACE and GRACE-FO (Park *et al*., 2023)

White ellipses: In the Y_{SRF} and Z_{SRF}, we highlight the terminator near the equator and during full Sun orbit, with white ellipses. The variances of the X_{SRF} are not significant because the orbit is nearly parallel to the terminator. However, the other two axes are affected by different intensities.

Blue Arrows: Along the three axes of the accelerometer during February to May 2019 and December 2019 to March 2020 a strong signature is evident only on the descending tracks in latitudes $0° - 90°N$. Conversely, during August to November 2019 and July to August 2019 there is a strong signature observed on both ascending and descending tracks covering the southern hemisphere. We show these arrows only on the Y_{SRF} for enhanced visualization clarity, but in the other two axes the variances denote strong disturbances during these periods as well, especially in the Z_{SRF}.

White Circles: The Y_{SRF}, being the least sensitive axis of the accelerometer, experiences the least disturbances. However, it interestingly depicts disturbances between the outer boundaries of the terminator that are not apparent in the other two axes. These disturbances could be attributed to crosswinds or elevated electron activity during daytime due to temperature fluctuations.

Red circles: The Z_{SRF}, showing the highest variances, displays a notable asymmetry between the September and March equinoxes, with higher disturbances observed in the Southern hemisphere during September and in the Northern hemisphere during March. This asymmetry is also observed in the X_{SRF} but not with the same intensity. This structured asymmetry suggests distinct atmospheric conditions or geophysical phenomena prevalent in each hemisphere during these equinox periods. We believe that these disturbances are particularly notable in the Z_{SRF} as the radial direction measures not only SRP but also ERP. The highest disturbances on Z_{SRF} may be attributed to the sensitivity of the accelerometer radial component to twangs (Peterseim *et al.*, 2013), which could be correlated with the presence of the whistlers[26] propagating in the radial direction (Schlicht, 2022).

Pink ellipses: In the Z_{SRF} a visible signal covering the Northern hemisphere emerges, starting on May 2019 and March 2020 and persisting for 4 months. For both periods, the disturbance shows the same structure, but it appears during the equinox and at the start of the June solstice. The source of this signal is unknown and requires further investigation.

Lastly, we can observe that the variances in the X_{SRF} and Z_{SRF} during March and September 2019 show the highest intensity, probably due to the Earth's magnetic field cracks that maximize in spring and fall letting through more solar wind energy (Zhao *et al.*, 2012; Jackson *et al.*, 2019).

From a month-to-month observation, short-duration disturbances associated with geomagnetic storms can be noticeable in both hemispheres during the examined period. From a preliminary analysis as shown in Fig. 5.11, it appears that disturbances occurring during geomagnetic storms exhibit a wavelike structure that persists for a few days, contingent upon the intensity of the storm. Interestingly, disturbances are observed in both hemispheres even during minor storms. The strong signals observed during solstices or equinoxes, along with the high correlation of variances with terminator crossings, sometimes make it challenging to differentiate disturbances associated with other phenomena.

---

[26] Whistlers are very low frequency (VLF) waves that can propagate through the Earth's atmosphere. When these waves enter the ionosphere, the signal is dispersed, meaning higher frequencies travel faster than lower frequencies, causing a characteristic whistle sound (Schlicht, 2022).

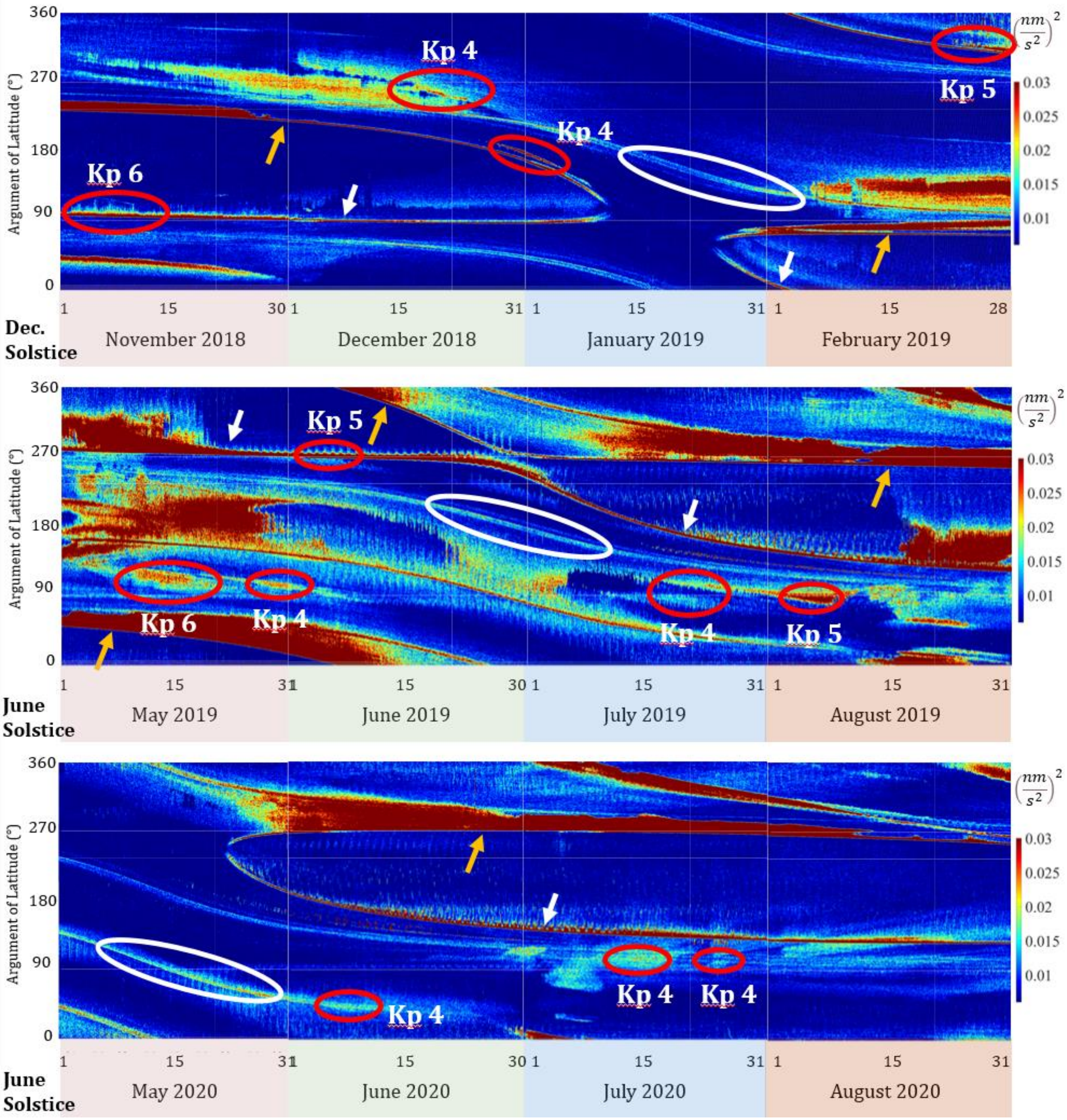

Figure 5.11 GRACE C: Variances in the X_{SRF} for different periods between 2018-2020. The red ellipses show disturbances linked to geomagnetic storms that occurred during each selected period. The white/orange arrows indicate the entrance/exit to/from the Earth's shadow. The white ellipses denote the terminator crossings.

5.4 Summary

In this chapter we emphasized the necessity of a weighted and decorrelated 1B accelerometer dataset (stochastic process). Such a dataset is crucial for eliminating the influence of unwanted disturbances without resorting to the deletion and interpolation of thruster or other spikes and noisy segments. On the other hand, it allows for the identification of periods with increased disturbances, supporting investigations of various phenomena related to space weather. This dataset could also be used as a reference during the modeling of the non-gravitational accelerations, which will be discussed in Chapter 6, and is also quite valuable during the extraction of the thermospheric densities, particularly because the accelerations resulting from thruster activations must be eliminated, a task that can be challenging otherwise. The accelerometer is generally affected by the state of the thermosphere in a similar manner along all three axes, although possibly not to the same degree of intensity. However, it is evident that disturbances impact each axis differently, and their durations vary across the axes. Therefore, it is essential to account for these errors appropriately when utilizing the accelerometer measurements in various studies from gravity field solutions to thermospheric densities and space weather.

The variances indicate that a significant portion of the phenomena affecting the accelerometer is associated with terminator crossings, which are known sources of atmospheric irregularities. The dominant waves observed before the satellite enters the Earth’s shadow warrant further investigation to determine if there is a correlation with the AGWs observed in thermospheric densities (Vadas & Nicolls, 2012; Vadas & Crowley, 2017).

6 Data-Driven Radiation Pressure and Drag model: Insights from GRACE-FO Residuals

In this chapter, we present an original method to model the radiation pressure (RP) and atmospheric drag acting on GRACE-FO. Our models are exclusively data-driven, based on the spectral characteristics of the two dominant non-gravitational forces influencing the satellite, which exhibit periodicities closely aligned with the satellite orbital period and its harmonics. This modeling is implemented using weighted Least-Squares methods, to analyze the weighted ACW1B dataset developed in Chapter 5. Following the modeling, we use wavelet decomposition of the residual series to isolate higher frequency drag effects into the model. Finally, we investigate the residual series during different local times, providing valuable insights into the satellite response to these non-gravitational forces.

6.1 Solar Radiation Forces on GRACE missions

Before exploring the various modeling methods of nongravitational accelerations for different applications, it is important to introduce the sunspot number F10.7 and the solar cycle. The Sunspot Number, in conjunction with the F10.7 cm radio flux, is usually regarded as one of the most often used solar indices for describing the gradual changes in solar activity over time, known as *solar cycle*. Comprehending the fluctuations in the solar cycle is advantageous not only for analyzing the response of the accelerometers but also for verifying the precision of the current, state-of-the-art physical (theoretical) models developed for GRACE missions.

Sunspot Number: This is a measurement of how many individual sunspots and sunspot clusters are present on the Sun surface. Sunspots are regions of reduced temperature and darkness on the surface of the Sun, resulting from magnetic disturbances. The sunspot number fluctuates with the solar cycle, which lasts for about 11 years. Increased solar activity is correlated with larger sunspot numbers, and this can affect satellite operations, space weather, and even the temperature on Earth (Hathaway *et al.*, 2002; Clette *et al.*, 2014).

F10.7 cm Radio Flux: The F10.7 cm Radio Flux is a quantification of solar radio emissions specifically at a wavelength of 10.7 centimeters ($2800\ MHz$). It serves as an additional significant measure of solar activity. The F10.7 cm flux is measured in solar flux units (sfu), with 1 sfu = $10^{-22} Wm^{-2} Hz^{-1}$.

The F10.7 cm flux is closely connected to the sunspot number but gives a more consistent and reliable estimate of solar activity. It is less sensitive to short-term fluctuations and more reflective of the overall level of solar activity. High F10.7 cm flux levels imply higher solar activity, which can have a significant impact on satellite communications, GPS systems, and ionosphere conditions (Tapping, 2013).

Solar Cycle: The solar cycle is an approximately 11-year cycle of fluctuating solar activity driven by the Sun's magnetic field. It comprises the following phases: solar minimum (fewest sunspots and low activity), ascending phase (increasing sunspots and activity), solar maximum (peak sunspots and activity), descending phase (decreasing activity), and returning to solar minimum. Key features include sunspots, Solar Radio Flux, solar flares, and coronal mass ejections (CMEs) (Hathaway, 2015).

As Fig. 6.1 shows, the GRACE mission monitored the Earth and provided measurements starting near the solar maximum of Solar Cycle 23[27] and covering most of the Solar Cycle 24[28]. The GRACE-FO mission, launched in 2018, began providing measurements during the solar minimum of Solar Cycle 24 and is currently ongoing, covering Solar Cycle 25[29].

The phase of the solar cycle and solar activity play a crucial role in modeling non-gravitational accelerations. Most proposed models, which will be discussed in Section 6.2, exhibit decreased accuracy during periods of high solar activity due to the difficulty in determining the atmospheric drag acting on satellites. On the other side, during periods of low solar activity the small amplitude of drag compared to the SRP acting on the satellite can reduce the accuracy of estimating the calibration parameters of accelerometer (as discussed in Chapter 4) using the physical models (Wöske *et al*., 2019)

---

[27] Solar Cycle 23 started in May 1996 and ended in December 2008. Its solar maximum occurred around April 2000.

[28] Solar Cycle 24 started in December 2008 and ended in December 2019. Its solar maximum occurred around April 2014.

[29] Solar Cycle 25 started in December 2009.

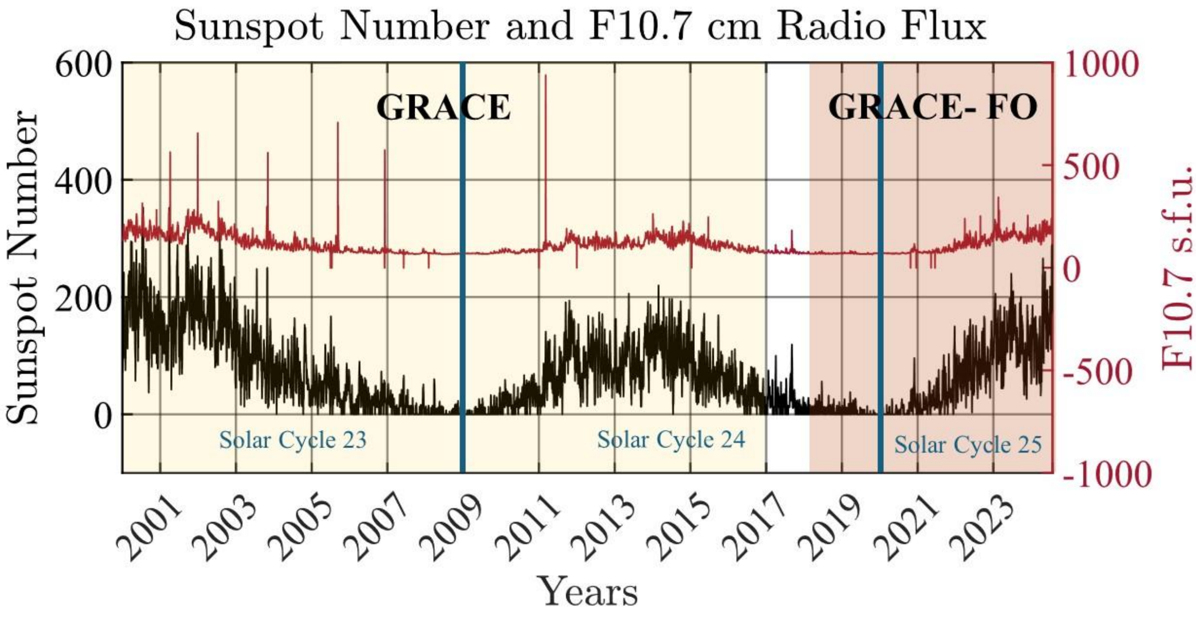

Figure 6.1 Sunspot Number (left y-axis) and F10.7 cm Radio Flux (right y-axis) from 2000 to 2024. The coloured bands denote the operational years of GRACE (yellow) and the operational years of GRACE-FO (orange). The blue vertical lines indicate the transitions between solar cycles[30].

6.2 The significance of Modelling Non-Gravitational Accelerations

Nongravitational accelerations are crucial for precise orbit determination (POD), gravity field estimations, and thermospheric density modeling (Kang *et al.*, 2006; Siemes *et al.*, 2023). However, accelerometer measurements can be compromised by temperature changes, spurious spikes, systematic errors, or data gaps (see Chapter 5 for more details) and therefore are often modeled. This physical (theoretical or force) modeling utilizes advanced Solar Radiation Pressure (SRP), Earth Radiation Pressure (ERP), Thermal Radiation Pressure (TRP), and drag models. These non-conservative forces were introduced in Chapter 2. However, we provide here a more

---

[30] The Sunspot Number and the F10.7 Radio Flux datasets can be found at ftp://ftp.gfz-potsdam.de/pub/home/obs/Kp_ap_Ap_SN_F107/

detailed explanation on the importance of these dominant forces acting on satellites in the following subsections.

6.2.1 Solar Radiation Pressure – SRP

The Solar Radiation Pressure (SRP) generates a force that the Sun's radiation applies to a spacecraft. It is the result of the momentum of photons being transferred to the satellite surface. While the gravitational forces are much stronger, the SRP plays a crucial role in the accurate navigation and stability of satellites. Comprehending the concept of SRP is key for achieving precise orbit determination and mission planning, particularly for lightweight spacecraft that are more vulnerable to the impacts of SRP, since even minor inaccuracies in SRP modeling could result in significant discrepancies in the predicted positions of satellites over time (Keating *et al.,* 1999; Fienga *et al.* 2009). The SRP effect can impact the attitude dynamics of a spacecraft, especially those that pose irregular forms or changing surface qualities. This is particularly relevant for solar sails, as they use SRP to generate propulsion, allowing for trips without the need for conventional fuel. This specific concept has been proposed for the IKAROS mission, effectively showcasing the controllable propulsion of a solar sail (Tsuda *et al*. 2011), following the study of Krikov (2006) and McInnes (1999) which extensively investigated the possibilities of SRP in deep space exploration, offering detailed analysis of solar sail dynamics and the associated difficulties.

6.2.2 Atmospheric Drag

One of the most significant forces acting on LEO satellites that arise from their interaction with the atmosphere is the atmospheric drag; the most challenging non-gravitational force to be modelled. Even at altitudes ranging from 160 to 2,000 km, where the atmosphere is extremely thin and the number of gas molecules decreases significantly, the impact of atmospheric drag is substantial, always opposing the satellite motion and results in gradual deceleration and eventual orbital decay if not properly mitigated.

The importance of accurately modeling and predicting drag forces in LEO cannot be overstated. Precise drag models are essential for orbit determination, prediction, and control, for collision avoidance and re-entry predictions, ensuring the longevity and stability of satellite missions (Doornbos & Klinkrad, 2006). One of the critical challenges in drag modeling is the variability of atmospheric density (also referred to as thermospheric density, for altitudes 80 to 600 km). During periods of high solar activity, increased solar ultraviolet irradiance[31] and X-ray radiation[32] heats and expands the Earth's atmosphere, significantly increasing the drag on LEO satellites. The atmospheric drag observed for the first time in the late 1950s (Harris & Priester, 1962) when the orbital periods of artificial satellites experienced a much higher rate of orbital decay. The magnitude of atmospheric drag is affected by factors such as the shape and the material of the satellite, surface roughness, orientation, and altitude as well as the density and composition of the atmosphere.

The atmospheric density is affected by solar activity, geomagnetic conditions, diurnal and semiannual variations and seasonal changes, making the modeling of drag forces a complex task (Harris & Priester, 1962; King-Hele, 1987) and the retrieval of thermospheric densities a primary concern (Bruinsma *et al*., 2023). Another critical challenge is the accurate retrieval of the drag coefficient C_D, which is computed by modelling the momentum and energy exchange between the particles of the atmosphere and the satellite. The inaccurate computation of the drag coefficient C_D, is because it is influenced by critical parameters, such as temperature, molecular composition, velocity, the spacecraft geometry and the gas-surface interactions[33].

Models of the upper atmosphere such as the NRLMSISE-00, incorporate solar[34] and geomagnetic indices[35] to provide more accurate density estimates, improving the precision of drag predictions (Picone *et al*., 2002). Other important empirical models include the Jacchia-Bowman 2008 (JB2008) model, which also integrates solar activity indices for enhanced predictions (Bowman *et*

---

[31] Solar ultraviolet irradiance is the total radiative energy of the Sun (Chatzistergos *et al*., 2023).

[32] X-ray radiation is emitted from the solar corona, the outermost layer in the atmosphere of the Sun (Murase *et al*., 2023).

[33] GSI quantifies the interaction between free-stream molecules and the satellite surface enabling the flow of energy and momentum (Cercignani & Lampis, 1971).

[34] Solar indices are observations that describe the solar activity. Some of the most commonly used are: Sunspot number, solar flux F10.7, K-index and A-index (Tobiska *et al*., 2008).

[35] Geomagnetic indices observe the geomagnetic activity. The officially recognized indices are: aa, Am Kp, Dst, AE (Rostoker, 1972; Menvielle *et al*., 2010).

al., 2008), and the semi-empirical Drag Temperature Model (DTM), which has integrated accelerometer derived thermospheric densities from GOCE, CHAMP, GRACE and Swarm missions to improve density forecasting capabilities (Bruinsma *et al*., 2012; Bruinsma & Boniface, 2021).

The atmospheric drag also plays a crucial role in the design and operational strategies of LEO missions. Engineers must account for drag in mission design, when planning fuel budgets for orbit maintenance and maneuvers, in collision avoidance and in navigation and control (Mehta *et al*., 2023). As the number of satellites in LEO increases, along with space debris, predicting the trajectories of objects becomes increasingly complex, necessitating accurate modeling for collision prediction and avoidance maneuvers (Klinkrad, 2006).

Additionally, atmospheric drag considerations influence the selection of orbital altitudes and the design of satellite shapes to minimize aerodynamic resistance. For instance, designs and materials preferred to reduce the impact of atmospheric drag on satellites are presented in Vallado, (2013).

Lastly, drag is important for end-of-life disposal strategies. Satellites at the end of their operational life re-enter the atmosphere and burn up, minimizing space debris. This technique, known as aerobraking, involves lowering the satellite altitude to increase drag, thus accelerating orbital decay. The success of such strategies depends heavily on precise drag predictions to ensure controlled re-entry within targeted areas (Virgili *et al*., 2015; La Marca *et al*., 2024). This is increasingly important since all space agencies have introduced the “Zero Debris approach”, meaning that an atmospheric reentry or re-orbiting the satellite to a safe altitude will be mandatory by 2030 (Giudici *et al*., 2024).

6.2.3 Earth Radiation Pressure – ERP

The Earth radiation pressure (ERP) introduces a significant force on satellites, particularly those in Low Earth Orbit (LEO) and Geostationary Orbit (GEO), which arises from the interaction between the satellite and radiation emitted and reflected by the Earth (Klinkrad, 2006). This force, while smaller than the SRP, can influence satellite trajectories, attitudes, and long-term orbital stability. Understanding and accurately modeling the ERP is essential for the precise orbit determination, station-keeping, and attitude control of satellites, ensuring the success of various satellite missions (Knocke *et al*., 1988).

The ERP affects satellites through direct thermal radiation from the Earth's surface and atmosphere as well as reflected sunlight, commonly known as albedo. The force exerted by the ERP is variable, depending on factors such as the satellite altitude, the Earth's surface and atmospheric conditions, and the satellite orientation and surface properties. The ERP computation includes the determination of solar irradiance received by the Earth, the computation of the irradiance received by the satellite, assuming the Earth as a Lambertian sphere[36] and the interaction of irradiance from each surface element of the Earth with the satellite macro geometry model (Rodriquez-Solano *et al*., 2012). Advanced atmospheric and radiation models, such as the NRLMSISE-00 and the Global Earth Radiation Budget (GERB) instrument data, provide more accurate estimates of atmospheric density and radiation, improving the precision of the ERP predictions (Picone *et al*., 2002; Harries *et al*., 2005).

The impact of the ERP on satellite missions is multifaceted. For instance, accurate ERP modeling is crucial for geostationary satellites, which must maintain precise positions relative to the Earth's surface to provide continuous communication and weather monitoring services. Studies have shown that neglecting the ERP can lead to significant deviations in the predicted positions of geostationary satellites, affecting their operational effectiveness (Knocke *et al*., 1988). Moreover, ERP-induced perturbations must be accounted for in the design and operation of solar sails, which leverage radiation pressure for propulsion, as demonstrated in missions such as IKAROS (Tsuda *et al*., 2011).

6.2.4 Thermal Radiation Pressure − TRP

The thermal radiation pressure (TRP) arises from the emission of infrared radiation by the satellite surface as it absorbs sunlight and re-emits it as thermal energy. This force, although subtle compared to solar radiation pressure, especially during low solar activity, can significantly impact the orbit and attitude of a satellite. Mismodelling of the TRP, resulting from inaccurate geometry

---

[36] A Lambertian sphere is an idealized object that reflects light uniformly in all directions, meaning that the brightness of the sphere appears constant regardless of the viewing angle (Blinn, 1977).

models of satellites due insufficient information from engineering teams, can be introduce errors up to 10% in the thermospheric densities derived from accelerometer measurements during high solar activity (Bruinsma *et al.,* 2023). The TRP is particularly important for spacecraft with large surface areas, such as solar panels or thermal blankets, which can experience differential heating and thus differential radiation forces (Rodriguez-Solano *et al*., 2012).

The impact of the TRP on satellites is complex, because it relies on the thermal characteristics of the satellite materials, the geometry of the spacecraft, and its orientation relative to the Sun and the Earth. Creating new coatings and materials with different thermal emissivity properties can reduce the impact of the TRP on satellites. Recent research on enhanced thermal control materials has proven that the use of low-emissivity thermal coatings can reduce the TRP-induced disturbances (Zhang *et al*., 2024). Additionally, researchers are investigating the possibility of real-time monitoring and adaptive thermal control systems to adjust to changing thermal conditions (Gao *et al*., 2021).

Advances in computational modeling and simulation techniques that consider both conductive and radiative heat transfer, have enabled more detailed analysis of the TRP effects (Wöske *et al*., 2019; Hładczuk *et al*., 2024). Depending on the β' angle, thermal radiation forces can induce torques that affect the orientation of the spacecraft, which is particularly challenging for missions requiring high-precision pointing, such as Earth observation and deep space missions (Santoni *et al*., 2018; McGirr *et al*., 2022).

6.2.5 Modelling of Non-Gravitational Accelerations on GRACE Missions

Recent advancements in modeling and observational techniques have furthered our understanding of non-gravitational forces acting on satellites. The integration of satellite accelerometer measurements from GRACE missions has provided valuable insights into the spatial and temporal variability of these forces. These measurements have been critical in refining empirical and physics-based thermospheric density models, leading to more accurate drag, SRP, TRP and ERP predictions (Bruinsma *et al*., 2012).

Many physical models have been proposed for modeling the non-gravitational accelerations for the GRACE missions, which can be used to study the upper atmosphere and calibrate the instruments. The SRP models are highly precise and almost uncorrelated with solar activity, because the SRP remains unaffected by varying solar activity levels. In contrast, drag models show increased accelerations due to rising atmospheric density during periods of high solar activity (Wang *et al*., 2005).

One common method for modeling nongravitational accelerations is the satellite acceleration approach (Bezděk, 2010). This method involves deriving the total acceleration acting on the satellite by performing a double numerical differentiation of the positions estimated from GPS measurements. Although this approach increases the noise of the calculated total accelerations due to the double differentiation, it remains highly accurate, with satellite positions determined to be within a few centimeters. Subsequently, modeled gravitational accelerations are subtracted from the total accelerations to estimate the nongravitational accelerations. Bezděk proposed a physical model using the neutral thermospheric density model DTM-2000, zonal and seasonal models of the ERP, and the satellite shape and physical properties. The modeled drag is observed to be the most significant force affecting the satellite in the X_{SRF}. The SRP affects the Y_{SRF} the most while the SRP and albedo are dominant in the radial direction Z_{SRF}, with the drag acceleration being almost zero.

A physical high-precision non-gravitational acceleration model for the purpose of calibrating the accelerometer of GRACE missions was developed by Wöske *et al*., (2019), based on a detailed finite element analysis of the satellite, specifically for calculating the TRP. Radiative forces show excellent agreement with modeled accelerations, with residuals of 1-3 nm/s^2. However, atmospheric drag modeling has higher uncertainty, with along-track residuals varying from 7 to 50 nm/s^2 based on solar radio flux F10.7. The TRP models reduce the residuals by up to 6 nm/s^2 during rapid illumination changes compared to static models. The POD-based accelerometer calibration methods, in which the gravitational accelerations are subtracted from the total accelerations of the satellite, outperform others in the along-track direction due to their GPS sensitivity but in the cross-track and radial directions, where radiative forces dominate, model-based calibration is advantageous.

Another SRP and ERP model was proposed by Vielberg & Kusche (2020), in which the extended SRP and ERP model differed from standard models depending on at least two channels of the solar spectrum instead of only the visible wavelengths. This method was applied to GRACE but could be applied to any mission that carries an accelerometer. In this model, the solar constant was replaced by the solar irradiance and considered the reflection of the solar radiation from the surface of the satellite (thermal reradiation of the satellite), and a shadow function that considered the Earth as a spheroid. This model was also used in the calculations of the new thermospheric densities[37]for CHAMP, GRACE and GRACE-FO and the improvement in the radiation pressure modelling was particularly notable during periods of low solar activity where the SRP is more substantial compared to the atmospheric drag acting on the satellite (Siemes *et al*., 2023). Utilizing state-of-the-art SRP, TRP, and ERP models along with the Horizontal Wind Model (HWM) and the semi-empirical model DTM2020 which determines the thermospheric temperature, density and composition. It is noted that during lower solar activity, the relatively weaker drag signal makes accurate crosswinds retrieval challenging. The radiation pressure model for GRACE-FO, including temperature measurements from thermistors on the solar arrays of GRACE C for the retrieval of thermospheric densities and crosswind is presented in Hładczuk *et al*. (2024).

Lastly, in GRACE-FO, as mentioned in previous chapters, the accelerometer measurements of satellite D are not available due to instrument malfunction and decommission early in the mission. Therefore, many different transplant methods have been proposed, incorporating non-gravitational force models to create an accelerometer dataset for GRACE D (Behzadpour *et al*., 2021; Huckfeldt *et al*., 2024; Nie *et al*., 2024). In these methods, by incorporating force models, the estimation of higher degrees in monthly gravity field solutions is enhanced.

It is evident that modeling non-gravitational accelerations is crucial for various aspects of satellite missions. Unfortunately, due to our insufficient knowledge of all the forces acting on the satellite, there are many inconsistencies in the physical models presented in the literature for GRACE (Bezdek, 2010; Chen *et al*., 2016; Wöske *et al*., 2019; Vielberg & Kusche, 2020) and the GRACE-FO mission (Harvey *et al*., 2022; Siemes *et al*., 2023; Wang *et al*., 2023; Hładczuk *et al*., 2024). The modeled non-gravitational accelerations vary depending on the different levels of solar activity, satellite geometry model, different surface radiation coefficients, the reradiation from the

---

[37] The thermospheric density dataset is available on the FTP server ftp://thermosphere.tudelft.nl.

satellite itself (if taken into consideration), and the retrieval of the drag. Some researchers retrieve the drag from the Drag Temperature Models, while others retrieve it after the subtraction of the modeled SRP, TRP and ERP. It is notable that in the literature, there is no direct comparison among the different models presented, nor an extensive analysis of the residuals, making it difficult to validate our findings with other studies.

In the following section, we propose a data-driven model of the SRP, drag and TRP for GRACE C satellite, based on a) the spectral characteristics of the measured non-gravitational accelerations and b) the wavelet decomposition of the residuals, allowing us to account for the higher frequency components of the drag.

6.3 Data-Driven Modeling of Non-gravitational Accelerations

Our methodology for the proposed data-driven modeling is implemented in the frequency domain using Least Squares methodology. We can model the dominant forces of radiation pressure (RP) and drag using their spectral characteristics because these forces exhibit dominant frequencies close to the orbital period (1 cycle per revolution-cpr) and the semi-period (2 cpr) of the satellite (Harvey *et al.*, 2022; Harvey *et al.*, 2024) plus additional harmonics. Importantly, this analysis relies solely on the accelerometer measurements from ACW1B dataset introduced in Chapter 5, without using any physical models. To our knowledge, this is the first study to model nongravitational accelerations using the spectral characteristics of the measurements. It is expected that the results of our research will shed light into the modelling of these forces to resolve the differences among the different physical models and further enhance our knowledge in the physics of the non-gravitational forces.

The Least Squares Spectral Analysis (LSSA) is used in this study to analyze both equally and unequally spaced time series, unlike Fourier analysis, which can only be used for equally spaced and stationary time series (Wells *et al.*, 1985). The software used for this analysis is in MATLAB code called LSWAVE (Ghaderpour & Pagiatakis, 2019; Ghaderpour *et al.,* 2020), which can analyze any equally or unequally spaced, nonstationary or stationary time series. This analysis is based on the least squares spectrum, providing the best measure of the power contributed by different frequencies to the variance of the data (Pagiatakis, 1999).

6.3.1 Modelling Atmospheric Drag and Radiation Pressure Using LSSA

From the extensive literature on the physical modelling of the non-gravitational forces mentioned above, the dominant ones acting on the satellites are:

a) X_{SRF}: Drag, SRP
b) Y_{SRF}: SRP, TRP and small magnitude atmospheric drag (depending on the solar activity)
c) Z_{SRF}: SRP, ERP, TRP.

In the literature, physical models typically separate ERP into two components: albedo and the irradiation force (IR) reflected by the Earth. With our modelling method, we are unable to separate all these components. Therefore, whenever we refer to ERP, we tacitly assume that it encompasses both the albedo and the IR. We note that the experimental splitting of all acceleration components in this research is not necessary. The splitting of the total non-gravitational force into its many components when performing physical modelling is necessary for the estimation of the total accelerations either to determine the calibration factor of the accelerometers or estimate the drag for the purpose of modelling the density of the thermosphere and estimation of thermospheric winds. To this effect, our data-driven modelling of the drag alone satisfies by-and-large these needs.

The proposed modelling method is based on separating the orbit into two segments: the illuminated orbital arc, where the satellite is fully exposed to the Sun, and the shadow orbital arc, where the satellite crosses the Earth's shadow. The reason for this separation is that different forces act on the satellite when it is exposed to the Sun as opposed to its passage through the Earth's shadow. From the physical models, the forces acting on the satellite during the umbra crossings are the drag in the X_{SRF}, the TRP in the Y_{SRF} and the TRP and the ERP in the Z_{SRF}. In Fig. 6.2, three orbital revolutions of GRACE C are shown along the three axes of the accelerometer, with the shadow segments also indicated. Consequently, since our models are based primarily on the umbra crossings, we are able to model the SRP along all three axes, incorporating low frequency drag in the X_{SRF} and the TRP in the Y_{SRF} and Z_{SRF}. Once the models are developed, they are scaled by the scale factors determined from our calibration method.

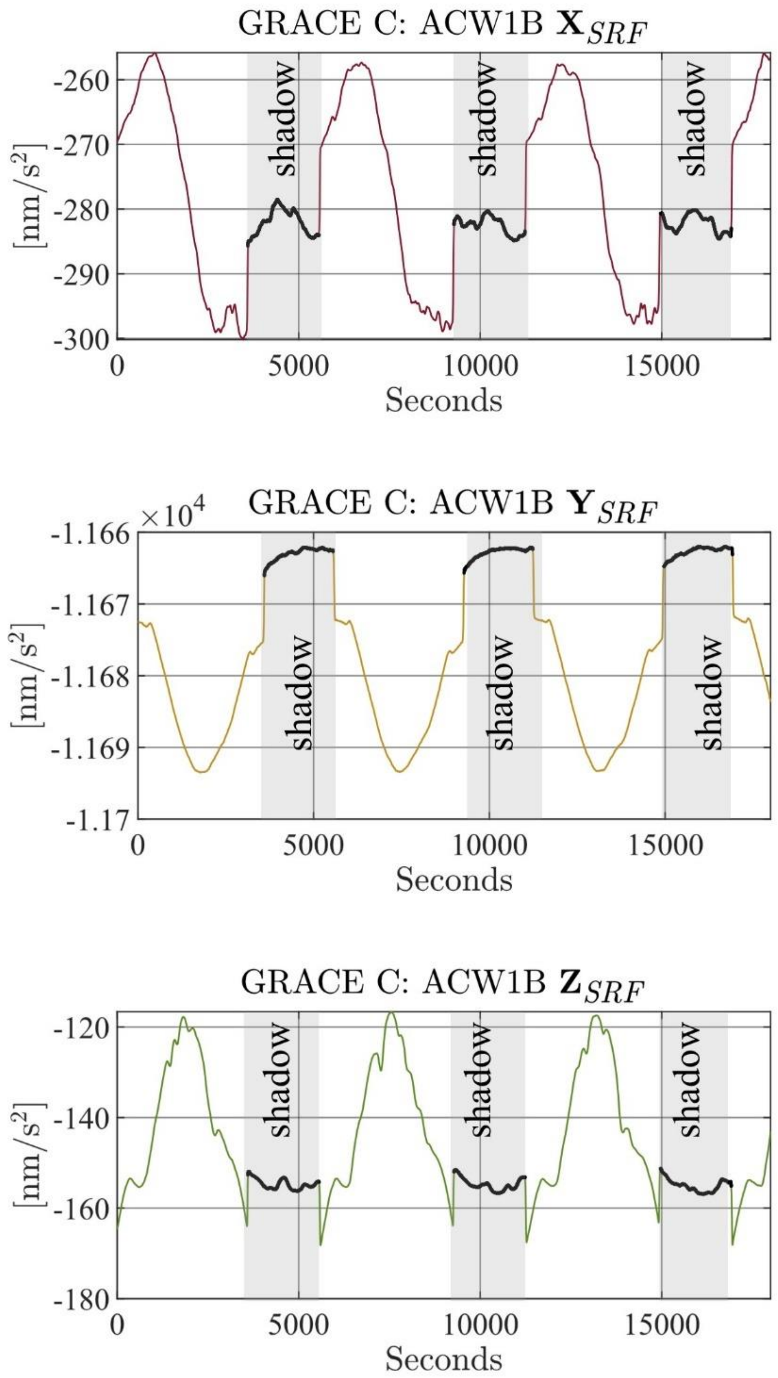

Figure 6.2 GRACE C, October 1st, 2018: Three orbital revolutions along the three axes of the accelerometer in the SRF. The grey-colored bands denote when the satellite is in the Earth's shadow.

The method is as follows, with each step corresponding to the letter next to each of the panels in Fig. 6.3:

a) To model the drag in the X_{SRF}, the shadow and the mid-point of the sun-illuminated segments are selected to form the weighted time series because in these orbital segments SRP=0 and the drag is the dominant force acting on the satellite. In the X_{SRF}, at the mid-point of the illuminated segment, the drag is the dominant force acting on the satellite, since the satellite top surface is the only one that is exposed directly to the Sun (in the radial direction). This is also clear from the physical SRP models that show a transition of the SRP from positive to zero and then to negative at the midpoint. This change in the SRP from positive to negative is due to the position of the satellite w.r.t. the Sun.

b) After modelling the drag with two resonant frequencies, very close to the period and the semi-period of the satellite (0.176 mHz and 0.358 mHz, respectively), the modelled low frequency drag component is subtracted from the ACW1B dataset. The residual series after this subtraction contains the radiation pressure (RP), which includes the SRP, ERP, TRP and shorter wavelength drag variations.

c) Next, we model the SRP component of the RP, by fitting 4 sinusoids, based on the weighted Least Squares spectrum, with frequencies close to the period and its three harmonics. We can claim that we model the SRP component of the RP since these low frequencies are consistent with those found in the literature (Kim, 2000) and agree with the spectral characteristics of the SRP.

d) Since we apply this method to the weighted ACW1B dataset, after subtracting the two models from the ACW1B dataset, we obtain a residual series containing some structured signals which we further investigate using signal decomposition.

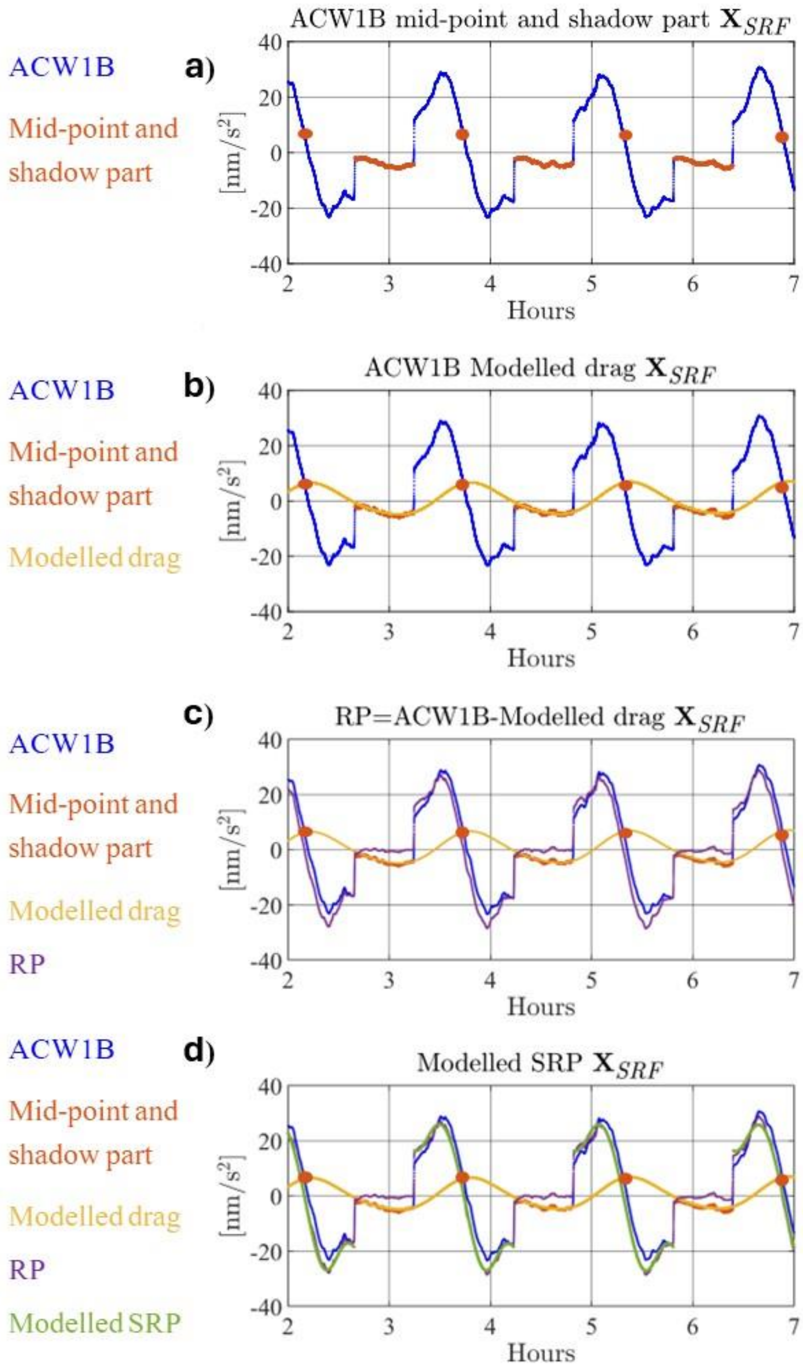

Figure 6.3 GRACE C X_{SRF} (November18,2018): a) ACW1B (blue). The selected mid-point and the shadow segment of the orbit (red). b) The modelled drag using the LSSA with two resonant frequencies (yellow). c) RP= ACW1B measurements -modelled drag (purple). d) The modelled SRP by fitting 4 sinusoids (green).

In the final drag and TRP models depicted along the three axes in Fig. 6.4, we must add a bias so the drag can be positive in the X_{SRF} due to the convention of the SRF and nearly zero in the other two axes. The TRP in the Y_{SRF} should also be positive, while the TRP in the Z_{SRF} is negative in the shadow segments and positive in the sun-illuminated segments. Since this method is based on accelerometer measurements which have an inherent bias, it is not feasible to accurately retrieve the bias for the drag, contrastingly to the SRP because it is known that SRP=0 in the shadow segments of the orbit.

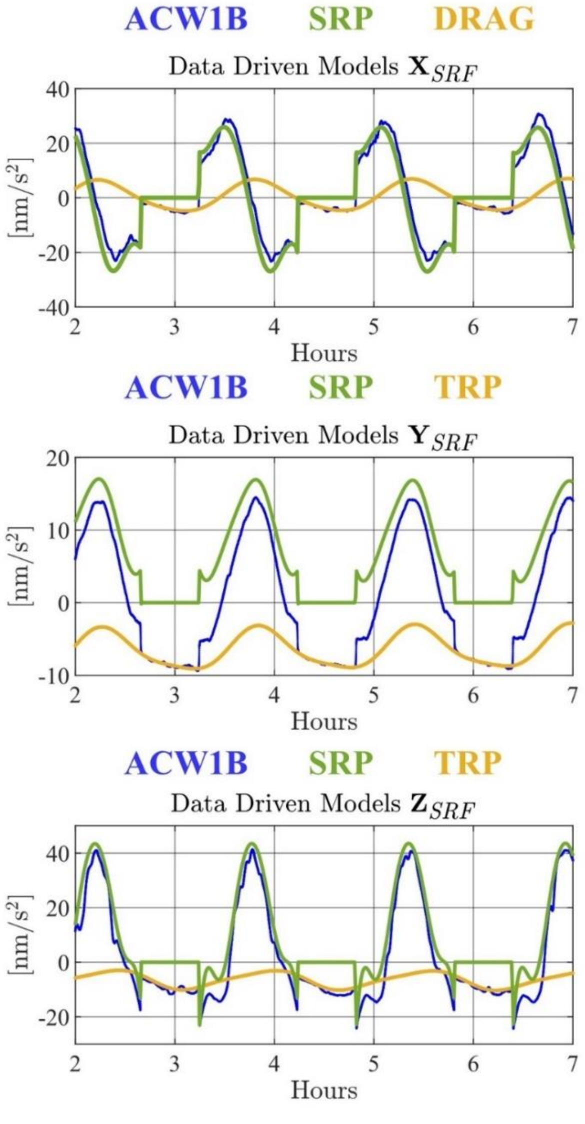

Figure 6.4 GRACE C (November 18, 2018): Top panel: The ACW1B measurements along the X_{SRF} (blue), modelled SRP (green) and drag (yellow). Middle panel: The ACW1B measurements along the Y_{SRF} (blue), modelled SRP (green) and TRP (yellow). Bottom panel: The ACW1B measurements along the Z_{SRF} (blue), modelled SRP (green) and the TRP (yellow). The drag signal is w.r.t mean zero for direct comparison with the SRP and includes a constant bias as explained in the text.

The drag bias can be estimated either through the gravity field solutions (via parameterization) or by direct regression methods using the unbiased physical models. We note that the determination of these biases through linear regressions necessitates the availability of physical models, which at the moment, are not widely accessible and perhaps not at the appropriate accuracy level. However, this is beyond the scope of this research. The approach for modelling the SRP and TRP on the Y_{SRF} as well as the SRP and the drag on the Z_{SRF}, is similar. The key difference is that for modelling the TRP on the Y_{SRF} and the Z_{SRF}, only the shadow segments of the orbits are considered, excluding the midpoint of the illuminated segment of the orbit. This is because the SRP is zero only in the shadow and does not alternate between negative and positive values like in the X_{SRF}. The final data driven models of drag, SRP and TRP are illustrated in Fig. 6.4 for the three axes.

6.3.2 Error Analysis

Since we are applying modeling using the accelerometer measurements of the ACW1B dataset, it is necessary to provide the error estimates of the models starting from the errors of the measurements (ACW1B) as derived in Chapter 5. The error estimates of the models and the residuals thereof are the results of the least squares estimation process followed here (LSSA). Error bars (3σ) in the previous plots are now shown for clarity in Fig. 6.5, which zooms in on a specific part of the orbit. For the error analysis, the following steps are taken:

a) The accelerometer measurements in each desired axis are selected. We select the shadow part and the mid-point of the sun part of the orbit (the mid-point applies only to the X_{SRF}) along with their corresponding variances from our ACW1B.

b) Using the LSSA remove (suppress) the mean, and the orbital and semi-orbital components from the series with frequencies 0.1761 mHz and 0.3526 mHz determined by the LSSA .

c) Calculate the variances of the modelled drag: The modelled drag comprises two signals

$$S_{1drag=}A_1 \cos(\omega_1 t) + B_1\, sin(\omega_1 t) \tag{6.1}$$

$$S_{2drag=}A_2 \cos(\omega_2 t) + B_2\, sin(\omega_2 t), \tag{6.2}$$

where A_1, A_2, B_1, B_2 are the amplitude coefficients derived from the least squares solution and are used to calculate the amplitude A and the phase φ of each signal and ω_1 and ω_2 are the orbital and semi-orbital frequencies.

The variances of the modelled drag are calculated from

$$\sigma_{drag}^2 = \left(\frac{\partial S_{1drag}}{\partial t}\right)^2 \sigma^2{}_{S_{1drag}} + \left(\frac{\partial S_{2drag}}{\partial t}\right)^2 \sigma^2{}_{S_{2drag}} + 2\left(\frac{\partial S_{1drag}}{\partial t}\right)\left(\frac{\partial S_{2drag}}{\partial t}\right)\sigma_{S_{1drag},S_{2drag}} \tag{6.3}$$

d) Calculate the covariance matrix of the residuals:

$$C_{rdrag} = \sigma^2(I - D), \tag{6.4}$$

where I is the identity matrix and

$$D = H(H^T P H)^{-1} H^T P \tag{6.5}$$

where H is the design matrix and P is the weight matrix.

e) Since $RP = ACW1B - modelled\ drag$, then assuming zero correlation between the two we get

$$\sigma_{RP} = \sqrt{\sigma_{drag}^2 + \sigma_{ACW1B}^2} \tag{6.6}$$

f) The variances of the modelled drag are calculated as in Step (c).

g) Calculate the covariance matrix of the residuals C_{rSRP} using the formula from step 4.

In Fig. 6.5 we show the ACW1B measurements and the derived drag and SRP models in the X_{SRF} along with the standard deviations calculated from the analysis above. The error bars in Fig. 6.5 represent the 3σ. In Fig. 6.6, we illustrate the residuals (grey error bars represent (1σ) and their standardized residuals while in Fig. 6.7 we show the histograms of the residuals and the standardized series.

From Fig. 6.6, we draw the following conclusions:

a) The residuals in the X_{SRF} do not exceed $2\,nm/s^2$ during quiet days but can exceed $10\,nm/s^2$ during disturbed days, as is further discussed in Section 6.3.3.

b) The residuals in the Y_{SRF} are less than $0.5\,nm/s^2$. This is expected since in the Y_{SRF} the SRP and the TRP are the most dominant forces acting on the satellite.

c) In the Z_{SRF}, the residuals exceed $2\,nm/s^2$ during penumbra transitions. This is because the magnitude of the entry penumbra transition can differ by up to $5\,nm/s^2$ compared to the exit penumbra transition, making it difficult to model the penumbra transitions accurately.

d) In the radial direction, the component of the ERP in the residuals is significant, therefore the Z_{SRF} has larger residuals in magnitude.

e) The histograms of the daily residuals ($N = 86400$) are constructed using 100 bins (Fig. 6.7). The black curves show the experimental normal distribution (the mean and variance are taken for the residuals). This overlay allows for a comparison between the observed (experimental) residual distribution and the experimental normal distribution. For this specific day the standardized residuals in the X_{SRF} and Y_{SRF} do not exceed the value of 3 contrastingly to the Z_{SRF}, which as mentioned, contains the ERP variations.

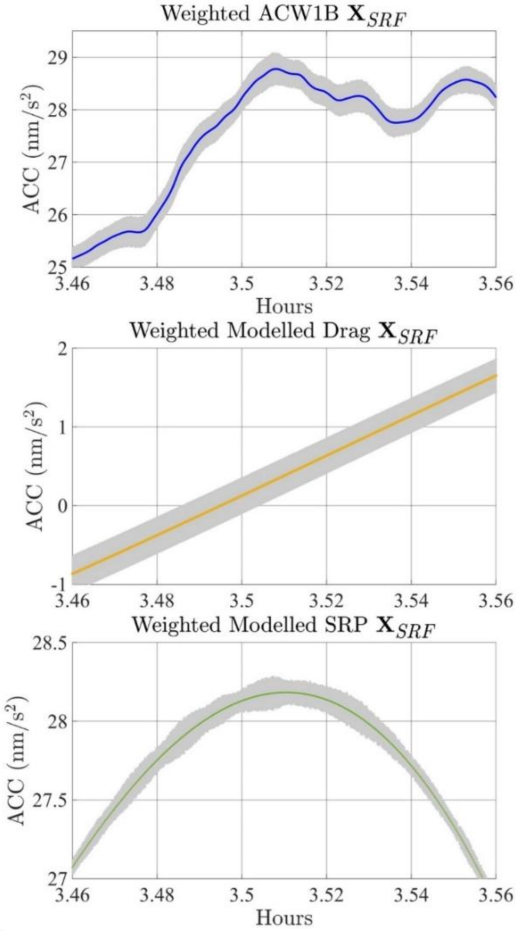

Figure 6.5 Orbital segments of each step with the corresponding standard deviation. The grey error bars represent 3σ to enhance visualization clarity. From top to the bottom: ACW1B in the X_{SRF}, the modelled drag (yellow), the modelled SRP (green).

In Table 6.1 we show the mean and the standard deviation of the residuals $\hat{\boldsymbol{r}}$ and the standardized residuals $\tilde{\hat{\boldsymbol{r}}}$ along the three axes of the accelerometer.

Table 6.1 The mean and the standard deviation of the residuals and the standardized residuals along the three axes (units: $\boldsymbol{nm/s^2}$).

Axis	Mean $\hat{\boldsymbol{r}}$	$\boldsymbol{\sigma_{\hat{r}}}$	Mean $\tilde{\hat{\boldsymbol{r}}}$	$\boldsymbol{\sigma_{\tilde{\hat{r}}}}$
$\boldsymbol{X_{SRF}}$	0.07	1.17	0.04	0.85
$\boldsymbol{Y_{SRF}}$	0.03	0.09	0.01	0.83
$\boldsymbol{Z_{SRF}}$	-0.29	2.3	-0.02	0.97

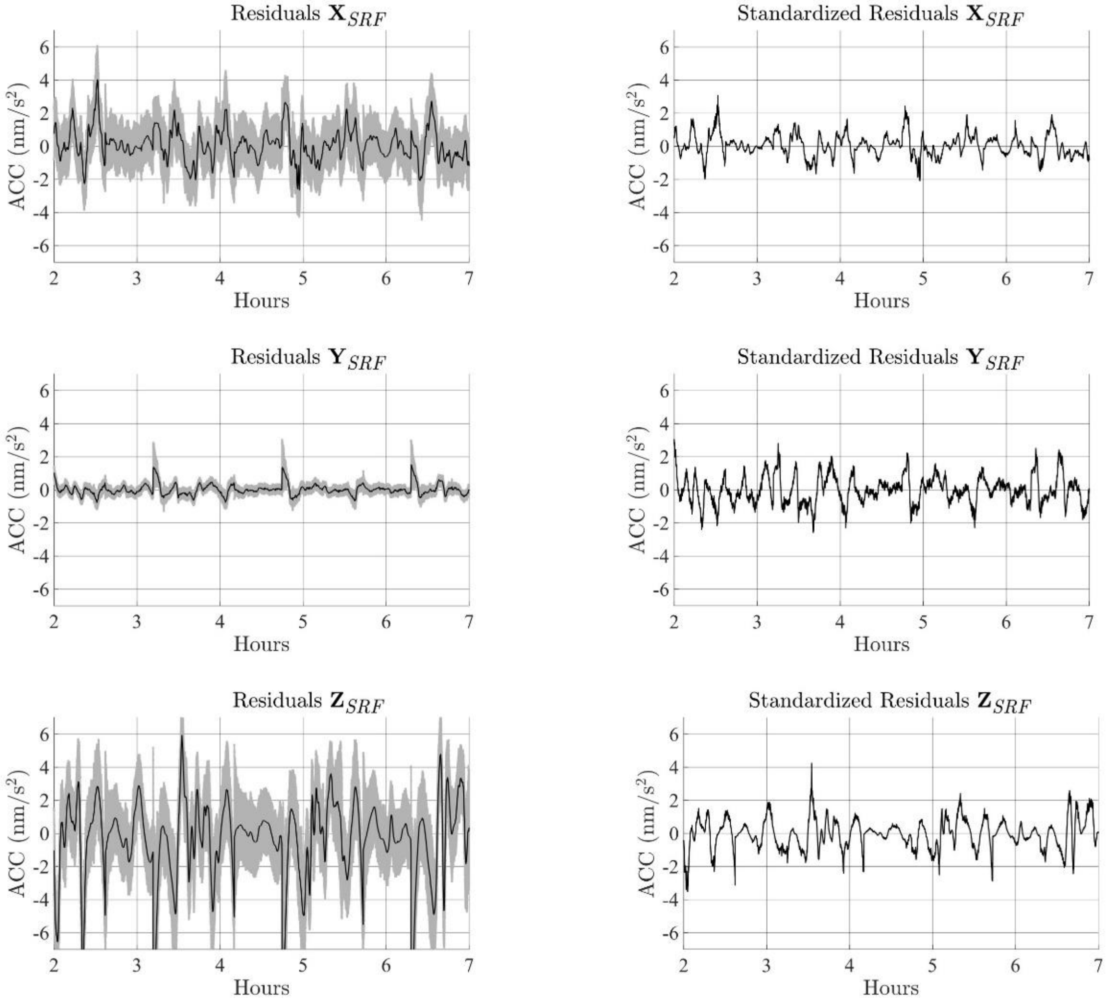

Figure 6.6 GRACE C (November 18, 2018): Left panels: Three orbital evolutions of the residuals after the subtraction of the drag and the SRP model from the ACW1B measurements. The corresponding standard deviations are shown in grey (1σ). Right panels: The standardized residuals along the three axes.

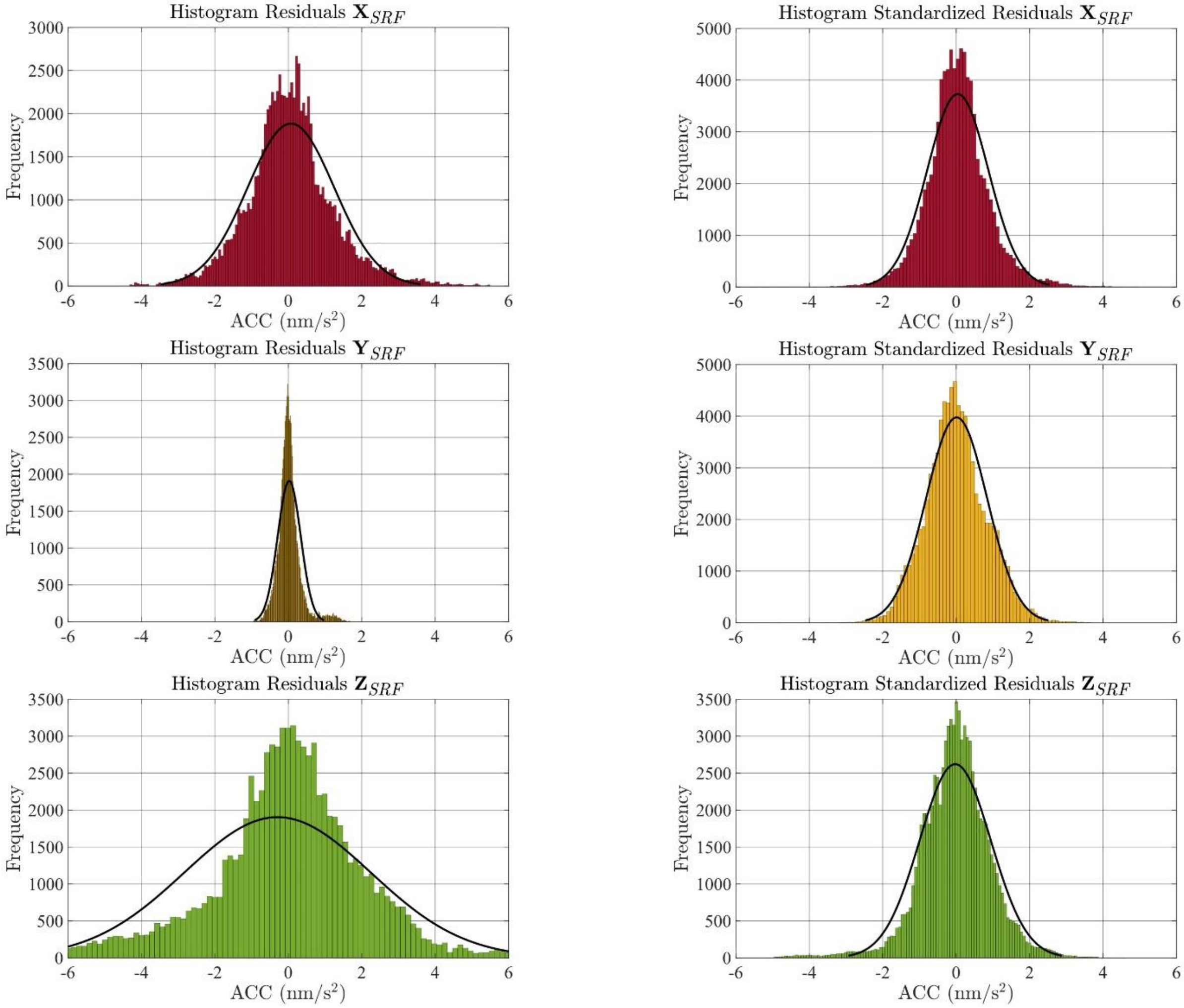

Figure 6.7 Left panels: The histograms of the residuals along the three axes (number of bins=100). Right panels: The histograms of the standardized residuals along the three axes (number of bins=100). The black curves in the histograms denote the experimental normal distribution.

6.3.3 Residual Series

We apply our modelling method described previously to a one-year-long ACW1B along the three axes namely, from August 1st, 2018, to July 31st, 2019. The residual series after subtracting the modelled drag and the SRP are shown in Fig. 6.8, along with the β' variations (light gray line) and the Power Spectral Densities (PSDs). To the best of our knowledge, no other published study has presented an extensive analysis of the residuals w.r.t. the acceleration measurements that would indicate the accuracy of their models. The red circles in the Y_{SRF} and Z_{SRF} series point out to large residuals due to the mismodelling of the SRP, because the penumbra transitions cannot be modelled properly due to their small magnitude when $\beta' \approx 65°$. The vertical lines in the PSDs mark the $9mHz$ frequency, which is subsequently used as a cut-off frequency in the analysis of the residual series in Section 6.4. This cut-off frequency has been selected after examining the behavior of the PSDs, which show that at about $9mHz$ the PSD tends to change to a smaller slope at higher frequencies, indicating the start of noise (close to flicker noise).

In the X_{SRF} all the residuals exceeding $7\ nm/s^2$ correspond to geomagnetic storm, minor ($Kp = 3$) or major ($Kp > 6$). In contrast, the residuals in the other two axes do not show any correlation with these storms, which is expected since the drag in these axes (which is enhanced during a storm) is almost negligible compared to the drag in the along track direction. All the geomagnetic storms observed during the examined period are shown with grey arrows in Fig. 6.8.

In the X_{SRF} and Z_{SRF}, the smallest residuals occur when $\beta' > 50°$, as the satellite approaches its full Sun orbit and the penumbra transitions significantly decrease in amplitude, contrastingly to the Y_{SRF}, which shows the highest residuals during these periods. In the Y_{SRF} the smallest residuals are observed when $\beta' = 0°$. As mentioned in Chapter 4, the penumbra transitions in the Y_{SRF} are absent when $\beta' = 0°$, resulting in minimal SRP. Consequently, the SRP, being the dominant force acting on the Y_{SRF} can be modelled more accurately.

For a better representation of the dependency of residuals on variations in β', we adopt the concept of relative fluctuation amplitude, as referenced by Park *et al.* (2023). This concept was originally employed to analyze the residuals of thermospheric densities after applying a Savitzky-Golay filter (order = 3, window size = 17) to data extracted from GRACE-FO. While we do not apply this filter to our accelerometer residual series, we use the relative fluctuation amplitude to represent the undulation levels of the accelerations. The relative fluctuation amplitude is calculated as follows:

$$fluctuation_{relative} = \left|\frac{acc_{res}}{acc_{modelled}}\right| \tag{6.7}$$

where the acc_{res} represent the residuals after subtracting the modelled non-gravitational accelerations and the $acc_{modelled}$ represent the data-driven modelled non-gravitational accelerations. We choose to use the absolute value because our focus is on the amplitude of the residuals, therefore, whether the accelerations are positive, or negative is irrelevant. Please note that the relative fluctuation amplitude is utilized exclusively in Fig. 6.9 to show the dependency on β' variations. For the remainder of the analysis, we will focus on the residuals obtained after subtracting the modeled dominant forces. The relative amplitude fluctuations are shown in Fig. 6.9.

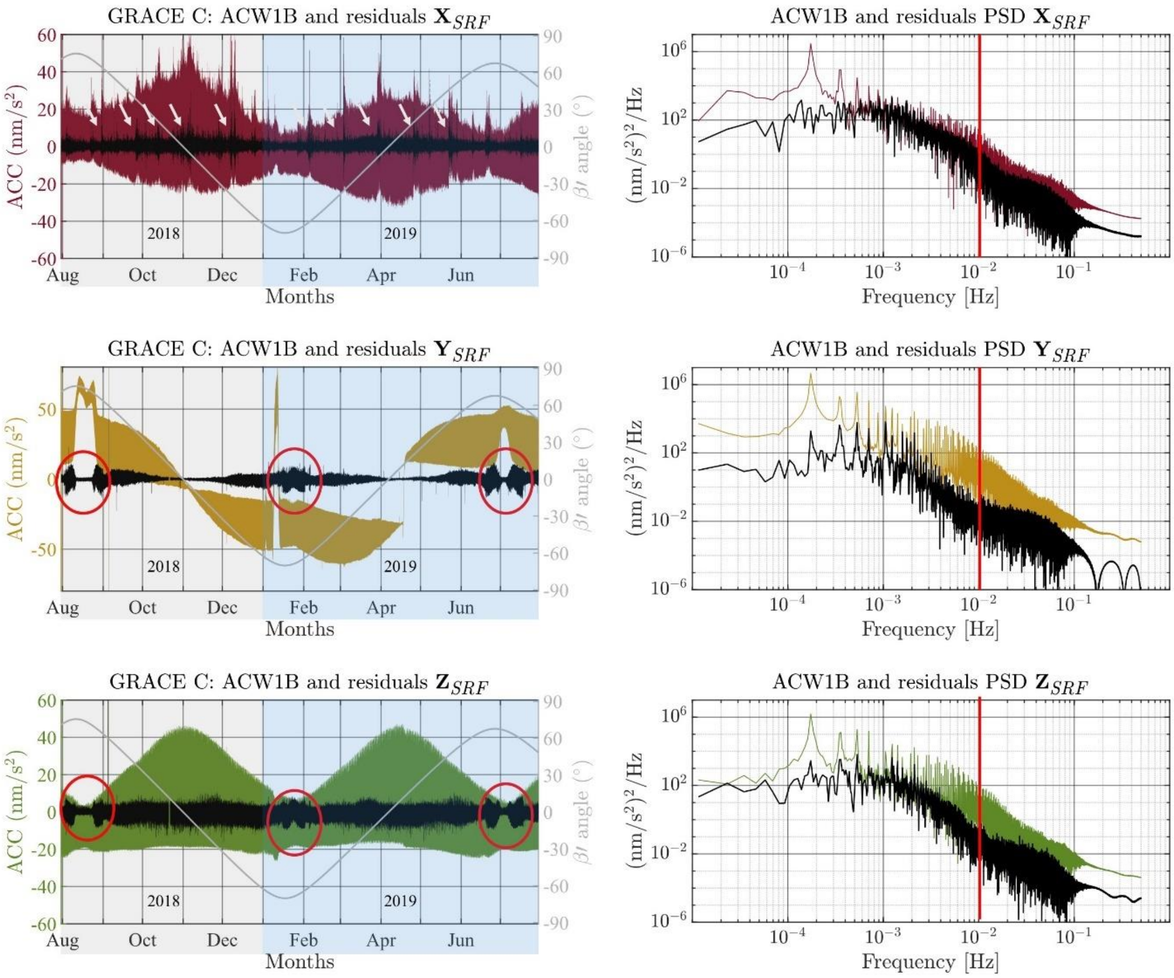

Figure 6.8 GRACE C, August – December 2019: The ACW1B measurements (red, yellow, green) along the three axes of the SRF and the corresponding residuals (black) (left column). The PSDs of the ACW1B (red, yellow, green) and the residuals (black). The red circles on the left figures indicate the mismodelling of the penumbra transitions and the vertical red lines on the right indicate the $0.009Hz$ frequency, which is used as a cut-off frequency during the analysis of the residuals.

From Fig. 6.9, it is evident that the residuals in the Y_{SRF} exhibit the highest dependency on β' variations. This observation is expected as β' significantly influences the thermal environment in which the satellite orbits the Earth, and the cross-track direction is the most sensitive to thermal fluctuations.

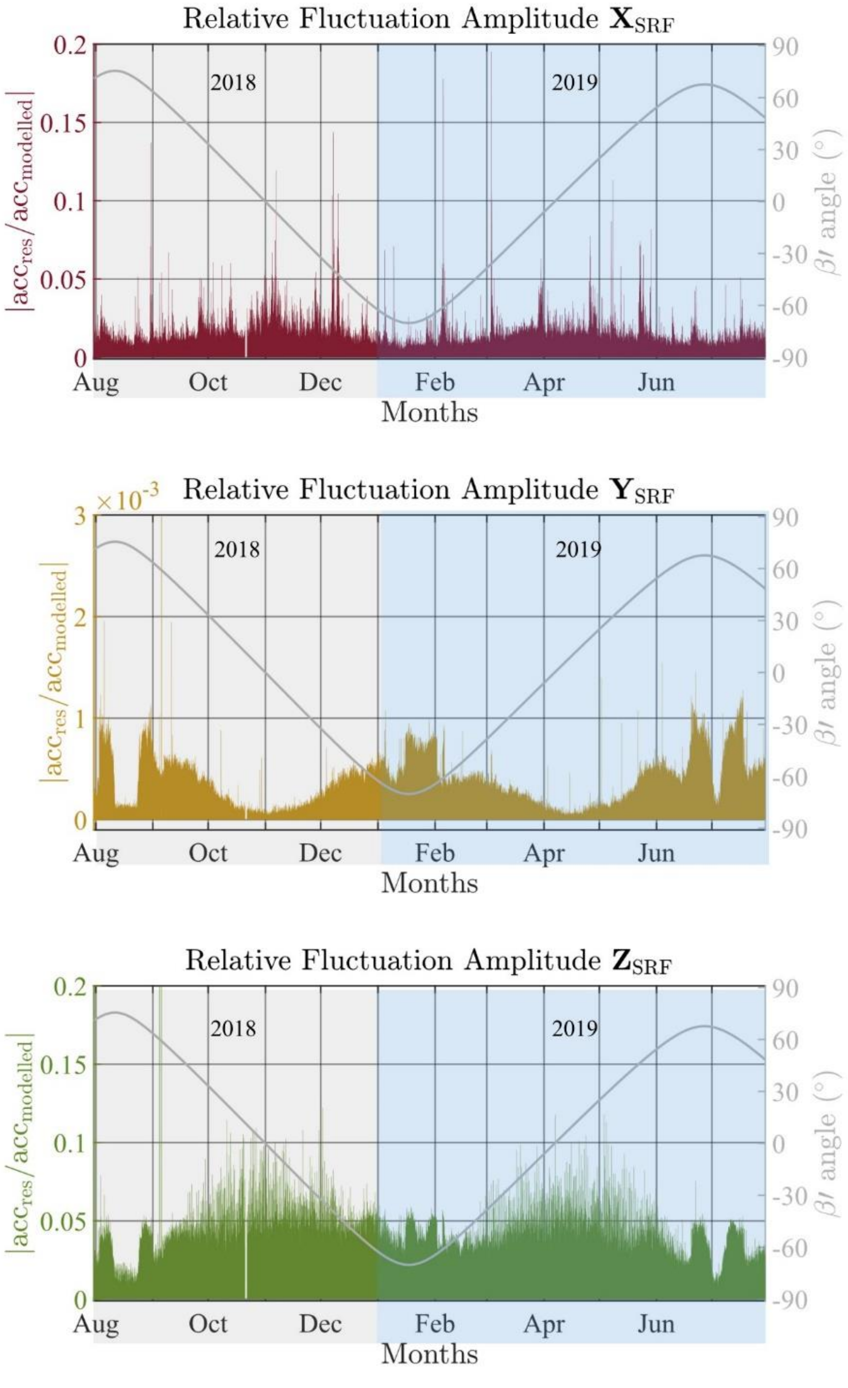

Figure 6.9 GRACE C, August – December 2019: Relative Fluctuation Amplitude along the three axes of the accelerometer. The β' variations are shown in light grey (right y-axis).

Figure 6.10 displays the ACW1B dataset (left column) with the corresponding residuals (right column) plotted versus the argument of latitude, allowing for the examination of any noticeable trends. The argument of latitude plot is explained in Chapter 5. The sections where the satellite crosses the Earth's shadow are indicated on the left panels to enhance the understanding of the plots. These plots resemble, as expected, the plots of the variances of the ACW1B produced in Chapter 5. The most dominant patterns in the residuals along the three axes occur during the entrance and the exit of the satellite to/from the Earth's shadow.

In the Z_{SRF} strong disturbances start in September 2018 during the descending orbits in the northern hemisphere and in February 2019 in the ascending orbits extending across both hemispheres. This inconsistency between the ascending and descending orbits has not yet been explained but since the residuals in the radial direction contain the ERP, we can attribute this asymmetry in the ERP.

To aid the reader's understanding, we provide in Fig. 6.11 the residual series in the X_{SRF} highlighting some of the disturbances that we can attribute to reasons other than the mismodelling of the penumbra transitions. The mismodeling of the penumbra transitions is highlighted with grey-filled dots. Additionally, strong disturbances during the terminator crossings, occurring before and after the penumbra transitions, are indicated with light, orange-filled dots. As noted, the residual series in the X_{SRF} show intense disturbances during geomagnetic storms, which are highlighted with white arrows. Furthermore, within the Earth's shadow, there are some well-structured signals with no latitude dependency, highlighted with blue circles. The intense vertical lines on the Y_{SRF} in August 2018, January and April 2019 are due to a sudden jump in the accelerometer measurements (see Fig. 6.8).

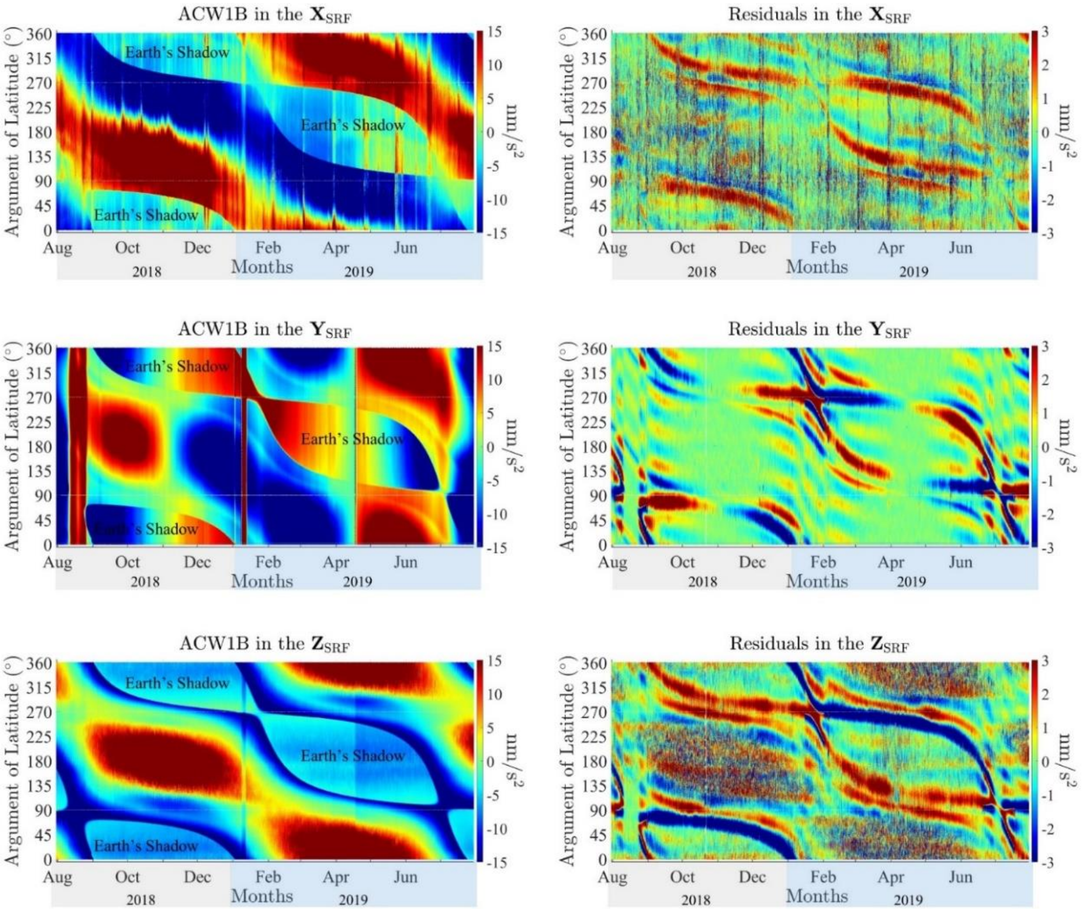

Figure 6.10 GRACE C, August – July 2019: Argument of Latitude vs Time. Left column: The ACW1B measurements along the three axes w.r.t. mean zero. Right column: The residual series w.r.t. mean zero along the three axes.

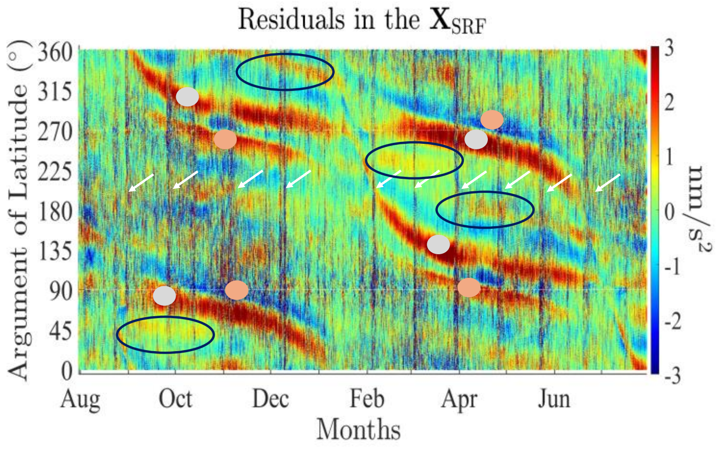

Figure 6.11 Argument of latitude plot during August 2018 – July 2019 of the residuals in X_{SRF}. The white arrows indicate the enhances disturbances during minor and major geomagnetic storms, the grey-filled dots highlight the entrance and the exit to/from the Earth's shadow and the light, orange-filled dots the terminator crossings. Unknown structured signals inside the Earth's shadow, with no latitudinal dependency are shown in blue circles.

6.4 Signal Decomposition

In this approach, by modelling the two dominant forces of Drag and SRP directly from the measurements of ACW1B, we result to a residual series that contains shorter wavelength drag variations, ERP and TRP. Using the LSSA it is impossible to model separately these non-gravitational forces due to their shorter variations and their coupling. Therefore, a signal decomposition using Daubechies wavelet is implemented, and this analysis reveals that signals in different frequency bands are connected to the ERP, shorter drag variations and others that can be connected to ionospheric disturbances. In the literature, usually the TRP is modelled using a finite element approach dependent on the satellite shape, the altitude of the orbit and the environmental condition (Rievers *et al.*, 2016) therefore it is very challenging to derive a model for TRP directly and accurately from the measurements. For the signal decomposition, the Daubechies mother wavelet is used as it performs very well in power system engineering and has been used in the studies of interplanetary magnetic field fluctuations (Gonzalez *et al*., 2014; Mandrikova *et al*., 2021).

The signal decomposition has been carried in the X_{SRF}, since the along-track measurements are affected the most by the drag. In the residual series of the X_{SRF}, signals connected to geomagnetic storms are observed. For the investigation of the residual series, signal decomposition is mandatory to decipher the disturbances included in the signals. From the PSDs of the residual signals (see Fig. 6.7), it is shown that above $9mHz$, the signal contains high frequency noise, therefore we filter further the residual series with a low-pass filter of a $9mHz$ cut-off frequency. The filtered series is then decomposed into different frequency bands to investigate the residuals (disturbances). In this analysis the Daubechies mother wavelet (db8) of 13 levels is used and the length of the series used for the decomposition was one month. There are several Daubechies wavelets (eg. db2, db4, db8, db10) with the number indicating the order of the wavelet. The higher the order, the smoother and more extended the wavelet functions are.

Monthly data are used for this analysis to avoid the length restrictions in the numbers of the levels that we can decompose our series. Each level of decomposition splits the signal into the approximation coefficients with the detail coefficients, representing the low and the high-frequency components respectively. The different frequency bands from signal decomposition are the following:

Table 6.2 Relative energy of different levels from the signal decomposition of db8 of 13 Levels.

Levels	Frequencies (mHz)	Relative Energy
Level 11-13	0.1 mHz - 0.5 mHz	28.6%
Level 8-10	0.5 mHz - 4 mHz	65%
Level 7	4 mHz - 8 mHz	3.8%

In the lowest frequency bands (Levels 11-13) that contain 28.6 % of the energy of the residual series, low frequency signals very close to the orbital period and its harmonics are observed. Since these signals contain residuals of the suppressed orbital period and its harmonics, they represent the RP components that cannot be modelled using the LSSA (residuals of RP).

In the next levels (Levels 8-10) of decomposition, from 0.5 mHz - 4 mHz, the disturbances in the signal do not show any spatial correlation. Their magnitude is much higher during a geomagnetic storm, and they agree with the shorter disturbances when the satellite is in the shadow of the Earth. From this agreement, we attribute the signals in this frequency band to shorter drag variations. The last frequency band (Level 7) is between 4 mHz - 8 mHz and contains disturbances that vary with latitude. Levels 1 to 6 are not shown in Table 6.1 as they contain less than 3% of the total energy of the signal.

Figure 6.12 depicts the residuals of levels 8-10 (shorter drag variations). Since there is no visual dependency on β', the β' variations are not plotted (panels (a)). From the argument of latitude plots (panels (b)) between August and December 2018, it is shown that the residuals of Level 7 apart from the disturbances during the geomagnetic storms, show disturbances in the polar regions (the darker areas on the left panel (b)) The residuals of Levels 8-10 apart from the disturbances during the penumbra transitions exhibit stronger disturbances during geomagnetic storms and terminator crossings (before and after the entrance and from the Earth's shadow). Additionally, a strong signal is observed when the satellite is in the Earth's shadow, starting from September and continuing until December.

In Figure 6.12, the spectrograms of the two Levels are depicted from August 24-28, 2018. On August 25, a geomagnetic storm of $Kp = 7$ occurred. The CME event arrived at the Earth on August 25 at 0200 UT, causing a compression of the magnetosphere at 1200 UT. At 1600 UT, a negative direction in the Bz[38] component triggered the main phase of the storm. The minimum $Dst = -175\ nT$[39] was reached at 0600 UT on August 26 (Piersanti *et al*. 2020). From July 2018 to December 2020, this was the only storm to reach $Kp = 7$. In the spectrogram of Level 7, high frequency disturbances are shown, while in the spectrogram of Levels 8-10, it is clear when the satellite was affected by the storm on August 25th.

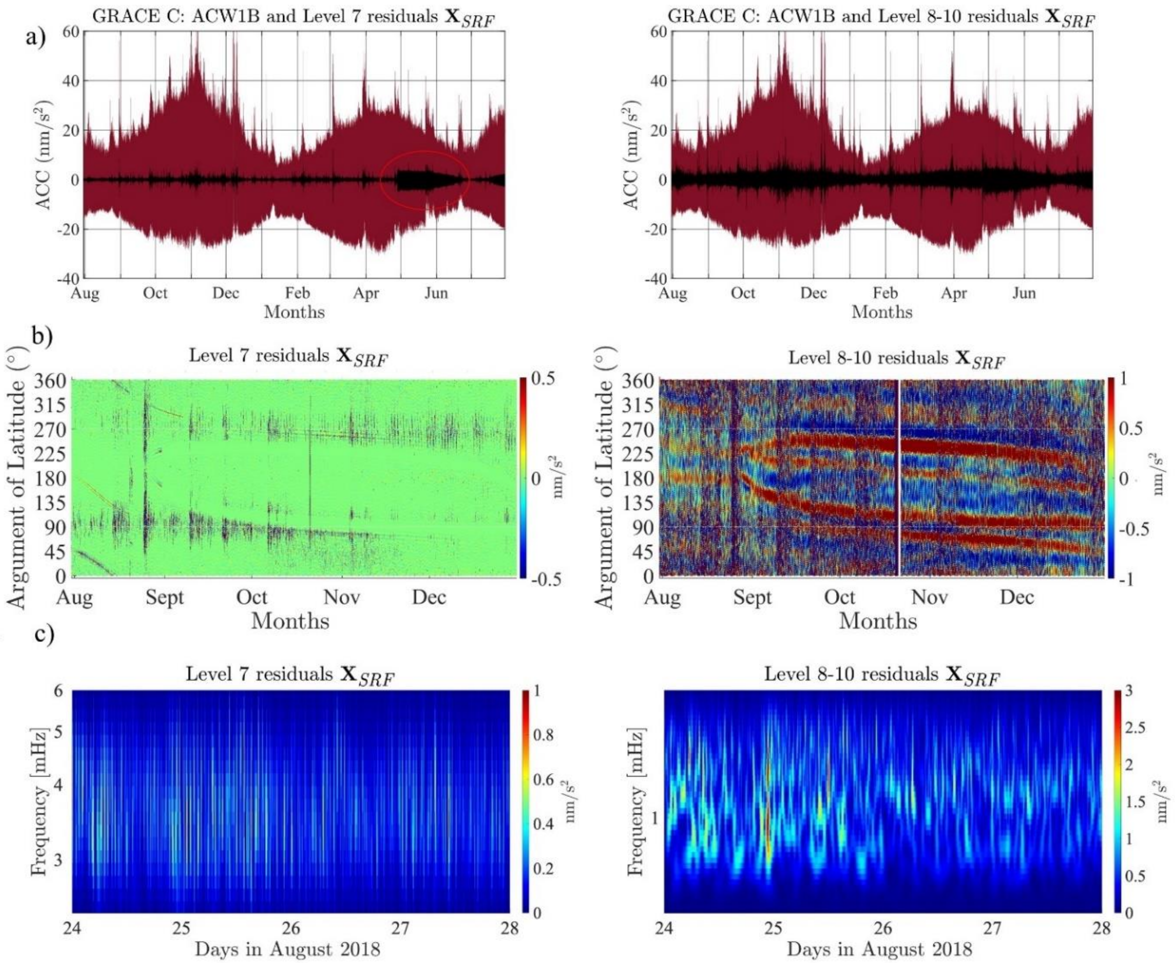

Figure 6.12 GRACE C, August – December 2018: a) ACW1B in the X_{SRF} (red) and residuals (black line) on Level 7 (left) and on Level 8-10 (right); The red circle in May and June indicates larger residuals due to the mismodelling of the penumbra transitions. b) Argument of Latitude plot from August to December 2018. c) Spectrograms from August 24th to August 28, 2018.

---

[38] Bz is the geomagnetic flux density along the vertical.

[39] The Disturbance-storm-time (*Dst*) index is a measure of the severity of geomagnetic storm. The range of the *Dst* index is generally $-400 < Dst < +100\ nT$, with large negative values indicating a geomagnetic storm.

Figure 6.13 shows the residuals of Level 7 in the X_{SRF} for seven orbital revolutions of the satellite on the first day of each month from August 2018 to January 2019. The red zigzag lines indicate the latitude of the satellite during these orbital revolutions, with the zigzag line indicating the satellite tracks. The different colors in the time series correspond to various local times, as defined in the color bar on the right side of the figure. Dark blue indicates a local time (LT) of 0000, while red indicates a LT of 2400. For example, the orange segments of the time series correspond to LT 1800, while the light blue segments correspond to LT 0600.

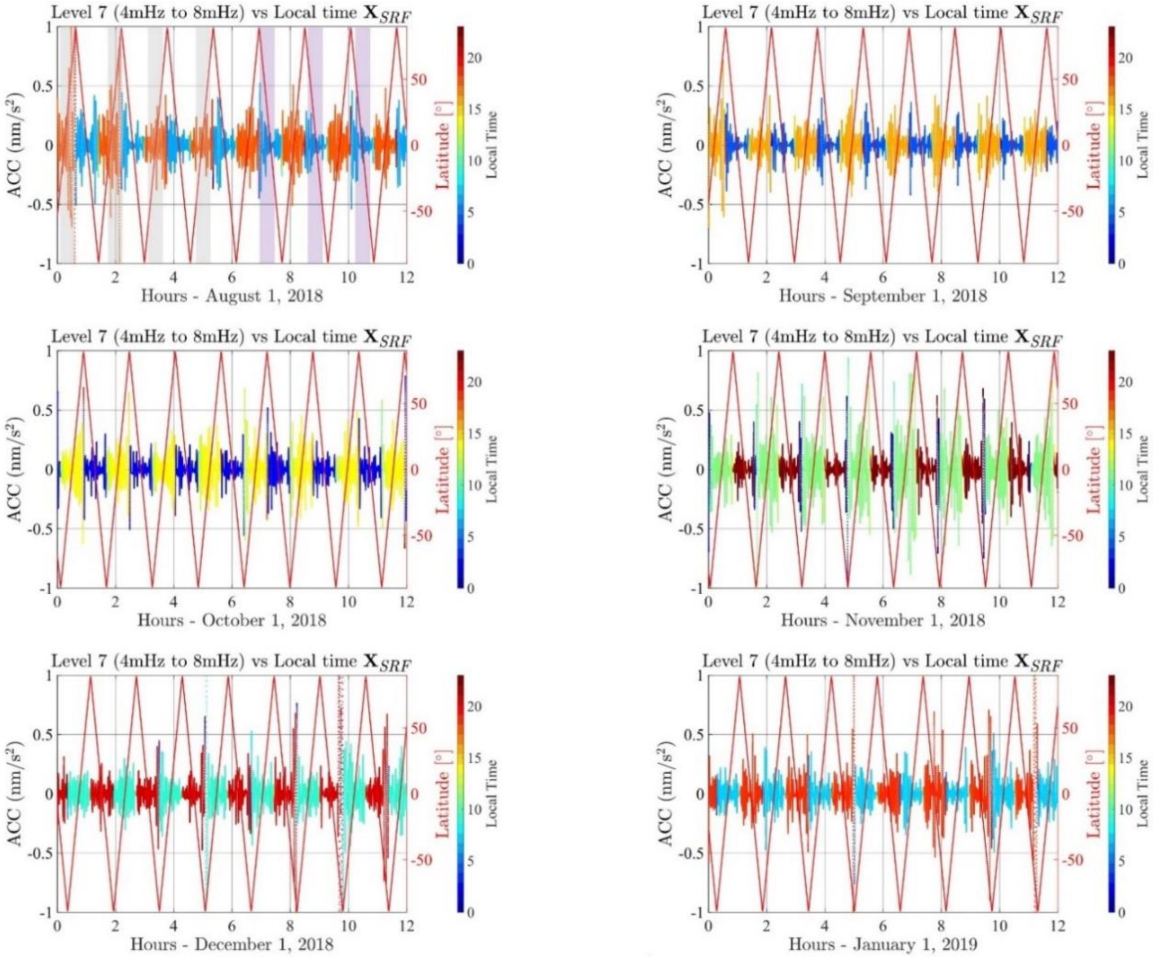

Level 7 (4mHz to 8mHz) vs Local time $\mathbf{X}_{SRF}$

Figure 6.13 Residuals from Level 7 in the X_{SRF} are shown for seven orbital revolutions of the satellite on the first day of each month from August 2018 to January 2019. The left side of the vertical axis of the graph indicates the magnitude of the residual time series in Level 7, while the right side indicates the latitude. The different colours of the time series represent the local time, as defined by the colour bar. The grey bands on the top left panel indicate the ascending segment of the orbits, while the purple bands indicate the descending orbits from the Northern Hemisphere to the Southern Hemisphere. These coloured bands are shown only in the top left figure to enhance the readability of the data.

From our analysis, carried out over multiple days, we can conclude that the residuals (disturbances) exhibit a dependency on latitude rather than on local time. The largest residuals occur when the satellite crosses the equator in an ascending orbit, rather than in a descending one. These disturbances could be linked to the satellite's alignment with Earth's magnetic field lines. The inconsistency between the ascending and descending orbits could be attributed to the emergence of the magnetic field lines from near the geographic south pole and their convergence at the north pole.

6.5 Summary

In this chapter, innovative data-driven models for the non-gravitational accelerations were presented, based solely on the spectral characteristics of the dominant forces acting on the satellite: Drag, Solar Radiation Pressure (SRP) and Thermal Radiation Pressure (TRP). The significance of modeling non-gravitational accelerations in various contexts has been emphasized, and all the necessary steps to derive the weighted models of these dominant forces have been thoroughly explained. The importance of our contribution lies in the determination of the calibrated atmospheric drag at LEO altitudes, directly from the accelerometer measurements (up to a bias term) that can be used to model thermospheric density and neutral winds in the upper atmosphere, thus contributing to space weather research. Additionally, further study of the residuals could enhance our understanding of various phenomena that affect the satellite. Through signal decomposition using wavelets, the residual series in the X_{SRF} were investigated, and disturbances due to geomagnetic storms or disturbances with latitudinal dependency have been identified. However, no correlation with local time has been found from this analysis.

During this analysis, important questions have arisen that should be highlighted for future studies in non-gravitational acceleration. First, a comparison between different physical models is essential to clearly understand the variations among methods. Secondly, an extensive analysis of the measurement residuals is mandatory to identify different patterns. However, due to spurious spikes in the ACT1B dataset, this analysis is currently impossible because any useful signal is buried in the noise of the Y_{SRF} and Z_{SRF}. We were able to conduct this analysis using the proposed ACW1B dataset (presented in Chapter 5), which underscores the importance of a weighted accelerometer dataset. Lastly, an extensive analysis of the physical models of ERP (albedo and IR) on GRACE missions is missing from the literature, which makes the investigation of the ERP forces quite difficult. For all these reasons, we are confident that modeling the non-gravitational forces using our method and investigating the residuals presented in Chapter 6 could enhance our understanding of how different forces depend on latitude, the crossings of the satellite through the terminator, and the Earth's shadow. Additionally, this approach could help identify regions where the drag is enhanced, not only due to geomagnetic storms but also due to other conditions.

There are many things yet to be explained, such as the difference in the intensity of the disturbances during the ascending and descending orbits, the reason for enhanced disturbances during terminator crossings (as explained in detail in Chapter 5), and the difference in the intensity of disturbances at the North and South Poles. More details will be presented in Chapter 7.

7 Conclusions and Future Work

7.1 Conclusions

In this dissertation, three significant challenges related to the accelerometer on GRACE missions were addressed using original methods: the on-orbit calibration of the accelerometer, the occurrence of spurious spikes in the measurements, and the error assessment and modelling of the dominant non-gravitational forces acting on GRACE satellites. These challenges have been preoccupying the international research community for the last 25 years since the first space gravity mission CHAMP was launched. The significant advances in space geodesy, the determination of Earth mass change, and the studies of the thermosphere/ionosphere system using these missions continue with improvements and enhancements. Improvements are required in the measurement quality, their processing methodologies, the calibration of the accelerometers, the modelling of the non-gravitational accelerations and development of new and more accurate gravitational models. Along these lines, and in anticipation of the planned follow-on Mass Change (MC) and MAGIC missions, we tackled the three challenges mentioned above from an entirely new perspective.

Since it is impossible to calibrate the accelerometer on the ground, the state-of-the-art calibration parameters are typically retrieved either with the gravity field solutions, estimated among thousands of unknown parameters, or by using physical models after subtracting the gravitational accelerations from the total acceleration of the satellite derived from precise orbit determination (POD). Clearly, the use of theoretical models in the calibration of an instrument or sensor is liable to the level of accuracy of the theoretical models due to unavoidable omission and commission errors. In the case of GRACE missions, the parameterization of the calibration parameters of the accelerometers along with thousands of other unknown parameters for the retrieval of the gravitational field models introduces unknown and perhaps significant correlations that bias the estimated parameters.

In this research, the most critical challenge of the accelerometer calibration was to avoid entirely the state-of-the-art force models (physical or theoretical), by using only the accelerometer measurements and precise kinematic orbit position estimates. This challenge was tackled with an all-new thinking that considered a possible “matching” or “correlation” of the accelerometer measurements (to be calibrated) with the total accelerations derived from the precise kinematic POD positions. More specifically, we strove to “match” characteristic waveforms (in our case the penumbra transitions) that we knew were present in both datasets. The striking hurdle however was the shear difference between the two data sets, reaching nine orders of magnitude. The penumbra transitions, while clearly visible in the accelerometer measurements, were deeply buried in the noise of the POD accelerations. To bypass this hurdle, we employed, for the first time, the concept of *wave focusing* methodologies as applied in radar applications for signal detection, specifically the *time reversal* approach (matched filter). The key to applying the matched filter in our context was that the penumbra transitions are synchronous in both signals. Knowing the exact timing of the penumbra transitions allowed us to focus on detecting these transitions precisely when they occurred.

To retrieve the scale factor i.e., the ratio between the penumbra transitions measured by the accelerometer and those hidden in the POD data, we used energy normalization of the signals to account for the significant difference in their power. Daily scale factors were derived for GRACE A, GRACE B, and GRACE C satellites and compared with those derived from the sate-of-the-art methods presented in other studies, showing reasonable agreement. The bias of the accelerometer was retrieved by applying a daily quadratic fit to the accelerometer measurements. The calculated bias values can be used as initial weighted parameters along with the scale factor in the gravity field recovery process.

A long-expected improved level 1B accelerometer dataset namely the weighted ACW1B was derived in this research by processing the raw accelerometer measurements from the Level 1A (ACC1A) dataset considering, for the first time, that the ACC1A measurements form a stochastic process and by extension the derived ACW1B is a random process. Currently, both ACC1A and ACT1B are considered errorless in the retrieval of the gravity field parameters. This new ACW1B dataset is highly valuable for retrieving thermospheric densities due to the absence of the dominant spikes present in the existing 1B accelerometer datasets (ACT1B) of GRACE missions. The accelerometer measurements in the cross-track and radial directions are often contaminated by spurious spikes, making it almost impossible to retrieve useful information from these axes. This novel ACW1B effectively addresses this issue, ensuring more accurate and reliable data for further analysis and modelling.

The variances of the new ACW1B dataset revealed a strong dependency on β' angle variations. The variances increase when the satellite enters and exits the Earth's shadow, attributed to temperature changes in the upper atmosphere, to which the accelerometer is sensitive. Interesting patterns were revealed before and after the penumbra transitions, where the satellite crosses the terminator. The terminator, due to intense temperature changes and subsonic speed, generates acoustic gravity waves (AGWs). The disturbances shown in the variances could be attributed to AGWs, though this requires further investigation. Additionally, disturbances during geomagnetic storms, which can last for several days, were observed, highlighting that the accelerometer measurements can reveal many phenomena related to thermospheric changes.

The new ACW1B, which does not contain spurious spikes was used to model the dominant non-gravitational forces of drag, solar radiation pressure (SRP), and thermal radiation pressure (TRP) acting on GRACE C using, for the first time, a data-driven approach. An extensive and in-depth analysis of the residuals after subtracting the models from the ACW1B enabled the extraction of valuable shorter wavelength information on the measured accelerations, which may significantly enhance the accuracy and reliability of the non-gravitational models. The detailed residuals analysis facilitated by the clean ACW1B dataset allowed for the identification and understanding of subtle phenomena that were previously obscured by noise.

New insights into the effects of the non-gravitational accelerations on the satellites were revealed for the first time using the ACW1B and the new data-driven modelling approach. Based on the spectral characteristics of drag, SRP, and TRP, we could effectively model the dominant forces: SRP and drag in the X_{SRF} direction, and SRP and TRP in the Y_{SRF} and Z_{SRF} directions. The drag force in the Y_{SRF} and Z_{SRF}, especially during periods of low solar activity, is nearly zero. The analysis of the residuals indicated that penumbra transitions cannot be modelled precisely. This is due to the different trends in measurements before and after the transitions, as well as the varying magnitudes between entry and exit transitions.

Apart from these disturbances of known reasons, we observed that the residuals connected to geomagnetic storms are only present in the X_{SRF}. An asymmetry between the ascending and descending orbits in the Z_{SRF}, attributed to Earth's radiation pressure (ERP), warrants further investigation. In the Y_{SRF}, being the least sensitive axis, the residuals did not reveal any signals apart from the mismodeling of the penumbra transitions and the strong dependency on β' variations. To better understand the residuals in the X_{SRF}, a signal decomposition using Daubechies wavelets was employed. This axis was selected because the along-track direction is crucial for retrieving thermospheric densities and estimating drag. The signal decomposition revealed that disturbances up to 4 mHz can be attributed to drag, as this frequency band contains around 70% of the energy of the series. Disturbances in the 4 to 8 *mHz* range were linked to geomagnetic storms and polar region disturbances. An analysis with respect to local time (LT) revealed that these disturbances have a latitudinal dependency rather than an LT dependency.

In summary, this thesis presents an original comprehensive analysis of accelerometer measurements, addressing key challenges and introducing novel approaches that have not been previously explored. A new robust calibration method, the creation of weighted datasets, and an extensive residuals analysis are pivotal contributions that will significantly impact future research in the field of non-gravitational accelerations. This innovative work not only aims to improve gravity field recovery but, more importantly, proposes novel methods to enhance our understanding of non-gravitational accelerations and the various phenomena affecting satellites. These methods will help us identify similar disturbances in thermospheric densities, a crucial aspect for the space weather scientific community.

7.2 Recommendations and Future Research

Several important avenues for future research are identified based on the findings of this thesis:

a) Enhanced Retrieval of the Scale Factor Parameter:

Further investigation is recommended into the sensitivity of the matched filter method using different interpolation techniques to retrieve the kinematic POD-derived total accelerations. A possible use of the KBR measurements instead of the total accelerations from POD, will also be investigated. Along with future improved kinematic orbits using GNSS on board future missions MC and MAGIC we will be able refine the method for more accurate scale retrievals for upper atmosphere studies.

b) Extended ACW1B Dataset Creation:

The ACW1B dataset should be extended to cover periods of both low and high solar activity. This extended dataset will provide a broader understanding of the disturbances affecting the satellite, particularly during varying solar conditions. The variances of the ACW1B need to be explored using advanced techniques, such as pattern recognition, to identify the source of specific signatures that can be further used to understand how the non-gravitational accelerations affect the satellites, particularly the upcoming follow-on missions MC and MAGIC.

c) Extended Data-Driven Model and Residuals Analysis:

Data-driven modeling of non-gravitational accelerations requires further improvement and validation by comparison with theoretical models, which are currently limited in availability. Models should be extended over longer periods and include a more detailed analysis of radial residuals. This could improve understanding of ERP variations and address inconsistencies between ascending and descending satellite orbits.

d) Correlation with ACE Satellite Measurements:

Investigating residuals related to drag against measurements from the ACE satellite at the L1[40] could provide valuable insights. This could help correlate disturbances during geomagnetic storms at L1 and the impulse response of the accelerometer, improving space weather forecasting and understanding the propagation mechanisms between L1 and the Earth.

e) Thermospheric Density Extraction:

Using the ACW1B dataset to extract thermospheric densities could prove highly valuable. The absence of spurious spikes in the dataset eliminates the need for manual removal and interpolation of spikes in the process of extracting thermospheric densities and enhancing data accuracy.

These future research directions will not only build on the advancements presented in this thesis but also contribute significantly to the fields of space weather forecasting, satellite-based Earth observation, and atmospheric dynamics.

---

[40] The L1 point, or Lagrange Point 1, is one of the five Lagrange points in a two-body system, such as the Earth-Sun system, where a small object can maintain a stable position relative to the two larger bodies since the gravitational forces of the Earth and the Sun, along with the centripetal force of the orbit, balance out. The L1 point is located approximately 1.5 million km from Earth towards the Sun.

References

Abadi, P., Otsuka, Y., Shiokawa, K., Husin, A., Liu, H., & Saito, S. (2017). Equinoctial asymmetry in the zonal distribution of scintillation as observed by GPS receivers in Indonesia. Journal of Geophysical Research: Space Physics, 122(8), 8947-8958. https://doi.org/10.1002/2017JA024146

Abich, K., Abramovici, A., Amparan, B., Baatzsch, A., Okihiro, B. B., Barr, D. C., ... & Zimmermann, M. (2019). In-orbit performance of the GRACE Follow-On laser ranging interferometer. Physical Review Letters, 123(3), 031101. https://doi.org/10.1103/PhysRevLett.123.031101

Afraimovich, E. L., Edemskiy, I. K., Voeykov, S. V., Yasyukevich, Y. V., & Zhivetiev, I. V. (2009). Spatio-temporal structure of the wave packets generated by the solar terminator. Advances in Space Research, 44(7), 824-835. https://doi.org/10.1016/j.asr.2009.05.017

Astrua, M., Pisani, M., Santiano, M., & Audrito, E. (2023). Calibration of high accuracy accelerometers for ESA missions BepiColombo and JUICE at INRIM. Measurement Science and Technology, 34(10), 104001. https://doi.org/10.1088/1361-6501/ace20c

Balmino, G., Perosanz, F., Rummel, R., Sneeuw, N., & Sünkel, H. (1999). CHAMP, GRACE and GOCE: Mission concepts and simulations. Applicata, 40(3-4), 309-319.

Bandikova, T., McCullough, C., Kruizinga, G. L., Save, H., & Christophe, B. (2019). GRACE accelerometer data transplant. Advances in Space Research, 64(3), 623-644. https://doi.org/10.1016/j.asr.2019.05.021

Barnoud, A., Pfeffer, J., Cazenave, A., Fraudeau, R., Rousseau, V., & Ablain, M. (2023). Revisiting the global mean ocean mass budget over 2005–2020. Ocean Science, 19(2), 321-334. https://doi.org/10.5194/os-19-321-2023

Bazargani, F., & Snieder, R. (2016). Optimal source imaging in elastic media. Geophysical Journal International, 204(2), 1134–1147. https://doi.org/10.1093/gji/ggv494

Beaussier, J., Mainguy, A. M., Olivero, A., & Rolland, R. (1977). In orbit performance of the Cactus accelerometer (D5B spacecraft). Acta Astronautica, 4(9-10), 1085-1102. https://doi.org/10.1016/0094-5765(77)90008-X

Beer, T. (1973). Supersonic generation of atmospheric waves. Nature, 242(5392), 34–35. https://doi.org/10.1038/242034a0

Bell, B. and Reynolds, S. (1991) ‘A matched filter Network For Estimating Pulse Arrival Times’, IEEE Transactions on signal processing, 39(2), pp. 477–481.

Bell, M. R. (1993). Information theory and radar waveform design. IEEE Transactions on Information Theory, 39(5), 1578–1597. https://doi.org/10.1109/18.259642

Behzadpour, S., Mayer-Gürr, T., & Krauss, S. (2021). GRACE Follow-On accelerometer data recovery. Journal of Geophysical Research: Solid Earth, 126(5), e2020JB021297. https://doi.org/10.1029/2020JB021297

Bertiger, W., Bar-Sever, Y., Dorsey, A., Haines, B., Harvey, N., Hemberger, D., ... & Willis, P. (2020). GipsyX/RTGx, a new tool set for space geodetic operations and research. Advances in Space Research, 66(3), 469-489. https://doi.org/10.1016/j.asr.2020.04.015

Bettadpur, S. (2009). Recommendation for a-priori bias & scale parameters for level-1B ACC Data (Version 2).

Bettadpur, S. (2012). Gravity recovery and climate experiment: Product specification document. Technical report, GRACE 327-720, Center for Space Research, University of Texas, Austin.

Bettadpur, S. (2018). CSR Level-2 processing standards document for product release 06. GRACE 327–742, revision 5.0.

Bezděk, A. (2010). Calibration of accelerometers aboard GRACE satellites by comparison with POD-based nongravitational accelerations. Journal of Geodynamics, 50(5), 410-423. https://doi.org/10.1016/j.jog.2010.05.001

Blinn, J. F. (1977). Models of light reflection for computer synthesized pictures. Proceedings of the 4th Annual Conference on Computer Graphics and Interactive Techniques (SIGGRAPH '77), 192–198. https://doi.org/10.1145/563858.563893

Boudon, Y., Barlier, F., Bernard, A., Juillerat, R., Mainguy, A. M., & Walch, J. J. (1979). Synthesis of flight results of the Cactus accelerometer for accelerations below 10^{-9} g. Acta Astronautica, 6(11), 1387-1398. https://doi.org/10.1016/0094-5765(79)90097-7

Bouman, J., & Koop, R. (2003). Geodetic methods for calibration of GRACE and GOCE. Space Science Reviews, 108(1), 1-22. https://doi.org/10.1023/A:1026127409015

Bowman, B., Tobiska, W.K., Marcos, F. et al., 2008. A New Empirical Thermospheric Density Model JB2008 Using New Solar and Geomagnetic Indices. In: AIAA/AAS Astrodynamics Specialist Conference and Exhibit. American Institute of Aeronautics and Astronautics. https://doi.org/10.2514/6.2008-6438

Bruinsma, S., & Biancale, R. (2003). Total densities derived from accelerometer data. Journal of Spacecraft and Rockets, 40(2), 230-236. https://doi.org/10.2514/2.3937

Bruinsma, S., Tamagnan, D., & Biancale, R. (2004). Atmospheric densities derived from CHAMP/STAR accelerometer observations. Planetary and Space Science, 52(4), 297-312. https://doi.org/10.1016/j.pss.2003.11.004

Bruinsma, S. L., & Forbes, J. M. (2010). Large-scale traveling atmospheric disturbances (LSTADs) in the thermosphere inferred from CHAMP, GRACE, and SETA accelerometer data. Journal of Atmospheric and Solar-Terrestrial Physics, 72(13), 1057-1066. https://doi.org/10.1016/j.jastp.2010.06.010

Bruinsma, S. L., Sánchez-Ortiz, N., Olmedo, E., & Guijarro, N. (2012). Evaluation of the DTM-2009 thermosphere model for benchmarking purposes. Journal of Space Weather and Space Climate, 2, A04. https://doi.org/10.1051/swsc/2012005

Bruinsma, S., & Boniface, C. (2021). The operational and research DTM-2020 thermosphere models. Journal of Space Weather and Space Climate, 11, 47. https://doi.org/10.1051/swsc/2021032

Bruinsma, S., de Wit, T. D., Fuller-Rowell, T., Garcia-Sage, K., Mehta, P., Schiemenz, F., ... & Elvidge, S. (2023). Thermosphere and satellite drag. Advances in Space Research. https://doi.org/10.1016/j.asr.2023.05.011

Bruinsma, S., Siemes, C., Emmert, J. T., & Mlynczak, M. G. (2023). Description and comparison of 21st century thermosphere data. Advances in Space Research, 72(12), 5476-5489. https://doi.org/10.1016/j.asr.2022.09.038

Calabia, A., & Jin, S. G. (2015). GPS-based non-gravitational accelerations and accelerometer calibration. In Satellite Positioning: Methods, Models and Applications (pp. 47-72). Springer. https://doi.org/10.1007/978-3-662-46759-6_3

Calabia, A., Jin, S., & Tenzer, R. (2015). A new GPS-based calibration of GRACE accelerometers using the arc-to-chord threshold uncovered sinusoidal disturbing signal. Aerospace Science and Technology, 45, 265–271. https://doi.org/10.1016/j.ast.2015.05.013

Calabia, A., & Jin, S. (2016). New modes and mechanisms of thermospheric mass density variations from GRACE accelerometers. Journal of Geophysical Research: Space Physics, 121(11), 11,191-11,205. https://doi.org/10.1002/2016JA023046

Calabia, A., & Jin, S. (2017). Thermospheric density estimation and responses to the March 2013 geomagnetic storm from GRACE GPS-determined precise orbits. Journal of Atmospheric and Solar-Terrestrial Physics, 154, 167-179.

Callejón, M., Siemes, C., & Pastor, A. (2023). Improving orbit prediction. Advances in Space Research, 63(8), 2495-2505. https://doi.org/10.1016/j.asr.2019.01.025

Canuto, E. (2008). Drag-free and attitude control for the GOCE satellite. Automatica, 44(7), 1766-1780. https://doi.org/10.1016/j.automatica.2008.01.016

Capon, C. J., Smith, B., Brown, M., Abay, R., & Boyce, R. R. (2019). Effect of ionospheric drag on atmospheric density estimation and orbit prediction. Advances in Space Research, 63(8), 2495-2505. https://doi.org/10.1016/j.asr.2019.01.038

Case, K., Kruizinga, G., & Wu, S. (2002). GRACE level 1B data product user handbook. JPL Publication D-22027. Jet Propulsion Laboratory, California Institute of Technology.

Case, K., Kruizinga, G. and Wu, S.-C. (2010) 'GRACE Level 1B Data Product User Handbook', Jet Propulsion Laboratory, California Institute of Technology, JPL D-22027, p. 62.

Cercignani, C., & Lampis, M. (1971). Kinetic models for gas-surface interactions. *Transport theory and statistical physics*, *1*(2), 101-114.

Champion, K. S. W., & Marcos, F. A. (1973). The triaxial-accelerometer system on Atmosphere Explorer. Radio Science, 8(4), 297-303. https://doi.org/10.1029/RS008i004p00297

Chatzistergos, T., Krivova, N. A., & Yeo, K. L. (2023). Long-term changes in solar activity and irradiance. Journal of Atmospheric and Solar-Terrestrial Physics, 252, 106150. https://doi.org/10.1016/j.jastp.2023.106150

Chen, Q., Shen, Y., Chen, W., Zhang, X., & Hsu, H. (2016). An improved GRACE monthly gravity field solution by modeling the non-conservative acceleration and attitude observation errors. Journal of Geodesy, 90, 503-523. https://doi.org/10.1007/s00190-016-0891-3

Chen, Q., Shen, Y., Francis, O., Wu, C., Zhang, X., & Hsu, H. (2018). Tongji-GRACE02S and Tongji-GRACE02K: high-precision static GRACE-only global Earth's gravity field models derived by refined data processing strategies. Journal of Geophysical Research: Solid Earth, 123(7), 6111-6137. https://doi.org/10.1029/2018jb015641

Chen, J., Tapley, B., Tamisiea, M. E., Save, H., Wilson, C., Bettadpur, S., & Seo, K. W. (2021). Error assessment of GRACE and GRACE Follow-On mass change. Journal of Geophysical Research: Solid Earth, 126(9), e2021JB022124. https://doi.org/10.1029/2021JB022124

Cheng, K. C., Miller, E. L., Hughes, M. C., & Aeron, S. (2020). On matched filtering for statistical change point detection. IEEE Open Journal of Signal Processing, 1, 159-176.

Cheremnykh, O. K., Fedorenko, A. K., Kryuchkov, E. I., Klymenko, Y. O., & Zhuk, I. T. (2023).

Development of models of acoustic-gravity waves in the upper atmosphere (overview). arXiv preprint arXiv:2308.01619. https://doi.org/10.48550/arXiv.2308.01619

Chimonas, G., & Hines, C. O. (1971). Atmospheric gravity waves induced by a solar eclipse, 2. Journal of Geophysical Research, 76, 7003–7005.

Clette, F., Svalgaard, L., Vaquero, J. M., & Cliver, E. W. (2014). Revisiting the sunspot number: A 400-year perspective on the solar cycle. Space Science Reviews, 186, 35-103. https://doi.org/10.1007/s11214-014-0074-2

Cook, G. E. (1965). Satellite drag coefficients. Planetary and Space Science, 13(10), 929-946. https://doi.org/10.1016/0032-0633(65)90112-2

Corripio, J. G. (2002). Modelling the energy balance of high altitude glacierised basins in the Central Andes (Doctoral dissertation, University of Edinburgh).

Crombie, D. D. (1964). Periodic fading of VLF signals received over long paths during sunrise and sunset. Journal of Research National Bureau of Standards, Radio Science D, 68(1), 27-35.

Croteau, M. J., Sabaka, T. J., & Loomis, B. D. (2021). GRACE fast mascons from spherical harmonics and a regularization design trade study. Journal of Geophysical Research: Solid Earth, 126(8), e2021JB022113. https://doi.org/10.1029/2021JB022113

Crowley, G., Knipp, D. J., Drake, K. A., Lei, J., Sutton, E., & Lühr, H. (2010). Thermospheric density enhancements in the dayside cusp region during strong BY conditions. Geophysical Research Letters, 37(7), L07110. https://doi.org/10.1029/2010GL042548

Dahle, C., Murböck, M., Flechtner, F., Dobslaw, H., Michalak, G., Neumayer, K. H., ... & Förste, C. (2019). The GFZ GRACE RL06 monthly gravity field time series: Processing details and quality assessment. Remote Sensing, 11(18), 2116. https://doi.org/10.3390/rs11182116

Davis, M. J., & Da Rosa, A. V. (1970). Possible detection of atmospheric gravity waves generated by the solar eclipse. Nature, 226(5251), 1123.

Desai, S. D. (2002). Observing the pole tide with satellite altimetry. Journal of Geophysical Research: Oceans, 107(C11), 7-1. https://doi.org/10.1029/2001JC000975

Develter, P., Bosse, J., Rabaste, O., Forster, P., & Ovarlez, J. P. (2021, July). Off-grid radar target detection with the normalized matched filter: A monopulse-based detection scheme. In 2021 IEEE Statistical Signal Processing Workshop (SSP) (pp. 226-230). IEEE. https://doi.org/10.1109/SSP49601.2021.9496018

Develter, P., Bosse, J., Rabaste, O., Forster, P., & Ovarlez, J. P. (2022, May). On the false alarm probability of the normalized matched filter for off-grid target detection. In ICASSP 2022-2022 IEEE International Conference on Acoustics, Speech and Signal Processing (ICASSP) (pp. 5782-5786). IEEE. https://doi.org/10.1109/ICASSP43922.2022.9747357

Dobslaw, H., Bergmann-Wolf, I., Dill, R., Poropat, L., Thomas, M., Dahle, C., ... & Flechtner, F. (2017). A new high-resolution model of non-tidal atmosphere and ocean mass variability for de-aliasing of satellite gravity observations: AOD1B RL06. Geophysical Journal International, 211(1), 263-269. https://doi.org/10.1093/gji/ggx013

Doornbos, E., & Klinkrad, H. (2006). Modelling of space weather effects on satellite drag. Advances in Space Research, 37(6), 1229-1239. https://doi.org/10.1016/j.asr.2005.04.097

Doornbos, E., Van Den Ijssel, J., Luhr, H., Forster, M., & Koppenwallner, G. (2010). Neutral density and crosswind determination from arbitrarily oriented multiaxis accelerometers on satellites. Journal of Spacecraft and Rockets, 47(4), 580-589. https://doi.org/10.2514/1.46685

Duan, B., Wu, Y., Zhao, Y., & Liu, J. (2016). Mitigation of orbit integration errors for eclipsing satellites. Lecture Notes in Electrical Engineering, 390, 167–174. https://doi.org/10.1007/978-981-10-0940-2_15

Drinkwater, M. R., Floberghagen, R., Haagmans, R., Muzi, D., & Popescu, A. (2003). VII: Closing session: GOCE: ESA's first Earth Explorer Core mission. Space Science Reviews, 108(1), 419-432. https://doi.org/10.1023/A:1026117716030

Emmert, J. T. (2015). Thermospheric mass density: A review. Advances in Space Research, 56(5), 773-824. https://doi.org/10.1016/j.asr.2015.05.038

Emmert, J. T. (2015). Altitude and solar activity dependence of 1967–2005 thermospheric density trends derived from orbital drag. Journal of Geophysical Research: Space Physics, 120(4), 2940-2950. https://doi.org/10.1002/2015JA021047

Ferraz-Mello, S. (1972). Analytical study of the Earth's shadowing effects on satellite orbits. Celestial Mechanics, 5(1), 80-101. https://doi.org/10.1007/BF01230242

Fienga, A., Manche, H., Laskar, J., & Gastineau, M. (2009). INPOP06: a new numerical planetary ephemeris. Astronomy & Astrophysics, 507(3), 1675-1686. https://doi.org/10.1051/0004-6361/200911755

Fink, M., Cassereau, D., Derode, A., Prada, C., Roux, P., Tanter, M., ... & Wu, F. (2000). Time-reversed acoustics. Reports on progress in Physics, 63(12), 1933.

Fink, M., & Prada, C. (2001). Acoustic time-reversal mirrors. Inverse problems, 17(1), R1.

Fink, M. (2006). Time-reversal acoustics in complex environments. Geophysics, 71(4), SI151-SI164. https://doi.org/10.1190/1.2226476

Fixler, S. Z. (1964). Umbra and penumbra eclipse factors for satellite orbits. AIAA Journal, 2(8), 1455–1457. https://doi.org/10.2514/3.2577

Flechtner, F., Morton, P., Watkins, M., & Webb, F. (2014). Status of the GRACE follow-on mission. In Gravity, Geoid and Height Systems: Proceedings of the IAG Symposium GGHS2012, October 9-12, 2012, Venice, Italy (pp. 117-121). Springer International Publishing. https://doi.org/10.1007/978-3-319-10837-7_15

Flechtner, F., Neumayer, K. H., Dahle, C., Dobslaw, H., Fagiolini, E., Raimondo, J. C., & Güntner, A. (2016). What can be expected from the GRACE-FO laser ranging interferometer for Earth science applications? In Remote Sensing and Water Resources (pp. 263-280). Springer. https://doi.org/10.1007/978-3-319-29911-7_15

Flury, J., Bettadpur, S., & Tapley, B. D. (2008). Precise accelerometry onboard the GRACE gravity field satellite mission. Advances in Space Research, 42(8), 1414-1423. https://doi.org/10.1016/j.asr.2008.05.004

Földváry, L. (2007). Determination of satellite velocity and acceleration from kinematic LEO orbits. Acta Geodaetica et Geophysica Hungarica, 42(4), 399–419. https://doi.org/10.1556/AGeod.42.2007.4.3

Forbes, J. M., Bruinsma, S. L., Miyoshi, Y., & Fujiwara, H. (2008). A solar terminator wave in thermosphere neutral densities measured by the CHAMP satellite. Geophysical Research Letters, 35(14). https://doi.org/10.1029/2008GL034071

Forootan, E., Kosary, M., Farzaneh, S., Kodikara, T., Vielberg, K., Fernandez-Gomez, I., ... & Schumacher, M. (2022). Forecasting global and multi-level thermospheric neutral density and ionospheric electron content by tuning models against satellite-based accelerometer measurements. Scientific Reports, 12(1), 2095. https://doi.org/10.1038/s41598-022-06105-4

Frappart, F., & Ramillien, G. (2018). Monitoring groundwater storage changes using the Gravity Recovery and Climate Experiment (GRACE) satellite mission: A review. Remote Sensing, 10(6), 829. https://doi.org/10.3390/rs10060829

Friis-Christensen, E., Lühr, H., & Hulot, G. (2006). Swarm: A constellation to study the Earth's magnetic field. Earth, Planets and Space, 58, 351-358. https://doi.org/10.1186/BF03351933

Frommknecht, B., Oberndorfer, H., Flechtner, F., & Schmidt, R. (2003). Integrated sensor analysis for GRACE–development and validation. Advances in Geosciences, 1, 57–63. https://doi.org/10.5194/adgeo-1-57-2003

Frommknecht, B., Fackler, U., & Flury, J. (2006). Integrated sensor analysis GRACE. In Observation of the Earth System from Space (pp. 99-113). Springer. https://doi.org/10.1007/3-540-29522-4_7

Gagne, R. M., & Wagner, R. F. (1998, July). Prewhitening matched filter: practical implementation, SNR estimation, and bias reduction. In Medical Imaging 1998: Physics of Medical Imaging (Vol. 3336, pp. 231-242). SPIE.

Gao, Y., Wang, J., & Li, X. (2021). Adaptive thermal control system for mitigating thermal radiation pressure effects on satellites. Acta Astronautica, 181, 11-20. https://doi.org/10.1016/j.actaastro.2021.01.010

Ge, H., Li, B., Ge, M., Nie, L., & Schuh, H. (2020). Improving low Earth orbit (LEO) prediction with accelerometer data. Remote Sensing, 12(10), 1599. https://doi.org/10.3390/rs12101599

Gérard Petit and Brian Luzum, editors. "IERS Conventions (2010) (IERS Technical Note No. 36)." International Earth Rotation and Reference Systems Service (IERS), Verlag des Bundesamts für Kartographie und Geodäsie, 2010.

Ghaderpour, E., & Pagiatakis, S. D. (2019). LSWAVE: A MATLAB software for the least-squares wavelet and cross-wavelet analyses. GPS Solutions, 23(2), 50. https://doi.org/10.1007/s10291-019-0890-1

Ghaderpour, E., Ben Abbes, A., Rhif, M., Pagiatakis, S. D., & Farah, I. R. (2020). Non-stationary and unequally spaced NDVI time series analyses by the LSWAVE software. International Journal of Remote Sensing, 41(6), 2374-2390. https://doi.org/10.1080/01431161.2019.1673915

Ghaderpour, E., Pagiatakis, S. D., & Hassan, Q. K. (2021). A survey on change detection and time series analysis with applications. Applied Sciences, 11(13), 6141. https://doi.org/10.3390/app11136141

Ghobadi-Far, K., Han, S. C., McCullough, C. M., Wiese, D. N., Ray, R. D., Sauber, J., ... & Dobslaw, H. (2022). Along-orbit analysis of GRACE Follow-On inter-satellite laser ranging measurements for sub-monthly surface mass variations. Journal of Geophysical Research: Solid Earth, 127(2), e2021JB022983. https://doi.org/10.1029/2021JB022983

Giannakis, G. B., & Tsatsanis, M. K. (1990). Signal detection and classification using matched filtering and higher order statistics. IEEE Transactions on Acoustics, Speech, and Signal Processing, 38(7), 1284-1296.

Giudici, L., Colombo, C., Horstmann, A., Letizia, F., & Lemmens, S. (2024). Density-based evolutionary model of the space debris environment in low-Earth orbit. Acta Astronautica, 219, 115-127. https://doi.org/10.1016/j.actaastro.2023.12.011

González, A. O., Junior, O. M., Menconi, V. E., & Domingues, M. O. (2014). Daubechies wavelet coefficients: A tool to study interplanetary magnetic field fluctuations. Geofísica Internacional, 53(2), 101-115. https://doi.org/10.1016/S0016-7169(14)71494-1

Goswami, S., Devaraju, B., Weigelt, M., & Mayer-Gürr, T. (2018). Analysis of GRACE range-rate residuals with focus on KBR instrument system noise. Advances in Space Research, 62(2), 304-316. https://doi.org/10.1016/j.asr.2018.04.016

Guo, J., Forbes, J. M., Wei, F., Feng, X., Liu, H., Wan, W., ... & Deng, Y. (2015). Observations of a large-scale gravity wave propagating over an extremely large horizontal distance in the thermosphere. Geophysical Research Letters, 42(16), 6560-6565. https://doi.org/10.1002/2015GL065069

Haddadin, S., & Ebini, S. (1998). Ultrasonic focusing through inhomogeneous media by application of the inverse scattering problem. The Journal of the Acoustical Society of America, 104(2), 1184-1192. https://doi.org/10.1121/1.423291

Hamilton, P. S., & Tompkins, W. J. (1988, November). Adaptive matched filtering for QRS detection. In Proceedings of the Annual International Conference of the IEEE Engineering in Medicine and Biology Society (pp. 147-148). IEEE.

Harris, I., & Priester, W. (1962). Time-Dependent Structure of the Upper Atmosphere. Journal of Geophysical Research, 67(1), 103-114. https://doi.org/10.1029/JZ067i001p00103

Harries, J. E., Russell, J. E., & Hanafin, J. A. (2005). The Geostationary Earth Radiation Budget (GERB) experiment. Advances in Space Research, 36(5), 832-839. https://doi.org/10.1016/j.asr.2005.03.073

Harvey, N., McCullough, C. M., & Save, H. (2022). Modeling GRACE-FO accelerometer data for the version 04 release. Advances in Space Research, 69(3), 1393-1407. https://doi.org/10.1016/j.asr.2021.11.021

Harvey, N., Bertiger, W., McCullough, C. M., Miller, M., Save, H., & Yuan, D. N. (2024). Recovering differential forces from the GRACE-D accelerometer. Earth and Space Science, 11(4), e2023EA003200. [DOI: 10.1029/2023EA003200](https://doi.org/10.1029/2023EA003200).

Hathaway, D. H., Wilson, R. M., & Reichmann, E. J. (2002). Group sunspot numbers: Sunspot cycle characteristics. Solar Physics, 211, 357-370. https://doi.org/10.1023/A:1022416218683

Hathaway, D. H. (2015). The solar cycle. Living reviews in solar physics, 12(1), 4. https://doi.org/10.1007/lrsp-2015-4

Helleputte, T. Van, Doornbos, E., & Visser, P. (2009). CHAMP and GRACE accelerometer calibration by GPS-based orbit determination. Advances in Space Research, 43(12), 1890–1896. https://doi.org/10.1016/j.asr.2009.02.017

Helleputte, T. Van, & Visser, P. (2008). GPS based orbit determination using accelerometer data. Aerospace Science and Technology,1(6), 478–484. https://doi.org/10.1016/j.ast.2007.11.002

Helstrom, C. W. (1960). The comparison of digital communication systems. IRE Transactions on Communications Systems, 8(3), 141–150. https://doi.org/10.1109/TCOM.1960.1097629

Hesar, S. G., Scheeres, D. J., McMahon, J. W., & Rozitis, B. (2017). Precise model for small-body thermal radiation pressure acting on spacecraft. Journal of Guidance, Control, and Dynamics, 40(10), 2432-2441. https://doi.org/10.2514/1.G002642

Hładczuk, N. A., van den IJssel, J., Kodikara, T., Siemes, C., & Visser, P. (2024). GRACE-FO radiation pressure modeling for accurate density and crosswind retrieval. Advances in Space Research, 73(5), 2355-2373. https://doi.org/10.1016/j.asr.2023.11.020

Hu, J., Ruan, H., Lei, J., Zhong, J., & Owolabi, C. (2022). An investigation on the longitudinal variation in mid-latitude ionosphere based on CHAMP satellite observations. Earth and Space Science, 9(10), e2022EA002496. https://doi.org/10.1029/2022EA002496

Huckfeldt, M., Wöske, F., Rievers, B., & List, M. (2024). GRACE Follow-On accelerometer data recovery by high-precision environment modelling. Advances in Space Research, 73(12), 5783-5805. [DOI: 10.1016/j.asr.2024.03.012](https://doi.org/10.1016/j.asr.2024.03.012).

Ikari, S., Tokunaga, K., Ebinuma, T., Funase, R., & Nakasuka, S. (2016). A study of shadow representation for high-fidelity solar radiation pressure calculation. In AIAA/AAS Astrodynamics Specialist Conference (p. 5680). https://doi.org/10.2514/6.2016-5680

Iorfida, E., Daras, I., Haagmans, R., & Strømme, A. (2023). Swarm A and C accelerometers: Data validation and scientific interpretation. Earth and Space Science, 10(2), e2022EA002458. https://doi.org/10.1029/2022EA002458

Iziomon, M. G., & Mayer, H. (2002). Assessment of some global solar radiation parameterizations. Journal of Atmospheric and Solar-Terrestrial Physics, 64(15), 1631-1643. https://doi.org/10.1016/S1364-6826(02)00129-1

Jäggi, A., Bock, H., Meyer, U., Beutler, G., & van den IJssel, J. (2015). GOCE: Assessment of GPS-only gravity field determination. Journal of Geodesy, 89, 33-48. https://doi.org/10.1007/s00190-014-0760-3

Jacchia, L. G. (1963). Variations in the Earth's upper atmosphere as revealed by satellite drag. Reviews of Modern Physics, 35(4), 973. https://doi.org/10.1103/RevModPhys.35.973

Jackson, G. S., Imponenti, L., Albrecht, K. J., Miller, D. C., & Braun, R. J. (2019). Inert and reactive oxide particles for high-temperature thermal energy capture and storage for concentrating solar power. Journal of Solar Energy Engineering, 141(2), 021016. https://doi.org/10.1115/1.4042314

Jastrow, R., & Pearse, C. A. (1957). Atmospheric drag on the satellite. Journal of Geophysical Research, 62(3), 413-423. https://doi.org/10.1029/JZ062i003p00413

Jin, Y. and Moura, J. M. F. (2009) 'Time-reversal detection using antenna arrays', IEEE Transactions on Signal Processing, 57(4), pp. 1396–1414. doi: 10.1109/TSP.2008.2010425.

Jin, Y. et al. (2011) 'Time reversal detection in clutter: Additional experimental results', IEEE Transactions on Aerospace and Electronic Systems, 47(1), pp. 140–154. doi: 10.1109/TAES.2011.5705665.

Kammoun, A., Couillet, R., Pascal, F., & Alouini, M. (2015). Optimal design of the adaptive normalized matched filter detector using regularized Tyler estimators. IEEE Transactions on Aerospace and Electronic Systems, 54, 755-769. https://doi.org/10.1109/TAES.2015.1209692

Kang, Z., Tapley, B., Bettadpur, S., Ries, J., & Nagel, P. (2006). Precise orbit determination for GRACE using accelerometer data. Advances in Space Research, 38(9), 2131-2136. https://doi.org/10.1016/j.asr.2005.03.120

Kang, Z., Bettadpur, S., Nagel, P., Save, H., Poole, S., & Pie, N. (2020). GRACE-FO precise orbit determination and gravity recovery.Journal of Geodesy, 94, 1-17. https://doi.org/10.1007/s00190-020-01366-5

Karam, R. D. (1998). Satellite thermal control for systems engineers (Vol. 181). AIAA.

Keating, G. M., Tolson, R. H., & Bradford, M. S. (1999). TOPEX/Poseidon mission: Models of solar radiation pressure for precise orbit determination. Journal of Spacecraft and Rockets, 36(4), 525-531. https://doi.org/10.2514/2.3506

Kelly, E. J. and Wishner, R. P. (1965) 'Matched-Filter Theory for High-Velocity, Accelerating Targets', IEEE Transactions on Military Electronics, 9(1), pp. 56–69. doi: 10.1109/TME.1965.4323176.

Kim, J. (2000). Simulation study of a low-low satellite-to-satellite tracking mission. The University of Texas at Austin.

King-Hele, D. G., & Walker, D. M. (1987). The contraction of satellite orbits under the influence of air drag. VII. Orbits of high eccentricity, with scale height dependent on altitude. Proceedings of the Royal Society of London. A. Mathematical and Physical Sciences, 411(1840), 1-17. https://doi.org/10.1098/rspa.1987.0136

Kirkpatrick, D. (1999). Space mission analysis and design (Vol. 8). In J. R. Wertz, W. J. Larson, & D. Klungle (Eds.). Torrance: Microcosm.

Klinger, B., & Mayer-Gürr, T. (2016). The role of accelerometer data calibration within GRACE gravity field recovery: Results from ITSG-Grace2016. Advances in Space Research, 58(9), 1597-1609. https://doi.org/10.1016/j.asr.2016.08.007

Klinkrad, H. (2006). Space Debris: Models and Risk Analysis. Springer. https://doi.org/10.1007/3-540-37674-1

Klokočník, J., Wagner, C. A., Kostelecký, J., Bezděk, A., Novák, P., & McAdoo, D. (2008). Variations in the accuracy of gravity recovery due to ground track variability: GRACE, CHAMP, and GOCE. Journal of Geodesy, 82, 917-927. https://doi.org/10.1007/s00190-008-0221-1

Knabe, A., Schilling, M., Wu, H., HosseiniArani, A., Müller, J., Beaufils, Q., … & Santos, F. P. D. (2022). The benefit of accelerometers based on cold atom interferometry for future satellite gravity missions. International Association of Geodesy Symposia, 213-220. https://doi.org/10.1007/1345_2022_151

Knocke, P., Ries, J., & Tapley, B. (1988, August). Earth radiation pressure effects on satellites. In Astrodynamics Conference (p. 4292). https://doi.org/10.2514/6.1988-4292

Koch, I., Shabanloui, A., & Flury, J. (2019). Calibration of GRACE Accelerometers Using Two Types of Reference Accelerations. In International Symposium on Advancing Geodesy in a Changing World: Proceedings of the IAG Scientific Assembly, Kobe, Japan, July 30–August 4, 2017 (pp. 97-104). Springer International Publishing

Koch, I., Duwe, M., Flury, J., & Shabanloui, A. (2021). Earth's time-variable gravity from GRACE Follow-On K-band range-rates and pseudo-observed orbits. Remote Sensing, 13(9), 1766. https://doi.org/10.3390/rs13091766

Koch, I., Duwe, M., & Flury, J. (2023). Spectral analysis of residual GRACE and GRACE-FO range accelerations. Geophysical Research Letters, 50(15). https://doi.org/10.1029/2023GL103040

Kodikara, T., Fernandez-Gomez, I., Forootan, E., Tobiska, W. K., & Borries, C. (2023). Understanding the errors in CHAMP accelerometer-derived neutral mass density data. Authorea Preprints. https://doi.org/10.22541/essoar.168394738.80108429

Koop, R., Bouman, J., Schrama, E. J. O., & Visser, R. (2002). Calibration and error assessment of GOCE data. In Vistas for Geodesy in the New Millennium: IAG 2001 Scientific Assembly, Budapest, Hungary September 2–7, 2001 (pp. 167-174). Springer Berlin Heidelberg. https://doi.org/10.1007/978-3-662-04709-5_28

Kornfeld, R. P., Arnold, B. W., Gross, M. A., Dahya, N. T., Klipstein, W. M., Gath, P. F., & Bettadpur, S. (2019). GRACE-FO: The Gravity Recovery and Climate Experiment Follow-On Mission. Journal of Spacecraft and Rockets, 56(3), 931-951. https://doi.org/10.2514/1.A34326

König, R., Reigber, C., Neumayer, K. H., Schmidt, R., Zhu, S., Baustert, G., ... & Meixner, H. (2003). Satellite dynamics of the CHAMP and GRACE LEOs as revealed from space-and ground-based tracking. Advances in Space Research, 31(8), 1869-1874. https://doi.org/10.1016/S0273-1177(03)00158-3

Kopeikin, S. M., Mazurova, E. M., & Karpik, A. P. (2015). Towards an exact relativistic theory of Earth's geoid undulation. Physics Letters A, 379(26-27), 1555-1562. https://doi.org/10.1016/j.physleta.2015.04.037

Krasnov, A., Sokolov, A., Bolotin, Y., Golovan, A., Parusnikov, N., Motorin, A., ... & Vyazmin, V. (2022). Data processing methods for onboard gravity anomaly measurements. In Methods and Technologies for Measuring the Earth’s Gravity Field Parameters (pp. 63-150). Cham: Springer International Publishing. https://doi.org/10.1007/978-3-031-11158-7_2

Krivov, A. V., Löhne, T., & Sremčević, M. (2006). Dust distributions in debris disks: effects of gravity, radiation pressure and collisions. Astronomy & Astrophysics, 455(2), 509-519. https://doi.org/10.1051/0004-6361:20065111

Krivov, A. V. (1997). Dynamics of debris from satellites at geosynchronous altitude. Journal of Spacecraft and Rockets, 34(4), 649-655. https://doi.org/10.2514/2.3245

Kuang, D., Bertiger, W., Desai, S. D., Haines, B. J., & Yuan, D. N. (2019). Observed geocenter motion from precise orbit determination of GRACE satellites using GPS tracking and accelerometer data. Journal of Geodesy, 93, 1835-1844. https://doi.org/10.1007/s00190-019-01220-1

Kvas, A., Behzadpour, S., Ellmer, M., Klinger, B., Strasser, S., Zehentner, N., & Mayer-Gürr, T. (2019). ITSG-Grace2018: Overview and evaluation of a new GRACE-only gravity field time series. Journal of Geophysical Research: Solid Earth, 124(8), 9332-9344. https://doi.org/10.1029/2019JB017415

Kvas, A., Brockmann, J. M., Krauss, S., Schubert, T., Gruber, T., Meyer, U., ... & Pail, R. (2020). GOCO06s–a satellite-only global gravity field model. Earth System Science Data Discussions, 2020, 1-31. https://doi.org/10.5194/essd-2020-163

La Marca, T. A., Nocerino, A., Opromolla, R., & Grassi, M. (2024). Incremental model predictive control for satellite de-orbiting based on drag modulation. Acta Astronautica, 215, 708-724. https://doi.org/10.1016/j.actaastro.2024.01.008

Landerer, F. W., Flechtner, F. M., Save, H., Webb, F. H., Bandikova, T., Bertiger, W. I., ... & Yuan, D. N. (2020). Extending the global mass change data record: GRACE Follow-On instrument and science data performance. Geophysical Research Letters, 47(12), e2020GL088306. https://doi.org/10.1029/2020GL088306

Lemoine, F. G., Goossens, S., Sabaka, T. J., Nicholas, J. B., Mazarico, E., Rowlands, D. D., ... & Zuber, M. T. (2013). High-degree gravity models from GRAIL primary mission data. Journal of Geophysical Research: Planets, 118(8), 1676-1698. https://doi.org/10.1002/jgre.20118

Li, M., Zhang, J., Wu, Y., & Xu, X. (2022). Calibration of GRACE on-board accelerometers for thermosphere density derivation. Geo-Spatial Information Science, 25(1), 74–87. https://doi.org/10.1080/10095020.2021.2010506

Liu, H., Lühr, H., Henize, V., & Köhler, W. (2005). Global distribution of the thermospheric total mass density derived from CHAMP. Journal of Geophysical Research: Space Physics, 110(A4). https://doi.org/10.1029/2004JA010741

Liu, H., Lühr, H., & Watanabe, S. (2009). A solar terminator wave in thermospheric wind and density simultaneously observed by CHAMP. Geophysical Research Letters, 36(10). https://doi.org/10.1029/2009GL037642

Liu, J., Zhao, Q., & Zhou, J. (2020). Comprehensive thermal modeling of spacecraft for accurate thermal radiation pressure prediction. Aerospace Science and Technology, 104, 105904. https://doi.org/10.1016/j.ast.2020.105904

Loomis, B. D., Nerem, R. S., & Luthcke, S. B. (2012). Simulation study of a follow-on gravity mission to GRACE. Journal of Geodesy, 86, 319-335. https://doi.org/10.1007/s00190-011-0521-8

Loomis, B. D., Rachlin, K. E., Wiese, D. N., Landerer, F. W., & Luthcke, S. B. (2020). Replacing GRACE/GRACE-FO with satellite laser ranging: Impacts on Antarctic Ice Sheet mass change. Geophysical Research Letters, 47(3), e2019GL085488. https://doi.org/10.1029/2019GL085488

Lu, G. *et al.* (2014) 'Global ionospheric and thermospheric response to the 5April 2010 geomagnetic storm', *Journal of Geophysical Research*, 2(7), pp. 5364–5381. doi: 10.1002/2013JA019607.: Space Physics, 110(A4). https://doi.org/10.1029/2004JA010741

Lühr, H., Rother, M., Köhler, W., Ritter, P., & Grunwaldt, L. (2004). Thermospheric up-welling in the cusp region: Evidence from CHAMP observations. Geophysical Research Letters, 31(6).

https://doi.org/10.1029/2003GL019314

Lühr, H., Kervalishvili, G., Rauberg, J., & Stolle, C. (2016). Zonal currents in the F region deduced from Swarm constellation measurements. Journal of Geophysical Research: Space Physics, 121(1), 638-648. https://doi.org/10.1002/2015JA022051

MacDonald, M., Hughes, G., McInnes, C. R., & Lyngvi, A. (2015). Analytical and numerical study of solar radiation pressure on interplanetary spacecraft. Advances in Space Research, 56(2), 281-290. https://doi.org/10.1016/j.asr.2015.02.012

Macmillan, S., & Olsen, N. (2013). Observatory data and the Swarm mission. Earth, Planets and Space, 65, 1355-1362. https://doi.org/10.5047/eps.2013.06.013

Mandrikova, O., & Rodomanskaya, A. (2021, September). Method for detecting geomagnetic disturbances based on the wavelet model of geomagnetic field variations. In 2021 International Conference on Information Technology and Nanotechnology (ITNT) (pp. 1-7). IEEE.

March, G., Van Den Ijssel, J., Siemes, C., Visser, P. N., Doornbos, E. N., & Pilinski, M. (2021). Gas-surface interactions modelling influence on satellite aerodynamics and thermosphere mass density. Journal of Space Weather and Space Climate, 11, 54. https://doi.org/10.1051/swsc/2021035

Marcos, F. A. (1982). Application of the satellite triaxial accelerometer experiment to atmospheric density and wind studies (Vol. 82). Air Force Geophysics Laboratory, Air Force Systems Command, United States Air Force.

Massotti, L., Bulit, A., Daras, I., Dominguez, B. C., Carraz, O., Hall, K., ... & Wallace, N. (2022, October). Next generation gravity mission design activities within the mass change and geoscience international constellation. In Sensors, Systems, and Next-Generation Satellites XXVI (Vol. 12264, pp. 6-17). SPIE. https://doi.org/10.1117/12.2631110

McCullough, C. M. et al. (2019) 'Description of Calibrated GRACE-FO Accelerometer Data Products (ACT)', p. 8.

McGirr, R., Tregoning, P., Allgeyer, S., McQueen, H., & Purcell, A. (2022). Mitigation of thermal noise in GRACE accelerometer observations. Advances in Space Research, 69(1), 386-401. https://doi.org/10.1016/j.asr.2021.08.030

McGirr, R., Tregoning, P., Allgeyer, S., McQueen, H., & Purcell, A. P. (2023). Interplay of altitude, ground track coverage, noise, and regularization in the spatial resolution of GRACE gravity field models. Journal of Geophysical Research: Solid Earth, 128(1), e2022JB024330. https://doi.org/10.1029/2022JB024330

McInnes, C. R. (1999). Solar sailing: Technology, dynamics and mission applications. Springer Praxis Books. https://doi.org/10.1007/978-1-4471-3992-8

McMahon, J. W., & Scheeres, D. J. (2010). New solar radiation pressure force model for navigation. Journal of Guidance, Control, and Dynamics, 33(5), 1418-1428. https://doi.org/10.2514/1.48202

Mehta, P. M., Lühr, H., Rother, M., & Stolle, C. (2017). New density estimates derived using accelerometers on board the CHAMP and GRACE satellites. Space Weather, 15(4), 558–576. https://doi.org/10.1002/2016SW001562

Mehta, P. M., Paul, S. N., Crisp, N. H., Sheridan, P. L., Siemes, C., March, G., & Bruinsma, S. (2023). Satellite drag coefficient modeling for thermospheric science and mission operations. Advances in Space Research, 72(12), 5443-5459. https://doi.org/10.1016/j.asr.2023.09.030

Menvielle, M., Iyemori, T., Marchaudon, A., & Nosé, M. (2010). Geomagnetic indices. In Geomagnetic observations and models (pp. 183-228). Dordrecht: Springer Netherlands. https://doi.org/10.1007/978-90-481-9858-0_7

Milani, A., Nobili, A. M., & Farinella, P. (1987). Non-gravitational perturbations and satellite geodesy. Advances in Space Research, 7(2), 117-126. https://doi.org/10.1016/0273-1177(87)90347-3

Misra, P., & Enge, P. (2011). Global Positioning System: Signals, Measurements, and Performance. Ganga-Jamuna Press.

Montenbruck, O., & Gill, E. (2000, June). Real-time estimation of SGP4 orbital elements from GPS navigation data. In International Symposium Space Flight Dynamics, Biarritz, France (pp. 26-30).

Montenbruck, O., et al. (2005). Reduced dynamic orbit determination using GPS code and carrier measurements. Aerospace Science and Technology, 9(3), 261–271. https://doi.org/10.1016/j.ast.2005.01.003

Montenbruck, O., Schmid, R., Mercier, F., Steigenberger, P., Noll, C., Fatkulin, R., ... & Ganeshan, A. S. (2015). GNSS satellite geometry and attitude models. Advances in Space Research, 56(6), 1015-1029. https://doi.org/10.1016/j.asr.2015.06.019

Moore, P., Turner, J. F., & Qiang, Z. (2003). CHAMP orbit determination and gravity field recovery. Advances in Space Research, 31(8), 1897-1903. https://doi.org/10.1016/S0273-1177(03)00148-8

Murböck, M., Abrykosov, P., Dahle, C., Hauk, M., Pail, R., & Flechtner, F. (2023). In-orbit performance of the GRACE accelerometers and microwave ranging instrument. Remote Sensing, 15(3), 563. https://doi.org/10.3390/rs15030563

Murase, K., Kataoka, R., Nishiyama, T., Sato, K., Tsutsumi, M., Tanaka, Y., ... & Sato, T. (2023). Atmospheric Ionizations by Solar X-Rays, Solar Protons, and Radiation Belt Electrons in September 2017 Space Weather Event. Space Weather, 21(12), e2023SW003651. https://doi.org/10.1029/2023SW003651

Musen, P. (1960). The influence of the solar radiation pressure on the motion of an artificial satellite. Journal of Geophysical Research, 65(5), 1391-1396. https://doi.org/10.1029/JZ065i005p01391

Muzi, D., & Allasio, A. (2004). GOCE: The first core Earth explorer of ESA's Earth observation programme. Acta Astronautica, 54(3), 167-175. https://doi.org/10.1016/j.actaastro.2003.09.017

Neta, B., & Vallado, D. (1997). On satellite umbra/penumbra entry and exit positions. Advances in the Astronautical Sciences, 95(2), 715–724. https://doi.org/10.1007/bf03546195

Nie, Y., Shen, Y., Chen, J., & Chen, Q. (2024). Improved GRACE-FO gravity field solution by combining different accelerometer transplant products. Journal of Geophysical Research: Solid Earth, 129(5), e2023JB028013. https://doi.org/10.1029/2023JB028013

Olsen, N., Friis-Christensen, E., Floberghagen, R., Alken, P., Beggan, C. D., Chulliat, A., ... & Visser, P. N. (2013). The Swarm satellite constellation application and research facility (SCARF) and Swarm data products. Earth, Planets and Space, 65, 1189-1200. https://doi.org/10.5047/eps.2013.09.008

Pail, R., Bruinsma, S., Migliaccio, F., Förste, C., Goiginger, H., Schuh, W. D., ... & Tscherning, C. C. (2011). First GOCE gravity field models derived by three different approaches. Journal of Geodesy, 85, 819-843. https://doi.org/10.1007/s00190-011-0467-5

Pagiatakis, S. D. (1999). Stochastic significance of peaks in the least-squares spectrum. Journal of Geodesy, 73(2), 67-78. (https://doi.org/10.1007/s001900050220).

Pagiatakis, S. D., & Peidou, A. (2021). The intriguing structure of stripes in GRACE geopotential models. Remote Sensing, 13(21), 4362. https://doi.org/10.3390/rs13214362

Park, J., Stolle, C., Yamazaki, Y., Rauberg, J., Michaelis, I., & Olsen, N. (2020). Diagnosing low-/mid-latitude ionospheric currents using platform magnetometers: CryoSat-2 and GRACE-FO. Earth, Planets and Space, 72, 1-18. https://doi.org/10.1186/s40623-020-01280-5

Park, J., van den IJssel, J., & Siemes, C. (2023). Dayside upper-thermospheric density fluctuations as observed by GRACE and GRACE-FO at ~500 km height. Journal of Geophysical Research: Space Physics, 128(1), e2022JA030976. https://doi.org/10.1029/2022JA030976

Parvulescu, A. (1961). Filters for Near-Field Noise. The Journal of the Acoustical Society of America, 33(11_Supplement), 1681-1681.

Perona, G., et al. (2013). Thermal modeling and impact on satellite dynamics: A case study of the ESA SMOS mission. IEEE Transactions on Geoscience and Remote Sensing, 51(4), 2042-2055. https://doi.org/10.1109/TGRS.2012.2227756

Peterseim, N., Flury, J., & Schlicht, A. (2012). Magnetic torquer induced disturbing signals within GRACE accelerometer data. Advances in Space Research, 49(9), 1388-1394. https://doi.org/10.1016/j.asr.2012.02.021

Peterseim, N., Schlicht, A., Flury, J., & Dahle, C. (2014). Identification and reduction of satellite-induced signals in GRACE accelerometer data. In Observation of the System Earth from Space-CHAMP, GRACE, GOCE and Future Missions: GEOTECHNOLOGIEN Science Report No. 20 (pp. 53-61).

Picone, J. M., Hedin, A. E., Drob, D. P., & Aikin, A. C. (2002). NRLMSISE-00 empirical model of the atmosphere: Statistical comparisons and scientific issues. Journal of Geophysical Research: Space Physics, 107(A12), 1468. https://doi.org/10.1029/2002JA009430

Piersanti, M., De Michelis, P., Del Moro, D., Tozzi, R., Pezzopane, M., Consolini, G., ... & Diego, P. (2020). From the Sun to the Earth: August 25, 2018 geomagnetic storm effects. Annales Geophysicae, 38, 703-724. https://doi.org/10.5194/angeo-38-703-2020

Proakis, J. G., & Salehi, M. (2008). Optimum receivers for AWGN channels. Digital communications, 5, 178-182.

Punnoose, R. J., Jacklin, N., & Counsil, D. (2011, November). Spatially focusing a radio signal and simultaneously nulling it at another location using time-reversal signal processing. In 2011-MILCOM 2011 Military Communications Conference (pp. 401-405). IEEE.

Qian, L., & Solomon, S. C. (2012). Thermospheric density: An overview of temporal and spatial variations. Space Science Reviews, 168, 147-173. https://doi.org/10.1007/s11214-011-9810-z

Raitt, W. J., & Clark, D. H. (1973). Wave-like disturbances in the ionosphere. Nature, 243(5409), 508-509. https://doi.org/10.1038/243508a0

Reigber, C., Lühr, H., & Schwintzer, P. (2002). CHAMP mission status. Advances in Space Research, 30(2), 129-134. https://doi.org/10.1016/S0273-1177(02)00276-4

Reigber, C., Jochmann, H., Wünsch, J., Petrovic, S., Schwintzer, P., Barthelmes, F., ... & Perosanz, F. (2005). Earth gravity field and seasonal variability from CHAMP. In Earth observation with CHAMP: results from three years in orbit (pp. 25-30). Springer.

Rievers, B., & Wöske, F. (2022, December). Thermospheric Density Estimation from Accelerometer Data of Geodetic Satellites–Evaluation of Sensitivity towards Non-Gravitational Force Modeling, POD calibration, and Comparison of Results. In AGU Fall Meeting Abstracts (Vol. 2022, pp. SA45C-2177).

Rhoden, E. A., Forbes, J. M., & Marcos, F. A. (2000). The influence of geomagnetic and solar variabilities on lower thermosphere density. Journal of Atmospheric and Solar-Terrestrial Physics, 62(11), 999-1013. https://doi.org/10.1016/S1364-6826(00)00089-0

Rievers, Benny, Maike List, and Stefanie Bremer. Advanced Thermal Radiation Pressure modeling and its benefits for the MICROSCOPE mission. Advances in the Astronautical Sciences Spaceflight Mechanics 158 (2016): 2997-3012.

RM, S. (2019). Computation of eclipse time for low-earth orbiting small satellites. International Journal of Aviation, Aeronautics, and Aerospace, 6(5), 15. https://doi.org/10.15394/ijaaa.2019.1474

Robertson, R. V. (2015). Highly physical solar radiation pressure modeling during penumbra transitions. Virginia Polytechnic Institute and State University.

Robertson, R., Flury, J., Bandikova, T., & Schilling, M. (2015). Highly physical penumbra solar radiation pressure modeling with atmospheric effects. Celestial Mechanics and Dynamical Astronomy, 123, 169-202. https://doi.org/10.1007/s10569-015-9635-3

Rodriguez-Solano, C. J., Peter, H., & Steigenberger, P. (2012). Impact of Earth radiation pressure on GPS satellites. Journal of Geodesy, 86(11), 1055-1064. https://doi.org/10.1007/s00190-012-0564-6

Rodrigues, M., Bergé, J., Boulanger, D., Christophe, B., Dalin, M., Lebat, V., & Liorzou, F. (2022, May). Space accelerometers for micro and nanosatellites: Fundamental physics and geodesy missions from MICROSCOPE, GOCE and GFO return of experience. In 4S Symposium 2022.

Roh, K., Bang, H., Kim, Y., Kim, J., & Bang, H. (2019). Solar radiation pressure modeling for deep space navigation. Journal of Guidance, Control, and Dynamics, 42(6), 1158-1165. https://doi.org/10.2514/1.G003623

Roman, J. R., Rangaswamy, M., Davis, D. W., Zhang, Q., Himed, B., & Michels, J. H. (2000). Parametric adaptive matched filter for airborne radar applications. IEEE Transactions on Aerospace and Electronic Systems, 36(2), 677-692.

Rostoker, G. (1972). Geomagnetic indices. *Reviews of Geophysics*, *10*(4), 935-950.

Rummel, R., Yi, W., & Stummer, C. (2011). GOCE gravitational gradiometry. Journal of Geodesy, 85(11), 777-790. https://doi.org/10.1007/s00190-011-0452-0

Sack, M., Ito, M. R., & Cumming, I. G. (1985, February). Application of efficient linear FM matched filtering algorithms to synthetic aperture radar processing. In IEE Proceedings F (Communications, Radar and Signal Processing) (Vol. 132, No. 1, pp. 45-57). IET Digital Library.

Santoni, F., Cerri, L., Piergentili, F., Donati, A., & Cosmo, M. (2018). Analysis of the impact of thermal radiation pressure on small satellites attitude control. Acta Astronautica, 151, 1-11. https://doi.org/10.1016/j.actaastro.2018.06.018

Scheer, J., & Holm, W. A. (2010). Principles of modern radar.

Schlegel, K., Lühr, H., St.-Maurice, J. P., Crowley, G., & Hackert, C. (2005). Thermospheric density structures over the polar regions observed with CHAMP. Annales Geophysicae, 23(5), 1659-1672. Göttingen, Germany: Copernicus Publications.

Schlicht, A. (2022). GRACE accelerometers sensitive to ionosphere plasma waves: Similarities between twangs and whistlers. Geosciences, 12(6), 228. https://doi.org/10.3390/geosciences12060228

Sehnal, L. (1970). Radiation pressure effects in the motion of artificial satellites. In Dynamics of Satellites (1969) Proceedings of a Symposium held in Prague, May 20–24, 1969 (pp. 262-272). Berlin, Heidelberg: Springer Berlin Heidelberg. https://doi.org/10.1007/978-3-642-49300-2_34

Sibbett T., H. Moradi and B. Farhang-Boroujeny, "Normalized Matched Filter for Blind Interference Suppression," *MILCOM 2018 - 2018 IEEE Military Communications Conference (MILCOM)*, Los Angeles, CA, USA, 2018, pp. 1-6, doi: 10.1109/MILCOM.2018.8599836.

Siemes, C., Haagmans, R., Kern, M., Plank, G., & Floberghagen, R. (2012). Monitoring GOCE gradiometer calibration parameters using accelerometer and star sensor data: Methodology and first results. Journal of Geodesy, 86(8), 629-645. https://doi.org/10.1007/s00190-012-0545-8

Siemes, C., de Teixeira da Encarnação, J., Doornbos, E., Van Den Ijssel, J., Kraus, J., Pereštý, R., ... & Holmdahl Olsen, P. E. (2016). Swarm accelerometer data processing from raw accelerations to thermospheric neutral densities. Earth, Planets and Space, 68, 1-16.

https://doi.org/10.1186/s40623-016-0526-4

Siemes, C., Borries, C., Bruinsma, S., Fernandez-Gomez, I., Hładczuk, N., den IJssel, J., ... & Visser, P. (2023). New thermosphere neutral mass density and crosswind datasets from CHAMP, GRACE, and GRACE-FO. Journal of Space Weather and Space Climate, 13, 16. https://doi.org/10.1051/swsc/2023014

Siemes, C., van den IJssel, J., & Visser, P. (2024). Uncertainty of thermosphere mass density observations derived from accelerometer and GNSS tracking data. Advances in Space Research, 73(10), 5043-5063. https://doi.org/10.1016/j.asr.2024.04.012

Somsikov, V. M., & Troitskii, B. V. (1975). The generation of disturbances in the atmosphere due to the passage through it of the solar terminator. Geomagnetism and Aeronomy, 15, 856-860.

Somsikov, V. M. (1995). On mechanisms for the formation of atmospheric irregularities in the solar terminator region. Journal of Atmospheric and Terrestrial Physics, 57(1), 75-83. https://doi.org/10.1016/0021-9169(94)00069-B

Somsikov, V. M. (2011). Solar terminator and dynamic phenomena in the atmosphere: A review. Geomagnetism and Aeronomy, 51, 707-719.

Spence, H. E., et al. (2010). Thermal influence on satellite drag and the space environment: A study using the NASA TIMED satellite. Journal of Space Weather and Space Climate, 1(1), A02. https://doi.org/10.1051/swsc/2010002

Stephens, G. L., et al. (2015). The albedo of Earth. Reviews of Geophysics, 53(1), 141–163. https://doi.org/10.1002/2014RG000449

Suesser-Rechberger, B., Krauss, S., Strasser, S., & Mayer-Guerr, T. (2022). Improved precise kinematic LEO orbits based on the raw observation approach. Advances in Space Research, 69(10), 3559-3570. https://doi.org/10.1016/j.asr.2022.02.013

Sutton, E. K., Forbes, J. M., & Nerem, R. S. (2005). Global thermospheric neutral density and wind response to the severe 2003 geomagnetic storms from CHAMP accelerometer data. Journal of Geophysical Research: Space Physics, 110(A9). https://doi.org/10.1029/2004JA010985

Sutton, E. K., Nerem, R. S., & Forbes, J. M. (2007). Density and winds in the thermosphere deduced from accelerometer data. Journal of Spacecraft and Rockets, 44(6), 1210-1219. https://doi.org/10.2514/1.28641

Tanter, M., Thomas, J. L., & Fink, M. (2000). Time reversal and the inverse filter. The Journal of the Acoustical Society of America, 108(1), 223-234.

Tapley, B. D., Bettadpur, S., Watkins, M., & Reigber, C. (2004). The gravity recovery and climate experiment: Mission overview and early results. Geophysical Research Letters, 31(9), L09607. https://doi.org/10.1029/2004GL019920

Tapley, B. D., Watkins, M. M., Flechtner, F., Reigber, C., Bettadpur, S., Rodell, M., ... & Velicogna, I. (2019). Contributions of GRACE to understanding climate change. Nature Climate Change, 9(5), 358-369. https://doi.org/10.1038/s41558-019-0456-2

Tapping, K. F. (2013). The 10.7 cm solar radio flux (F10.7). Space weather, 11(7), 394-406. https://doi.org/10.1002/swe.20064

Teixeira da Encarnação, J., Visser, P., Arnold, D., Bezdek, A., Doornbos, E., Ellmer, M., ... & Dahle, C. (2020). Description of the multi-approach gravity field models from Swarm GPS data. Earth System Science Data, 12(2), 1385-1417. https://doi.org/10.5194/essd-12-1385-2020

Tobiska, W. K., Bouwer, S. D., & Bowman, B. R. (2008). The development of new solar indices for use in thermospheric density modeling. Journal of Atmospheric and Solar-Terrestrial Physics, 70(5), 803-819. https://doi.org/10.1016/j.jastp.2007.11.006

Touboul, P., Willemenot, E., Foulon, B., & Josselin, V. (1999). Accelerometers for CHAMP, GRACE and GOCE space missions: synergy and evolution. Boll. Geof. Teor. Appl, 40(3-4), 321-327.

Tozzi, R., Pezzopane, M., De Michelis, P., & Piersanti, M. (2015). Applying a curl-B technique to Swarm vector data to estimate nighttime F region current intensities. Geophysical Research Letters, 42(15), 6162-6169. https://doi.org/10.1002/2015GL065168

Trucco, A. (2001). Experimental results on the detection of embedded objects by a prewhitening filter. IEEE journal of oceanic engineering, 26(4), 783-794.

Tsuda, Y., Mori, O., Funase, R., Sawada, H., Yamamoto, T., Saiki, T., & Endo, T. (2011). Achievement of IKAROS—Japanese deep space solar sail demonstration mission. Acta Astronautica, 69(9-10), 833-840. https://doi.org/10.1016/j.actaastro.2011.05.016

Turin, G. (1960). An introduction to matched filters. IRE Transactions on Information Theory, 6(3), 311–329. https://doi.org/10.1109/TIT.1960.1057571

Ulrich, T. J., Anderson, B., Le Bas, P. Y., Payan, C., Douma, J., & Snieder, R. (2012, July). Improving time reversal focusing through deconvolution: 20 questions. In Proceedings of Meetings on Acoustics (Vol. 16, No. 1). AIP Publishing.

Vadas, S. L., & Nicolls, M. J. (2012). The phases and amplitudes of gravity waves propagating and dissipating in the thermosphere: Theory. Journal of Geophysical Research: Space Physics, 117(A5). https://doi.org/10.1029/2011JA017414

Vadas, S. L., & Crowley, G. (2017). Neutral wind and density perturbations in the thermosphere created by gravity waves observed by the TIDDBIT sounder. Journal of Geophysical Research: Space Physics, 122(6), 6652-6678. https://doi.org/10.1002/2017JA024233

Vallado, D. A., & McClain, W. D. (2001). Fundamentals of Astrodynamics and Applications. Space Technology Library.

Vallado, D. A. (2007). An analysis of state vector prediction accuracy. Paper USR, 07-S6.

Vallado, D. A. (2013). Fundamentals of Astrodynamics and Applications. Springer.

van den IJssel, J., Encarnação, J., Doornbos, E., & Visser, P. (2015). Precise science orbits for the Swarm satellite constellation. Advances in Space Research, 56(6), 1042-1055. https://doi.org/10.1016/j.asr.2015.06.016

van den IJssel, J., Doornbos, E., Iorfida, E., March, G., Siemes, C., & Montenbruck, O. (2020). Thermosphere densities derived from Swarm GPS observations. Advances in Space Research, 65(7), 1758-1771. https://doi.org/10.1016/j.asr.2020.01.029

van der Meijde, M., Pail, R., Bingham, R., & Floberghagen, R. (2015). GOCE data, models, and applications: A review. International Journal of Applied Earth Observation and Geoinformation, 35, 4-15. https://doi.org/10.1016/j.jag.2014.08.003

Van Helleputte, T., & Visser, P. (2008). GPS based orbit determination using accelerometer data. Aerospace Science and Technology, 12(6), 478-484. https://doi.org/10.1016/j.ast.2007.10.005

Vielberg, K., Forootan, E., Lück, C., Löcher, A., Kusche, J., & Börger, K. (2018, May). Comparison of accelerometer data calibration methods used in thermospheric neutral density estimation. In Annales Geophysicae (Vol. 36, No. 3, pp. 761-779). Copernicus GmbH. https://doi.org/10.5194/angeo-36-761-2018

Vielberg, K., & Kusche, J. (2020). Extended forward and inverse modeling of radiation pressure accelerations for LEO satellites. Journal of Geodesy, 94(4), 43. https://doi.org/10.1007/s00190-020-01374-4

Vielberg, K. (2024). Thermosphere and radiation effects in forward and inverse non-gravitational force modelling (Doctoral dissertation, Universitäts-und Landesbibliothek Bonn). https://orcid.org/0000-0001-5429-0988

Virgili, J., Roberts, P. C., & Hara, N. C. (2015). Atmospheric interface reentry point targeting using aerodynamic drag control. Journal of Guidance, Control, and Dynamics, 38(3), 403-413.

Visser, P. N. (2011). A glimpse at the GOCE satellite gravity gradient observations. Advances in Space Research, 47(3), 393-401. https://doi.org/10.1016/j.asr.2010.06.009

Visser, P. A., & van den IJssel, J. (2016). Calibration and validation of individual GOCE accelerometers by precise orbit determination. Journal of Geodesy, 90, 1-13. https://doi.org/10.1007/s00190-015-0850-0

Volkov, I. I., Semenov, A. I., & Suevalov, V. V. (2008). Analysis of thermospheric density variations neglected in modern atmospheric models using accelerometer data. Solar System Research, 42, 51-62. https://doi.org/10.1134/S003809460801005X

Wang, Y. M., Lean, J. L., & Sheeley Jr, N. R. (2005). Modeling the Sun's magnetic field and irradiance since 1713. The Astrophysical Journal, 625(1), 522. [DOI: 10.1086/429689](https://doi.org/10.1086/429689).

Wang, Y., Li, M., Jiang, K., Li, W., Zhao, Q., Fang, R., ... & Mu, R. (2023). Improving precise orbit determination of LEO satellites using enhanced solar radiation pressure modeling. Space Weather, 21(1), e2022SW003292. https://doi.org/10.1029/2022SW003292

Wei, G., Lu, J., Wang, W., Tian, Y., Li, J., Xiong, S., ... & Wang, J. (2023). Temperature variations in the mesosphere and lower thermosphere during geomagnetic storms with disparate durations at high latitudes. Universe, 9(2), 86. https://doi.org/10.3390/universe9020086

Wells, D., Vanicek, P., & Pagiatakis, S. (1970). Least-Squares spectral analysis revisited. Nature, 225(5232), 569. [DOI: 10.1038/225569a0](https://doi.org/10.1038/225569a0).

Wermuth M, Montenbruck O, van Helleputte T (2010) GPS high precision orbit determination software tools (GHOST). In: 4th International conference on astrodynamics tools and techniques, 3–6 May 2010, Madrid

Wen, H. Y., Kruizinga, G., Paik, M., Landerer, F., Bertiger, W., Sakumura, C., Bandikova, T., & McCullough, C. M. (2019). Gravity Recovery and Climate Experiment Follow-On (GRACE-FO) Level-1 data product user handbook (Technical Report JPL D-56935). NASA Jet Propulsion Laboratory, California Institute of Technology.

Wermuth M, Montenbruck O, van Helleputte T (2010) GPS high precision orbit determination software tools (GHOST). In: 4th International conference on astrodynamics tools and techniques, 3–6 May 2010, Madrid

Wood, M., Chen, W. H., & Fertin, D. (2006, October). Model predictive control of low earth orbiting spacecraft with magneto-torquers. In 2006 IEEE Conference on Computer Aided Control System Design, 2006 IEEE International Conference on Control Applications, 2006 IEEE International Symposium on Intelligent Control (pp. 2908-2913). IEEE. https://doi.org/10.1109/CACSD-CCA-ISIC.2006.4777147

Wöske, F., Kato, T., Rievers, B., & List, M. (2019). GRACE accelerometer calibration by high precision non-gravitational force modeling. Advances in Space Research, 63(3), 1318-1335. https://doi.org/10.1016/j.asr.2018.11.019

Wöske, F. (2021). Gravity Field Recovery from GRACE Satellite Data and Investigation of Sensor, Environment and Processing-Option Influences by Closed Loop Mission Simulation (Doctoral dissertation, Universität Bremen).

Wu, S.C., Kruizinga, G., and Bertiger, W. (May 2006). "Algorithm Theoretical Basis Document for GRACE Level-1B Data Processing V.1.2." GRACE Document 327-741 (JPLD-27672), p. 9. Retrieved from http://podaac.jpl.nasa.gov/grace/documentation.html#1b

Wu, S. C., & Bar-Sever, Y. (2001, September). Orbit determination of VSOP-2 with GPS measurements. In Proceedings of the 14th International Technical Meeting of the Satellite Division of The Institute of Navigation (ION GPS 2001) (pp. 2272-2276).

Yamazaki, W., & Arakawa, Y. (2015). Inexpensive airfoil shape optimization for vertical axis wind turbine and its validation. Journal of Fluid Science and Technology, 10(2), JFST0015-JFST0015. https://doi.org/10.1299/jfst.2015jfst0015

Yang, Z., Zhang, H., Xu, P., & Luo, Z. (2023). Unsupervised noise reductions for gravitational reference sensors or accelerometers based on the Noise2Noise method. Sensors, 23(13), 6030. https://doi.org/10.3390/s23136030

Yuan, D. (2018). JPL level-2 processing standards document for level-2 product release 06. Jet Propulsion Laboratory, California Institute of Technology.

Zehentner, N., & Mayer-Gürr, T. (2016). Precise orbit determination based on raw GPS measurements. Journal of Geodesy, 90, 275-286.

Zhang, Y., Liu, X., & Wang, Y. (2019). Experimental investigation of thermal control coatings for reducing thermal radiation pressure on spacecraft. International Journal of Heat and Mass Transfer, 140, 1035-1045. https://doi.org/10.1016/j.ijheatmasstransfer.2019.06.061

Zhang, Z., Chen, B., & Yang, M. (2021). Time reversal detection in a multistatic radar system with a varying environment. IET Radar, Sonar & Navigation, 15(7), 796-811.

Zhang, J., You, W., Yu, B., & Fan, D. (2023). GRACE-FO accelerometer performance analysis and calibration. GPS Solutions, 27(4), 158. https://doi.org/10.1007/s10291-023-01410-2

Zhao, L., & Zeng, B. (2012, July). Robust unit commitment problem with demand response and wind energy. In 2012 IEEE Power and Energy Society General Meeting(pp. 1-8). IEEE. https://doi.org/10.1109/PES.2012.6335811

Zheng, W., Hsu, H., Zhong, M., & Yun, M. (2011). Efficient calibration of the non-conservative force data from the space-borne accelerometers of the twin grace satellites. Transactions of the Japan Society for Aeronautical and Space Sciences, 54(184), 106-110. https://doi.org/10.2322/tjsass.54.106

Ziebart, M., Adhya, S., Sibthorpe, A., Edwards, S., & Cross, P. (2005). Combined radiation pressure and thermal modelling of complex satellites: Algorithms and on-orbit tests. Advances in Space Research, 36(3), 424-430. https://doi.org/10.1016/j.asr.2005.03.035